UNIVERSITY OF SOUTHAMPTON

Distributed Feedback Fibre Laser Strain and Temperature Sensors

by

Oliver Hadeler

A thesis submitted for
the degree of Doctor of Philosophy

Faculty of Engineering and Applied Science
Department of Electronics and Computer Science
Optoelectronics Research Centre

November 2001

UNIVERSITY OF SOUTHAMPTON

ABSTRACT

FACULTY OF ENGINEERING AND APPLIED SCIENCE
DEPARTMENT OF ELECTRONICS AND COMPUTER SCIENCE

Doctor of Philosophy

DISTRIBUTED FEEDBACK FIBRE LASER STRAIN AND TEMPERATURE SENSORS

by Oliver Hadeler

This thesis presents the development of two new types of polarimetric distributed feedback (DFB) fibre laser sensors for simultaneous strain and temperature measurements. These fibre Bragg grating (FBG) based sensors offer strain and temperature measurement accuracies of $\pm 0.3 - \pm 15\,\mu\epsilon$ and $\pm 0.04 - \pm 0.2\,^{\circ}\mathrm{C}$ which are suitable for many applications. The main advantage of these DFB fibre laser sensors over other FBG based sensors is the simplicity of their interrogation system. The first type of sensor operates stably in a single longitudinal mode which splits into two orthogonally polarised modes. This sensor utilises the wavelength of one polarisation mode and the RF beat frequency between the two polarisation modes. The system complexity is reduced to a minimum in the dual longitudinal mode polarimetric DFB fibre laser sensor which utilises the RF beat frequencies between two longitudinal modes and their associated orthogonal polarisations, therefore requiring only a simple and cost effective frequency counter.

The ability of measuring strain and temperature simultaneously is demonstrated with prototype sensors embedded in a concrete test specimen. Miniature sensor packages are used to protect the sensors from their harsh environment and to enable handling by personnel who is inexperienced with fibre optic sensors.

The reduction of measurement resolution caused by external feedback into DFB fibre laser sensors, which is likely to occur in serially multiplexed sensor networks and remote sensors, is investigated.

Furthermore, operation of DFB fibre lasers up to $400\,^{\circ}\mathrm{C}$ is demonstrated. This yields important information about grating decay in sensor and telecommunication applications, the required annealing temperatures to prevent this decay and the initial grating strength to obtain the maximum output power of DFB fibre lasers.

This experimental work is supported by extensive theoretical modelling. For the first time an $Er^{3+}:Yb^{3+}$ DFB fibre laser model is presented which takes homogeneous upconversion of paired Er^{3+}-ions and pump excited state absorption into account. An extended version of this model incorporates, for the first time, self-heating in DFB fibre lasers which is caused by non-radiative decays. The performance of DFB fibre lasers employed in telecommunication applications is likely to benefit from these modelled results, which are also verified by experimental data.

Contents

1 Introduction

1.1 Motivation

Fibre optic technology is being applied in two major areas: telecommunication and sensing. The former plays an important role in today's global community where an ever increasing bandwidth is required to transmit vast amounts of data over large distances in shortest times. Optical fibre telecommunication networks offer larger bandwidth, lower transmission loss and less noise than their conventional electronic counterparts [1]. These advantages have been recognised by the industry and economy, reflected in the rapid growth of installed fibre optic networks and the steep increase of turnover of fibre optic telecommunication companies in recent years.

In parallel, but generating less economical and social impact, fibre optic sensors have been developed for a variety of applications. These include measuring concentration of chemicals in gases and liquids, electric current, pressure, temperature, strain and vibration [2]. Most research and development in fibre optic sensing is devoted to the last four physical parameters. The advantages of fibre optic sensors over conventional sensing techniques include reduced size and weight, immunity to electromagnetic interference and the potential to withstand harsh environments in which conventional sensors tend to fail [2, 3].

Furthermore, due to a higher signal to noise ratio many fibre optic sensors offer a better measurement resolution and accuracy than conventional sensors. Finally, multiplexed and distributed fibre optic sensors open the way for sophisticated sensor

networks, monitoring the environment with much higher spatial resolution and measurement accuracy than conventional sensors [2].

The key areas employing fibre optic sensors are aerospace [4], marine [5, 6] and civil [7, 8, 9] engineering and medical applications [10]. However, compared with conventional sensors the above stated advantages of fibre optic sensors are often outweighed by higher cost, increased system complexity and unfamiliar installation and operating procedures [3]. Consequently, fibre optic sensors play only a small role compared to well established conventional sensors. Clearly, in order to promote the application of fibre optic sensors and make use of their advantages the above mentioned drawbacks have to be addressed.

This thesis presents two novel accurate fibre optic strain and temperature sensors employing distributed feedback (DFB) fibre lasers as sensor heads. The minimised system complexity and the use of low cost standard fibre optic telecommunication and electronics components are key characteristics. Multiplexing capabilities and flexible package designs, which can also facilitate installation and handling procedures, are built into this sensor, offering the potential for its widespread application in all of the above mentioned areas.

Traditionally fibre optic sensing benefits from the technological developments in the telecommunications area, such as optical amplifiers (EDFAs), wavelength division multiplexers (WDMs) or fast optical modulators (AOMs, EOMs), and the cost reduction of optical components as a result of mass production. A second original and important result presented in this thesis is a demonstration of how knowledge can be transferred in the opposite direction, i.e. from fibre optic sensing to fibre optic telecommunication. Precise fibre optic temperature sensing technology is shown to provide valuable information to improve the understanding and performance of DFB fibre lasers, which are potential light sources in modern telecommunication networks.

1.2 Synopsis

Following this introduction, fundamental background information on fibre optic strain and temperature sensing is presented in Chapter 2. First the effects of strain, stress, temperature and thermal expansion of structures are briefly described. The need for simultaneous strain and temperature sensors is addressed in particular. This is followed by a brief and critical review of the most common fibre optic strain and temperature sensors. The expected advantages of DFB fibre laser sensors over passive gratings and other relevant fibre optic sensors will be highlighted

In Chapter 3 a comprehensive DFB fibre laser model is developed. This is, to my knowledge, the first DFB fibre laser model to include Er^{3+} and Yb^{3+} ions. Furthermore, homogeneous upconversion, pump ESA and non-radiative decays are included in the steady state laser rate equations which are solved using a new fast iterative algorithm. The close link between experimental and simulated data ensures that a thorough understanding of a real DFB fibre laser is obtained.

This model is significantly extended in Chapter 4 to incorporate, for the first time, self-heating of DFB fibre lasers caused by non-radiative decays. Using this model in conjunction with experimental data wavelength shift, output power drop and heat induced grating chirp as a result of the internal temperature distribution along a telecommunication type DFB fibre laser can be explained in great detail. In addition, the temperature distribution is measured along this DFB fibre laser by using the highly accurate DFB fibre laser temperature sensor presented in Section 5.1. This an example of how fibre optic sensing can offer valuable information to fibre optic telecommunication applications, and possible solutions to reduce the detrimental self-heating effects will be presented.

In Chapter 5 the first polarimetric DFB fibre laser sensor for simultaneous strain and temperature measurements is demonstrated. This sensor is based on previous work on a polarimetric DFB fibre laser sensor for separate temperature and pressure measurements [11]. This new sensor offers excellent strain and temperature accuracy and three sensors were subsequently packaged and embedded in a concrete test specimen. Results from the embedment process, temperature cycling and a three

point bending test are discussed in Section 5.2. During the last part of this Chapter lasing operation up to 400 °C and temperature sensing from room temperature to 200 °C are demonstrated in Section 5.3.

The first dual longitudinal mode polarimetric DFB fibre laser sensor is demonstrated in Chapter 6. This advanced fibre optic sensor employs RF beat frequencies between two longitudinal modes and two polarisation modes of a DFB fibre laser to measure strain and temperature simultaneously and with high accuracy. Simple and cost effective RF frequency counters can potentially be used to interrogate this sensor.

In Chapter 7 laser stability and measurement accuracy are investigated as a function of external feedback. Rayleigh scattering from long lead fibres and back-reflections from other DFB fibre laser sensors are considered. The former limits the maximum length of lead fibres allowed for remote DFB fibre laser sensors. The latter has a large influence on the measurement accuracy of multiplexed DFB fibre laser sensors.

Finally Chapter 8 concludes this thesis with a summary and an outlook towards future work.

2 Fibre optic strain and temperature sensing

2.1 Strain and temperature of structures

The theories of strain and temperature of solid bodies, or structures, are covered by many textbooks on general physics, mechanics and thermodynamic, e.g. [12, 13].

2.1.1 Strain and stress

A solid body will be deformed to some extent when an external force is acting on it. This deformation, which is described by a second rank tensor ϵ_{ik}, will change the shape and the volume of the body. For small deformations the relative extensions along the principal axes of the diagonalised strain tensor become [12]

$$\frac{\mathrm{d}x_i' - \mathrm{d}x_i}{\mathrm{d}x_i} \approx \epsilon_{ii}, \tag{2.1}$$

where $\mathrm{d}x_i$ and $\mathrm{d}x_i'$ are the components of the radius vector joining two closely spaced points before and after the deformation. In one dimension the last equation is usually written as

$$\frac{l' - l_0}{l_0} = \frac{\Delta l}{l_0} = \epsilon, \tag{2.2}$$

where l' and l_0 are the distances between two points in the strained and unstrained body, respectively and the dimensionless quantity ϵ is the 'mechanical strain' along the gauge length l_0. If ϵ is non-uniform along l_0 then the last equation yields only the average strain. In engineering sciences ϵ is also used as a strain unit. Since

the relative deformations of a solid body are usually very small a practical unit is $1\mu\epsilon \hat{=} \Delta l/l_0 = 10^{-6}$.

In a body which is not deformed all parts are in mechanical equilibrium, i.e. the resultant forces on any part of the body are zero. Under deformation the body moves away from its equilibrium state and internal forces, so-called internal stresses, arise which try to move the body back to its original state. Within the elastic limit of a solid body, the deformation is a linear function of the applied forces [12]:

$$\epsilon_{ik} = \frac{1}{E}\sigma_{ik}, \qquad \text{Hooke's law,} \tag{2.3}$$

where σ_{ik} is the second rank stress tensor and E is Young's modulus. The stress tensor describes the ith component of the force acting on a unit area perpendicular to the x_k-axis. In particular σ_{xx} is the normal force on a unit area perpendicular to the x-axis and σ_{yx} and σ_{zx} are the tangential, or shear, forces on the same surface element.

In the special case of the linear extension of a rod, or an optical fibre for that matter, where the forces are applied perpendicular to the end faces of the rod, Hooke's law reduces to [12]

$$\epsilon_{zz} = \frac{1}{E}\sigma_{zz}, \tag{2.4-a}$$

$$\epsilon_{xx} = \epsilon_{yy} = -\mu\epsilon_{zz}, \tag{2.4-b}$$

where the component ϵ_{zz} describes the relative longitudinal extension of the rod. As a result of its longitudinal extension the radius of the rod decreases. The ratio μ of the transverse compression to the longitudinal extension is called Poisson's ratio.

2.1.2 Temperature and thermal expansion

One of the fundamental concepts of thermodynamics defines heat as the random movement of atoms or molecules. Temperature is just a measure for the mean kinetic energy of the atoms or molecules [13]. A change in temperature will result in a deformation of a solid body. If the body can expand freely, i.e. without external forces acting on it, the relative extension in one dimension is given by [12]

$$\frac{\Delta l}{l_0} = \alpha(T - T_0) = \alpha\Delta T, \tag{2.5}$$

where α is the thermal expansion coefficient and $\Delta T = T - T_0$ is the temperature change.

The absence of external forces implies that the body remains in its mechanical equilibrium. Therefore, no internal stresses σ_{ik} occur and the structural strength of the body is not affected as long as its temperature remains below a critical value where the body starts to soften. Thus the integrity of a structure is not affected by free thermal expansion. However, in most real structures thermal expansion is restricted in one way or the other. Then external forces act against the expansion or contraction of members of the structure, inducing 'thermal stresses' which can eventually lead to mechanical failure if they exceed the maximum permissible stress of the structure. If, e.g., the thermal expansion of one part of a structure is completely prevented along the z-axis the internal stress becomes $\sigma_{zz} = E\epsilon_{zz} = E\alpha\Delta T$.

It should be pointed out here that a fair amount of confusion still exists over free and restricted thermal expansion in the scientific literature. Free thermal expansion is often regarded as apparent or thermally induced strain although internal stresses are absent. This view becomes potentially dangerous in the case of completely restricted thermal expansion where the body does not deform and the internal stress remains undetected. According to Hooke's law (2.3) strain and stress cannot occur without each other. Therefore, in this thesis free and restricted thermal expansion and the associated internal stresses and strains will distinguished.

2.1.3 The need for simultaneous strain and temperature monitoring

The immediate consequence of the last Section, with respect to structural monitoring, is the need to measure strain and temperature simultaneously in order to fully assess the 'health state' of a structure. This usually requires two conventional sensors, one measuring the mechanically and thermally induced deformations, the other measuring the temperature. Then the three dimensional versions of equations (2.2) and (2.5) can be used to determine the integrity of the structure. However, the need for two separate sensors is undesirable for three reasons:

1. the need for twice as many sensors than sensing points,
2. the potential difficulty of placing two sensors close together in confined space,
3. the potential difficulty to ensure that temperature sensors do not experience any strain.

Some fibre Bragg grating (FBG) sensors, whose fundamental properties are outlined in the next Section, and especially the two novel active FBG sensors presented in this thesis (see Chapters 5 and 6), overcome these problems, making them very attractive for structural monitoring in a wide range of applications, e.g. aerospace and civil engineering.

2.2 Fibre Bragg grating strain and temperature sensors

2.2.1 Overview of fibre optic strain and temperature sensors

A large variety of fibre optic strain and temperature sensors has been developed since its first demonstration by Butter and Hocker in 1978 [14]. For a detailed overview the reader is referred to a number of review articles [2, 3, 15, 16, 17]. A list of common fibre optic strain and temperature sensors together with their basic properties is compiled in Table 2.1. More details about those sensors can be found in the literature cited within the Table.

As every strain and temperature sensing application has different requirements, no fibre optic strain and temperature sensor can be employed satisfactorily across the whole range of applications. As a guideline, the most important sensor characteristics which have to be taken into account when choosing the appropriate sensor are:

- measurement resolution and accuracy,
- measuring range,

Table 2.1. Five commonly used types of fibre optic strain and temperature sensors. Sensors based on fibre Bragg gratings (FBGs) are probably the most versatile and therefore most widespread type of sensor. See main text for a brief review of fibre optic sensors, their particular advantages and disadvantages. Further information can be found in [2, 16, 17, 18, 19, 20] and in the literature cited in the last column.

Sensor type		Classification		Serial multiplexing	Measurand	Measuring method	References
Interferometer	Fabry-Perot	extrinsic	point	limited	elongation	free spectral range, wavelength λ, low coherence	[21, 22, 23, 24]
	Michelson	intrinsic & extrinsic	point	yes	elongation	low coherence	[25]
OTDR		intrinsic	point	yes	elongation	time delay	[26]
OFDR		intrinsic	point	yes	elongation	phase delay	[27]
Bragg gratings (FBG)	passive	intrinsic	point	yes	strain	λ, spectral width	[16, 18, 28, 29, 30]
	active (fibre laser)	intrinsic	point	yes	strain	λ, birefringence (polarisation mode spacing)	[11, 31, 32, 33, 34]
Brillouin scattering	spontaneous	intrinsic	distri-	NA	strain	Brillouin frequency	[35, 36]
	stimulated		buted			shift	[37, 38]
Polarimetric	transmission	intrinsic	point	no	strain	polarisation state	
	reflection (e.g. FBG)	intrinsic	point	yes	strain	birefringence	[39]

- response time,
- gauge length,
- interrupt resistant operation,
- number of sensing points,
- system complexity,
- practicality,
- size,
- cost.

2.2.2 Advantages and disadvantages of fibre Bragg grating sensors

Over the last two decades it has emerged that strain and temperature sensors based on FBGs are probably the most versatile and therefore most widespread type of sensor. A review on fabrication, basic properties and applications of FBGs can be found in [18, 19, 20]. The unique combination of three key properties make FBG sensors superior over other fibre optic strain and temperature sensors:

1. intrinsic sensors, i.e. entirely contained inside the fibre
2. strain resolution and measuring range independent of gauge length
3. wavelength encoded measurands.

The smallest fibre optic sensors are entirely contained within the fibre and require no external components. The size of these intrinsic sensors is therefore equal to the size of the fibre itself. They are mechanically more robust than extrinsic sensors. Extrinsic Fabry-Perot etalons, e.g., incorporate potentially weak mechanical joints between parts of the sensor [21, 22, 23, 24]. Furthermore, optical losses caused by beam divergence during free space propagation in extrinsic sensors [22, 40] are absent in intrinsic sensors.

Fibre optic strain sensors based on low-coherence Michelson interferometers [25], Fabry-Perot etalons or optical time domain reflectometry (OTDR) [26] measure elongation $\Delta l = l' - l_0$ rather than strain $\epsilon = \Delta l / l_0$. Therefore, for a given length resolution $\sigma(l)$ the strain resolution $\sigma(\epsilon) = \sigma(l)/l_0$ depends on the gauge length l_0 of the sensor. Furthermore, the measurement range $\Delta l_{\max}$ is usually limited by the interrogation system leading to a further trade-off between maximum strain measurement range and gauge length: $\epsilon_{\max} = \Delta l_{\max}/l_0$. Because FBG based sensors, on the other hand, measure strain directly, $\sigma(\epsilon)$ and $\epsilon_{\max}$ are independent of l_0.

Wavelength can be measured with high precision and good signal to noise ratio with relatively simple interrogation systems, e.g. tunable filters, edge filters or spectrometers [28, 29, 31]. The wavelength of a FBG sensor is absolute and a linear function of strain and temperature. Although strain and temperature sensors based on Brillouin scattering offer linear responses they require complex interrogation systems which offer only a relatively low signal to noise ratio and a low measurement resolution [35, 37]. Furthermore, sensors based on stimulated Brillouin scattering require access to both ends of the sensing fibre [37]. Fabry-Perot etalons and some interferometers make use of the length dependent phase difference between two coherent light waves. The sinusoidal output of such sensors demands advanced signal processing techniques to resolve periodic ambiguities and nonlinearities. The periodicity of the output signal generally requires that the sensor has to be interrogated continuously to avoid the loss of interference fringes. Low coherence interferometry can overcome this last drawback, but its elongation measurement resolution is low, approximately equal to the coherence $l_c \sim \lambda^2/(2\delta\lambda)$, which for a typical broad band source (linewidth $\delta\lambda = 40\,\text{nm}$ centred at $\lambda = 1540\,\text{nm}$) is $30\,\mu\text{m}$ [25].

In addition to the above stated advantages over other fibre optic strain and temperature sensors FBG sensors offer further favourable properties, some of which, however, are shared with other types of sensors too. Like most other practical strain and temperature sensors FBG sensors work in reflection so only one end of the sensing fibre needs to be accessed. Several FBG sensor can be serial multiplexed along a single fibre, where each sensor is addressed by its own unique wavelength. This simplifies the installation of sensor network and allows more flexible network de-

signs than would be possible with other fibre optic sensors. Simultaneous strain and temperature measurements with a single sensing element have been demonstrated by superimposing two gratings [30], making this type of sensors ideal for structural monitoring as described in Section 2.1.3.

However, under some circumstances other fibre optic sensors may be more appropriate. Some interferometric strain sensors offer a resolution better than $30\mathrm{n}\epsilon$, a factor of 10–100 better than FBGs, but only over a limited measurement range [24]. Strain and temperature sensors based on Brillouin scattering offer quasi continuous strain and temperature measurement along a length of fibre several tens of kilometres long [37, 38]. Over shorter distances spatial resolutions between 1–20 cm were demonstrated [35, 36].

Besides system complexity and ease of operation, cost are a crucial factor when deciding for or against fibre optic sensors in general. Nowadays the costs of most fibre optic sensors are still higher compared with conventional sensors. The price for commercial FBGs is likely to fall in the wake of the expansion of the fibre optic telecommunication industry as a result of mass production. This is not necessarily true for other fibre optic sensor which incorporate highly specialised components.

2.2.3 Strain and temperature response

In simple terms light is backreflected from a FBG when the Bragg condition

$$\lambda = 2n_{\mathrm{eff}}\Lambda, \tag{2.6}$$

is met [41]. Here Λ is the period of the refractive index modulation, n_{eff} is the effective refractive index and λ is the wavelength of the reflected light.

When a longitudinal strain ϵ is applied to a FBG its Bragg wavelength λ increases by [20]

$$\frac{\Delta\lambda}{\lambda_0} = \left(\frac{1}{\Lambda_0}\frac{\mathrm{d}\Lambda}{\mathrm{d}\epsilon} + \frac{1}{n_0}\frac{\mathrm{d}n}{\mathrm{d}\epsilon}\right)\epsilon, \tag{2.7}$$

where the index 0 refers to the unstrained values. The first term accounts for the physical length change of the grating period with strain and simply equates to

$$\frac{1}{\Lambda_0}\frac{\mathrm{d}\Lambda}{\mathrm{d}\epsilon} = 1. \tag{2.8}$$

The second term in equation (2.7) accounts for the refractive index change due to the strain optic effect [42]. Assuming that the optical fibre is isotropic, the refractive index change due to the strain optic effect is given by [43]

$$\frac{1}{n_0}\frac{\mathrm{d}n}{\mathrm{d}\epsilon} = -\frac{n_0^2}{2}[p_{12} - \mu(p_{11} + p_{12})] = p_e, \tag{2.9}$$

where p_{11} and p_{12} are the photo-elastic coefficients of the fibre core and μ is the Poisson ratio of the fibre. For standard silica fibre $n_0 = 1.46$, $p_{11} = 0.12$, $p_{12} = 0.27$, $\mu = 0.17$ [44] and therefore $p_e = -0.22$. Inserting (2.8) and (2.9) into (2.7) gives

$$\frac{\Delta\lambda}{\lambda_0} = \left(1 - \frac{n_0^2}{2}[p_{12} - \mu(p_{11} + p_{12})]\right)\epsilon \tag{2.10-a}$$

$$= 0.78\epsilon. \tag{2.10-b}$$

The strain-optic effect reduces the strain response of the fibre by approximately 22 % so the strain response becomes approximately $1.15\,\mathrm{pm}/\mu\epsilon$ at $\lambda_0 = 1550\,\mathrm{nm}$.

Similarly λ changes with temperature:

$$\frac{\Delta\lambda}{\lambda_0} = \left(\frac{1}{\Lambda_0}\frac{\mathrm{d}\Lambda}{\mathrm{d}T} + \frac{1}{n_0}\frac{\mathrm{d}n}{\mathrm{d}T}\right)\Delta T, \tag{2.11}$$

where the first term accounts for the thermal expansion of the fibre and the second for the refractive index change. It follows from (2.5) that

$$\frac{1}{\Lambda_0}\frac{\mathrm{d}\Lambda}{\mathrm{d}T} = \alpha. \tag{2.12}$$

The refractive index change with temperature arises from a change in the of the fibre density ρ and is given by [45]

$$\frac{1}{n_0}\frac{\mathrm{d}n}{\mathrm{d}T} = \frac{1}{n_0}\left(\frac{\partial n}{\partial T} + \frac{\partial n}{\partial \rho}\frac{\partial \rho}{\partial T}\right) = \xi, \tag{2.13}$$

The thermal expansion coefficient of silica fibre is $\alpha = 0.5 \times 10^{-6}\,\mathrm{K}^{-1}$ [40], while the thermo-optic coefficient is $\xi = 9 \times 10^{-6}\,\mathrm{K}^{-1}$ [40], i.e. the thermo-optic effect causes a 20 times larger sensor response than the linear expansion of silica fibre. Inserting α and ξ into (2.11) gives

$$\frac{\Delta\lambda}{\lambda_0} = 9.5 \times 10^{-6}\Delta T. \tag{2.14}$$

Comparing (2.10-b) and (2.14) reveals that a temperature change of 1 °C induces approximately the same wavelength change as a strain of 10 $\mu\epsilon$.

2.2.4 Overcoming the strain-temperature cross-sensitivity

The previous section revealed that the wavelength change of a FBG sensor is cross-sensitive to strain and temperature. Several techniques have been developed and demonstrated to separate the strain and temperature response of FBG sensors. These include compensating temperature drifts by employing two independent sensors [16], one subject to strain and temperature and the second one subject to temperature only. Careful packaging and positioning of the sensors is required to ensure that the temperature difference between the two sensors remains constant and that the second sensor does not experience any strain (see also p. 7). A more compact design can be achieved by using a single FBG sensor capable of measuring strain and temperature simultaneously. By superimposing two gratings at different wavelengths such a sensor has been demonstrated [30], making use of the different strain and temperature responses at the two grating wavelengths. The measurement errors were $\pm 10\,\mu\epsilon$ and $\pm 5°C$. While such a sensor needs two light sources at widely separated wavelengths, Sudo *et al.* [39] have reported a sensor utilising a FBG written into birefringent fibre where the grating wavelengths of the two orthogonal polarisations responded differently to strain and temperature. The maximum measurement errors of that polarimetric sensor were $\pm 20\,\mu\epsilon$ and $\pm 2°C$. Alternatively the thermal response of a FBG strain sensor can be cancelled by using a chirped grating in a tapered fibre [46]. However, the elimination of the temperature response limits the practicality of this strain sensor for structural monitoring since the important thermally induced stress remains undetected (see Section 2.1.3).

2.3 Active fibre Bragg grating sensors

2.3.1 Potential for improved resolution

Passive FBG sensors, which were described in Section 2.2, reflect only the small fraction of the incident spectrally broad band light that falls within their narrow bandwidth. The following example illustrates the limitations these sensors and shows potential improvements by employing active FBG sensors, i.e. sensors where

FBGs form part of a fibre laser. The centre wavelength of a FBG can, e.g., be determined by measuring the power transmitted through an optical filter scanned across the reflection spectrum of the FBG [29]. If P_{in} is the power incident on the FBG, and its reflection spectrum and the filter transmission spectrum can be approximated by a Gaussian distribution then the received power as a function of the centre wavelengths of the FBG λ_G and the filter λ_F is

$$\begin{aligned} P &= P_{\text{in}} \int_{-\infty}^{\infty} R_G \exp\left(-\frac{(\lambda-\lambda_G)^2}{2\sigma_G^2}\right) T_F \exp\left(-\frac{(\lambda-\lambda_F)^2}{2\sigma_F^2}\right) \mathrm{d}\lambda \\ &= \sqrt{2\pi}\frac{\sigma_G\sigma_F}{\sigma_{G,F}} P_{\text{in}} R_G T_F \exp\left(-\frac{(\delta\lambda)^2}{2\sigma_{G,F}^2}\right), \end{aligned} \tag{2.15}$$

where R_G is the peak reflectivity of the FBG, T_F is the peak transmissivity of the filter, σ_G and σ_F are the spectral widths of the FBG and the filter, $\sigma_{G,F} = \sqrt{\sigma_G^2 + \sigma_F^2}$, and $\delta\lambda = \lambda_G - \lambda_F$. Approximating P by a Taylor polynomial around $\delta\lambda = 0\,\text{nm}$ gives

$$P = P_0 - \frac{P_0}{\sigma_{G,F}^2}(\delta\lambda)^2, \tag{2.16}$$

where $P_0 = P(\delta\lambda = 0\,\text{nm})$. The noise ΔP in the system is related to a measurement error of $\delta\lambda$ by

$$\Delta P = \frac{P_0}{\sigma_{G,F}^2}(\delta\lambda)^2 \tag{2.17}$$

$$\iff \Delta(\delta\lambda) = \sqrt{\frac{\sigma_{G,F}^2}{\text{SNR}_{\text{opt}}}}, \tag{2.18}$$

where $\text{SNR}_{\text{opt}} = P_0/\Delta P$ is the optical signal to noise ratio. It is evident from the last equation that by increasing the SNR or decreasing $\sigma_{G,F}$ the measurement error can be reduced, i.e. the resolution can be improved. The SNR can simply be increased by increasing R_G or the optical power incident on the FBG, e.g. by employing a superluminescent diode. This approach clearly is limited by the available optical power. Because $\sigma_{G,F} = \sqrt{\sigma_G^2 + \sigma_F^2}$, reducing σ_F much below σ_G does not reduce $\sigma_{G,F}$. Instead, the received power decreases which reduces the SNR. Therefore, the spectral power density[1] of the incident light should be increased. This allows σ_G and σ_F to be decreased at the same rate while keeping the received power and the

[1] Spectral power density = optical power per unit wavelength.

SNR constant. A wavelength swept laser could provide the required higher spectral power density. However, fast and continuous wavelength tuning over a sufficiently large spectrum might be difficult to achieve [47].

On the other hand, the light emitted from active FBG sensors fulfils the above stated requirements. The light is concentrated in a spectral band which is several orders of magnitude narrower than the bandwidth of a passive grating with an output power of several hundred μW to several mW [48]. Consequently the wavelength of an active FBG can be determined much more accurately.

2.3.2 State of the art DBR and DFB fibre laser sensors

The two types of commonly used fibre lasers which incorporate FBGs into their cavity are distributed Bragg reflection (DBR) lasers [31, 48] and distributed feedback (DFB) lasers [49, 50].

The sensor resolution of DBR fibre lasers potentially suffers from mode hopping of these highly multimoded lasers. The long length makes them susceptible to random parasitic environmental changes along the cavity [31, 48]. For single mode operation DBR fibre lasers must not be longer than a few centimetres and the grating bandwidth has to be below $\sim 0.2\,\text{nm}$ [51]. The short length usually limits the pump absorption and therefore the output power. However, a DBR fibre laser lasing only in two orthogonal polarisation modes was demonstrated by Ball et al. [32] while multiplexing of up to three DBR fibre laser sensors was achieved with negligible cross-talk between the sensors [33].

DFB fibre lasers are an alternative to DBR fibre lasers with the advantage that they consist of only one grating written into rare earth doped fibre. They offer single mode operation without mode hopping and kHz linewidth [11]. With a grating length of $\sim 50\,\text{mm}$ DFB fibre lasers are very compact. Furthermore, as most of the laser intensity is concentrated in the centre of the grating, the sensitive region is only $\sim 5 - 10\,\text{mm}$ long [52], making it ideal for 'point' sensing. Multiplexing of five DFB fibre lasers has been demonstrated [34], but only limited investigations into lasing stability and sensor accuracy have been carried out.

In low birefringent fibre a DFB fibre laser can operate on two orthogonal polarisation modes with a sufficiently small frequency separation between the two modes that allows this polarisation beat signal to be measured very accurately with a commercial RF spectrum analyser. A birefringent DFB fibre laser operating stably in two polarisation modes was employed as a polarimetric sensor for separately measuring lateral forces and temperature [11].

2.4 Conclusion

In conclusion, it was found that simultaneous strain and temperature measurements are required for structural monitoring. FBG sensors are the most versatile fibre optic sensors which can measure both parameters simultaneously. Active FBG sensors, i.e. fibre lasers which incorporate FBGs into their cavity, are expected to offer an improved accuracy compared with passive FBG sensors. Of the two types of FBG based fibre lasers, i.e. DBR and DFB fibre lasers, the latter is the better choice because it consists of only one FBG and offers a more stable mode of operation. State of the art birefringent DFB fibre laser sensors are capable of measuring two measurands separately. These sensors form the basis for the development of the two novel DFB fibre lasers sensors for simultaneous strain and temperature measurements which are described in Chapters 5 and 6.

However, before presenting the DFB fibre laser sensors it is important to analyse and understand some fundamental properties of DFB fibre lasers.

3 Characterisation and modelling of DFB fibre lasers

3.1 Introduction

The first distributed feedback (DFB) fibre laser was demonstrated during 1994 by Kringlebotn *et al.* in $Er^{3+}:Yb^{3+}$ codoped fibre [11]. The design was very rudimentary with a resistive wire heating the grating locally to induce the necessary π phase shift for single mode operation [53]. However, the design was soon improved by incorporating the π phase shift into the grating during the writing process [54] by means of the moving fibre-scanning beam technique [55]. This extremely versatile technique was also used to fabricate the DFB fibre lasers studied in this thesis.[1]

Gain and resonant feedback are the two fundamental parameters governing the behaviour of a DFB fibre laser — and indeed any other laser. In a DFB fibre laser the rare earth (RE) doped fibre core constitutes the gain medium. Resonant feedback is provided by a single fibre Bragg grating written into the same section of fibre. The gain is related to the concentration [RE] of the rare-earth dopants and the relative population density of their atomic energy levels [56]. The feedback is proportional to the grating coupling coefficient κ and the length L of the DFB fibre laser [41, 53]. Careful balancing of [RE] and κL is needed to achieve high output power, low threshold and low noise operation of DFB fibre lasers [57, 58, 59]. The $Er^{3+}:Yb^{3+}$ fibre has been designed earlier [60] and κL was optimised around the

[1] All DFB fibre lasers used in this thesis were fabricated by M. Ibsen, Optoelectronics Research Centre, University of Southampton.

fibre parameters prior to this work by E. Rønnekleiv[2] and M. Ibsen with the help of a standard DFB fibre laser model.

With the exception of [61] DFB fibre laser models usually treat Er^{3+} as a two level system [57, 59]. Although non-DFB $Er^{3+}:Yb^{3+}$ fibre lasers have been modelled successfully, including upconversion, [62, 63], to my knowledge no model of an $Er^{3+}:Yb^{3+}$ DFB fibre laser has been presented in the literature, possibly because of the complexity and long computation time of such models. In general there is also a lack of comparison between modelled and experimental data.

Therefore, this Chapter describes the development of a new versatile, fast and accurate steady state model for $Er^{3+}:Yb^{3+}$ DFB fibre lasers pumped at 980 nm or 1480 nm and operating around 1550 nm. The key feature of the model is to treat Er^{3+} as a multi-level system and accurately calculate their population densities. This allows to easily incorporate the energy transfer between Er^{3+} and Yb^{3+} ions, homogeneous upconversion, pump ESA and non-radiative decays. The implementation of a new fast algorithm permits to investigate the effects of various laser parameters on the behaviour of the DFB fibre laser. Thereby experimental and modelled data can be linked in a self-consistent way which is essential in order to verify if the inevitable assumptions and simplifications made in the theoretical model are indeed justified. In this way the understanding of real DFB fibre lasers can be significantly increased and possible options of improving the designs of the fibre and the DFB grating can be identified more easily.

While upconversion and pump ESA will be described in this Chapter, the self-heating caused by non-radiative decays will be investigated separately in Chapter 4 because of its great significance in sensor and telecommunication applications. It should be noted that this is a steady state model which therefore cannot predict power fluctuations such as relaxation oscillations. However, this could be implemented in a following stage.

[2]Then on leave from Optoplan AS, Box 1963, 7002 Trondheim, Norway and Norwegian Univ. of Science and Technology, Dept. of Phys. El., 7034 Trondheim, Norway

3.2 DFB fibre laser characterisation setup

The DFB lasers were written into a special $Er^{3+}:Yb^{3+}$ fibre shown in Figure 3.1 [60]. It consisted of an $Er^{3+}:Yb^{3+}$ phosphoaluminosilicate glass core with a photosensitive B/Ge-doped silica ring around it. A standard silica outer cladding completed the fibre. As the grating was formed entirely in the B/Ge ring the $Er^{3+}:Yb^{3+}$ core did not need to be modified to exhibit any photosensitivity but instead could be designed to provide maximum gain [60].

The exact radii of the fibre regions and the NA of the fibre were determined from an index profile measurement carried out by P. W. Turner[3]. The outer diameters of the $Er^{3+}:Yb^{3+}$ core, the B/Ge ring and the outer cladding were $2a_c = 4.6\,\mu$m, $2a_{B/Ge} = 18\,\mu$m and $2b = 125\,\mu$m, respectively. The NA of the fibre was 0.22. From these parameters the normalised frequency $V = 2\pi a_c \mathrm{NA}/\lambda$, the mode field diameter (MFD) $2w = 2a_c(0.65 + 1.619V^{-3/2} + 2.879V^{-6})$ and the confinement factor $\Gamma = 1 - \exp(-2a_c^2/w^2)$ could be calculated [1]. These values are listed in

[3]Optoelectronics Research Centre, University of Southampton and Southampton Photonics, Chilworth, Southampton

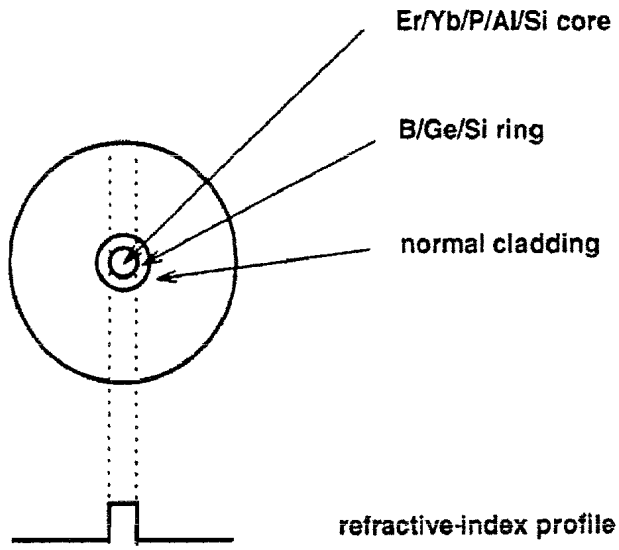

Figure 3.1. Special $Er^{3+}:Yb^{3+}$ fibre for DFB fibre lasers. The $Er^{3+}:Yb^{3+}$ doped core, which provided the gain, was separated from the photosensitive B/Ge ring in which the DFB structure was written. This allowed optimising the dopant concentrations separately in each section [60].

Table 3.1 for the two pump wavelengths ($\lambda = 980\,\text{nm}$ and $1480\,\text{nm}$) and two typical lasing wavelengths ($\lambda = 1534\,\text{nm}$ and $1550\,\text{nm}$). At 980 nm the fibre was two-moded ($2.405 < V = 3.24 < 3.832$ [64]) thus w could not be calculated by the equation given above. However, at 980 nm the confinement factor Γ, describing the transverse overlap of the propagating modes with the doped core, is $\approx 90\,\%$ for the LP_{01} mode and $\approx 73\,\%$ for the LP_{11} mode [64]. If one assumes that the power was equally shared between those two modes — supported by the fact that the power dropped by $\approx 3\,\text{dB}$ after a splice joining the two-moded $Er^{3+}:Yb^{3+}$ fibre and a fibre which was single moded at 980 nm — then the mean confinement factor was $\Gamma = 0.82$ and the MFD could be approximated by $2w = 5.0\,\mu\text{m}$. Finally, the nominal Er^{3+} and Yb^{3+} concentrations were $[Er^{3+}] = 1 \times 10^{25}\,\text{ions}\,\text{m}^{-3}$ and $[Yb^{3+}] = 20[Er^{3+}]$ [60].

The experimental arrangement used in this thesis for characterising DFB fibre lasers is shown in Figure 3.2. Half-a-metre to a metre-long pigtails of standard telecommunication fibre similar to Corning's SMF-28 were spliced onto both ends of the DFB fibre lasers to facilitate handling. The splice loss due to the dissimilar mode

Table 3.1. Optical properties of the $Er^{3+}:Yb^{3+}$ fibre at two pump wavelengths and two typical lasing wavelengths derived from its refractive index profile. $\text{NA} = \sqrt{n_1^2 - n_2^2}$, where n_1 and n_2 are the refractive indices of the core and cladding, respectively. $V = 2\pi a_c\,\text{NA}/\lambda$, $w = a_c(0.65 + 1.619V^{-3/2} + 2.879V^{-6})$ and $\Gamma = 1 - \exp(-2a_c^2/w^2)$. Note that the fibre was two-moded at $\lambda = 980\,\text{nm}$. Therefore, at this wavelength $2w$ and Γ represent an average over two guided modes.

core radius $a_c = 2.3\,\mu\text{m}$				
NA=0.22				
	lasing		pump	
λ / nm	1550	1534	1480	980
V	2.05	2.07	2.15	3.24
MFD=$2w$ / μm	5.7	5.7	5.5	5.0
confinement factor Γ	0.73	0.73	0.75	0.82

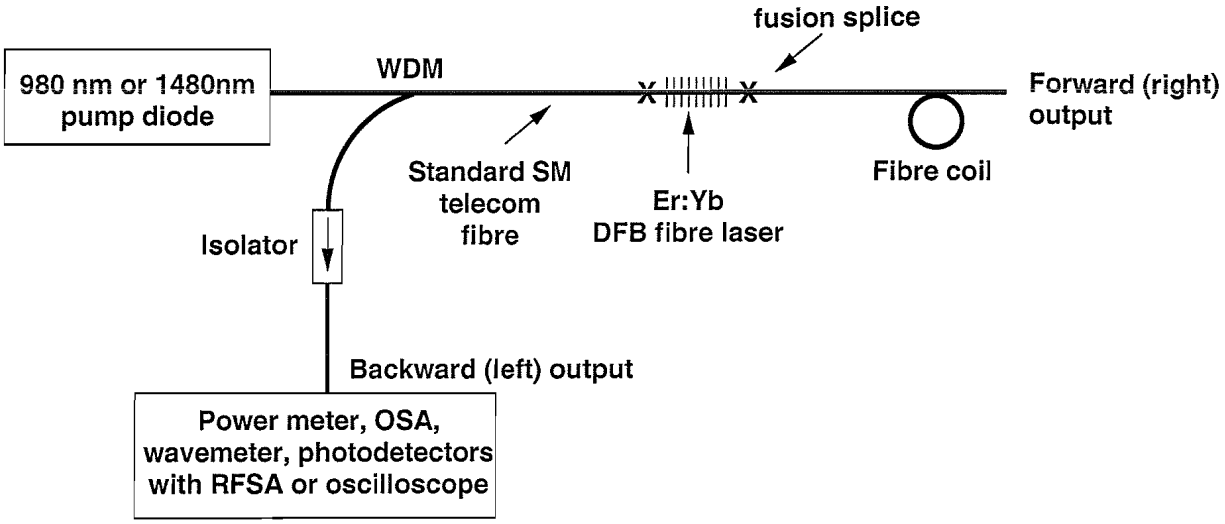

Figure 3.2. General layout of a DFB fibre laser. The laser was pumped by a semiconductor diode laser through a wavelength division multiplexer (WDM). Usually the backward (left) output of the DFB was used in telecommunication and sensor applications while the forward (right) output was terminated (see main text). The isolator prevented unwanted backreflections into the DFB fibre laser. Several instruments were used to characterise the emitted light from the laser. OSA = optical spectrum analyser, RFSA = RF spectrum analyser.

field diameters of the telecommunication and the $Er^{3+}:Yb^{3+}$ fibre was $\approx 0.2\,dB$ at 1480 nm and 1550 nm and $\approx 0.5\,dB$ at 980 nm.

The DFB fibre lasers were pumped with semiconductor lasers at 1480 nm or 980 nm. The pump was guided to the DFB fibre lasers through a 1480/1550 or 980/1550 wavelength division multiplexer (WDM)[4]. The backward (left) output from the DFB fibre lasers passed through the WDM and an isolator[5]. The latter prevented detrimental backreflections into the DFB fibre lasers which could cause intensity noise [65] (see also Chapter 7). The loss in the WDM at the pump wavelengths was $\sim 0.3\,dB$ while at the lasing wavelength the total losses through the WDM and isolator, including splice losses, were $\sim 1.6 - 1.8\,dB$.

The forward (right) output of the DFB lasers was usually terminated to minimise backreflections into the DFB fibre laser and the pump laser and to prevent unwanted laser radiation at the pump and lasing wavelengths being emitted from the fibre.

[4]SIFAM pump WDMs

[5]FOCI single stage isolators with FC/PC connector, isolation 36 dB.

Several tight coils with a bend radius of 2–3 mm in the fibre pigtail after the DFB fibre laser were sufficient for this purpose. However, the forward output can be used in serial multiplexing architectures [34], where the transmitted pump is used to pump the following DFB fibre laser. In order to reduce cost of a single DFB fibre laser it is advantageous to omit the WDM, pump the DFB fibre laser directly and use the forward laser output. However, under these circumstances it is usually necessary to minimise the transmitted pump power, i.e. most or all of the incident pump power has to be absorbed in the DFB fibre laser. In Section 4.4 it will be shown how the transmitted pump power depends on the efficiency of a DFB fibre laser.

The backward output from the DFB lasers was characterised after the isolator. Spectrum analysers with spectral resolutions of 0.01–0.05 nm[6] were used to measure output power and wavelength simultaneously. Measuring the laser output with a resolution of 0.01 nm was especially useful to detect if the lasers were actually lasing in a single longitudinal mode. More accurate wavelength measurements with a resolution of 0.1 pm could be taken with a wavemeter[7]. However, its limited dynamic range rendered it impossible to use at low output powers, i.e. just above threshold of the DFB fibre lasers. Output power fluctuations, such as spiking, relaxation oscillations and relative intensity noise, were monitored with photodetectors[8] and analysed on oscilloscopes[9] or RF spectrum analysers[10]. The laser linewidth was measured with the self-heterodyne technique [54]. Finally, the polarisation state of the laser output could be measured with a polarisation analyser[11].

The DFB fibre lasers were either placed on flat metal and non-metal surfaces or held in free air. The necessity of different mounting techniques followed from the

[6] Ando, Advantest Q8384

[7] Burleigh WA1500

[8] e.g. New Focus 1611, Tektronix SA42

[9] various 100-400MHz oscilloscopes, some with storage facilities

[10] Marconi, Tektronix 2782

[11] HP 8509

special requirements of telecommunication and sensor applications (see Chapter 4 and Section 5.2.2, respectively).

3.3 Gain medium characteristics

3.3.1 Er^{3+}:Yb^{3+}rate equations

The energy level diagrams of Er^{3+} and Yb^{3+} in Figure 3.3 show the relevant energy levels and transitions for an Er^{3+}:Yb^{3+} fibre laser operating around 1550 nm with a pump wavelength of 1480 nm or 980 nm [66]. The electrostatic fields of their neighbouring host ions cause the energy levels of the Er^{3+} and Yb^{3+} ions to split into Stark levels. Due to the amorphous structure of the host glass, the individual Er^{3+} and Yb^{3+} ions are subject to slightly different electrostatic fields. As a result the Stark levels appear to be smeared out and the optical transitions are broadened [66]. In Figure 3.3 this is only shown for the two lowest Er^{3+} and both Yb^{3+} energy levels, where the broadening has a significant effect on the behaviour of the investigated DFB fibre lasers. These broadened transitions are characterised by wavelength dependent absorption and emission cross-sections [66]. Because the population of the Stark levels within each manifold follows a Boltzmann distribution the absorption cross-section at the shorter wavelengths is larger than the emission cross-section. Similarly, the emission cross-section is larger at the longer wavelength side of the transition [66] (see also Figure 3.4).

Pumping at 1480 nm

It can be seen from the energy level diagram that the simplest Er^{3+} DFB fibre laser can be realised by pumping at 1480 nm from the lower energy levels of the ground state ${}^4I_{15/2}$ manifold into the upper energy levels of the ${}^4I_{13/2}$ manifold [67]. The pump level decays fast (lifetime < 1 ns) by non-radiative transitions to lower lying energy levels in the ${}^4I_{13/2}$ manifold. The lifetime of these meta stable levels in a silica glass are ≈ 10 ms depending on the exact composition of the host glass [67]. The laser transition takes place from the ${}^4I_{13/2}$ upper laser manifold to the ${}^4I_{15/2}$

ground state manifold. Possible lasing wavelengths typically range from 1525 nm to 1565 nm. The actual lasing wavelengths are determined by the allowed laser cavity modes and the relative gain between different modes. In DFB fibre lasers the lasing wavelength is determined by the grating wavelength [53]. The Yb^{3+} ions are not involved in the laser action when pumped at 1480 nm.

Because of the very short lifetime of the pump level the laser can be modelled as a two level system. Let N_1 and N_2 denote the population densities (ions/m^3) of the ${}^4I_{15/2}$ and ${}^4I_{13/2}$ levels. Then the rate equations can be written as [56]

$$\frac{dN_2}{dt} = -\frac{dN_1}{dt} = RN_1 + W_{12}N_1 - W_{21}N_2 - A_2N_2, \tag{3.1}$$

where R is the pump rate, W_{12} and W_{21} are the stimulated transition rates at the lasing wavelength and $A_2 = 1/\tau_2$ is the spontaneous emission rate of the ${}^4I_{13/2}$ level.[12] The transition rates are related to the optical powers $P_{p,s}$ and the transition cross-sections $\sigma_{p,ij}$ as follows [56]:

$$\begin{aligned} R &= \Gamma_p \frac{\sigma_p}{h\nu_p A_c} P_p, \\ W_{12} &= \Gamma_s \frac{\sigma_{12}}{h\nu_s A_c} P_s, \\ W_{21} &= \Gamma_s \frac{\sigma_{21}}{h\nu_s A_c} P_s, \end{aligned}$$

where the subscripts p, s, and ij stand for pump and lasing (signal) wavelength and the transition $i \to j$, respectively, $\nu_{p,s} = c/\lambda_{p,s}$ are the optical frequencies, A_c is the area of the doped core and $\Gamma_{p,s}$ is the confinement factor.

At steady state $dN_2/dt = dN_1/dt = 0$ and the solution of (3.1) is

$$N_1 = \frac{N_{Er}(W_{21} + A_2)}{R + W_{12} + W_{21} + A_2}, \tag{3.2-a}$$

$$N_2 = \frac{N_{Er}(R + W_{12})}{R + W_{12} + W_{21} + A_2}, \tag{3.2-b}$$

where $N_{Er} = N_1 + N_2$ is the total concentration of Er^{3+} ions. Subtracting (3.2-a)

[12] Additional information on laser rate equations can be found in various textbooks, e.g. [56, 68].

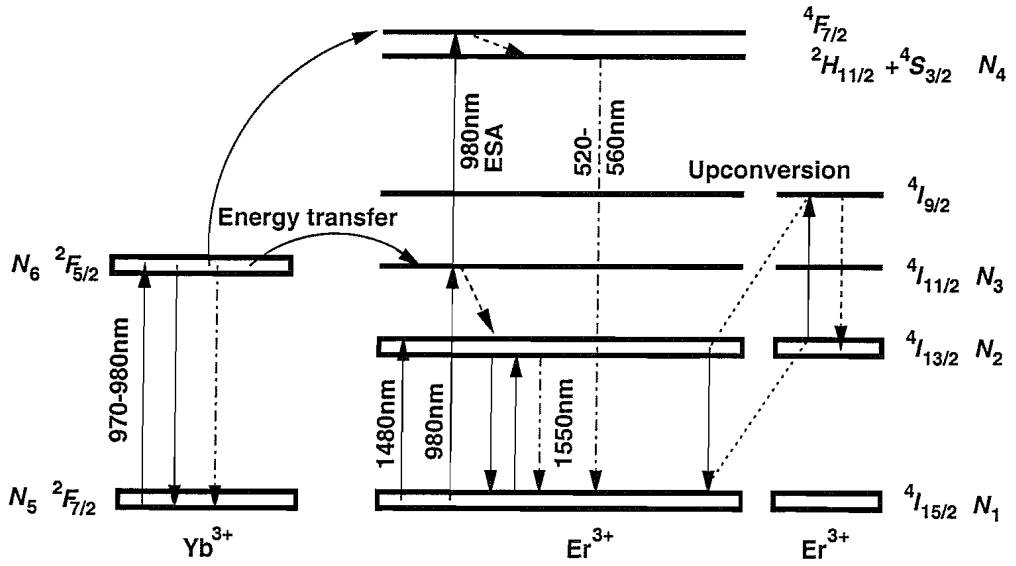

Figure 3.3. Relevant energy levels of Er^{3+} and Yb^{3+} for a laser operating around 1550 nm while pumped at 1480 nm or 980 nm. See main text for detailed explanation.

from (3.2-b) gives the population inversion

$$\Delta N = N_2 - N_1 = \frac{N_{Er}(R + W_{12} - W_{21} - A_2)}{R + W_{12} + W_{21} + A_2}.^{13} \tag{3.3}$$

Note that this simple model neglects homogenous and pair induced upconversion from $^4I_{13/2}$ depicted in Figure 3.3. A comparison between experimental and theoretical results in Section 3.6.1 will show that this simplification is not valid for the DFB fibre lasers investigated in this thesis.

Pumping at 980 nm

The pump transitions at 980 nm are $^4I_{15/2} \rightarrow ^4 I_{11/2}$ and $^2F_{7/2} \rightarrow ^2 F_{5/2}$ of the Er^{3+} and Yb^{3+} ions, respectively (see Figure 3.3). The excited Yb^{3+} ion acts as a sensitiser or donor, transferring its excitation energy very effectively in a dipole-dipole interaction [69, 70] to an Er^{3+} ion in the ground state, the acceptor. Upon this energy transfer the Yb^{3+} ion terminates in its ground state, while a neighbouring Er^{3+} ion is left in the $^4I_{11/2}$ level [70]. Since the 980 nm absorption cross section of Yb^{3+} is much larger than that of Er^{3+} and the energy transfer is highly efficient codoping with Yb^{3+} effectively increases the population density of the $^4I_{11/2}$ level. The

[13] Compare e.g. with [56], with $W_{12} = W_{21}, A_2 = 1/\tau_2$.

lifetime of the ${}^4I_{11/2}$ level is $\approx 10\mu$s [67]. Its dominant transition is a non-radiative decay to the upper lasing level ${}^4I_{13/2}$. Because of the fast transition ${}^4I_{11/2} \rightarrow {}^4I_{13/2}$, energy backtransfer from Er^{3+} to Yb^{3+} can be neglected [63].

The corresponding rate and conservation equations are [62]:

$$\frac{dN_3}{dt} = R_{13}(N_1 - N_3) - N_3A_3 + C_{tr}N_1N_6, \quad (3.4\text{-a})$$

$$\frac{dN_2}{dt} = W_{12}N1 - W_{21}N2 - N_2A_2 + N_3A_3, \quad (3.4\text{-b})$$

$$\frac{dN_6}{dt} = R_{56}N_5 - R_{65}N_6 - N_6A_6 - C_{tr}N_1N_6, \quad (3.4\text{-c})$$

$$N_{Er} = N_1 + N_2 + N_3, \quad (3.4\text{-d})$$

$$N_{Yb} = N_5 + N_6, \quad (3.4\text{-e})$$

where N_1, N_2, N_3, N_5, N_6 denote the ${}^4I_{15/2}$, ${}^4I_{13/2}$, ${}^4I_{11/2}$, ${}^2F_{7/2}$, ${}^2F_{5/2}$ energy levels of Er^{3+} and Yb^{3+}. The spontaneous emission rates of ${}^4I_{13/2}$, ${}^4I_{11/2}$ and ${}^2F_{5/2}$ are denoted as $A_2 = 1/\tau_2$, $A_3 = 1/\tau_3$ and $A_6 = 1/\tau_6$, respectively. The emission and absorption cross-sections of the Er^{3+} pump transition is assumed to be equal, i.e. $R_{13} = R_{31}$ [61]. The term $C_{tr}N_1N_6$ describes the energy transfer from ${}^2F_{5/2}$ Yb^{3+} to ${}^4I_{11/2}$ Er^{3+}. The energy transfer effectively leads to a lifetime reduction of the ${}^2F_{5/2}$ Yb^{3+} level.

The analytical solution of the system of linear equations 3.4-a–e is

$$N_1 = -\frac{g}{2f} + \frac{\sqrt{g^2 - 4fh}}{2f}, \quad (3.5\text{-a})$$

$$N_3 = (cN_{Er} - dN_1)/a, \quad (3.5\text{-b})$$

$$N_2 = N_{Er} - N_1 - N_2, \quad (3.5\text{-c})$$

$$N_6 = (R_{56}N_{Yb} + R_{13}N_1 - bN_3)/e, \quad (3.5\text{-d})$$

$$N_5 = N_{Yb} - N_6, \quad (3.5\text{-e})$$

with

$$a = W_{21} + A_2 + A_3,$$

$$b = R_{13} + A_3,$$

$$c = W_{21} + A_2,$$

$$d = W_{12} + W_{21} + A_2,$$

$$
\begin{aligned}
e &= R_{56} + R_{65} + A_6, \\
f &= C_{tr}(aR_{13} + bd), \\
g &= C_{tr}(aR_{56}N_{\mathrm{Yb}} - bcN_{\mathrm{Er}}) + eaR_{13} + ebd, \\
h &= -ebcN_{\mathrm{Er}}.
\end{aligned}
$$

Upconversion

Upconversion describes the energy transfer between two or more excited ions, where one ion finishes in an energy level higher than the highest initial excited state. The well known upconversion process from the $^4I_{13/2}$ level [71] is shown in Figure 3.3: two Er^{3+} ions are excited to the $^4I_{13/2}$ level. One ion, the donor, transfers its energy to the other, the acceptor. Upon this energy transfer the donor relaxes to the ground state whereas the acceptor is upconverted into the $^4I_{9/2}$ level. The upconverted ion undergoes a fast non-radiative transition back to the $^4I_{11/2}$ level from where it decays further to the $^4I_{13/2}$ level. A small fraction ($\sim 10^{-4}$) of upconverted ions undergoes a spontaneous radiative transition from $^4I_{11/2}$ to the ground state, emitting photons at 980 nm [71]. However, this process will be neglected in this thesis. The negative effect of upconversion is the loss of one ion in the $^4I_{13/2}$ (N_2) level, reducing the population inversion and therefore the available gain on the 1550 nm laser transition (cf. (3.16)). Furthermore, for each upconversion transition a pump photon has been wasted.

Two upconversion processes have to be distinguished, namely homogeneous upconversion and pair-induced quenching [71]. The difference lies in the lifetime of a pair of excited Er^{3+} ions in the $^4I_{13/2}$ level. Pair induced quenching takes place between two or more (clusters, [72]) Er^{3+} ions on a timescale of μs. Therefore, the doubly excited state of a pair is virtually non-populated. The dynamic in a cluster of many Er^{3+} ions can be regarded as a series of pair induced quenching processes, relaxing all but one ion to the ground state [72]. The formation of pairs, and more so clusters, of Er^{3+} ions has to be avoided to prevent the reduction of the available gain. In the fibre used here for the DFB fibre lasers, clustering could be avoided by codoping with Yb^{3+} and Al^{3+} [73].

Even if the detrimental formation of ion pairs and clusters can be prevented in the fibre, homogeneous upconversion as a result of dipole-dipole interactions between Er^{3+} ions separated by a mean distance r is present in highly doped fibre. Based on dipole-dipole interactions the upconversion probability is proportional to r^{-6} [69]. In this case of paired Er^{3+} ions separated by a relatively large distance the upconversion process takes a finite time, which is in the range of several hundred μs to ms [71]. Because of the distance dependence only a fraction of the total number of Er^{3+} ions experiences homogeneous upconversion. A straightforward way of incorporating homogeneous upconversion into this DFB fibre laser model is to divide the Er^{3+} population into two groups of which only one experiences homogeneous upconversion. In this group homogeneous upconversion is described by the following additional terms in the rate equations:

$$\frac{dN_2}{dt} = -2C_{up}N_2^2, \tag{3.6-a}$$

$$\frac{dN_3}{dt} = C_{up}N_2^2, \tag{3.6-b}$$

where the population density of the $^4I_{9/2}$ level has been neglected because of its fast spontaneous decay to the $^4I_{11/2}$ level. The analytical solution of these expanded rate equations contains an impractical number of terms as a result of the modified expression of dN_3/dt. Because the $^4I_{11/2} \rightarrow ^4 I_{13/2}$ transition is fast one can neglect the additional number of upconverted ions in the $^4I_{11/2}$ and regard them to re-populate the $^4I_{13/2}$ level directly. Then the above additional terms reduce to just

$$\frac{dN_2}{dt} = -C_{up}N_2^2, \tag{3.7}$$

where $C_{up}N_2 = 1/\tau_{up}$ can be regarded as the upconversion lifetime of the $^4I_{13/2}$ level. The reduced lifetime of the $^4I_{13/2}$ level due to homogeneous upconversion can therefore be written as

$$A_2 + C_{up}N_2 = 1/\tau_2 + 1/\tau_{up} = 1/\tau_2' = A_2'. \tag{3.8}$$

The shorter lifetime τ_2' of Er^{3+} ion pairs leads to an increase of N_1 which in turn affects the Yb^{3+} population densities. If one assumes that every paired Er^{3+} ion is surrounded by the same number of Yb^{3+} ions as a single Er^{3+} ion then one can

easily split the Yb^{3+} population into two groups, one interacting with single Er^{3+} ions and the other with paired ones.

In the case of pumping at 1480 nm the analytical solution of the modified rate equations becomes

$$N_{2,\text{pair}} = \frac{\sqrt{(W_{12}+W_{21}+R+A_2')^2+4C_{up}(W_{12}+R)N_{\text{Er,pair}}}}{2C_{\text{up}}} - \tag{3.9}$$

$$\frac{W_{12}+W_{21}+R+A_2'}{2C_{\text{up}}}, \tag{3.10}$$

$$N_{1,\text{pair}} = N_{\text{Er,pair}} - N_{2,\text{pair}} \tag{3.11}$$

where $N_{\text{Er,pair}}$, $N_{1,\text{pair}}$ and $N_{2,\text{pair}}$ are the total number of paired ions[14] and the corresponding population densities of the ${}^4I_{15/2}$ and ${}^4I_{13/2}$ levels, respectively.

In the case of pumping at 980 nm no analytical solution exists. However, by using (3.8) upconversion can be incorporated into the model by using an iterative process to calculate the population densities of paired Er^{3+} ions and their associated Yb^{3+} ions. First the solution (3.5-a–e) of the rate equations is found without upconversion. Then A_2 is adjusted to A_2' according to (3.8) and subsequently used in (3.5-a–e) again. This process is repeated until changes of A_2' from one iteration to the next are negligible. With this approach the model, which was written in C and running on a Pentium II, 266 MHz processor, could calculate the field distribution inside a DFB fibre laser and its output power in fractions of a second. In the same computing environment solving the rate equations by using a 4^{th}-order Runge-Kutta algorithm [74] with variable step size required several minutes and gave a similar result. Taking into account that laser parameters, such as cross-sections and ion concentrations, are subject to uncertainties, the accuracy potentially gained with a Runge-Kutta algorithm is negligible.

Pump excited state absorption

Excited state absorption (ESA) describes the absorption of photons by an already excited ion [56]. The pump ESA transition ${}^4I_{11/2} \rightarrow {}^4F_{7/2}$ at 980 nm is shown in the

[14]Note the difference between the number of ion pairs and the number of paired ions: each ion pair consists of two paired ions.

energy level diagram (Figure 3.3). From the $^4F_{7/2}$ level the ions undergo a fast non-radiative transition to the $^2H_{11/2}$ and $^4S_{3/2}$ levels. Due to the small energy difference the population density of the latter two levels follows a Boltzmann distribution [75]. The two levels can therefore be represented by a single level ($^2H_{11/2}/^4S_{3/2} = N_4$) and the $^4F_{7/2}$ level will be omitted throughout because of its negligible population density. The radiative decay from the $^2H_{11/2}/^4S_{3/2}$ level to the ground state gives rise to intense green fluorescence in the wavelength range of 525–560 nm with two distinctive peaks around 530 nm and 550 nm [76]. Besides pump ESA excitation of Er^{3+} ions to the $^4F_{7/2}$ level occurs when the energy of a second Yb^{3+} ion is transfered to an $^4I_{11/2}$ Er^{3+} ion (see Figure 3.3).

Although pump ESA at 1480 nm from the $^4I_{13/2}$ level is possible it is negligible in highly doped fibres, such as the one used here [71]. Signal ESA from the $^4I_{13/2}$ level is also neglected in this model because of the relatively large stimulated emission cross-section of the $^4I_{13/2} \rightarrow^4 I_{15/2}$ transition compared with the ESA cross-section [66].

Therefore, the additional pump ESA terms in the rate equations for 980 nm pumping are

$$\frac{\mathrm{d}N_3}{\mathrm{d}t} = -C_{\mathrm{ESA}} N_3 N_6 - R_{34} N_3, \tag{3.12-a}$$

$$\frac{\mathrm{d}N_4}{\mathrm{d}t} = C_{\mathrm{ESA}} N_3 N_6 + R_{34} N_3 - A_4 N_4, \tag{3.12-b}$$

$$\frac{\mathrm{d}N_6}{\mathrm{d}t} = -C_{\mathrm{ESA}} N_3 N_6, \tag{3.12-c}$$

where R_{34} is the pump ESA transition rate and A_4 is the spontaneous emission rate of the $^2H_{11/2}/^4S_{3/2}$ level. The energy transfer coefficient of the $^2F_{5/2}$ $Yb^{3+} \rightarrow^4 F_{7/2}$ Er^{3+} transition is given by C_{ESA}. The stimulated emission R_{43} can be neglected because of the short lifetime of the $^4F_{7/2}$ level and the mismatch between the energy separation $^2H_{11/2}/^4S_{3/2} \rightarrow^4 I_{11/2}$ and the energy of the pump photons.

Under the assumption that $R_{34} \sim R_{12}$ and $C_{\mathrm{ESA}} \sim C_{\mathrm{tr}}$ R_{34} is small compared to C_{ESA} and can therefore be neglected. In this case analytical solutions of the rate equations including the $^2F_{5/2}$ $Yb^{3+} \rightarrow^4 F_{7/2}$ Er^{3+} transition can be found by solving

the rate equations separately for Yb^{3+} and Er^{3+}:

$$N_2 = [W_{12}N_{Er}/(A_2A_3) - gd/(b-c)]/f, \quad (3.13\text{-a})$$

$$N_3 = -d/(b-c), \quad (3.13\text{-b})$$

$$N_4 = C_{ESA}N_3N_6/A_4, \quad (3.13\text{-c})$$

$$N_1 = N_{Er} - N_2 - N_3 - N_4, \quad (3.13\text{-d})$$

$$N_6 = R_{56}N_{Yb}/(aA_6), \quad (3.13\text{-e})$$

$$N_5 = N_{Yb} - N_6, \quad (3.13\text{-f})$$

with

$$\begin{aligned}
a &= 1 + C_{tr}N_1 + C_{ESA}N_3/A_6 + (R_{56} + R_{65})/A_6, \\
b &= (R_{13} + C_{tr}N_6)[1/A_2 - W_{12}(1 + C_{ESA}N_6/A_4)/(A_2A_3)]/A_3, \\
c &= -W_{12}/(A_2A_3) + (1 + W_{21}/A_2)/A_3^2 \times \\
&\quad [A_3 + R_{31} + C_{ESA}N_6 + (R_{13} + C_{tr}N_6)(1 + C_{ESA}N_6/A_4)], \\
d &= -N_{Er}(1 + W_{21}/A_2)(R_{13} + C_{tr}N_6)/A_3^2, \\
f &= (W_{12} + W_{21})/(A_2A_3) + 1/A_3, \\
g &= 1/A_2 - W_{21}(1 + C_{ESA}N_6/A_4)/(A_2A_3).
\end{aligned}$$

It is evident from equations (3.13-a–f) that in order to calculate the population densities of the Er^{3+} ion the population densities of Yb^{3+} ions has to be known, and vice versa. This apparent problem can be solved by using an iterative process. This process starts with estimated population densities of the Er^{3+} ions, e.g. $N_1 = N_{Er}$, $N_2 = N_3 = N_4 = 0$, and then calculates the population densities N_5 and N_6 of the Yb^{3+} ions. These values can then be used in turn to calculate the new Er^{3+} ion population densities. The process continues until all population densities $N_1 - N_6$ converge to their final value. The principle of calculating the population densities of one energy level based on the knowledge of all other levels is similar to the Runge-Kutta algorithm. However, like in the case of homogeneous upconversion (see p. 30), using the analytical solutions (3.13-a–f) of the rate equations is approximately three orders of magnitude faster than employing a 4^{th}-order Runge-Kutta algorithm while giving similar results.

3.3.2 Spectroscopy of the $Er^{3+}:Yb^{3+}$ fibre

In order to model the DFB fibre laser a good knowledge of the Er^{3+} and Yb^{3+} concentrations and the relevant transition cross-sections is needed. The easiest parameters to be measured experimentally are the ground state absorption (GSA) at the pump and lasing wavelengths and the gain at the lasing wavelength. The small signal GSA coefficient is simply given by [67]

$$\alpha_{\mathrm{GSA}} = \Gamma \sigma_a N_1, \tag{3.15}$$

where Γ is the confinement factor (see p. 20) and σ_a is the absorption cross-section at the particular wavelength, i.e. $\sigma_a = \sigma_{12}$ at the lasing wavelength and $\sigma_a = \sigma_{13}$ or σ_p at the pump wavelength, i.e. 980 nm and 1480 nm, respectively. Similarly the gain coefficient at the lasing wavelength is expressed by [56]

$$\gamma = \Gamma(\sigma_{21} N_2 - \sigma_{12} N_1). \tag{3.16}$$

The broadening of the RE transitions in glass are taken into account by allowing the cross-sections to be wavelength dependent, i.e. $\sigma_{12}(\lambda)$, $\sigma_{21}(\lambda)$ and $\sigma_{13}(\lambda)$.

In principle, the dopant concentration $N_{\mathrm{RE}} = N_1 + N_2$ is known from the fabrication process, while transition cross-sections, deduced from absorption measurements in fibres with known dopant concentrations, are reported in the literature. Although N_{RE}, σ_{ij}, α and γ are subject to measurement errors a good approximation can be found by combining the results from several experiments. Therefore, reported σ_{ij}, the nominal N_{RE} and measured α and γ have been combined to determine a set of reasonable numerical values to be used in the DFB fibre laser model.

Figure 3.4 shows the absorption and gain coeffcient spectra of the $Er^{3+}:Yb^{3+}$ fibre prior to UV-exposure. The wavelength span covers the typical lasing wavelength range of Er^{3+} lasers. Taking splice losses into account the launched power for the absorption and gain measurements was 9.5 μW and 79 μW, respectively, so bleaching of the GSA and gain saturation could be avoided [56]. The measured absorption coefficients at 1534 nm and 1550 nm were $\alpha_{1534} = 7.8\,\mathrm{m}^{-1} \hat{=} -10\log(e^{-\alpha}) = 33.8\,\mathrm{dB\,m}^{-1}$ and $\alpha_{1550} = 2.2\,\mathrm{m}^{-1} \hat{=} 9.6\,\mathrm{dB\,m}^{-1}$. Variations of the dopant concentration could ex-

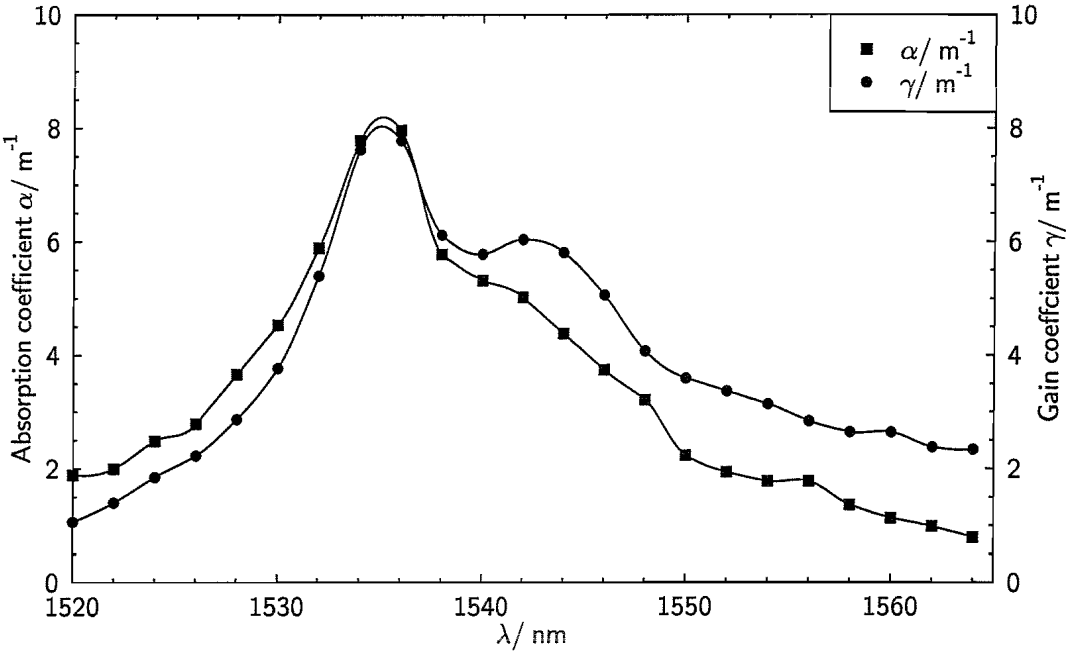

Figure 3.4. Measured absorption and gain coefficients of the Er^{3+} : Yb^{3+} fibre as a function of wavelength over the typical lasing wavelength range of Er^{3+} lasers. These measurements were corrected for splice losses.

plain why a higher value of $\alpha_{1550} = 2.7\,\mathrm{m}^{-1}$ has been reported for another section of the same fibre [77].

Combining the results from the absorption measurements at 1550 nm (Figure 3.4 and [77]) and at 1480 nm ([77]) with the reported absorption cross-sections at the two wavelengths ([67, 78]) the most reasonable combination of parameters was found to be $\sigma_{12}^{1534} = 0.89 \times 10^{-24}\,\mathrm{m}^2$, $\sigma_{12}^{1550} = 0.28 \times 10^{-24}\,\mathrm{m}^2$, $\sigma_{13}^{1480} = 0.22 \times 10^{-24}\,\mathrm{m}^2$, and $[Er^{3+}] = 1.2 \times 10^{25}\,\mathrm{ions\,m}^{-3}$.

The measured gain coefficients at 1534 nm and 1550 nm were $\gamma_{1534} = 7.6\,\mathrm{m}^{-1} \widehat{=} 33.1\,\mathrm{dB\,m}^{-1}$ and $\gamma_{1550} = 3.6\,\mathrm{m}^{-1} \widehat{=} 15.6\,\mathrm{dB\,m}^{-1}$, respectively. Calculating the emission cross-sections from the measured gain coefficients and the above $[Er^{3+}]$ gives $\sigma_{21}^{1534} = 0.87 \times 10^{-24}\,\mathrm{m}^2$ and $\sigma_{21}^{1550} = 0.42 \times 10^{-24}\,\mathrm{m}^2$ which is in agreement with the reported values in [67, 78].

Table 3.2-a lists these calculated cross-sections together with other relevant cross-sections and lifetimes of Er^{3+} presented in [67].

The absorption of the Er^{3+} : Yb^{3+} fibre as a function of pump power at three different wavelength around 975 nm is shown in Figure 3.5. The measurement was

Table 3.2. Absorption and emission cross-sections of Er^{3+} and Yb^{3+} at the relevant pump and lasing wavelengths and the lifetimes τ_2 and τ_3 of the $^4I_{13/2}$ and $^4I_{11/2}$ levels of Er^{3+} and τ_6 of the $^2F_{5/2}$ Yb^{3+} level. Er^{3+} values are derived from absorption and gain coefficient measurements presented in Figure 3.4 and in [67, 77]. The Er^{3+} concentration was estimated by combining the results from different absorption and gain measurements. A concentration of $[Er^{3+}] = 1.2 \times 10^{25}\,\text{ions}\,\text{m}^{-3}$ was found. Yb^{3+} values were fitted to experimental data in Figure 3.5 assuming an Yb^{3+} concentration of $20[Er^{3+}] = 24 \times 10^{25}\,\text{ions}\,\text{m}^{-3}$.

Er^{3+}			
λ	σ_{12}	σ_{21}	σ_{13}
/ nm	$/10^{-24}\,\text{m}^2$		
980			0.20
1480			0.22
1534	0.89	0.87	
1550	0.28	0.42	
$\tau_2 = 10\,\text{ms}$			
$\tau_3 = 10\,\mu\text{s}$			
$C_{\text{up}} = 2.5 \times 10^{-21}\,\text{m}^3\text{s}^{-1}$			
a			

Yb^{3+}		
λ	σ_{56}	σ_{65}
/ nm	$/10^{-24}\,\text{m}^2$	
970	0.53	1.5
975	1.65	2.5
980	0.58	2.2
$\tau_6 = 0.8\,\text{ms}$		
$C_{\text{tr}} = 5 \times 10^{-21}\,\text{m}^3\text{s}^{-1}$		
b		

carried out by G. G. Vienne[15]. The curves to the experimental data were fitted by solving the equations (3.5-a–e) iteratively taking homogenous upconversion into account. The upconversion parameter $C_{\text{up}} = 2.5 \times 10^{-21}\,\text{m}^3\text{s}^{-1}$ and the fraction of paired ions of 47 % were taken from experimental and simulated data of a DFB fibre laser pumped at 1480 nm which is presented in Section 3.6.1. The pump absorption and emission cross-sections of Er^{3+} and the lifetime of the $^4I_{11/2}$ level were set to $\sigma_{13}^{980} = \sigma_{31}^{980} = 0.2 \times 10^{-24}\,\text{m}^2$ and $A_3 = 10\,\mu\text{s}$ [67]. An Yb^{3+} concentration of $20[Er^{3+}] = 24 \times 10^{25}\,\text{m}^{-3}$ was assumed. The Yb^{3+} parameters τ_6, σ_{56}, σ_{65} and C_{tr} were varied within the range reported in the literature [62, 79] to obtain a best fit

[15]Then with the Optoelectronics Research Centre, University of Southampton.

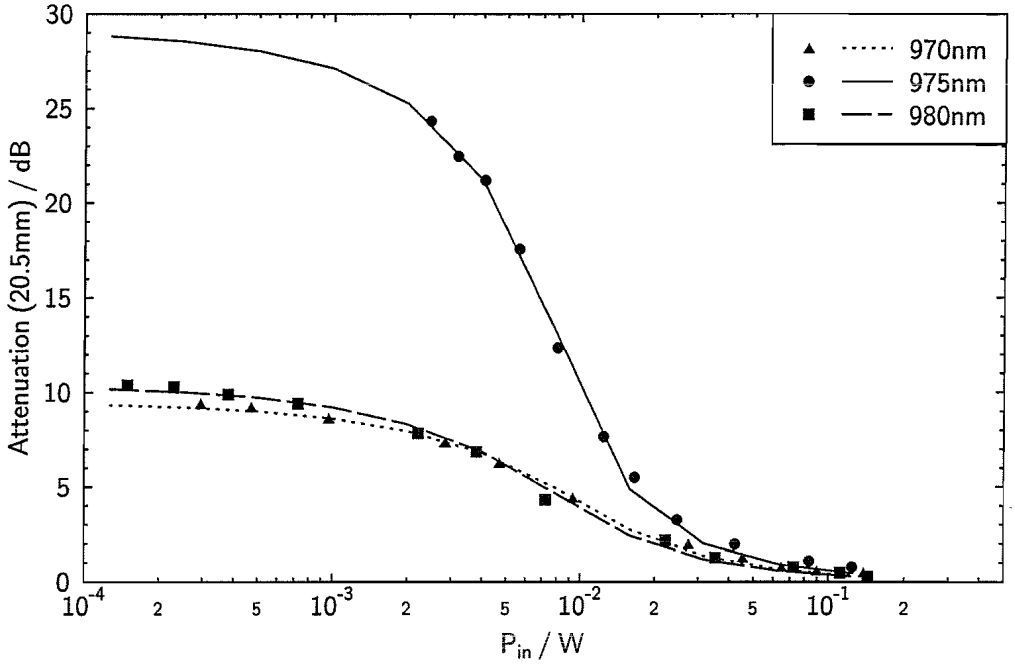

Figure 3.5. Pump absorption of a 20.5 mm long section of the Er^{3+} : Yb^{3+} fibre as a function of pump power for three different pump wavelength. The absorption was measured by G.G. Vienne (see footnote on previous page) and the curves were fitted using the numerical model explained in the main text. The fit parameters are listed in Table 3.2-b.

to the experimental data, leaving all previously determined parameters, i.e. $[N_{\mathrm{Er}}]$, Γ etc., constant.

Although ESA was present, manifesting itself through clearly visible green fluorescence of the fibre, it was not taken into account here because the exact ESA cross-sections and energy transfer rates of the fibre were unknown. An obvious assumption would be $C_{\mathrm{ESA}} = C_{\mathrm{tr}}$. However, the DFB fibre laser simulation showed that the output power would then be in strong disagreement with the measured output power. Determining the ESA cross-sections would require extensive spectroscopic studies at fibres with different Er^{3+} and Yb^{3+} concentrations, which lies outside the scope of this work. Once the relevant ESA parameters are known, they can be introduced into the model through equations (3.12-a–c).

The parameters σ_{56}, σ_{65}, τ_6 and C_{tr} obtained from the fit are listed in Table 3.2-b. All parameters are in good agreement with the values reported in the literature [62, 79]. The absorption and emission cross-sections of Yb^{3+} peak at 975 nm and drop significantly within 5 nm either side of this centre wavelength [80]. The effect

can be seen in Figure 3.5 where for low pump powers the absorption at 975 nm is about a factor 80–100 (19–20 dB) higher than at 971 nm and 980 nm. $\sigma_e > \sigma_a$, both cross-sections for Yb^{3+} doped [80].

3.4 Optical feedback in DFB fibre lasers

After having looked at the gain medium in detail, the following Section will focus on the optical feedback inside a DFB fibre laser. As briefly mentioned at the beginning of this Chapter, the feedback in DFB fibre lasers is provided by a FBG [53] which is a periodic perturbation of the refractive index of the fibre [41]. This index modulation is induced by exposing a section of photosensitive fibre to an intense interference pattern of UV radiation. A detailed presentation of FBGs is given in [18, 19, 20, 41]. Coupled mode theory is the essential tool to describe the energy coupling between the two counter propagating waves in a FBG. In the following this theory is briefly outlined and the relevant results for developing a DFB fibre laser model are presented.

3.4.1 Summary of fibre Bragg grating properties

The refractive index modulation is given by [41]

$$\delta n_{\text{eff}}(z) = \overline{\delta n}_{\text{eff}}(z)\left[1 + v\cos\left(\frac{2\pi}{\Lambda(z)}z + \Phi(z)\right)\right]. \tag{3.17}$$

Here $\overline{\delta n}_{\text{eff}}(z)$ is the spatially averaged UV induced index change, v is the fringe visibility of the index modulation, Φ accounts for phase shifts of the index modulation, and Λ is the grating period. Possible grating chirp is accounted for by the z-dependence of Λ. For all FBGs used in this thesis $v = 1$, which therefore will be omitted in the following. The grating period Λ, the grating length L and the grating coupling coefficient κ are the most important grating parameters. The latter is a measure for the feedback provided by the grating and is given by [41]

$$\kappa = \kappa^* = \frac{\pi}{\lambda}\overline{\delta n}_{\text{eff}}. \tag{3.18}$$

The electric field inside a FBG is given by the sum of the two counter propagating waves [53]

$$E(z) = R(z)\exp(-i\beta_0 z) + S(z)\exp(i\beta_0 z), \tag{3.19}$$

with the propagation constant $\beta_0 = \pi/\Lambda$ and complex amplitudes $R(z)$ and $S(z)$ of the forward and backward propagating wave, respectively. The following pair of coupled differential equations, the coupled mode equations, describes the coupling between the two modes and the spatial evolution of their complex amplitudes [53]:

$$\frac{\mathrm{d}R}{\mathrm{d}z} = (\gamma - i\delta)R - i\kappa S, \tag{3.20-a}$$

$$\frac{\mathrm{d}S}{\mathrm{d}z} = -(\gamma - i\delta)S + i\kappa^* R, \tag{3.20-b}$$

where γ accounts for possible gain, e.g. in DFB fibre lasers, and $\delta = \beta - \pi/\Lambda$ is the detuning from the "design wavelength" of an infinitesimally weak grating.

In order to solve the coupled mode equations (3.20-a,b) appropriate boundary conditions have to be applied. The boundary conditions for a passive FBG can be written as [41]

$$R(0) = 1 \text{ and } S(L) = 0, \tag{3.21}$$

i.e. a forward propagating wave with an arbitrary amplitude enters the grating at z=0, while the backward propagating wave vanishes at the other end (z=L).[16] The complex reflectance of the FBG is then

$$\rho = S(0)/R(0), \tag{3.22}$$

which can be translated into the power reflection coefficient $r = |\rho|^2$ and the time delay of the reflected light $\tau = -\lambda^2/(2\pi c)\,\mathrm{d}\theta_\rho/\mathrm{d}\lambda$, where θ_ρ denotes the phase of ρ. The maximum reflectivity and minimum transmissivity of the FBG are [41]

$$R_{\max} = 1 - T_{\min} = \tanh^2(\kappa L), \tag{3.23}$$

which occur at a wavelength [41]

$$\lambda_{\max} = 2n_{\mathrm{eff}}\left(1 + \frac{\overline{\delta n}_{\mathrm{eff}}}{n_{\mathrm{eff}}}\right)\Lambda. \tag{3.24}$$

[16] For computational purposes it is advantageous to set $R(L) = 1$ and $S(L) = 0$ and integrate backwards through the grating.

For infinitesimally weak gratings, $\overline{\delta n}_{\text{eff}} \to 0$, the last equation becomes the more widely stated equation for the Bragg condition (2.6). Since FBGs have a finite length the reflection is broadened over a finite spectral bandwidth. For strong FBGs, like the ones used for DFB fibre laser, this bandwidth $\delta\lambda$ can be approximated by [41]

$$\delta\lambda = \frac{\overline{\delta n}_{\text{eff}}}{n_{\text{eff}}}\lambda_{\max}. \tag{3.25}$$

In a DFB fibre laser no waves at the lasing wavelength enter the FBG and the boundary conditions therefore become [53]

$$R(0) = 0 \text{ and } S(L) = 0. \tag{3.26}$$

The forward and backward output powers of the DFB fibre laser become $|R(L)|^2$ and $|S(0)|^2$, respectively. A detailed discussion of the solutions of the coupled mode equations of a DFB laser was first presented by Kogelnik and Shank [53] in 1972. The analytical solutions presented in [53] neglect gain saturation and pump absorption and are therefore limited to near threshold conditions. Gain saturation and pump absorption have been taken into account by Lauridsen *et al.* [57] making it possible to model DFB lasers above threshold. However, the Er^{3+} gain medium was modelled as a 2-level system only.

3.4.2 Transfer matrix approach

The fastest and most versatile technique to solve the coupled mode equations for any FBG, with or without gain, is the transfer matrix approach [41]. The grating is divided into a sufficient number M of uniform sections of length Δz. Let R_i and S_i be the field amplitudes after section i. Then for each uniform section there exists a 2×2 matrix $\boldsymbol{F}_i$ such that

$$\begin{pmatrix} S_i \\ R_i \end{pmatrix} = \boldsymbol{F}_i \begin{pmatrix} S_{i-1} \\ R_{i-1} \end{pmatrix}. \tag{3.27}$$

For a FBG without gain the entries of $\boldsymbol{F}_i$ are [41]

$$f_{11} = f_{22}^* = \cosh(\gamma_B \Delta z) - i\frac{\hat{\sigma}}{\gamma_B}\sinh(\gamma_B \Delta z), \tag{3.28-a}$$

$$f_{12} = f_{21}^* = -i\frac{\kappa}{\gamma_B}\sinh(\gamma_B \Delta z), \tag{3.28-b}$$

where $\gamma_B = \sqrt{\kappa^2 - \hat{\sigma}^2}$ and $\hat{\sigma} = \delta + \sigma$. Here $\sigma = 2\pi\overline{\delta n}_{\text{eff}}/\lambda$ accounts for the shift of the Bragg wavelength $\lambda = 2n_{\text{eff}}\Lambda \rightarrow \lambda = 2(n_{\text{eff}} + \overline{\delta n}_{\text{eff}})\Lambda$ caused by the averaged background refractive index change $\overline{\delta n}_{\text{eff}}$.

When a net gain γ is introduced, e.g. in a DFB fibre laser, the entries of $\boldsymbol{F}_i$ can be written as [81]

$$f_{11} = f_{22}^* = \frac{1}{1-r^2}[\exp(iq\Delta z) - r^2\exp(-iq\Delta z)] \quad (3.29\text{-a})$$

$$f_{12} = -f21 = -\frac{r}{1-r^2}[\exp(iq\Delta z) - \exp(-iq\Delta z)], \quad (3.29\text{-b})$$

where $q = \pm i\sqrt{(\gamma + i\delta)^2 + \kappa^2}$ and $r = (q + i(\gamma + i\delta))/\kappa$. The sign in the definition of q is chosen such that $|r(q)| < 1$.

Discrete phaseshifts Φ of the refractive index modulation are described by a phaseshift matrix $\boldsymbol{F}_\Phi$ with the entries [41]

$$f_{\Phi,11} = f_{\Phi,22}^* = \exp(-i\Phi/2), \quad (3.3\text{-a})$$

$$f_{\Phi,12} = f_{\Phi,21} = 0. \quad (3.3\text{-b})$$

The amplitudes of the two counterpropagating waves at the two grating ends are then given by

$$\begin{pmatrix} S(L) \\ R(L) \end{pmatrix} = \boldsymbol{F}\begin{pmatrix} S(0) \\ R(0) \end{pmatrix}, \text{ with } \boldsymbol{F} = \boldsymbol{F}_M \cdot \boldsymbol{F}_{M-1} \cdot \ldots \cdot \boldsymbol{F}_1. \quad (3.4)$$

Figure 3.6 shows the calculated and measured reflection and time delay spectra of a 50 mm long unpumped DFB fibre laser with $\kappa = 231\,\text{m}^{-1} \hat{=} \overline{\delta n}_{\text{eff}} = 1.15 \times 10^{-4}$ and a $\Phi = \pi$ phaseshift at its centre. This type of laser will be used as a strain and temperature sensor in Chapter 5. The modelled grating was divided into 50 sections, with a $\Phi = \pi$ phaseshift between sections 25 and 26. Note, that this uniform grating could have been divided into just two sections, one before and one after the phaseshift. However, in order to model the active DFB fibre laser (see next Section) more sections are required because the amplitudes of the counterpropagating waves and the gain change rapidly along the grating. The introduction of a π phaseshift at the centre of the grating opens a narrow transmission peak at the centre of the grating stop band — here shown as a reflectivity dip in the calculated spectrum. Small imperfections of the actual grating, e.g. $\Phi \neq \pi$ and chirp, and noise in the measurement system cause the deviations from the calculated spectra.

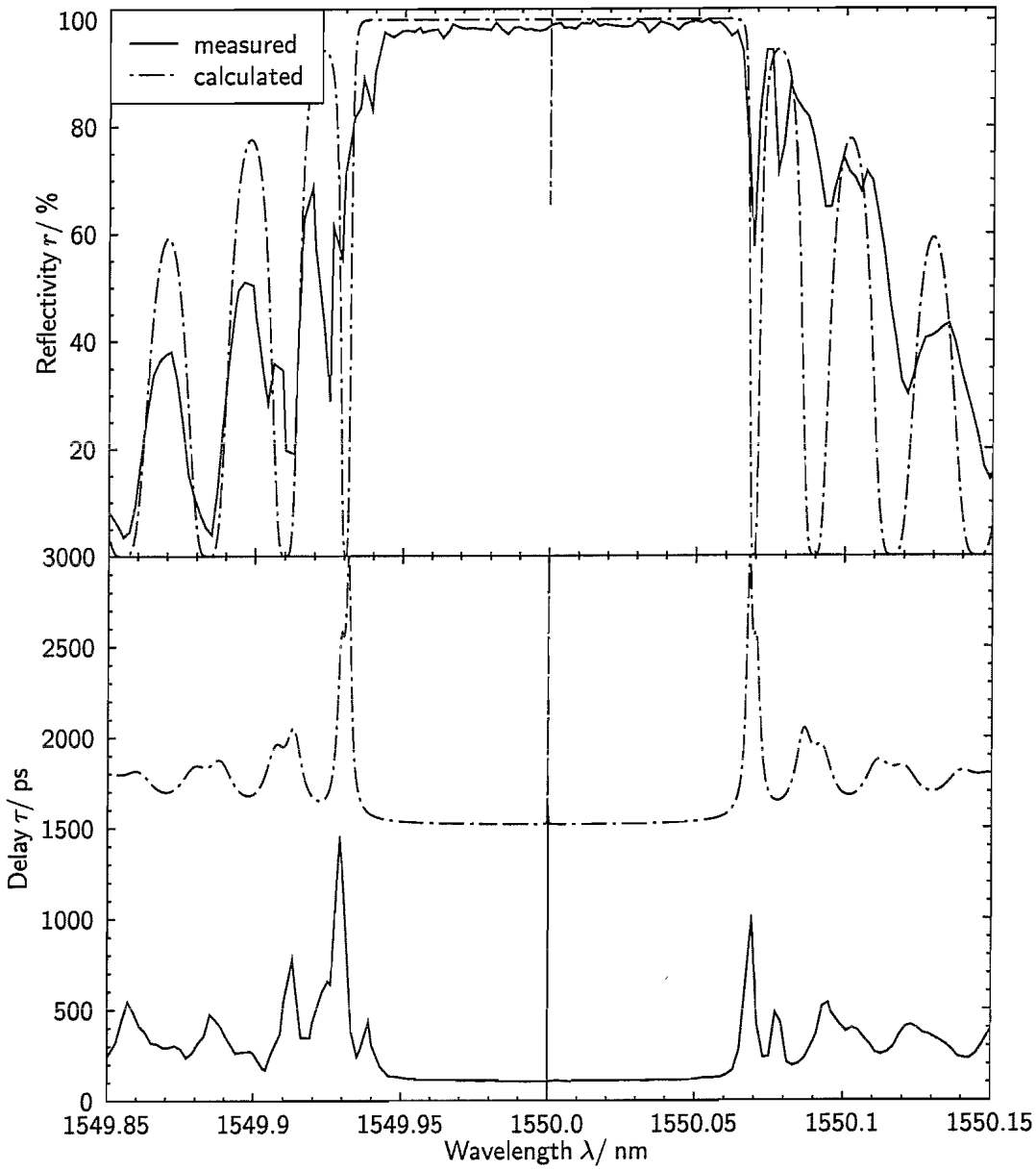

Figure 3.6. Calculated and measured reflection and time delay spectra of a 50 mm long DFB fibre laser with $\kappa = 231\,\mathrm{m}^{1-} \widehat{=} \overline{\delta n_{\mathrm{eff}}} = 1.15 \times 10^{-4}$ and $\Phi = \pi$ phaseshift in the centre. The laser would operate at the narrow reflection dip at the centre of the grating stop band. This feature is not resolved in the measured spectrum. Deviations from the calculated spectra are caused by small imperfections of the actual grating and noise in the measurement system.

3.5 The DFB fibre laser model

The flowchart of the DFB fibre laser model based on the algorithm described in [81] is shown in Figure 3.7. The DFB fibre laser was divided into $M = 50 - 100$ sections. The coupled mode equations were solved by a shooting algorithm [74]. This algorithm starts with the initial conditions at the left hand side of the DFB fibre laser, i.e. the known launched pump power $P_p(0)$, $R(0) = 0$, i.e. no forward propagating wave entering the laser, an estimated backward laser amplitude $S(0)$ and an estimated lasing wavelength λ. The algorithm then steps through the DFB fibre laser section by section. In each section the appropriate rate equations (see Section 3.3.1) could be solved by a 4^{th} order Runge-Kutta algorithm [74], however

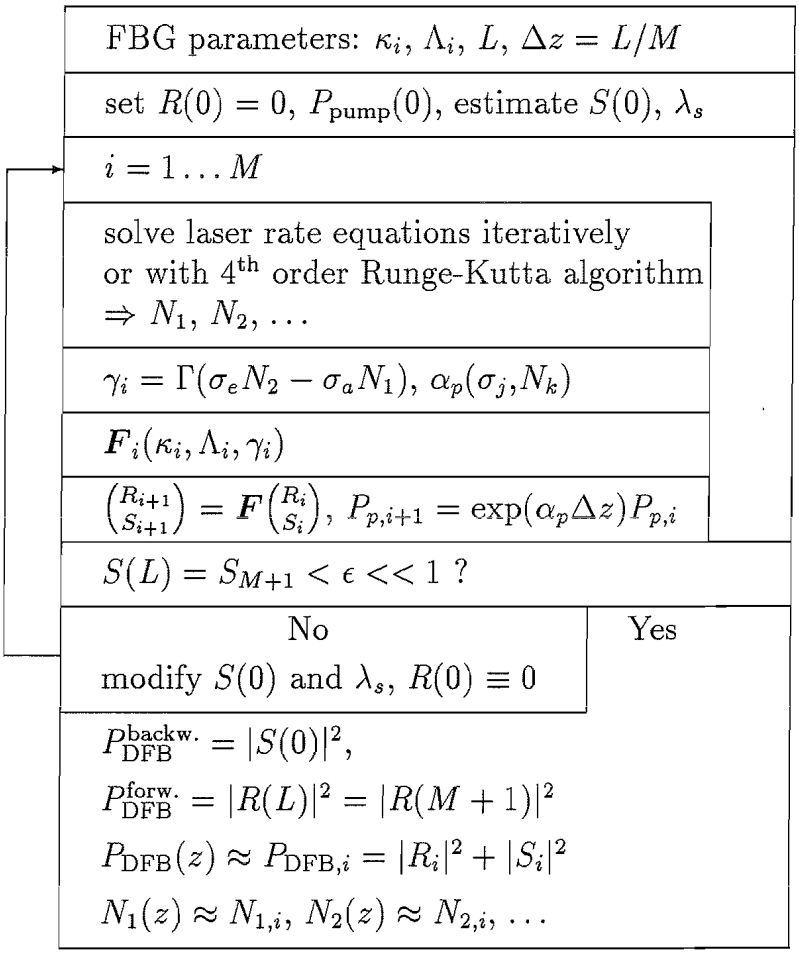

Figure 3.7. Flowchart of the DFB fibre laser model. The coupled mode equations are solved by a shooting algorithm, using transfer matrices. At each section the laser rate equations can be solved by a 4^{th}-order Runge-Kutta algorithm or the much faster iterative algorithm presented in the main text.

the faster iterative approach using the analytical solutions presented in Section 3.3.1 was employed here. This yields the steady state population densities of the energy levels involved in the laser action. Gain and loss at the laser and pump wavelengths inside one section are then calculated from these population densities using (3.15) and (3.16). The relevant data is then inserted into the transfer matrix $\boldsymbol{F}_i$ (3.29-a,b) which is used to calculate R and S of the next section. The absorption of the pump is taken into account by means of (3.15). After reaching the last section the boundary condition $S(M) = 0$, i.e. no backward propagating wave at the forward end of the laser, is tested. If $S(M) > \epsilon$, where $\epsilon << 1$, then $S(0)$ and λ are adjusted to minimise the deviation from the boundary condition [74] in the next propagation through the DFB laser. The procedure is repeated until $S(M) < \epsilon$. Sufficiently accurate results were obtained with $\epsilon = 10^{-4}$. The forward and backward laser output powers are $|R(M)|^2$ and $|S(0)|^2$, respectively. Gain saturation and pump absorption are automatically taken into account by calculating the population densities in each section. Also, green fluorescence power and heat generated by non-radiative decays are easily obtained for each section by calculating the relevant transition rates, e.g. N_4/τ_4 is proportional to the green fluorescence power and N_3/τ_3 is proportional to heat generated under 980 nm pumping.

3.6 Experimental and modelled results

3.6.1 Pumping at 1480 nm

The measured backward output power of a $L = 50$ mm long DFB fibre laser, with $\kappa = 231\,\mathrm{m}^{-1}$ and a π phase shift positioned at the centre, as a function of launched pump power is shown as filled circles in Figure 3.8. The laser was pumped with a 1480 nm semiconductor pump diode[17]. The output power of the DFB fibre laser was measured after the WDM and isolator. The total loss at the lasing wavelength, including splice losses, was 1.8 dB. A 0.2 dB splice loss between the single mode telecommunication fibre and the $Er^{3+}:Yb^{3+}$ fibre was assumed when calculating

[17]Manufactured by Anritsu.

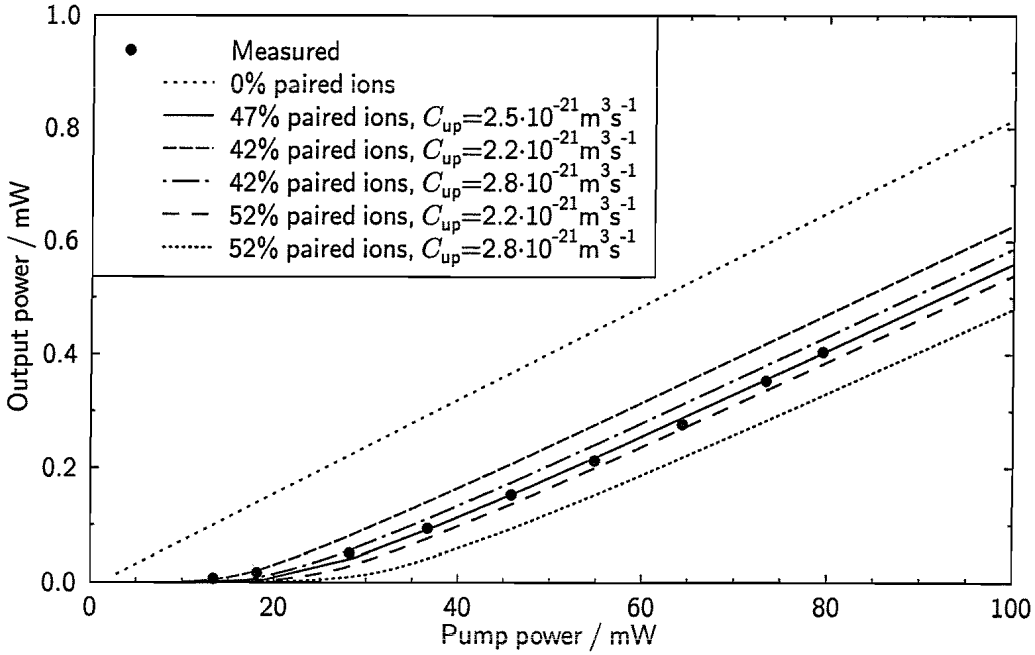

Figure 3.8. DFB fibre laser output power after WDM and isolator (1.8 dB combined loss at 1550 nm) as a function of launched pump power at 1480 nm, i.e. taking 0.2 dB splice loss at 1480 nm into account. Curves show calculated output power for different homogeneous upconversion parameters.

the launched pump power. The threshold power was $\approx$ 15 mW launched pump power. After reaching the lasing threshold the laser output power first increased slowly before reaching a steeper slope with a slope effciency of 0.7% above 35 mW of launched pump power. This behaviour can be explained by homogeneous upconversion. A good fit which was in excellent agreement with the experimental data was found by modelling the DFB fibre laser with the parameters obtained from the gain and absorption measurements of Section 3.3.2 and Table 3.2 and assuming a fraction of 47 % of paired Er^{3+} ions and $C_{up} = 2.5 \times 10^{-21}\,m^3s^{-1}$. This particular choice of upconversion parameters will be further justified shortly. The fit is shown as a solid line in Figure 3.8. As described in Section 3.5 the internal intensity distributions at the pump and lasing wavelengths, the population densities of single and paired ions and the corresponding gain and loss are automatically calculated by the model.

The simulated internal lasing and pump powers of the DFB fibre laser are shown in Figure 3.9 for 25 mW and 100 mW launched pump power i.e. just above threshold

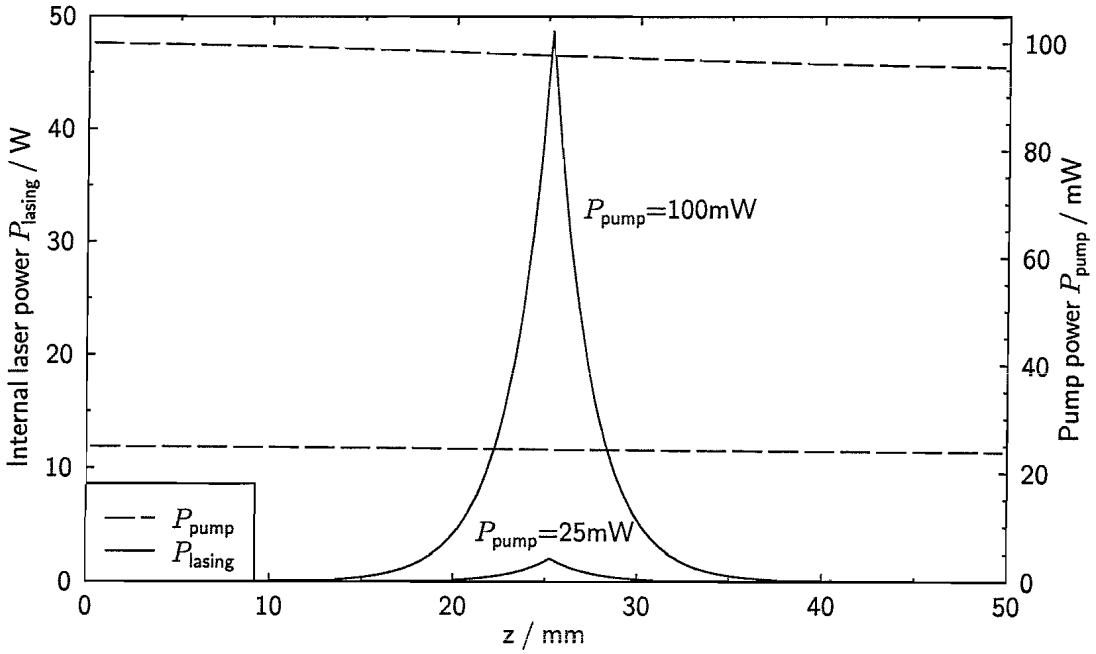

Figure 3.9. Total power distribution of the forward and backward propagating laser modes inside the DFB fibre laser. The laser power is concentrated around the position of the phase shift at the centre of the laser. At 1480 nm the pump power decreases by only 5% along the laser which allows serial multiplexing of several DFB fibre laser in sensor networks.

and at a typical operating level.[18] Because of the small absorption coefficient σ_p at 1480 nm only 5 % of the launched pump power are absorped inside the laser. The majority of the pump power is emitted from the forward end of the laser and can be used to pump further DFB fibre lasers in a serial multiplexed sensor network [34].

The total laser power $|R(z)^2 + S(z)^2|$ peaks at the position of the phaseshift (see Figure 3.9). The population densities, which are shown in the top graphs of Figures 3.10 and 3.11, on the other hand follow a significantly broader distribution, but are also centred at the position of the phaseshift. The gain and loss associated with the single ions and the ion pairs, respectively, are shown in the bottom graphs of those two figures. Although around the phaseshift $N_{1,\text{single}} > N_{2,\text{single}}$ the gain is positive because $\sigma_{21} > \sigma_{12}$. When pumped at 25 mW the population of paired ions is not inverted which therefore introduces a loss in the cavity. However, at 100 mW pump

[18] With modern 1480 nm pump diodes a power of 100 mW can easily be launched into the DFB fibre laser.

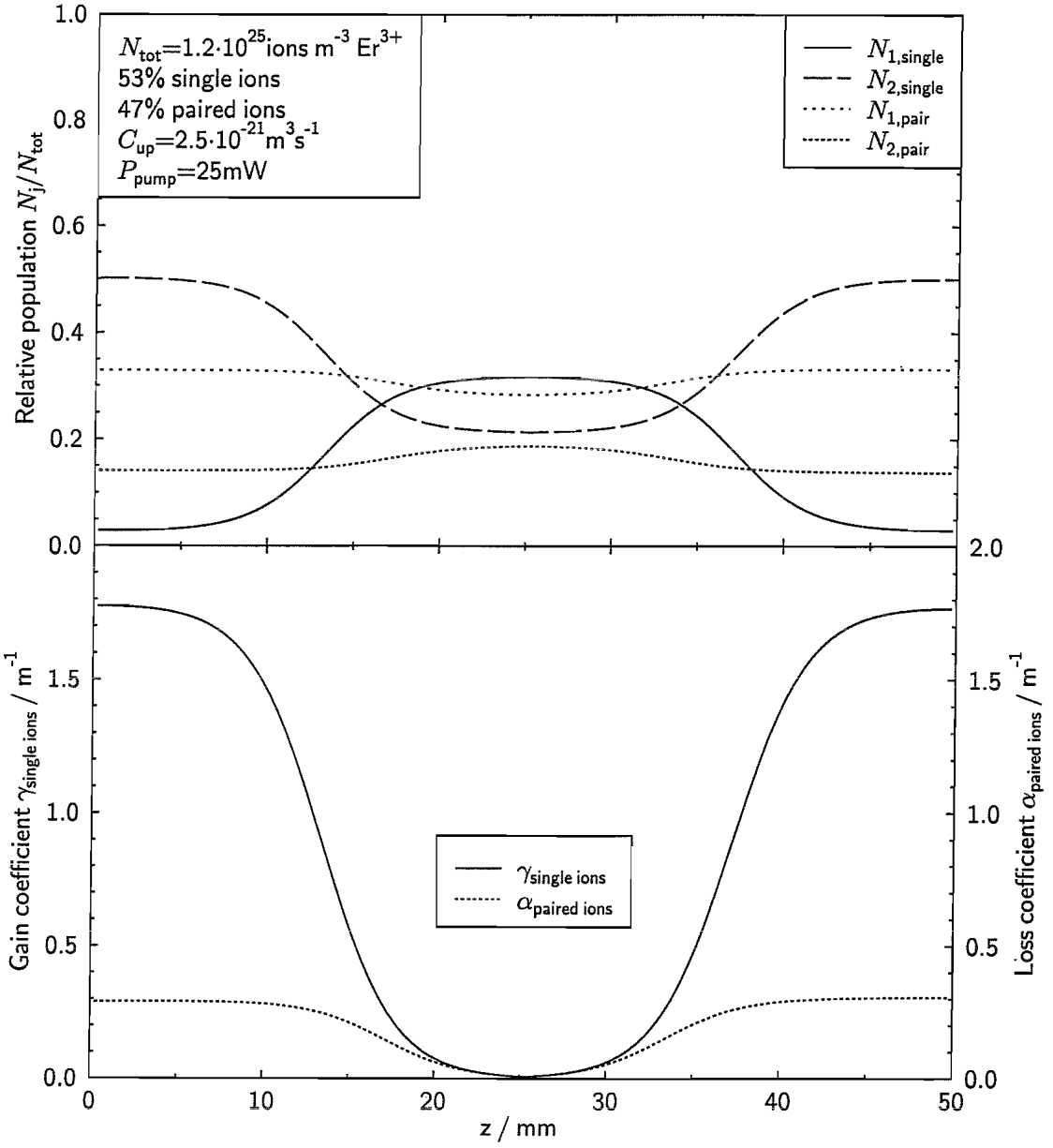

Figure 3.10. Top: Normalised population densities of the ground level $^4I_{15/2}$ (N_1) and upper laser level $^4I_{13/2}$ (N_2) along the DFB fibre laser at low pump power. Single and paired Er^{3+} ions are shown separately. Bottom: Gain is provided by single ions, whereas homogeneous upconversion of ion pairs causes loss.

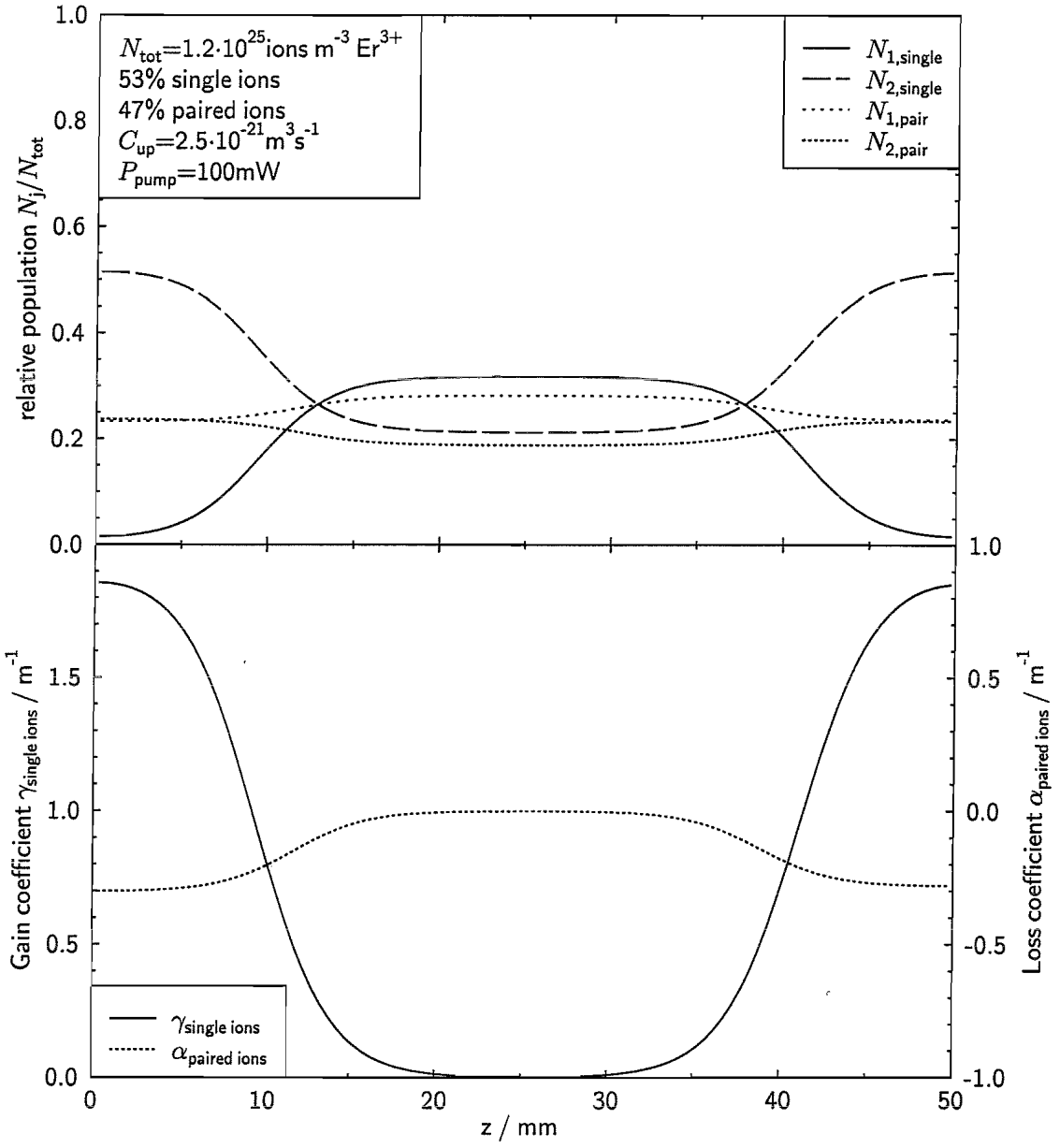

Figure 3.11. Top: Normalised population densities of the ground level $^4I_{15/2}$ (N_1) and upper laser level $^4I_{13/2}$ (N_2) along the DFB fibre laser at high 1480 nm pump power. Single and paired Er^{3+} ions are shown separately. Bottom: Gain is provided by single ions and ion pairs. Gain of the latter is shown as negative loss.

power this population is inverted, contributing a small gain — shown as $\alpha < 0$ in Figure 3.11.

The bottom graphs of 3.10 and 3.11 show the significant gain saturation around the position of the phaseshift and the gain clamping at the threshold value where the gain approaches zero [56]. Gain saturation explains the different shapes of the gain and laser intensity distributions. The small gain variations near the phaseshift exactly amount for the significant change in laser intensity at the same position.

In order to justify the chosen upconversion parameters the effect of their actual values on the laser output power has been simulated. Figure 3.8 also shows simulated output powers when the fraction of paired ions and the upconversion coefficient C_{up} were varied by $\pm 10\%$. Upon this variation the deviation from the measured data becomes significant. Figure 3.12 shows the local gain $\gamma(z)$ provided by the inverted population of single ions and local loss $\alpha(z)$ provided by the non-inverted population of paired ions along the DFB fibre laser as the upconversion parameters are varied.

The larger the fraction of paired ions the more upconversion processes take place per unit volume and time. Consequently the threshold power of the laser increases because for each upconversion process one pump photon is lost and the gain decreases. Furthermore, since one ion per pair terminates in the $^4I_{15/2}$ level the population inversion is reduced, leading to increased losses from paired ions which also increases the threshold power. While keeping the number of ion pairs constant, the initial slope efficiency of the laser output power decreases as the upconversion coefficient C_{up} increases. The lasing threshold increases by a negligible amount. As can be seen in the bottom two graphs of Figure 3.12 the larger C_{up} the more pump power is initially needed to overcome the losses produced by ion pairs and the slope efficiency decreases.

Finally, at high pump powers, for the experimental date above 35 mW, the ion pairs play only a minor role with respect to the output power. The slope efficiency is mainly a function of the grating strength κL and constant background losses.

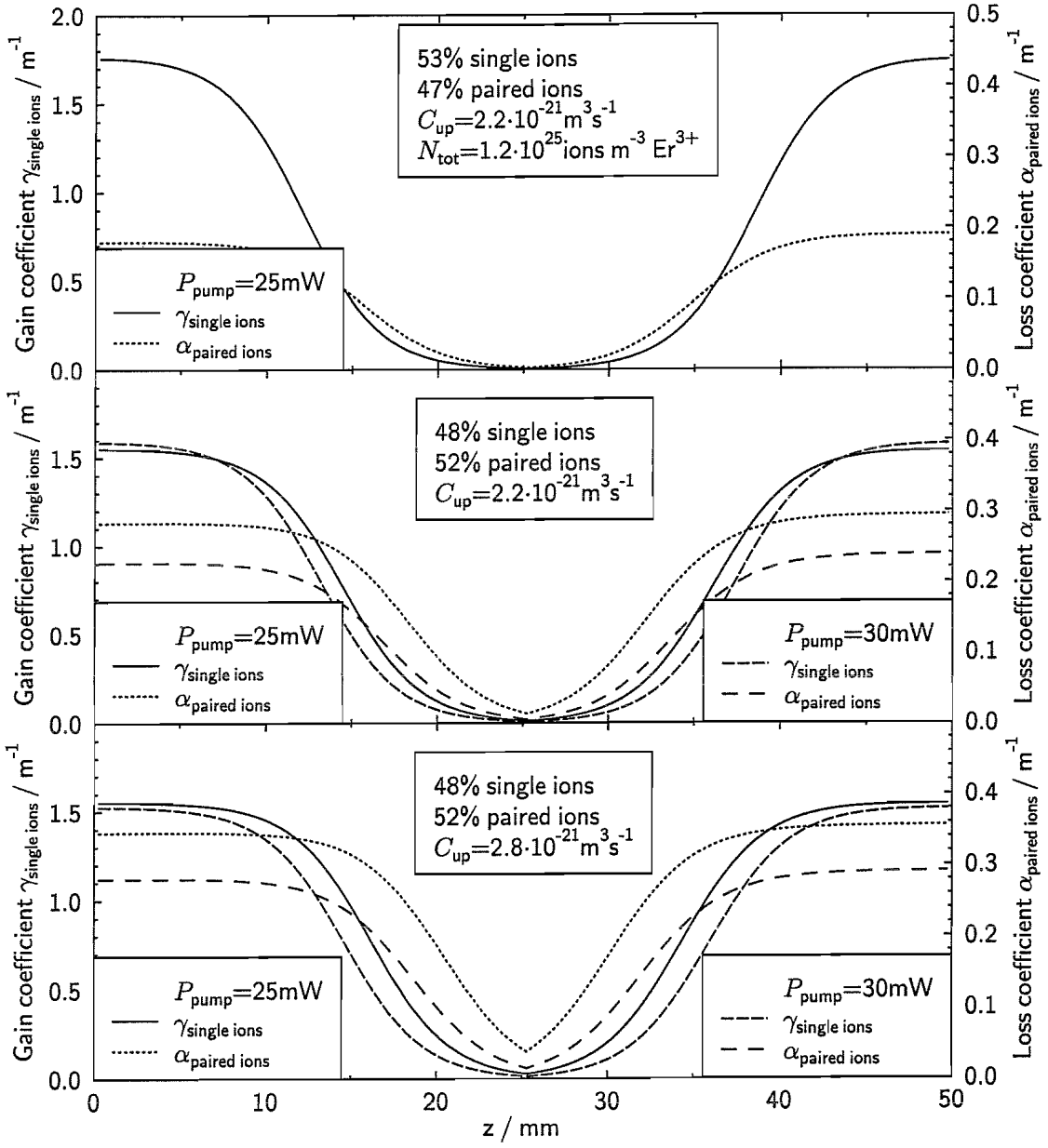

Figure 3.12. Gain γ and loss α provided by an inverted population of single ions and a non-inverted population of paired ions, respectively, at low 1480 nm pump power along the DFB fibre laser. The lower slope efficiency of the DFB fibre laser just above threshold is a consequence of the losses caused by paired ions. See main text for a detailed explanation.

3.6.2 Pumping at 980 nm

A DFB fibre laser with $L = 50\,\text{mm}$ and $\kappa \sim 230\,\text{m}^{-1}$ was pumped with a laser diode[19] operating at 980 nm. Taking splice loss into account the maximum launch pump power was approximately 110 mW. The phaseshift inside the DFB fibre laser was positioned asymmetrically at $0.44L$ [82]. This is the typical specification for telecommunication type DFB fibre lasers in order to increase the laser efficiency by emitting the available laser output predominantly in one direction. The position of the phase shift is of only minor importance to DFB fibre laser sensors where, in general, output power is not a critical parameter. The DFB fibre laser was placed on an aluminium heatsink to dissipate heat generated inside the laser by non-radiative decays — the detrimental effects caused by internal heat generation will be investigated separately in Chapter 4. Figure 3.13 shows the backward output power of the DFB fibre laser as a function of launched pump power. The change of pump wavelength from 1480 nm to 980 nm and the shift of the phaseshift towards the backward output resulted in an increase of the output power of the DFB fibre laser by a factor of 20 (cf. Figure 3.8). The lasing threshold, however, was independent of these changes.

The simulated output power, using the parameters listed in Table 3.4, is shown as a solid line in Figure 3.13. The simulation predicts a lower threshold and an initially higher slope efficiency than the experimental data. As the pump power increases beyond 80 mW the predicted slope efficiency decreases. A similar behaviour is observed experimentally. This decrease is caused by the finite energy transfer rate between Yb^{3+} and Er^{3+} [83] which leads to bleaching of the pump transition ${}^2F_{7/2} \rightarrow {}^2F_{5/2}$ and a reduction of absorbed pump power relative to the launched pump power (see also Figure 3.14). While homogeneous upconversion has been included in the simulation, ESA and energy backtransfer from Er^{3+} to Yb^{3+} have not been taken into account. However, incorporating the last two mechanisms into the simulation showed no significant influence on the calculated slope efficiency and lasing threshold. One possible explanation for the discrepancy between simulated

[19] Nortel LC-91D-20

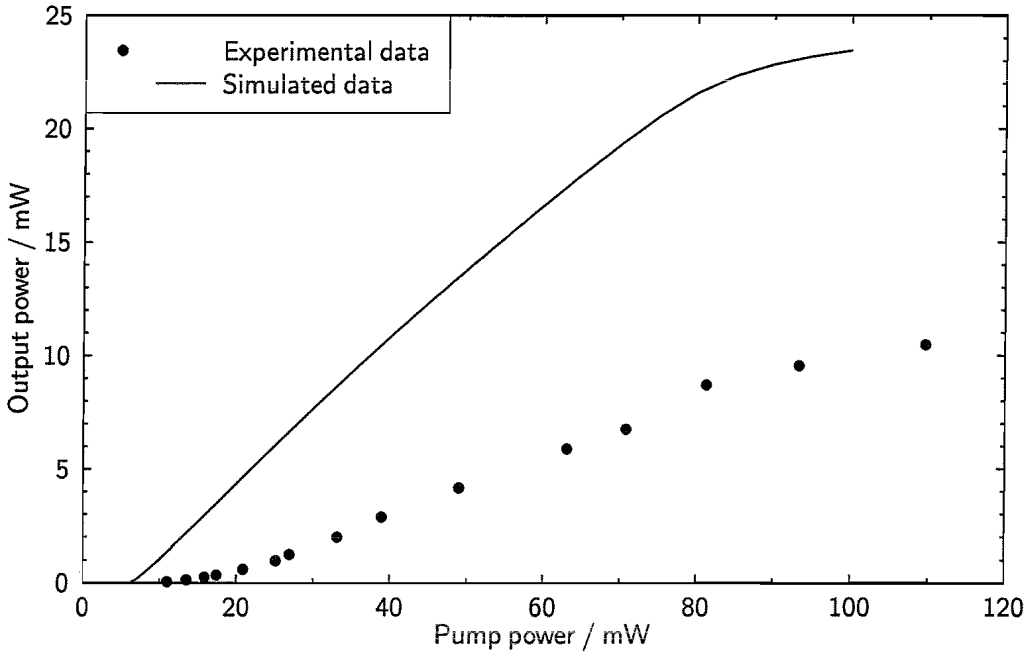

Figure 3.13. Experimental and simulated output power of a DFB fibre laser after the WDM and isolator as a function of launched pump power at 980 nm. The specifications of the DFB fibre laser are: $L = 50\,\mathrm{mm}$, $\kappa \sim 230\,\mathrm{m}^{-1}$ and a phaseshift positioned asymmetrically at $0.44L$. The parameters used in the simulation are listed in Table 3.4. For a discussion of the discrepancy between simulated and experimental data see main text.

and experimental data could be amplified spontaneous emission (ASE) which would lower the available gain near threshold and has not been implemented in the current model. Furthermore, it has been shown that a gain grating, generated by the static interference pattern of the forward and backward propagating waves, would reduce the laser output power [57]. However, data presented in that publication suggests that this effect is too small to explain the observed discrepancy. In Section 4.4.2 it will be shown that insufficient heat transfer from the fibre core to the environment of the fibre can explain some of the difference between measured and simulated data.

Figure 3.14 shows the internal pump and lasing power distribution along the DFB fibre laser. Because of the much larger pump absorption coefficient at 975 nm most of the pump power is absorbed inside the DFB fibre laser. Only at high pump powers the finite energy transfer rate $C_{\mathrm{tr}}N_1N_6$ and bleaching of the Yb^{3+} $^2F_{7/2}$ (N_6) state result in the transmission of $\sim 15\,\%$ of launched pump power. Clearly, this would not allow serial multiplexing of DFB fibre laser. However, this residual pump power emitted into the forward direction should be terminated to eliminate possible

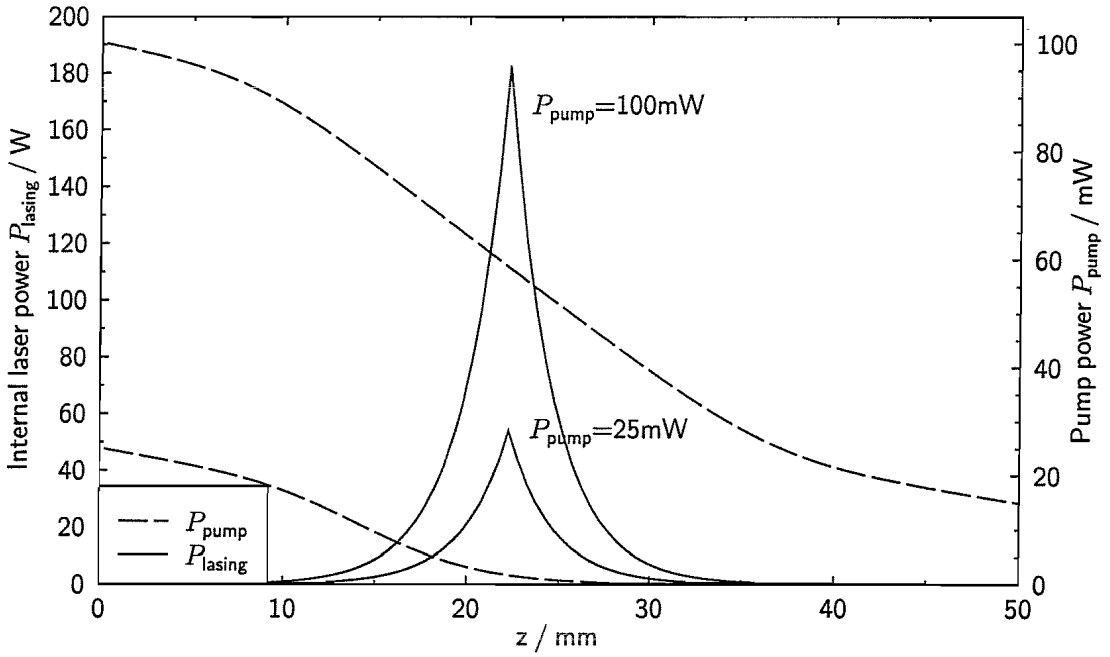

Figure 3.14. Total power distribution of the forward and backward propagating laser modes inside the DFB fibre laser under 980 nm pumping. At 25 mW of launched pump power 100 % of the pump power are absorbed along the laser. At 100 mW this fraction decreases to 85 % making the laser less efficient and wasting available pump power. Compared with pumping at 1480 nm (Figure 3.9) a fourfold increase of the peak internal laser power is observed.

health risks. It can also be seen in Figure 3.14 that the pump absorption $\mathrm{d}P_{\mathrm{pump}}/\mathrm{d}z$ is larger around the phase shift position than at the ends of the laser because of the high lasing power in this central region which requires a larger number of pump photons to be absorbed and converted into photons at the lasing wavelength.

The decrease of absorbed pump power and slope efficiency show that a Er^{3+} : Yb^{3+} DFB fibre laser becomes less efficient as the launched pump power at 980 nm is increased. As in Figure 3.9 the peak of the internal laser power distribution is situated at the phase shift position. As a result of the higher pump absorption the gain, shown in Figures 3.15 and 3.16, and the internal peak power increase compared with pumping at 1480 nm.

The relative population densities of the energy levels taken into account in this model are shown Figures 3.15 and 3.16 for launched pump powers of 25 mW and 100 mW, respectively. The majority of Yb^{3+} ions remain in the ground state because the emission cross-section around 980 nm is significantly larger than the ab-

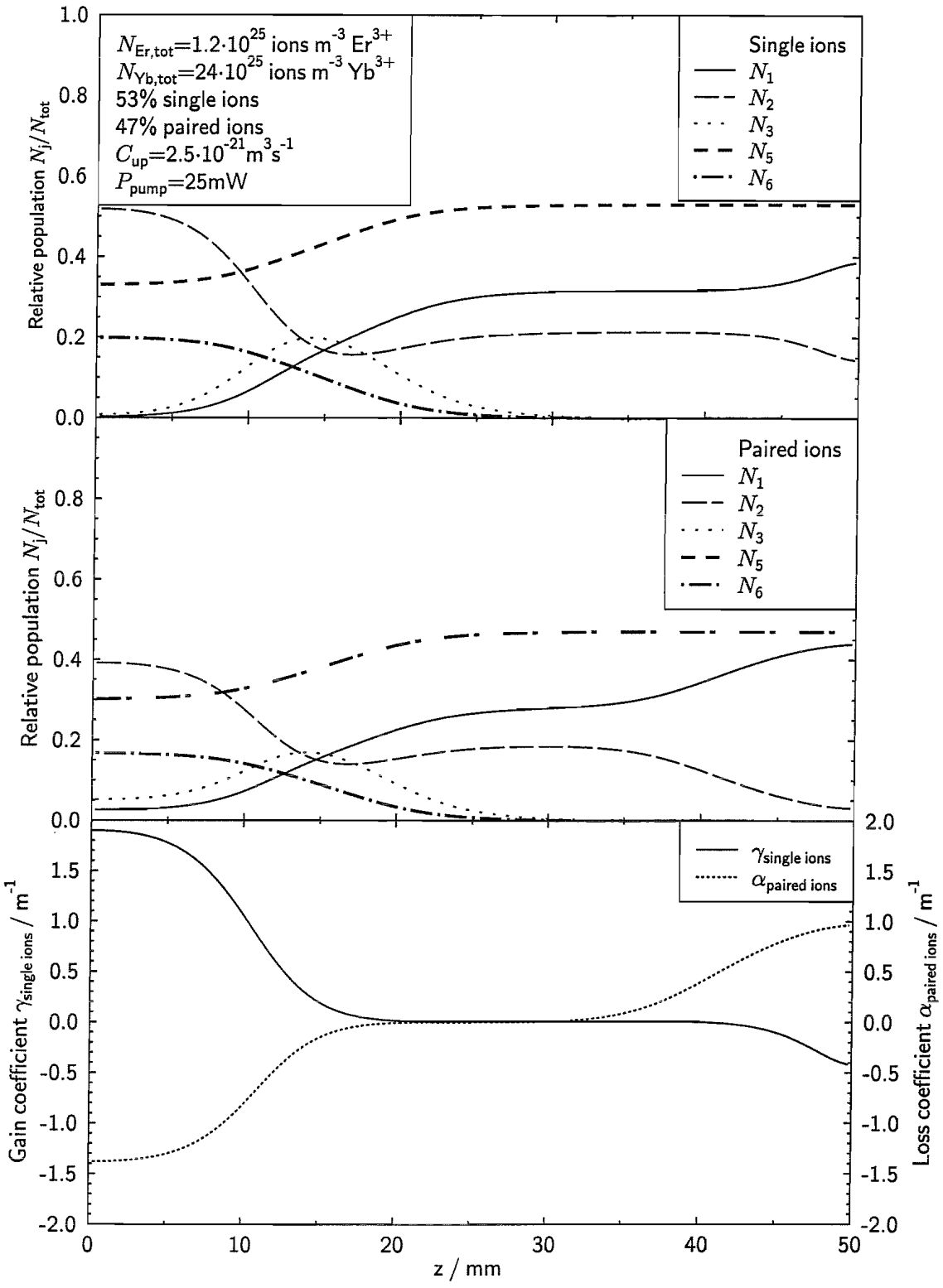

Figure 3.15. Internal population densities of the energy levels taken into account in the model near threshold (top two graphs). The population density distribution is asymmetric with respected to the phase shift at $z = 22\,\text{mm}$ because of the large pump absorption. Contrary to the assumption made in many models $N_3 > 0$. Gain and loss coefficients resulting from the population of single and paired ions are shown in the bottom graph where a negative loss coefficient corresponds to gain.

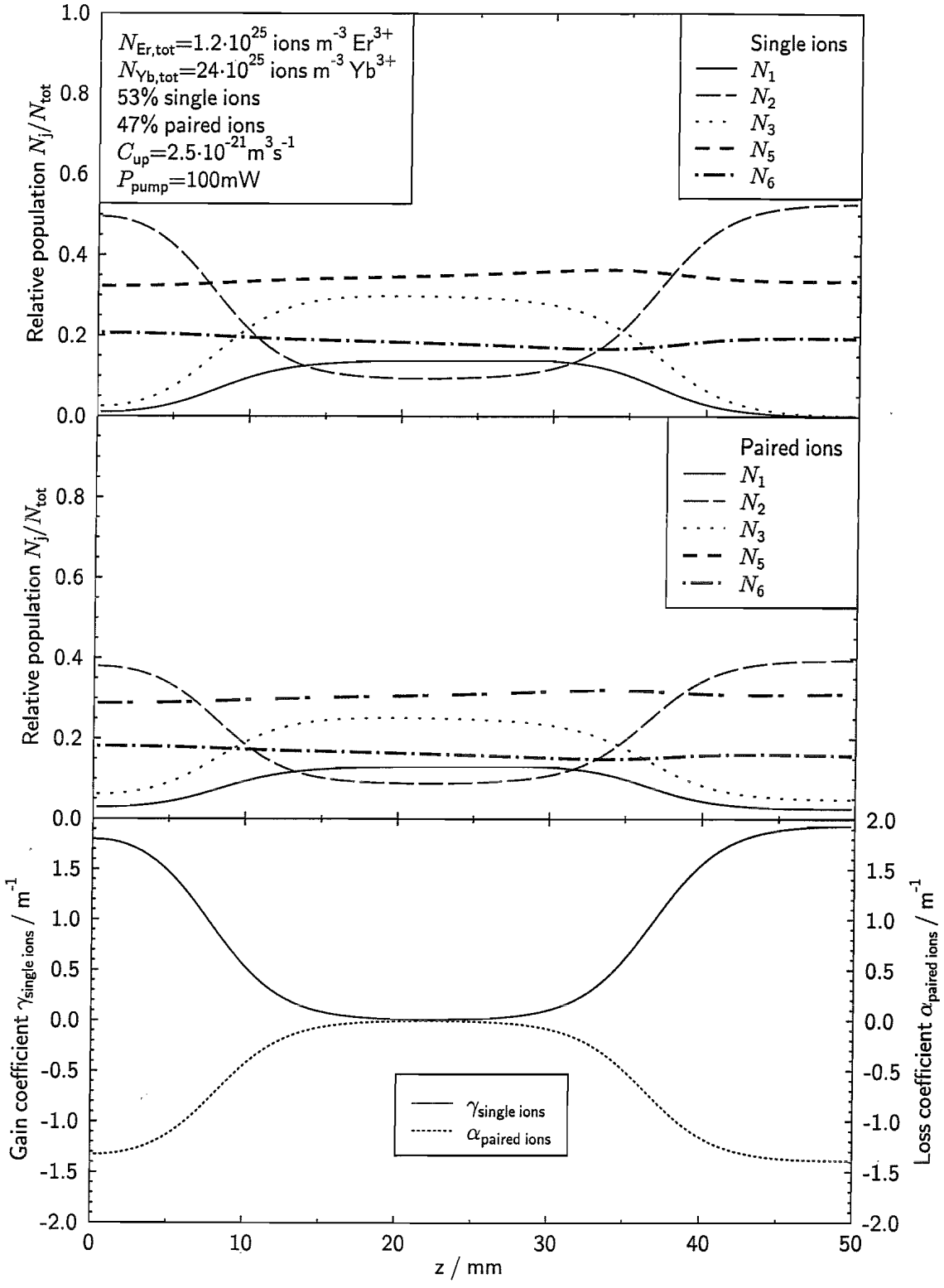

Figure 3.16. Internal population densities of the energy levels taken into account in the model at high pump power (top two graphs). The population density distribution is almost symmetric with respected to the phase shift at $z = 22$ mm because of the bleaching at high pump power. Contrary to the assumption made in many models $N_3 > 0$. Gain and loss coefficients resulting from the population of single and paired ions are shown in the bottom graph where a negative loss coefficient corresponds to gain.

sorption cross-section (see Table 3.2) and the efficient $Yb^{3+} \rightarrow Er^{3+}$ energy transfer. The large pump absorption at 25 mW launched pump power leads to a decrease of the $^2F_{5/2}$ level population along the DFB fibre laser and to asymmetric population densities of the Er^{3+} levels with respect to the position of the phase shift. Despite this asymmetry it can be seen in Figure 3.14 that the laser intensity distribution inside the laser remains symmetric around and centred at the position of the phase shift. At 100 mW pump power the Yb^{3+} population densities vary little along the length of the laser. In the centre region the population of the $^2F_{5/2}$ level (N_6) decreases slightly as the energy transfer rate from Yb^{3+} to Er^{3+} increases with increasing laser intensity.

The population of the $^4I_{11/2}$ level is often neglected in the literature because of its short lifetime. Figures 3.15 and 3.16 show that this simplification does not hold for strongly pumped Er^{3+} : Yb^{3+} codoped DFB fibre lasers, where $N_3 \approx N_1$ or even $N_3 > N_1$.

The simulated data shows that in contrast to pumping at 1480 nm, the paired ions, which undergo homogeneous upconversion, provide gain even at the left (pump input) side of the DFB fibre laser at 25 mW launched pump power. While the experimental slope efficiency still increases around this pump power the simulated one is already constant because of the gain provided by the paired ions. Further experiments with Er^{3+} : Yb^{3+} doped fibres with different dopant concentrations could be carried out to quantitatively characterise the population dynamics of paired Er^{3+} ions and their neighbouring Yb^{3+} ions.

3.7 Conclusion

In conclusion, this versatile numerical model, based on the transfer matrix approach, could accurately reproduce the steady state behaviour of a real DFB fibre laser pumped at 1480 nm. The laser parameters obtained from this simulation, e.g. cross-sections and doping concentration, of were in good agreement with the values reported in the literature and with the Er^{3+} : Yb^{3+} fibre specifications. The set of pump wavelength independent laser parameters was subsequently used together with the

980 nm pump cross-sections and $Yb^{3+} \rightarrow Er^{3+}$ energy transfer rate to simulate the output power of a DFB fibre laser pumped at this shorter wavelength. In this case the predicted output power and slope efficiency were higher than the experimental ones. However, the simulated results agreed qualitatively with the experimental data. Possible explanations of this discrepancy have been discussed, of which the omission of ASE in the model is the most likely.

In contrast to other DFB fibre laser models described in the scientific literature, this new model calculates the population densities of all the relevant energy levels of the rare earth ions. It was found that, in order to model an Er^{3+}:Yb^{3+} DFB fibre laser correctly, more than just the ground and upper laser level have to be taken into account. The effects of homogeneous upconversion, pump ESA and energy transfer rates from Yb^{3+} to Er^{3+} have been investigated. Homogeneous upconversion was identified as being the reason for the lower slope efficiency near threshold. The role of homogeneous upconversion will be further studied in Chapter 4 and Section 7.3 with regard to self-heating of DFB fibre lasers and lasing stability, respectively. Additional characterisation of different Er^{3+} : Yb^{3+} doped fibres would be necessary to obtain further important information about processes like ASE, ESA, green fluorescence and energy transfer between ions. However, this lies outside the scope of this work.

A new iterative method was employed to solve the laser rate equations considerably faster than the commonly used 4^{th}-order Runge-Kutta algorithm while yielding the same accuracy. This offers the possibility of almost instantly exploring the influence of various gain medium and fibre parameters on, e.g., the laser threshold and slope efficiency in order to optimise the design of real DFB fibre lasers.

The fast algorithm for calculating the population densities of the relevant energy levels allows this DFB fibre laser model to be easily extended to incorporate, for the first time, self-heating caused by non-radiative decays. This important extension of the model and the respective experimental foundations will be discussed in the next Chapter.

4 Internal heating of DFB fibre lasers caused by non-radiative decays

4.1 Evidence of self-heating

Self-heating of $Er^{3+}:Yb^{3+}$ DBR [84, 85] and DFB [60] fibre lasers pumped at 980 nm has been reported previously. The sources of this self-heating are non-radiative transitions of Er^{3+}. The most prominent non-radiative transition is the ${}^4I_{11/2} \rightarrow {}^4I_{13/2}$ which occurs under 980 nm pumping. When the lasers are pumped at 1480 nm the non-radiative transition within the ${}^4I_{13/2}$ manifold becomes important (see p. 24). In addition the ${}^4I_{9/2} \rightarrow {}^4I_{13/2}$ non-radiative transition which is part of the upconversion process described on p. 28 generates heat. One has to distinguish between uniform and non-uniform self-heating which have different effects on DBR and DFB fibre lasers. As a result of uniform self-heating along the laser its wavelength increases according to (2.11). In addition to the wavelength increase non-uniform self-heating can reduce the laser output power of DBR fibre lasers [84] due to a mismatch of the centre wavelengths of its FBGs. The reduction of laser output power of a DFB fibre laser reported in [60] is most probably caused by the same effect which chirps the DFB grating and reduces feedback. Furthermore, variations of the thermal environment along the laser, e.g. forced air convection, result in local temperature fluctuations and subsequently laser instability [85].

The detrimental effects of self-heating of $Er^{3+}:Yb^{3+}$ DFB fibre lasers were also observed during different experiments described later in this thesis. First, under 1480 nm pumping the laser wavelength shift due to self-heating was found to be a linear function of launched pump power, see Figure 5.7 which could potentially lead to measurement errors of strain and temperature sensors. When pumped at 980 nm the output power of the DFB fibre lasers depended strongly on the heat transfer from the lasers to their environment. Low heat transfer lead to a reduction of output power, and the lasers ultimately stopped operating. Good heat transfer could be achieved by forced air convection or by placing the DFB fibre lasers on good thermal conductors, e.g. metal plates. The first method easily induces vibrations of the laser and temperature fluctuations at the fibre surface. Both resulted in wavelength variations. Placing the DFB fibre lasers on metal plates increased the heat transfer only along the small surface area which was in contact with or in close proximity of the plates. By covering the lasers in oil the overall heat transfer could be increased further and a better lasing stability could be achieved.

This study, which combines experimental and modelled results, is of great importance in choosing the right materials and designing suitable structures for effective packaging of DFB fibre lasers. The DFB fibre laser model which has been developed in the previous Chapter provides an excellent base for theoretical investigations of self-heating effects. In this Section, for the first time, the generation of heat by non-radiative transitions and its transfer from the fibre core to the environment will be incorporated into a DFB fibre laser model.

4.2 Extended DFB fibre laser model with heat generation and heat transfer

For a three level laser like Er^{3+} the heat generated by non-radiative decay from the pump level N_3 to the upper laser level N_2 within a doped core section of length Δz per unit time is given by

$$Q_{\text{pump}}(z) = \frac{N_3(z)}{\tau_3} h \Delta\nu A_c \Delta z, \tag{4.1}$$

where N_3 and τ_3 are the population density and lifetime of the pump level, h is Planck's constant, $\Delta\nu = \nu_p - \nu_s = c(1/\lambda_p - 1/\lambda_s)$ is the optical frequency difference between the pump light at wavelength λ_p and the laser wavelength at λ_s and A_c is the core area. Equation (4.1) can be simplified for Er^{3+} lasers pumped at 1480 nm which are successfully modelled as two level systems (see Section 3.3.1). Because of the fast non-radiative decay from the pump level to the upper laser level within the $^4I_{13/2}$ manifold stimulated emission at 1480 nm can be neglected and each absorbed pump photon is converted into a photon at the lasing wavelength. Then the heat generated within a length of fibre is simply given by

$$Q_{\text{pump}}(z) = \eta \Delta P_p(z), \tag{4.2}$$

where $\eta = (\nu_p - \nu_s)/\nu_p$ is the fraction of pump photon energy converted into heat and ΔP_p is the absorbed pump power per fibre section of length Δz.

Homogeneous upconversion of paired Er^{3+} ions also contributes to self heating of DFB fibre lasers when the upconverted ion decays non-radiatively to the $^4I_{13/2}$ level. Using the simplified upconversion term (3.7) the heat generated by this process within one core section becomes

$$Q_{\text{upconv}}(z) = C_{up} N_2^2 h\nu_s A_c \Delta z. \tag{4.3}$$

The equilibrium temperature distribution inside the DFB fibre laser can be found by solving the steady state heat diffusion equation [86]

$$k\nabla^2 T(z) + Q(z) = 0, \tag{4.4}$$

where k is the thermal conductivity of the silica fibre. The boundary condition at the fibre surface is determined by the heat transfer from the fibre surface at temperature T_{surf} to its environment at temperature T_0 [86, 87]:

$$-k\nabla T_{\text{surf}}(z) = h_c(T_{\text{surf}}(z) - T_0), \tag{4.5}$$

where h_c is the heat transfer coefficient. The latter depends on the nature of the heat transfer, e.g. natural convection, forced convection or thermal conduction [86].

For uniform heat generation along the DFB fibre laser the longitudinal component of the heat transfer vanishes and only the radial component has to be taken into

account [87]. Under these conditions an analytical solution of (4.4) with boundary conditions (4.5) exists [86, 87]. However, as shown in Figures 3.9, 3.14 and 3.15 the pump power absorption and population density of the pump level N_3 vary along the DFB fibre laser, the heat generation becomes non-uniform and in general no analytical solution can be found. An elegant numerical approach for solving (4.4) is the Gauss-Siedel method [86] which has been incorporated into the DFB fibre laser model described in Section 3.5.

The DFB fibre laser is divided into a number of cells. An energy balance is performed for each cell, taking into account the heat generated within the cell and the heat flow in and out of it at its boundaries. The cylindrical symmetry allows the fibre to be divided into the cell grid shown in the top of Figure 4.1 where only one half of the fibre cross-section needs to be considered. This half is divided into core and cladding cells, whereby the latter include the B/Ge ring and the silica cladding (see Section 3.2. Along the longitudinal fibre axis the cells coincide with the fibre sections used in the transfer matrix approach for solving the coupled mode equations (see Section 3.5). A two-dimensional representation of the cells is shown in the bottom of Figure 4.1. All cells are located at the boundary of the fibre half under consideration. One boundary is the cladding surface which is in contact with the environment, the other is the iso-thermal surface between the two fibre halves.

The energy balance for the core cells is given by [86]

$$\frac{kA_{\text{core}}}{\Delta z}(T_{\text{core,i}-1} - 2T_{\text{core,i}} + T_{\text{core,i}+1}) + \frac{kA_{\text{int}}}{b}(T_{\text{surf,i}} - T_{\text{core,i}}) + Q_i = 0, \qquad (4.6)$$

where the $T_{\text{core,i}}$ and Q_i are the temperature of and the heat generated within the i^{th} core cell, respectively, and b is the cladding radius. The areas A_{core} and A_{surf} are shown in Figure 4.1. The first term in (4.6) describes the heat transfer by conduction across A_{core} at the left and right side of core cell i. The heat transfer is proportional to the temperature difference between the adjacent cells. The second term accounts for radial heat conduction from the core cell to the adjacent surface cell. No heat is transferred across the iso-thermal surface because the temperature gradient is zero. In thermal equilibrium the amount of heat inside a cell remains constant and the sum of all terms in (4.6) equals zero.

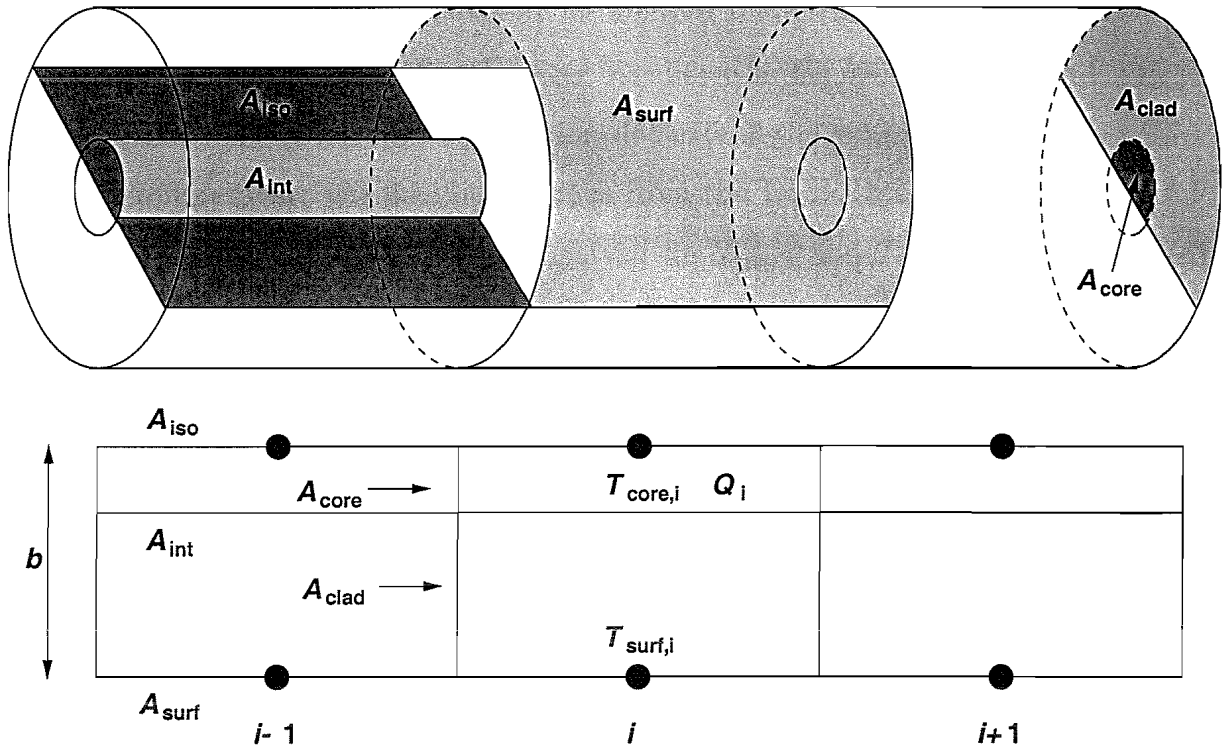

Figure 4.1. Division of the DFB fibre laser into core and cladding cells in order to calculate the temperature distribution along its length. Heat, which is generated by non-radiative transitions in the core cells, is transferred to neighbouring cells and the environment of the fibre by heat conduction and free convection, respectively. The fibre symmetry allows to reduce the 3-dimensional representation (top) into a 2-dimensional one (bottom). The Gauss-Siedel method is used to calculate the steady-state temperature distribution inside the core and on the fibre surface.

Similarly the energy balance for the surface cells is given by

$$\frac{kA_{\text{cald}}}{\Delta z}(T_{\text{surf,i}-1} - 2T_{\text{surf,i}} + T_{\text{surf,i}+1}) + \frac{kA_{\text{int}}}{b}(T_{\text{surf,i}} - T_{\text{core,i}}) - h_c A_{\text{surf}} T_{\text{surf,i}} = 0, \quad (4.7)$$

where the last term describes the combined heat transfer by conduction and convection from the fibre surface to the environment. Since only the temperature difference between the fibre and the environment is of interest, the latter is set to $T_0 = 0$. No heat is generated inside the surface cells. When the DFB fibre laser is in thermal equilibrium its surface temperature is proportional to the temperature of the Er^{3+}:Yb^{3+}-doped core [87].

In order to take longitudinal heat transfer from the DFB fibre laser to the lead fibre into account ten core and surface cells have been added on both sides of the laser. Depending on Δz these cells represent about 5-10 mm of fibre in which no

heat is generated. The temperature of the cell furthest away from the laser was set to $T_0 = 0$. This choice of additional fibre length was confirmed by temperature measurements which showed that the surface temperature of the fibre decayed to ambient temperature within this distance from the DFB fibre laser.

Equations (4.6) and (4.7) can be solved for $T_{\text{core,i}}$ and $T_{\text{surf,i}}$, respectively. After setting all initial temperatures to zero the Gauss-Siedel method then iteratively calculates $T_{\text{core,i}}$ and $T_{\text{surf,i}}$, $i = 1 \ldots N$, immediately overwriting the old cell temperatures with the new ones. This process is repeated until for all i $|T_{\text{new,i}} - T_{\text{old,i}}| < \epsilon$ which was chosen to be $10^{-5}\,\text{K}$.

After the equilibrium temperature distribution along the DFB fibre laser is found, the grating period Λ and the effective refractive index n_{eff} of each grating section is adjusted according to its temperature using (2.12) and (2.13) with the values $\alpha = 0.5 \times 10^{-6}\,\text{K}^{-1}$ [40] and $\xi = 4.6 \times 10^{-6}\,\text{K}^{-1}$ (see Section 5.1.4). Then the coupled mode equations are solved again for the new DFB grating. This process is repeated until the temperature distribution changes by less than a predefined value from one iteration to the next. An adequate choice is to demand that in average the cell temperatures between two iterations varies by less than 0.05 K. This way the temperature distribution and the thermally-induced FBG chirp are calculated in parallel with the resulting output power and lasing wavelength.

4.3 Experimental arrangement for investigating self-heating effects

A comprehensive study of self-heating of DFB fibre lasers requires the simultaneous measurement of laser output power, lasing wavelength and longitudinal temperature profile as a function of pump wavelength, pump power and heat transfer to the environment.

The experimental arrangement for studying self-heating while pumping in the 980 nm band is shown in Figure 4.2. A master oscillator power amplifier (MOPA)[1]

[1]SDL 8630

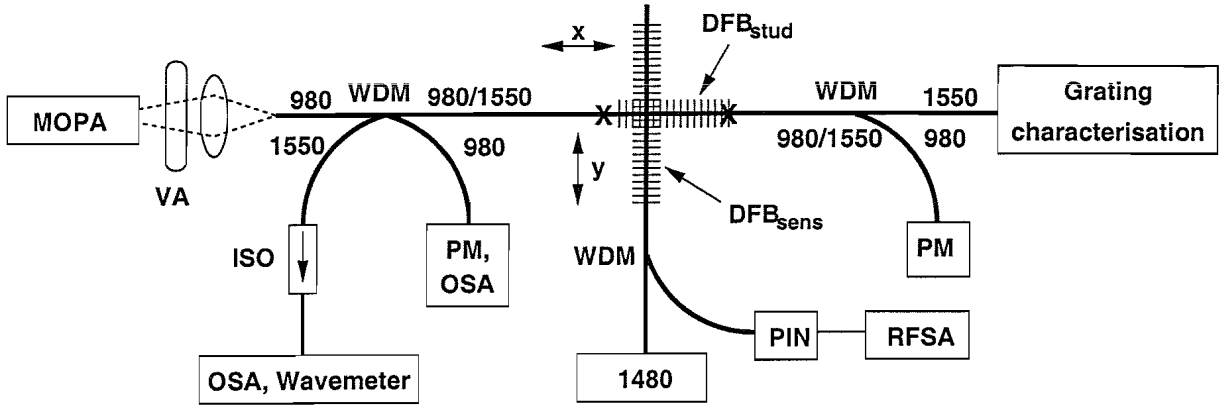

Figure 4.2. Experimental arrangement to study self heating effects of DFB fibre lasers. DFB_{stud} was subject to various self-heating conditions, determined by the pump power, pump wavelength dependent absorption and heat transfer from the fibre surface to its environment. The latter was changed by placing the DFB fibre laser in MDF board or an aluminium block without and with an additional oil cover. DFB_{sens} was used as a very sensitive temperature sensors (see Section 5.1).
MOPA=master oscillator power amplifier, VA=variable attenuator, WDM=wavelength division multiplexer, ISO=isolator, PM=power meter, OSA=optical spectrum analyser, 1480 = 1480 nm pump diode, PIN=photo detector, RFSA=RF spectrum analyser.

was used as a pump laser whose wavelength could be varied between 970 nm and 980 nm. The light from the MOPA was coupled into the 980 nm input of a four port WDM. The pump intensity could be varied with a variable attenuator positioned between the MOPA and the fibre launch optics. A maximum pump power of $\approx$ 130 mW was incident on the DFB fibre laser spliced to the 980/1550 output of the WDM. The backward output of the DFB laser passed through the WDM and an isolator. Output power and laser wavelength were measured with an optical spectrum analyser[2]. At the forth port of the WDM a small fraction of the pump light could be detected to monitor the pump wavelength and pump power. The ratio between the pump power in this arm of the WDM and the amount incident on the DFB fibre was approximately -38 dB and had been measured for different pump wavelengths before the DFB fibre laser was spliced to the WDM.

While the output power and lasing wavelength of DFB fibre lasers are of immediate importance in telecommunication and sensor applications, the surface temper-

[2]Manufactured by ANDO, resolution 0.1 nm.

ature distribution of the laser yields valuable information about its actual thermal environment. This information can be used to improve the thermal management of the laser and potentially increase the output power and decrease wavelength shifts. The surface temperature of the DFB fibre laser could potentially be measured with a small thermocouple. The available readout units for the thermocouple had a temperature resolution of only 0.1°C (see also Section 5.1.3). On the other hand, a DFB fibre laser temperature sensor with an accuracy of 0.04°C will be demonstrated in Section 5.1. Because of its higher accuracy this DFB fibre laser temperature sensor was used to measure the surface temperature distribution along the DFB fibre laser under investigation (DFB_{stud} in Figure 4.2). The DFB fibre laser sensor (DFB_{sens}) was pumped at 1480 nm[3] and its temperature dependent polarisation beat frequency was measured with an RF spectrum analyser[4] (see Section 5.1.3). The temperature response of the sensor was $-0.87\,\mathrm{MHz/°C}$.

DFB_{sens} was placed perpendicular across DFB_{stud} and could be moved along the axis of the latter with a manual translation stage. The surface temperature rise of DFB_{stud} was measured at intervals of 2–4 mm along the laser. At the cross-over point of the two lasers a polystyrene cube (3 mm × 3 mm × 3 mm) was placed on top of the two laser to achieve good thermal contact between them. The small weight of the cube ensured that its influence on the two lasers was kept to a minimum.

As the temperature sensitivity of DFB fibre lasers is greatest at the position of their phase shift [52] the cross-over point of DFB_{sens} and DFB_{stud} had to coincide with the phase shift position of the former. This optimum position of DFB_{sens} was found by translating the sensor perpendicular (y-direction in Figure 4.2) to the fibre axis of DFB_{stud} and measuring the polarisation beat frequency change induced by the surface temperature rise of the latter. Figure 4.3 shows the frequency response of DFB_{sens} as a function of the distance y between its phase shift and its contact point with the heated DFB_{stud}. A Lorentzian curve has been fitted to the data. The FWHM of the fitted curve is 5 mm, which is expected from the internal lasing intensity distribution of the DFB fibre laser shown in Figure 3.9. This curve shows

[3] 1480 pump diode: Philips, CQF 858

[4] Tektronix 2782

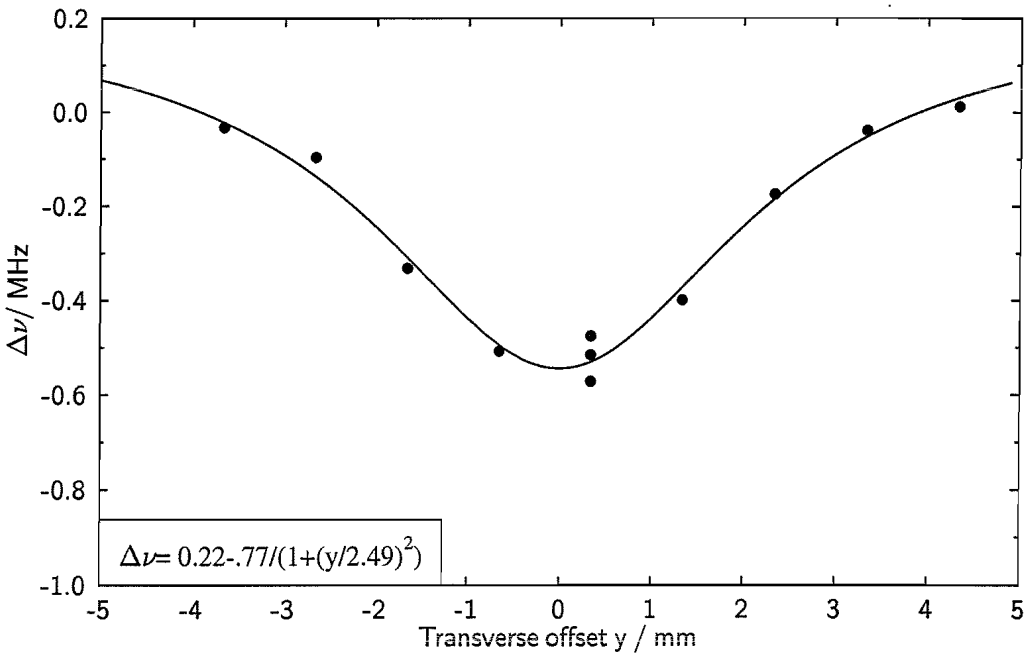

Figure 4.3. Polarisation beat frequency change of the DFB fibre laser sensor as a function of the distance between its phase shift and its contact point with the DFB fibre laser under investigation. The latter was heated by pump light at 975 nm. The FWHM of the Lorentzian curve is 5 mm. The sensor DFB is most sensitive at its phase shift which therefore has to be positioned exactly on the DFB laser whose temperature should be measured.

that small transverse movements of DFB_{sens} with respect to DFB_{stud} introduce errors in the order of a few percent when the frequency shift is converted into a temperature change.

The phase shift of DFB_{stud} was positioned asymmetrically at $0.44L$ so its output was predominantly towards the backward direction (see ref. [82] and p. 50) with only a negligible fraction of light being emitted in the forward direction. This allowed to measure the grating reflectivity and time delay from the forward output while the DFB fibre laser was operating. This additional measurement was used to verify the measured temperature distribution by comparing the measured spectrum with the spectrum calculated from the temperature distribution.

In order to vary the heat transfer properties at the fibre surface DFB_{stud} was either placed on a medium density fibre (MDF) board or an aluminium block. Aluminium has a thermal conductivity of $247\,Wm^{-1}K^{-1}$ [88] and h_c is expected to be high. The thermal conductivity of MDF was assumed to be similar to that of ply-

wood, i.e. 0.11 $Wm^{-1}K^{-1}$ [89] and h_c is expected to be small. Both DFB fibre lasers were covered by a polystyrene box in order to prevent unwanted airflows across the lasers and associated temperature fluctuations.

Because self-heating effects under 1480 nm pumping are small the experimental effort could be reduced to the setup shown in Figure 3.2. The main effect is a small wavelength increase with pump power which has been measured for a symmetric DFB fibre laser and is identified in Section 5.1.5 as an effect that could potentially reduce the measurement accuracy of a strain and temperature sensor.

In order to verify the extended DFB fibre laser model simulated output power and wavelength shift were compared with experimental data.

4.4 Laser efficiency and wavelength increase under different heat generation and heat transfer conditions

4.4.1 Self-heating under 1480 nm pumping

Figure 4.4 shows the experimental wavelength shift with pump power at 1480 nm and a straight line fit indicating a linear dependence on pump power as shown in Figure 5.7. The wavelength change with pump power predicted by the extended DFB fibre laser model is shown in addition. The thermal conductivity of the fibre was assumed to be $k = 1.4\,Wm^{-1}K^{-1}$ [87, 13]. All other laser parameters were the same as in Chapter 3. The linear fit is best approximated with $h_c = 11\,Wm^{-2}K^{-1}$, where the error of h_c is less than $\pm 10\,\%$. This value of h_c is a factor of eight smaller than the value reported in [87]. However, the reported value is valid for natural air convection which might have been reduced as the DFB fibre laser was placed inside a small oven (see Section 5.1.3) resulting in a smaller h_c. It is also shown in the Figure that homogeneous upconversion contributes only a marginal amount to the pump dependence of the wavelength shift.

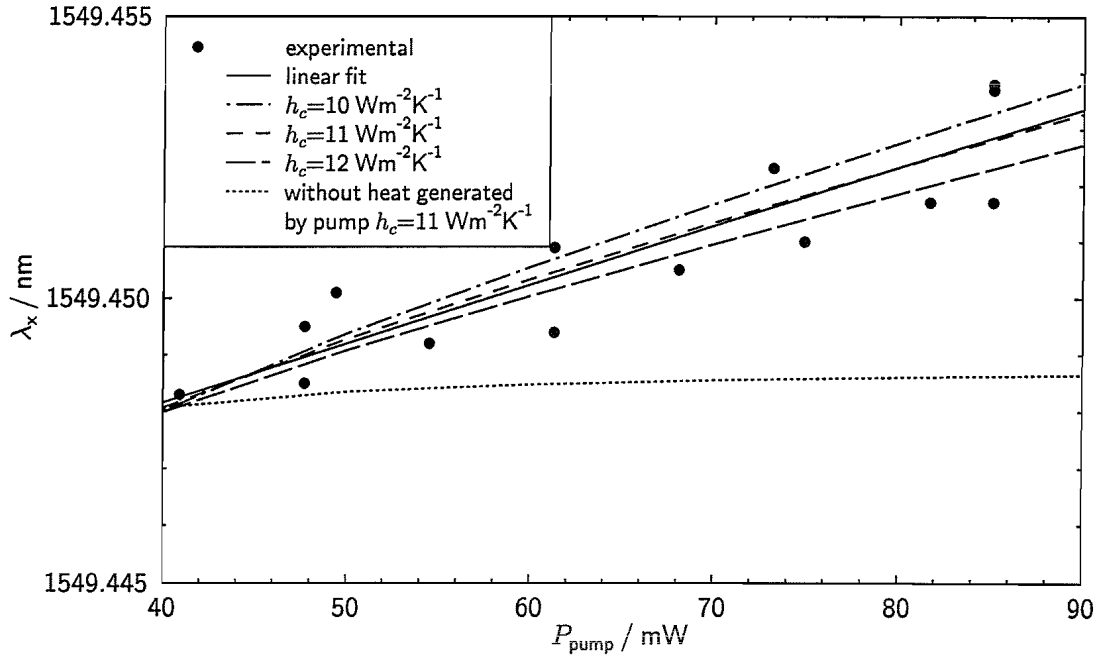

Figure 4.4. Laser wavelength change as a function of pump power at 1480 nm due to self-heating of the DFB fibre laser. The experimental values and the linear fit are the same as in Figure 5.7. The simulated wavelength change is shown for a heat transfer coefficient at the fibre-air interface of $h_c = (11 \pm 1)\,\mathrm{Wm^{-2}K^{-1}}$ with the thermal conductivity of the fibre $k = 1.4\,\mathrm{Wm^{-1}K^{-1}}$. Homogeneous upconversion contributes only a marginal amount of heat to the expected wavelength change.

Figure 4.5 shows the calculated temperature distribution along the DFB fibre laser using the thermodynamic parameters found from Figure 4.4. In the top graph heat contributions from non-radiative decay within the $^4I_{13/2}$ manifold and homogeneous upconversion are taken into account while in the bottom graph only the contribution of the latter is considered. Comparing the top and bottom graphs reveals that the shape of the temperature distribution is determined by the heat generated by homogeneous upconversion which according to (4.3) is proportional to $N^2_{2,\mathrm{pair}}$. The relation between the calculated $N_{2,\mathrm{pair}}$, shown in Figures 3.10 and 3.11 for 25 mW and 100 mW of pump power, and the resulting temperature distributions can clearly be seen.

From Figures 4.4 and 4.5 one can observe that despite the fact that the overall temperature distribution along the DFB fibre laser is determined predominantly by the homogeneous upconversion mechanism, the lasing wavelength shift with pump power is dominated by the non-radiative decay inside the $^4I_{13/2}$ manifold. The

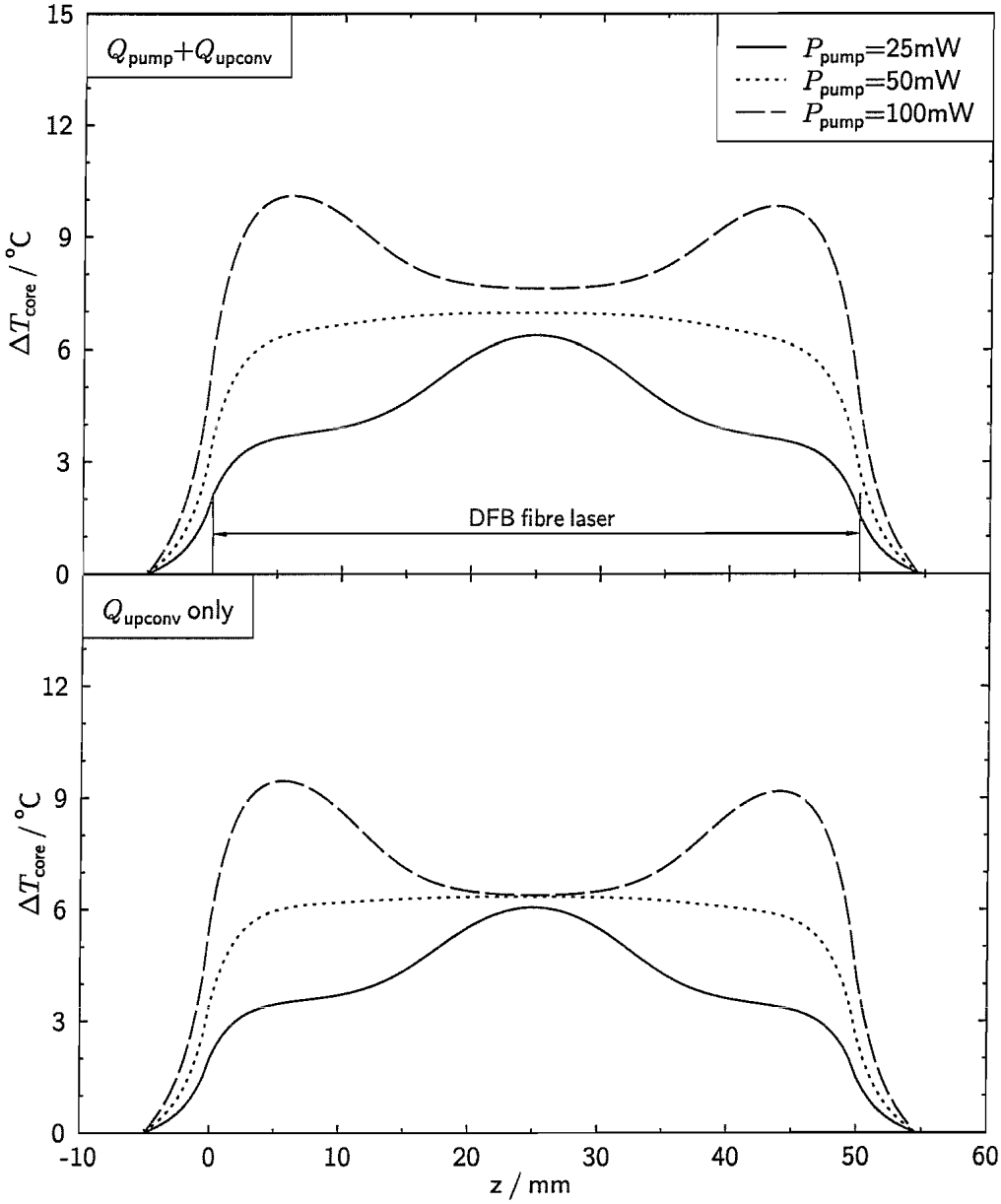

Figure 4.5. Calculated temperature distribution along a DFB fibre laser pumped at 1480 nm for three different pump powers. The top plot shows the temperature distribution when heat generated by non-radiative decay within the $^4I_{13/2}$ level and homogeneous upconversion is taken into account. The bottom graph shows the contribution from upconversion only.

latter is concentrated around the position of the phase shift where the local grating wavelength determines the lasing wavelength.

When taking the grating chirp due to self-heating into account the calculated output power increases by $< 3\,\mu$W below and $> 10\,\mu$W above 80 mW pump power compared to the calculated values without self-heating because κ decreases towards its optimum value. These small output power changes are not expected to pose any problems in wavelength based sensor application.

4.4.2 Self-heating under 980 nm pumping

Figure 4.6 shows the output power, lasing wavelength and pump absorption of a DFB fibre laser (DFB_{stud} in Figure 4.2) as a function of launched pump power for different pump wavelengths while the laser was placed on the MDF board with low thermal conductivity and low heat transfer. When the DFB fibre laser was pumped at 971 nm and 980 nm the lasing threshold was approximately 5 mW. The output power increased with pump power until a maximum of $\approx 2.3 - 2.4$ mW was reached for a launched pump power of 45 mW and 65 mW, respectively. Upon a further increase of pump power the laser output power decreased. When pumped at 975 nm the lasing threshold was ≈ 70 mW and the output power reached only 0.3 mW.

Depending on the pump wavelength the laser wavelength increased with pump power at an average rate of 1.12 pm/mW – 1.72 pm/mW. As expected from (2.14), the higher the pump absorption the larger the wavelength shift because the former results directly in an increase of the non-radiative transition rate dN_3/dt and therefore in an increase of Q_{pump} and T. It will be shown in Chapter 5 that for the DFB fibre lasers used in this thesis the temperature dependence of the laser wavelength is ≈ 8 pm/°C. Therefore, an effective temperature rise of $0.14 - 0.22$°C/mW pump power can be derived from the measured wavelength increase. Here 'effective temperature' means the average temperature of the DFB fibre laser which would cause the same wavelength shift. This wavelength shift with pump power is a factor of 10–16 higher compared with pumping at 1480 nm.

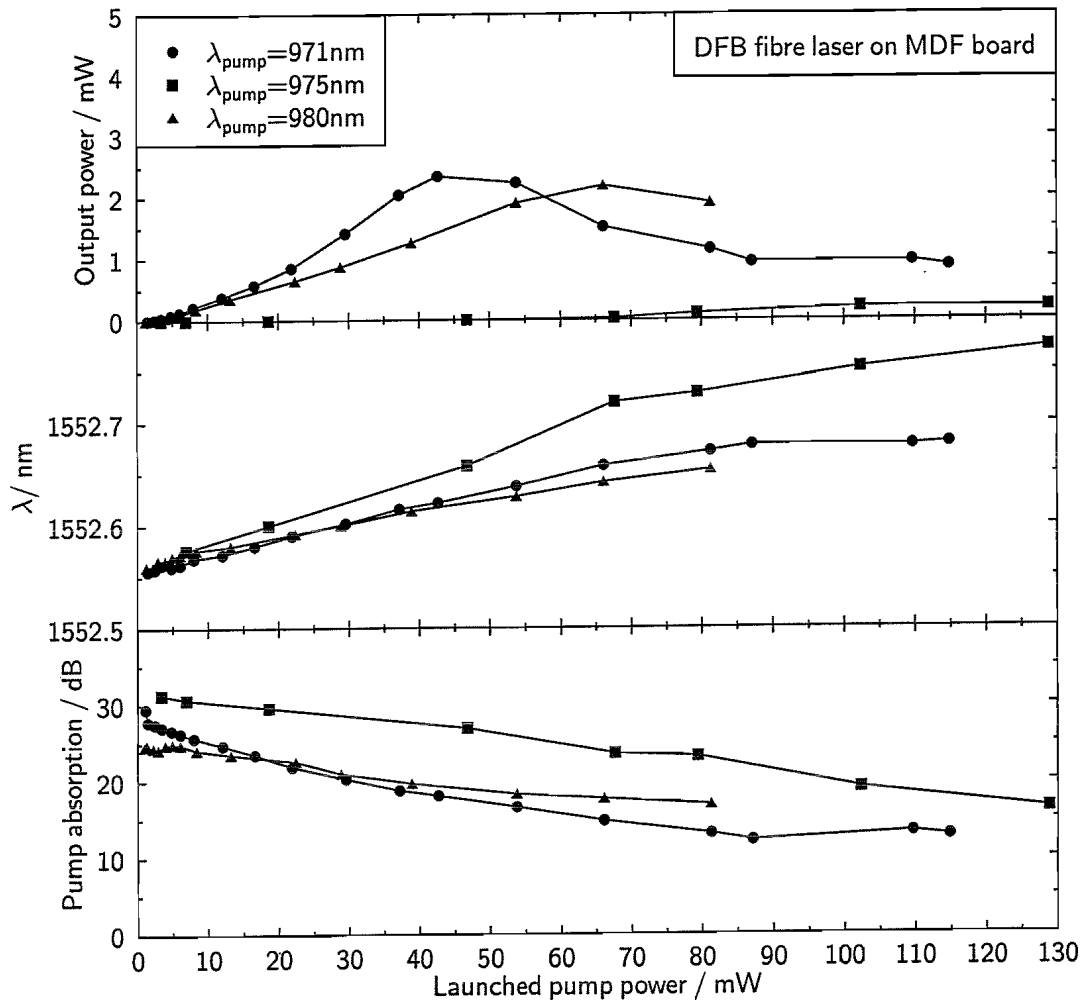

Figure 4.6. Measured DFB fibre laser output power and wavelength as a function of launched pump power for different pump wavelengths. The laser was placed on a medium density fibre (MDF) board which had an estimated heat conductivity of 0.11 W/(m K). At pump wavelengths with low absorption (971 nm and 980 nm) the laser output power showed a maximum before decreasing at a further increase of pump power. At pump wavelength with high absorption (975 nm and 977 nm) the output power was drastically reduced. The lasing wavelength increased with pump power as a result of self-heating of the laser. At high 971 nm pump powers Yb^{3+}-ions were bleached and the absorbed pump power remained constant, leading to an almost constant output power and a smaller wavelength increase.

The pump absorption decreases with increasing pump power. This is partly due to bleaching of the GSA, as well as thermal detuning of the cavity, i.e. chirp, caused by excessive heat generation. The latter reduces the laser efficiency and therefore the number of absorbed pump photons needed to support the laser action [56]. This can be observed by comparing the output powers and pump losses for 971 nm and 980 nm pumping. Although Figure 3.5 indicates that the absorption at both pump wavelengths is very similar Figure 4.6 shows that the lower the slope efficiency of the laser due to thermal detuning the smaller the absorbed pump power. It should, however, be noted that this interplay between absorbed pump power, emitted laser power and thermally induced chirp depends on the exact optical power and heat distributions along the DFB fibre laser. As expected from the much larger GSA shown in Figure 3.5 the absorbed pump power at 975 nm inside the laser is higher than at the other two pump wavelengths.

Above $P_{\text{pump}} \approx 85\,\text{mW}$ at 971 nm the output power, lasing wavelength and pump loss remained almost constant. An explanation for this behaviour is that in this regime the heat from the additional pump power is generated at positions away from the phaseshift. This increases the grating chirp while not affecting the grating wavelength at the phase shift position. The increase of available gain is offset by a reduction of grating feedback and the output power remains constant.

The same set of measurements was carried out while the DFB fibre laser was placed on an aluminium block. The results are presented in Figure 4.7. Compared to the previous case, the maximum laser output power had increased at all three pump wavelengths. The smaller wavelength increase of 0.6–0.7 pm/mW was almost independent of the pump wavelength. The heat transfer from the laser to the aluminium block is not perfect because only a small part of the surface of the DFB fibre laser is in direct contact with or in close proximity of the aluminium block. The laser performance can, however, be further increased by covering its surface in oil. This significantly improves the heat transfer from the laser surface to the aluminium block as shown in Figure 4.8.

The experimentally observed effects of self-heating under pumping in the 980 nm band in various thermal conditions will now be compared with predictions made by

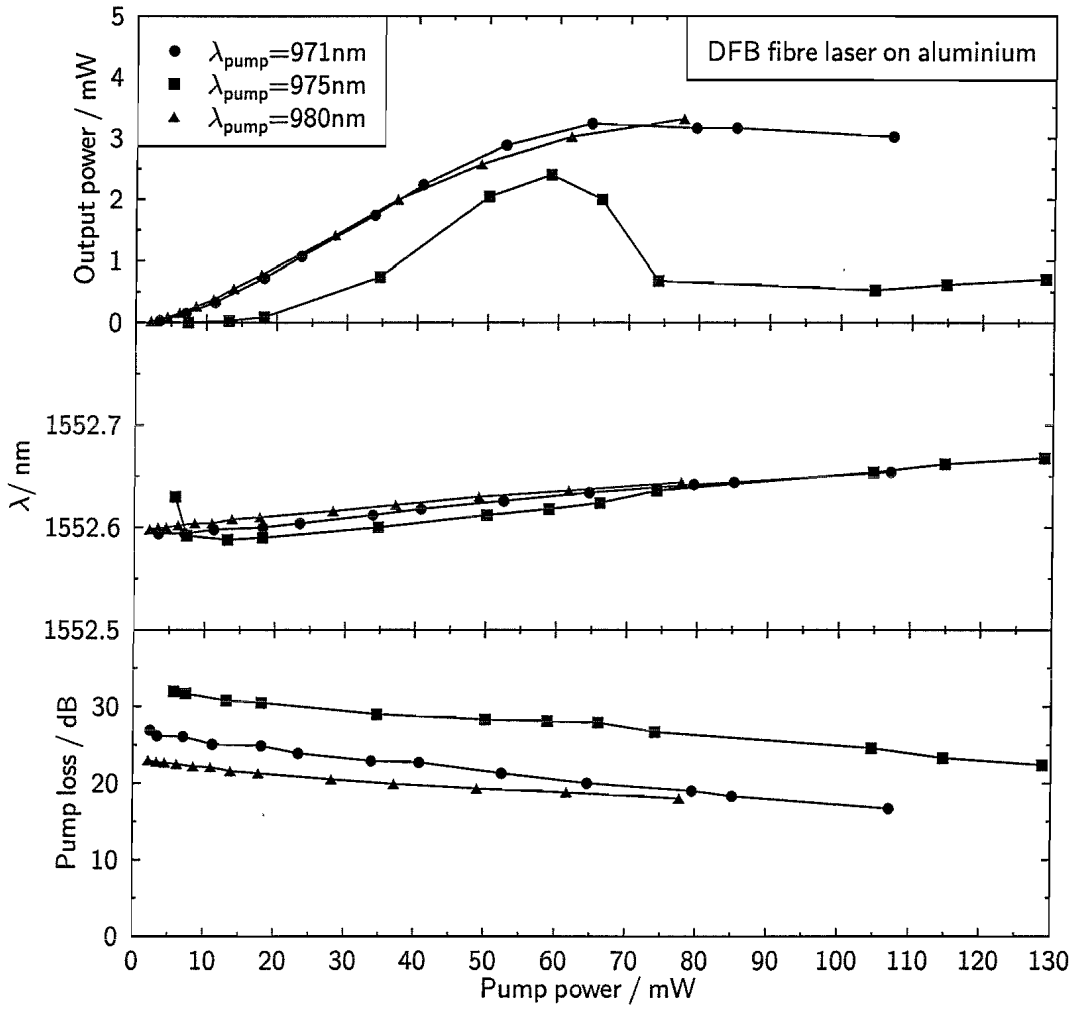

Figure 4.7. Measured DFB fibre laser output power and wavelength as a function of launched pump power for different pump wavelengths. The laser was placed on an aluminium block which has a higher thermal conductivity than MDF board. Larger heat transfer from parts of the laser's surface to its environment resulted in a smaller rise of its effective temperature and less chirp. This lead to a higher output power and less wavelength shift compared to the previous case on MDF board.

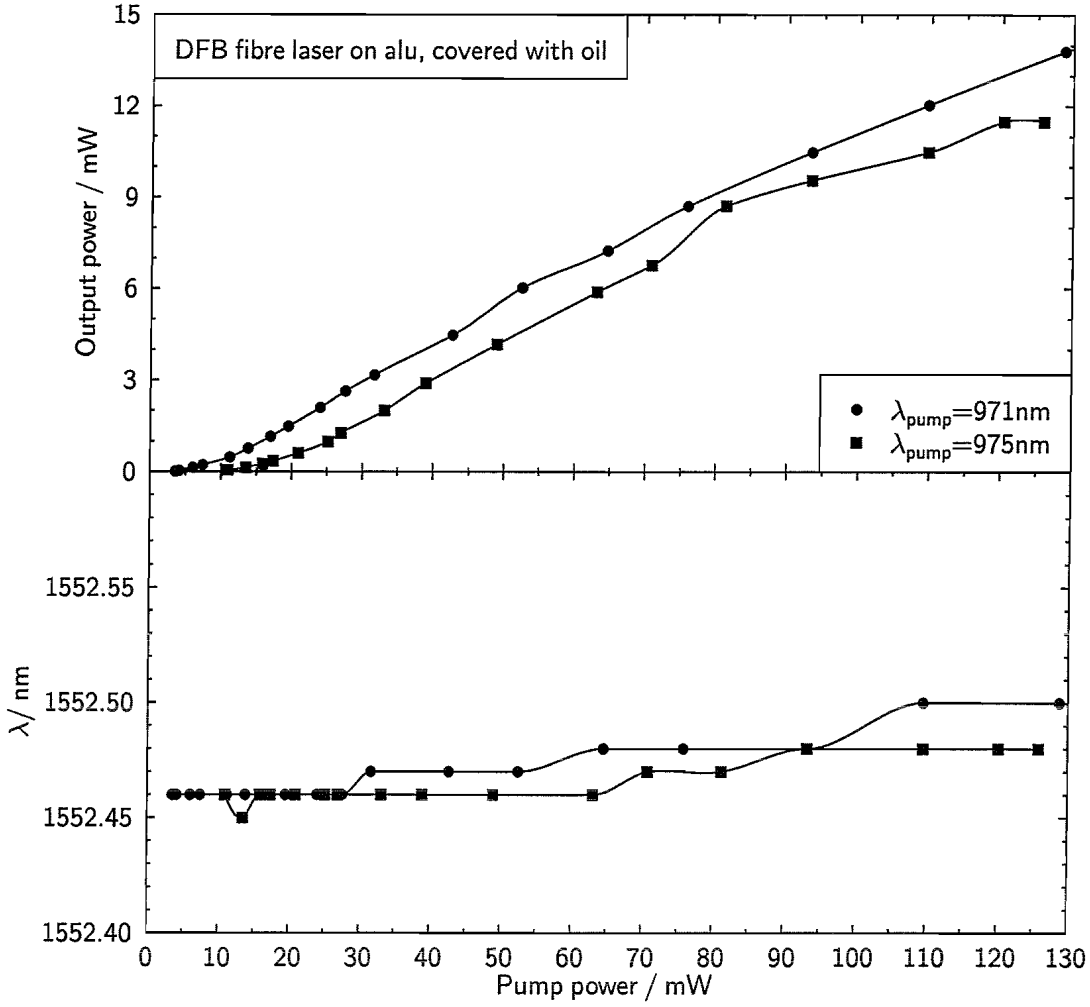

Figure 4.8. The laser output power increased significantly when the thermal contact between the fibre and the aluminium block was increased by covering the DFB fibre laser with oil. The wavelength shift has been further decreased to 0.2–0.3 pm/mW. The steps of the wavelength curve show the resolution of the optical spectrum analyser.

the extended DFB fibre laser model. Figure 4.9 shows the calculated output power, wavelength shift and pump loss as a function of pump power for three different values of h_c. Following the discussion in Section 3.6.2 arbitrary units are used in the Figure because the model overestimates the laser output power, possibly because ASE is not included in the model. It lies in the nature of real DFB fibre lasers and this model that the heat generation is closely related to the output power since both depend on the population densities. This implies that the model would then quantitatively overestimate the heat generation and the resulting effects on the laser output power and wavelength shift. However, Figure 4.9 shows that the simulated results are in qualitative agreement with the experimental data presented in Figures 4.6–4.8. In

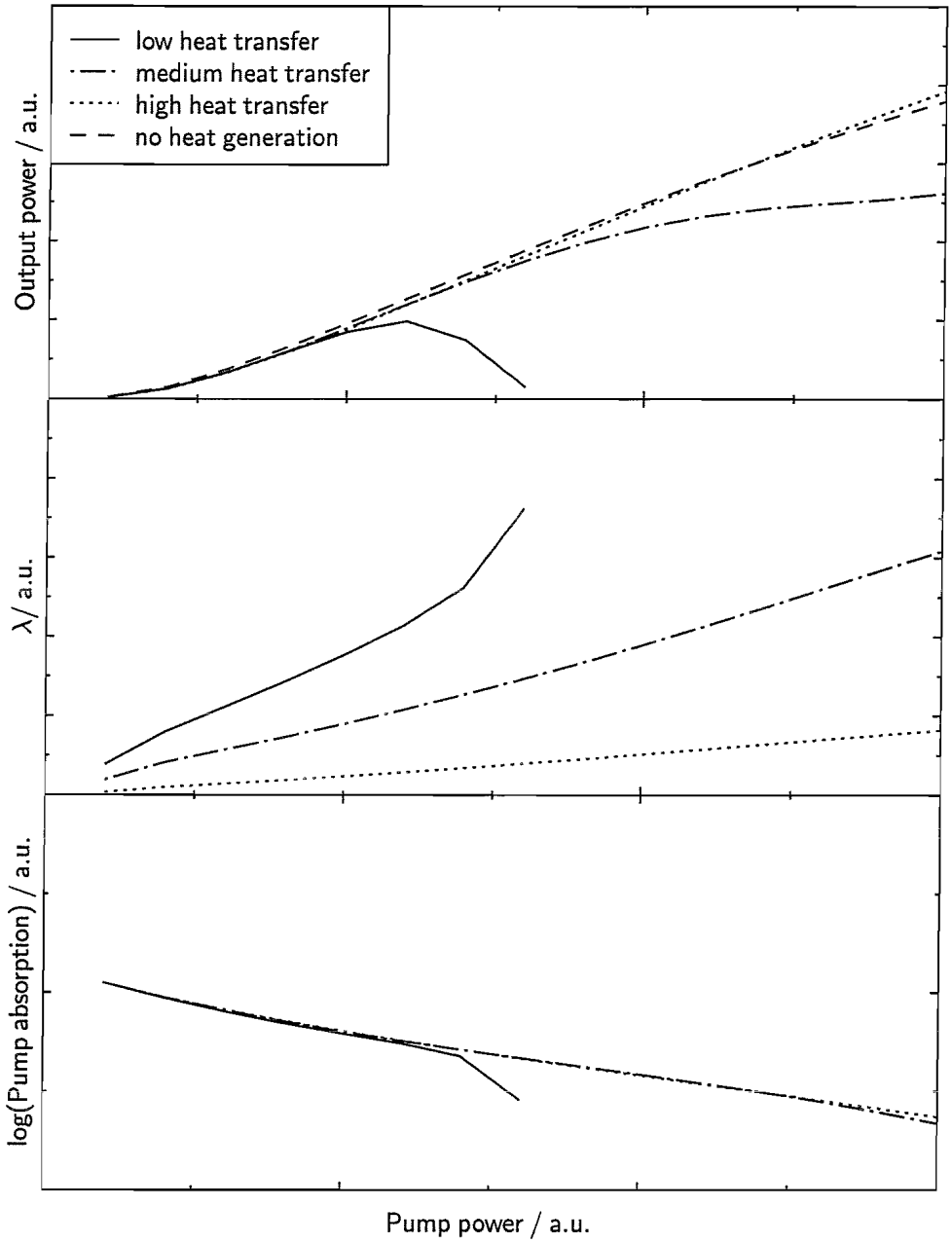

Figure 4.9. Simulated output power, wavelength shift and pump power absorption of the DFB fibre laser for different heat transfer coefficients h_c from the fibre surface to its environment, representing the MDF board and the aluminium block without and with additional oil bath. The calculated results are in qualitative agreement with the experimental data shown in Figures 4.6–4.8. The equivalence of the thermal effects caused by reducing h_c and increasing the amount of heat generated by changing the pump wavelength allowed to reduce the number of simulation runs. The reason for using arbitrary units is explained in the main text.

order to reduce the number of simulation runs without loss of generality only h_c was varied during these simulations. This approach is justified by the fact that the thermal effects caused by a decrease of h_c or an increase of absorbed pump power by varying the pump wavelength are similar. From the point of linking experimental and modelled data together this approach corresponds best to the case of pumping the DFB fibre laser at 971 nm while it was placed on the MDF board and on the aluminium block without and with the additional oil bath.

Also shown in the top graph of Figure 4.9 is the calculated output power in the absence of heat generation, i.e. the case considered in Figure 3.13. In this case the output power is similar to that calculated for high heat transfer and significantly larger than that calculated for medium and low heat transfer. It is therefore possible that part of the discrepancy between the calculated and measured output power observed in Figure 3.13 could have been caused by inadequate heat transfer during the experiment although the DFB fibre laser had been covered in oil. However, this hypothesis does not rule out the need for incorporating other mechanism, like ASE, into the model. Indeed, from the temperature distributions presented in the next Section it will become clear that further optical processes have to be incorporated into the model.

4.5 Temperature distribution along DFB fibre lasers under different heat generation and heat transfer conditions

The change of output power and the increase of lasing wavelength are the global result of local temperature variations along the DFB laser. Therefore, in order to increase the understanding of self-heating the surface temperature distribution has been measured along the DFB fibre laser. Figure 4.10 shows the surface temperature rise along the DFB fibre laser (DFB_{stud}) for different pump wavelengths and pump powers while it was placed on the MDF board. Thetemperature distribution above

the ambient temperature was calculated from the polarisation beat frequency change $\Delta\nu$ of the DFB fibre laser temperature sensor (DFB_{sens}).

The measured temperature distribution is not uniform. It decays along the DFB fibre laser and exhibits a peak of variable size to the left of the phase shift position ($z = 0.44L = 22\,\text{mm}$) or close to it. As expected the temperature increases with pump power and absorption cross-section of the pump light because the larger the number of absorbed pump photons the more non-radiative transitions ${}^4I_{11/2} \rightarrow {}^4I_{13/2}$ take place. Since homogenous upconversion of paired ions contributes to the heat generation the exact temperature distribution depends on the population density profile along the DFB fibre laser.

Calculated population density profiles have already been shown in Figure 3.15 for this type of asymmetric DFB fibre laser pumped in the 980 nm band. At low pump power (Figure 3.15) the population density of the ${}^4I_{11/2}$ level ($N_{3,\text{single}}$ and $N_{3,\text{pair}}$) peaks to the left of the phase shift. The population density of paired ions in the ${}^4I_{13/2}$ ($N_{2,\text{pair}}$) level has its maximum at the pump input (left) end of the DFB fibre laser. It then drops before increasing slightly and reaching a plateau which extends almost to the other end of the laser before it drops again.

To recapitulate, the DFB fibre laser model determines the expected core and surface temperature distributions along the DFB fibre laser by calculating the heat generation from these non-uniform population densities while taking longitudinal and radial heat conduction inside the fibre and heat transfer at the fibre surface into account. For low h_c Figure 4.11 shows the calculated core temperature distribution along the DFB fibre laser for three different levels of launched pump power. This represents the case when the DFB fibre laser was placed on the MDF board. For the same reasons stated in the previous Section, arbitrary units are used. Furthermore, the pump powers used in this simulation are significantly smaller than in the experiments. The reason for this will be explained in the next paragraph. The temperature distributions are in qualitative agreement with the measurements shown in Figure 4.10. The steep temperature increase near the pump input end of the DFB fibre laser which was observed experimentally, cannotbe explained by the model. A

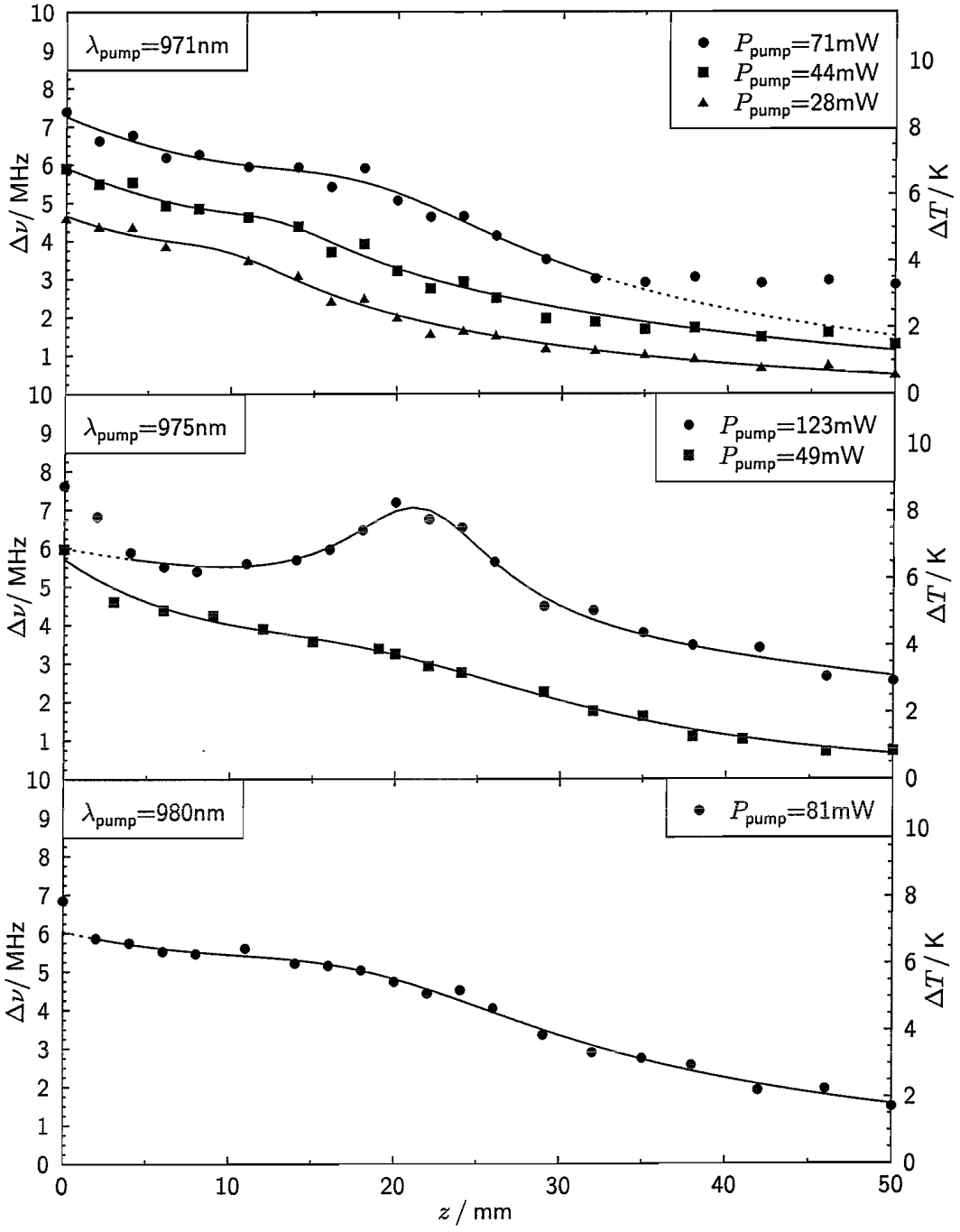

Figure 4.10. Measured temperature distribution above the ambient temperature along the DFB fibre laser (DFB_{stud}) while it was placed on the MDF board with low h_c. Heat generated by the non-radiative transitions ${}^4I_{11/2} \rightarrow {}^4I_{13/2}$ and ${}^4I_{9/2} \rightarrow {}^4I_{13/2}$ (see also Section 3.3.1) together with the heat transfer at the fibre surface determine the shape of the temperature distribution. Shown as solid lines are approximations of the temperature distributions by superimposing an exponential temperature decay and a Lorentzian temperature peak. These approximations will be used in Section 4.6 to calculate the reflection and time delay spectra of the chirped grating of the DFB fibre laser.

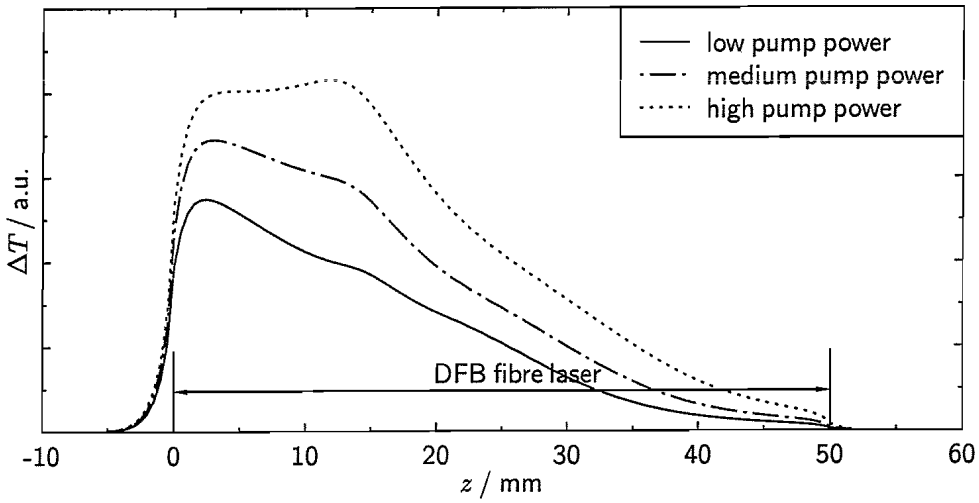

Figure 4.11. Calculated temperature distribution as a function of pump power while the heat transfer coeffcient h_c is low. The calculated distributions are in qualitative agreement with the experimental data presented in Figure 4.10 where the DFB fibre laser was placed on the MDF board.

possible reason could be non-radiative decays from the $^2H_{11/2}/^4S_{3/2}$ levels which is an alternative decay channel to green fluorescence [70].

From the calculated population densities at high pump power shown in Figure 3.16 one would expect a uniform temperature distribution across a $\approx$ 20 mm long region centred at the phase shift. However, the experimental temperature distributions at high pump powers (above $\sim$ 50 mW) in Figure 4.10 do not follow this temperature distribution. This finding, together with the overestimation of the output power (see Section 4.4.2), suggests that additional physical effects need to be incorporated into the DFB fibre laser model before it can fully describe the experimental results at high pump power.

It has been shown in Figures 4.7 and 4.8 that providing adequate heat transfer at the fibre surface can greatly reduce the detrimental effects of self-heating, i.e. low output power and large wavelength shift. Figure 4.12 shows the surface temperature profile of DFB_{stud} while the laser was placed on the aluminium block. The increased heat transfer from parts of the fibre surface to the aluminium resulted in a significant reduction of the surface temperature, which, because of equation (4.4), implies a similar reduction of the core temperature inside the DFB fibre laser. The large heat conduction inside the aluminium block lead to an almost uniform surface

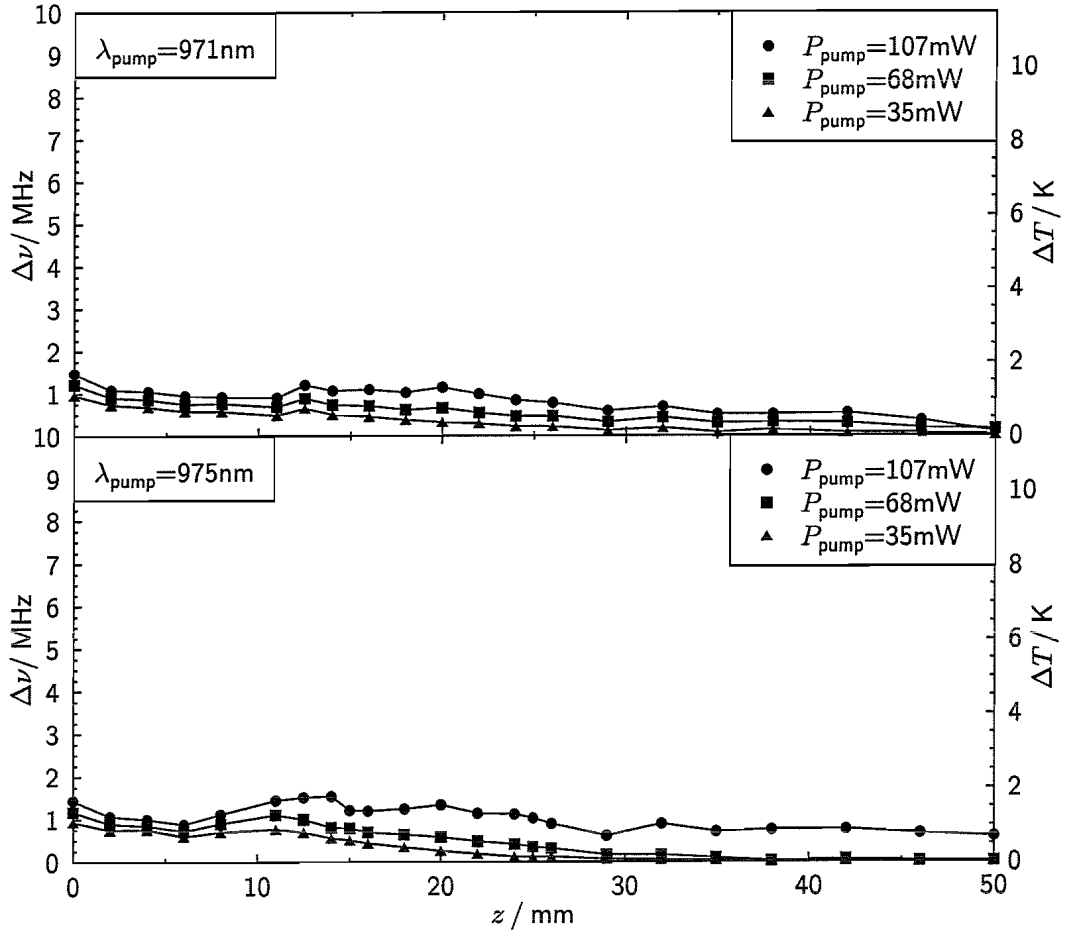

Figure 4.12. Measured surface temperature distribution of the DFB fibre laser placed on the aluminium block. The block provided good heat transfer at the fibre-aluminium interface. High thermal conductivity along the block equalises the temperature along the fibre.

temperature distribution and the disappearance of the temperature peak to the left of the phase shift. Only the at the fibre-air surface opposing the aluminium block heat conduction remained poor and a residual non-uniform temperature profile was observed which could explain the output power roll-off at 975 nm pumping (Figure 4.7) and the small wavelength increase with pump power. Therefore, increasing the heat transfer at the fibre-air surface by covering the DFB fibre laser in oil most probably lead to an even more uniform temperature distribution along the DFB fibre laser and the further increase of output power and reduction of wavelength shift shown in Figure 4.8.

4.6 Grating chirp as a result of self-heating

To further demonstrate that self-heating and the resulting internal temperature distribution is the cause of the observed decrease in laser efficiency, the reflection and time delay, or dispersion, spectra of the DFB fibre laser grating have been measured in the following under different heat generation and transfer conditions.

The DFB fibre laser temperature sensor (DFB_{sens}) was removed from DFB_{stud} while the spectra were recorded in order to eliminate any additional perturbation of the DFB grating spectra. Figures 4.13 and 4.14 show the grating spectra of the DFB fibre laser while it was placed on the MDF board and pumped at 971 nm and 975 nm, respectively. At both pump wavelengths the wavelength of the allowed laser mode, indicated by a vertical line inside the grating stop band, increased with pump power, which is in qualitative agreement with the increasing laser wavelength shown in Figure 4.6. For the unpumped DFB fibre laser the reflectivity of its grating was constant over the stop band while small time delay variations were observed. With increasing pump power the grating stop band broadened considerably on the long wavelength side and time delay peaks appeared in this very part of the spectrum. A comparison between Figures 4.13 and 4.14 shows that the spectral broadening was much stronger when the DFB fibre laser was pumped at 975 nm.

The spectral broadening of the reflection spectra is the consequence of the wavelength chirp along the DFB fibre laser caused by the non-uniform temperature distribution shown in Figure 4.10. The reflections from the warmer regions of the DFB fibre laser near the pump input end and around the temperature peak appear in the grating spectra at the longer wavelength edge of the stop band. Similarly, the cooler regions near the forward laser output appear at the shorter wavelength edge. As the temperature difference between the two DFB fibre laser ends increases with pump power and pump absorption the bandwidth of the grating stop band increases.

Because the grating spectra were measured from the forward laser output, the longer wavelength regions of the DFB fibre laser at the pump input end appeared furthest away. While the light at these wavelengths propagates through the grating

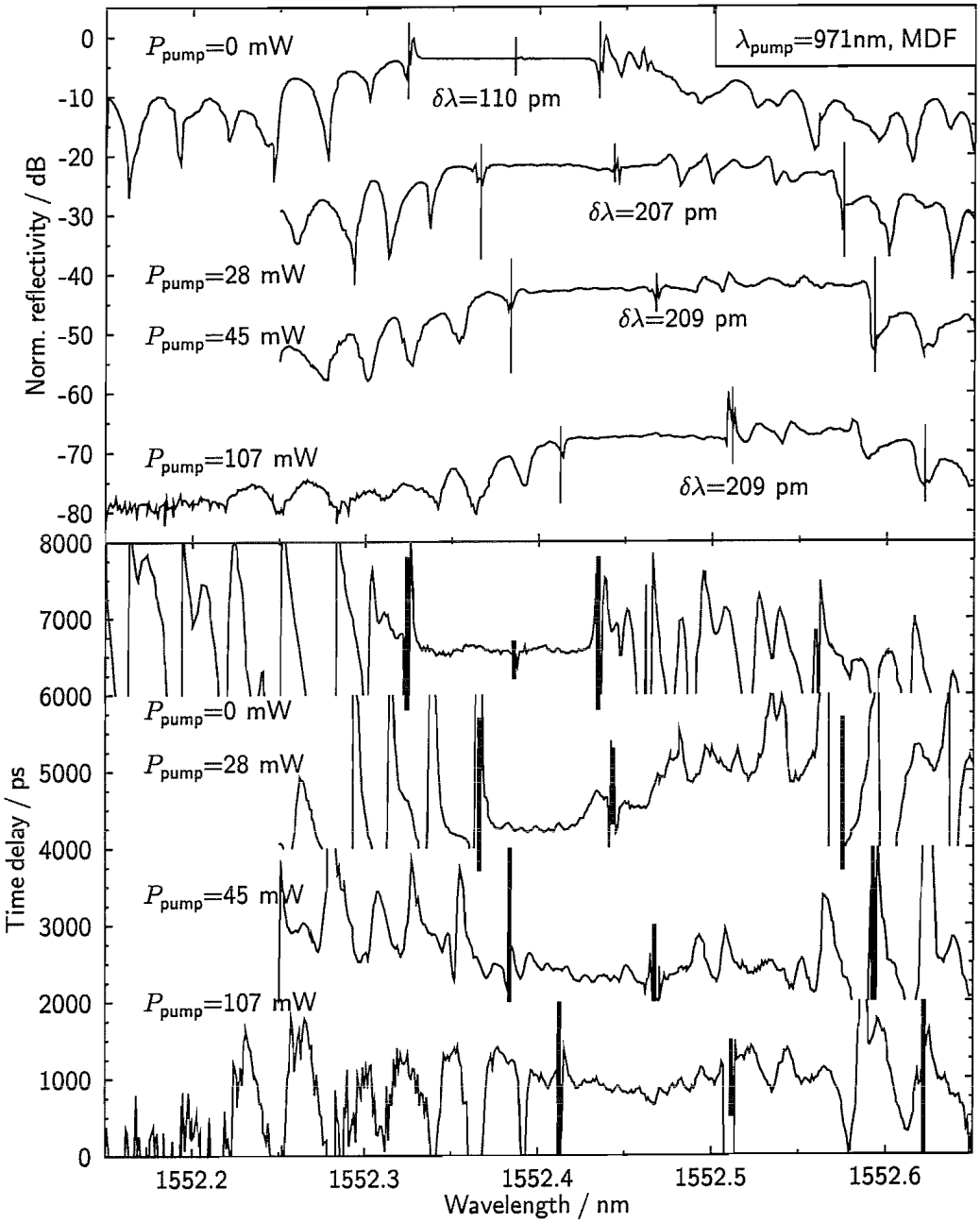

Figure 4.13. Measured grating reflectivity and time delay spectra of the DFB fibre laser while it was placed on the MDF board and pumped at 971 nm. The lasing wavelength, indicated by a vertical line inside the grating stop band, of the grating spectra increased with pump power which is in agreement with the temperature induced wavelength shifts shown in Figure 4.6. The broadening of the grating bandwidth, which is indicated by the vertical lines, was a result of temperature induced non-linear chirp caused by self-heating of the DFB fibre laser. The large time delay fluctuations are clipped in this superposition of several traces to focus on the important time delay features inside the grating stop band.

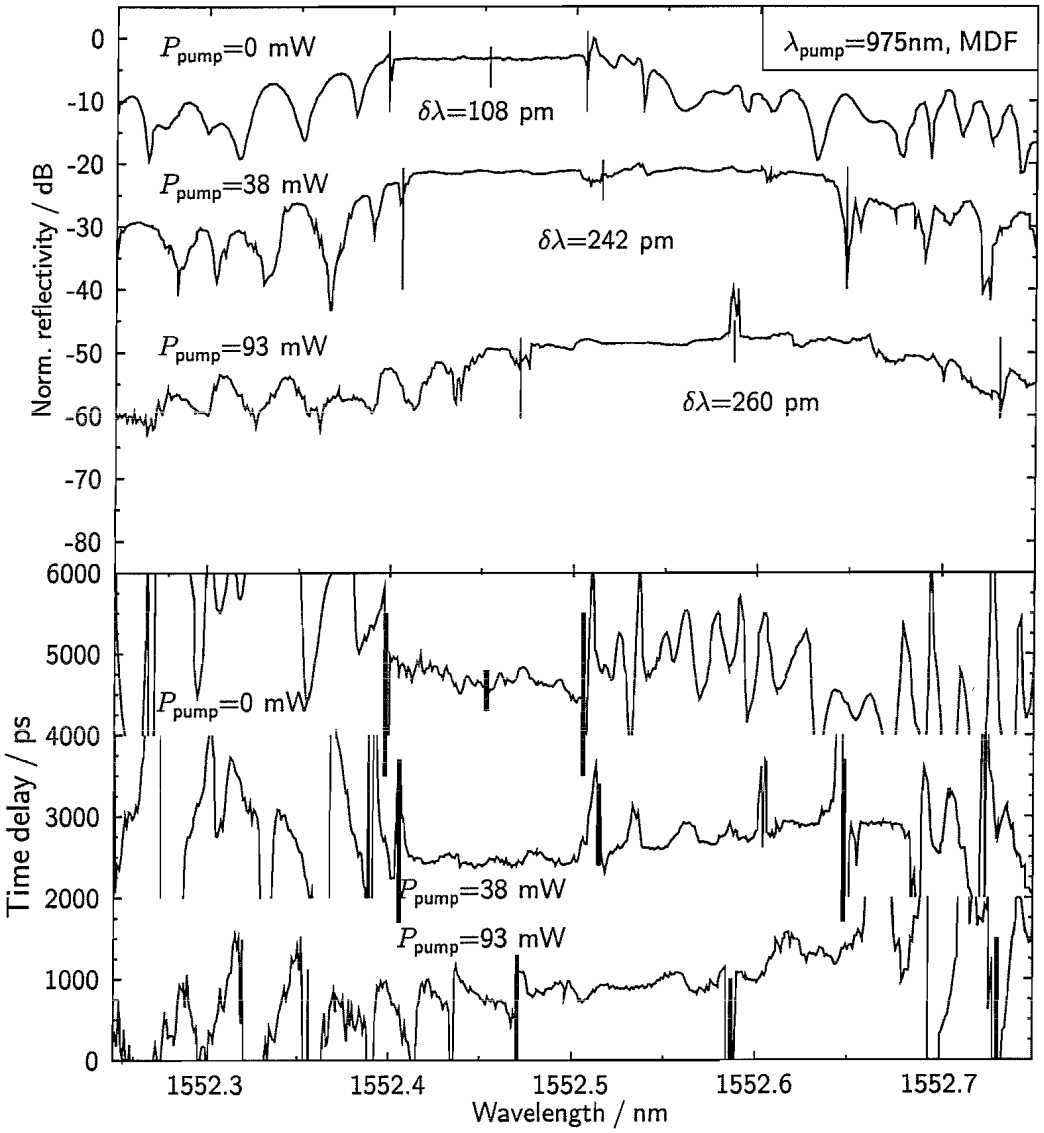

Figure 4.14. Measured grating reflectivity and time delay spectra of the DFB fibre laser while it was placed on the MDF board and pumped at 975 nm. The grating bandwidth and the lasing wavelength are indicated by the vertical lines. The spectral broadening is larger compared to Figure 4.13 due to the higher pump absorption which leads to a larger heat generation inside the laser. Residual laser output in the forward direction appears as a reflection peak inside the grating stop band.

it experiences large chirp induced time delay variations which appear as peaks at the longer wavelength edge of the grating stop band.

As shown in Figure 4.10 the measured surface temperature distributions can be approximated by a superposition of an exponential decay and a Lorentzian curve:

$$T(z) = A\exp(-Bz) + \frac{C}{(z-D)^2 + (E/2)^2}. \tag{4.8}$$

The parameters of the curves shown in Figure 4.10 are listed in Table 4.1. It should be noted that the superposition of the two curves is only a phenomenological description of the temperature distribution and does not originate from the extended DFB fibre laser model described in Chapter 4. The grating spectra calculated from these temperature distributions are shown in Figures 4.15 and 4.16 for $\lambda_p = 971\,\text{nm}$ and 975 nm. It was assumed here that the surface and core temperatures are very similar as a result of the small fibre diameter [87].

The calculated spectra are in qualitative agreement with the measured spectra, exhibiting the broadening of the grating stop band towards longer wavelengths and

Table 4.1. The temperature distributions shown in Figure 4.10 could be approximated by a superposition of an exponential decay and a Lorentzian curve $T(z) = A\exp(-Bz) + C/[(z-D)^2 + (E/2)^2]$. The fitparameters of this phenomenological description are listed below.

	A	B	C	D	E
$\lambda = 971\,\text{nm}$					
$P_{\text{pump}} = 28\,\text{mW}$	5.07	0.044	39.1	9.70	12.57
$P_{\text{pump}} = 44\,\text{mW}$	6.67	0.033	26.8	12.78	11.39
$P_{\text{pump}} = 71\,\text{mW}$	7.75	0.033	277.4	18.21	23.07
$\lambda = 975\,\text{nm}$					
$P_{\text{pump}} = 49\,\text{mW}$	5.14	0.081	935.3	17.66	37.01
$P_{\text{pump}} = 123\,\text{mW}$	6.67	0.016	113.7	21.47	11.57
$\lambda = 980\,\text{nm}$					
$P_{\text{pump}} = 81\,\text{mW}$	6.00	0.029	523.7	17.74	30.49

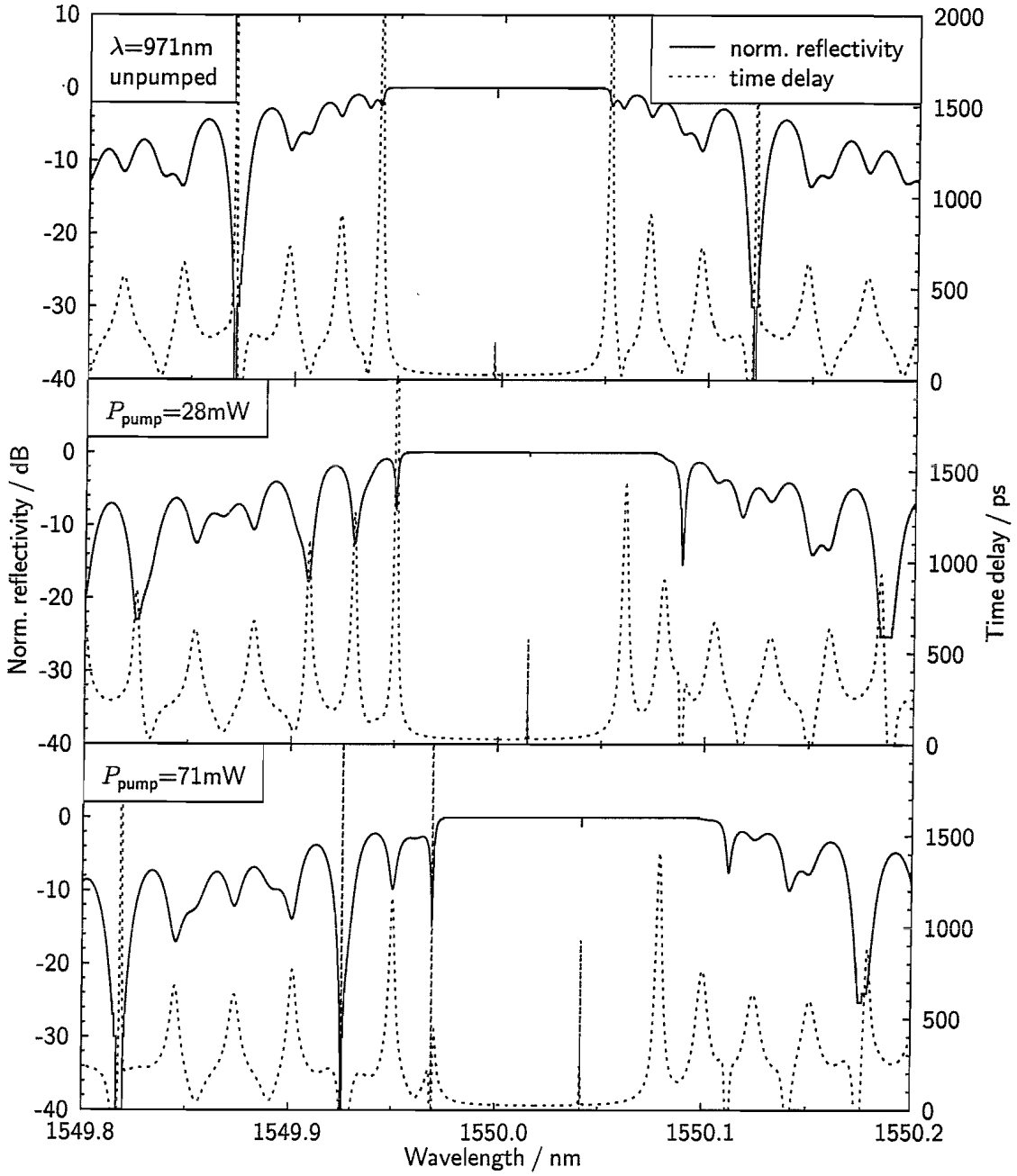

Figure 4.15. Calculated reflectivity and time delay spectra of the chirped DFB grating. The grating chirp was calculated from the temperature distributions shown in Figure 4.10 for $\lambda_p = 971$ nm which were described by the function and the parameters listed in Table 4.1.

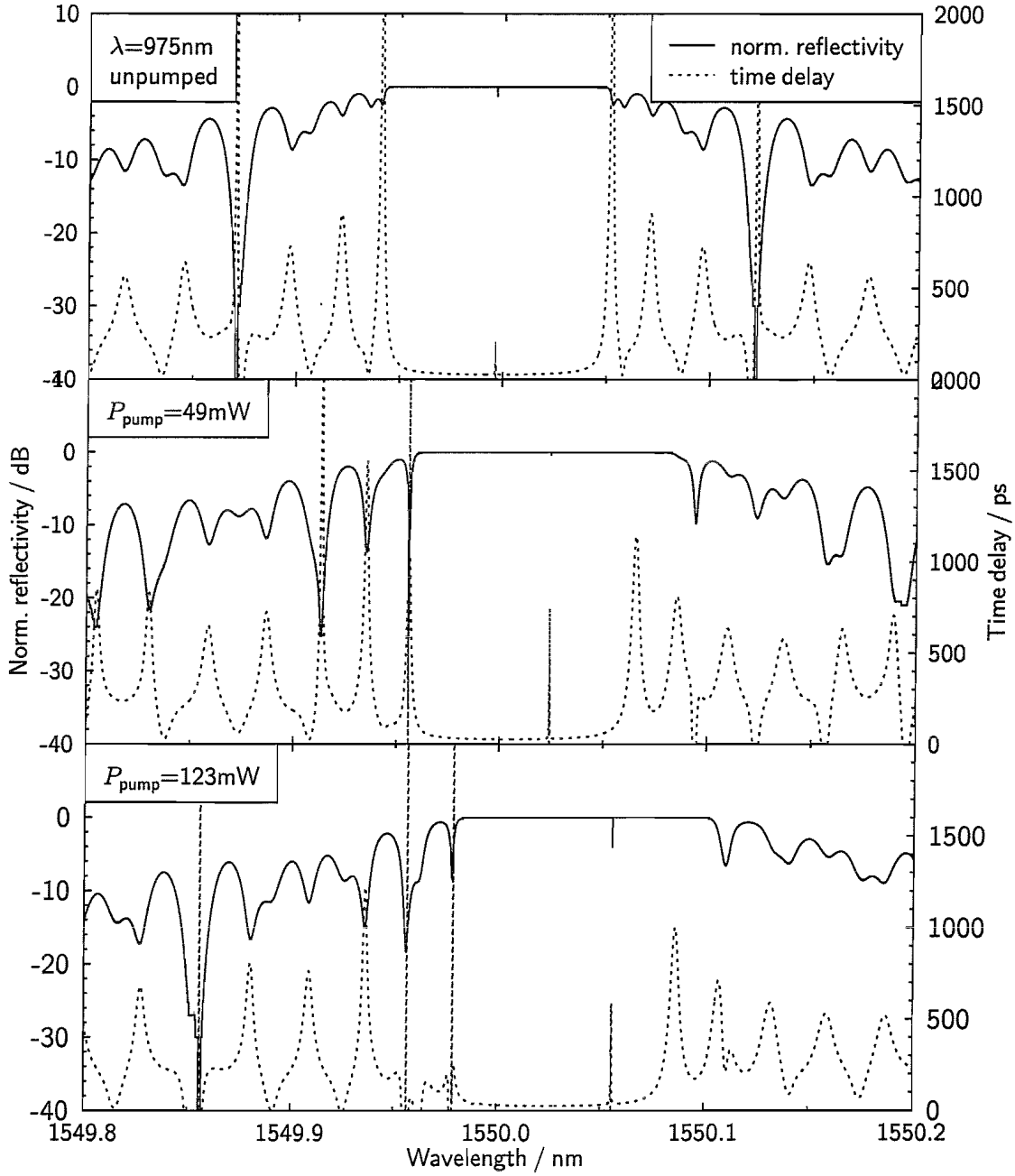

Figure 4.16. Calculated reflectivity and time delay spectra of the chirped DFB grating. The grating chirp was calculated from the temperature distributions shown in Figure 4.10 for $\lambda_p = 975\,\text{nm}$ which were described by the function and the parameters listed in Table 4.1.

the appearance of two time delay peaks in the same spectral region. In contrast to the measured spectra the calculated ones show no reflectivity ripples within the grating stop band. These ripples might have been a result of additional chirp caused by localised strain of the mounted DFB fibre laser or by manufacturing phase errors.

Finally, Figure 4.17 shows the grating reflectivity and time delay spectra under 975 nm pumping when the DFB fibre laser was placed on the aluminium block. As expected from the more uniform temperature distribution shown in Figure 4.12 the broadening of the grating bandwidth and the shift of its centre wavelength was reduced.

Conclusion The combination of experimental and theoretical investigations lead to a thorough understanding of the internal processes responsible for self-heating of DFB fibre lasers and the resulting detrimental effects on the laser output power and wavelength. Heat sources inside the DFB fibre laser are non-radiative decays of Er^{3+}-ions. These decays bridge the energy difference between pump and laser photons and also occur as part of the homogeneous upconversion process. If the heat transfer from the fibre to its environment is insufficient a non-uniform temperature distribution is established along the DFB fibre laser which follows the distribution of internal heat sources. As a result two detrimental effects can be observed: 1.) The temperature rise at the phase shift position leads to an increase of the lasing wavelength. 2.) The shape of the temperature distribution gives rise to grating chirp which subsequently reduces the optical feedback of the laser cavity. In general this reduction of feedback results in an increase of lasing threshold and a drop of laser output power. Extreme heat induced chirp prevents the laser from operating.

The new DFB fibre laser model used to predict these self-heating effects was based on the versatile model described in Chapter 3. The flexible structure of the model made it possible to include heat generation by non-radiative decays in a straight forward manner. For a DFB fibre laser pumped at 1480 nm the modelled results were in very good agreement with the experimental data. When the DFB fibre laser was pumped in the 980 nm band the model was in qualitative agreement with the experimental data. Quantitative agreement was not expected since it has

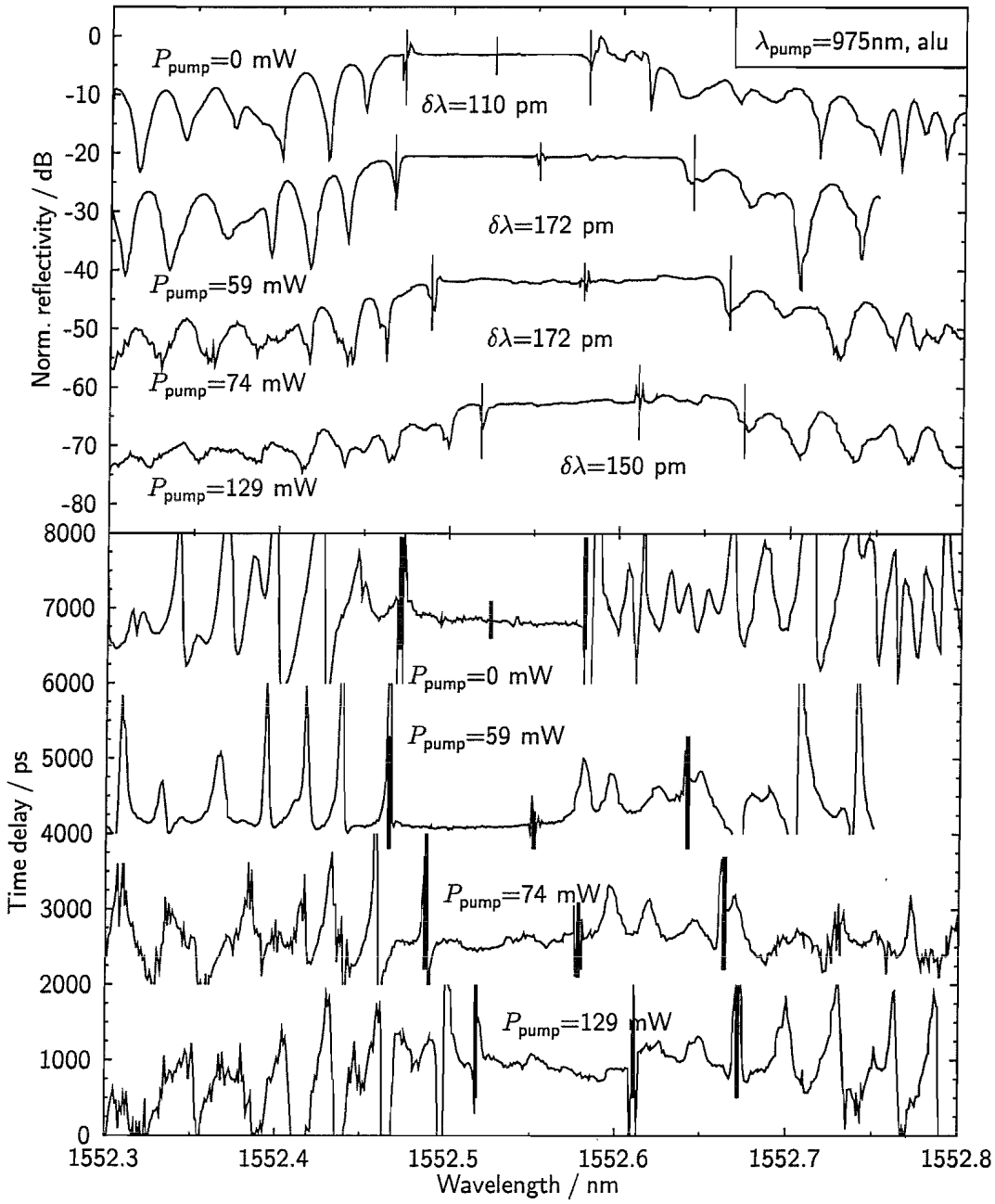

Figure 4.17. Measured grating reflection and time delay spectra of the DFB fibre laser placed on the aluminium block and pumped at 975 nm. Good heat transfer at the fibre-aluminium interface and the high thermal conductivity of aluminium lead to less broadening of the FBG bandwidth and a smaller shift of its centre wavelength.

been pointed out in Section 3.6.2 that further physical processes inside the DFB fibre laser have to be taken into account at this pump wavelength.

To minimise the detrimental effects of self-heating two avenues are possible:

- reduction of the heat generation inside the laser,
- increase of the heat transfer from the DFB fibre laser to its environment.

The heat generation can be reduced by choosing a pump wavelength with a small energy difference between pump and lasing photons, e.g. 1480 nm, or with a small pump absorption which deposits less energy inside the fibre. In the 980 nm region it might therefore be convenient to pump at a wavelength away from the absorption peak at 975 nm. Although smaller pump absorption would result in smaller output power if the heat transfer is sufficient, in the case of poor heat transfer the potential increase of output power is cancelled out by excessive heat generation and the resulting chirp of the DFB grating. Since homogeneous upconversion was found to shape the temperature distribution adjusting the Er^{3+} and/or codoping concentrations might lead to a reduction of this process while maintaining the available gain.

Pursuing the second avenue might require placing the DFB fibre laser on a metal plate or submerging it in heat conducting liquid or paste. This might cause packaging problems as care has to be taken to avoid localised mechanical strain or bends which would induce unwanted wavelength and output power changes. Furthermore, sufficient heat transfer has to be provided over the entire length of the laser to ensure a uniform temperature distribution. Providing this sufficient heat transfer certainly increases the complexity of DFB fibre laser packages used in telecommunication applications.

In order to minimise measurement errors pumping in the 980 nm region should not be used for DFB fibre laser sensors due to excessive self-heating. Although at this pump wavelength the pump induced wavelength shift could be reduced to 0.2–0.3 pm/mW while the heat transfer was maximised by an aluminium plate and an oil cover the potential build-up of localised strain as a result of the close contact between the laser and the heat sink would introduce measurement errors. On the

other hand, 1480 nm pumping induced a wavelength shift of only 0.1 pm/mW while the DFB fibre laser was surrounded by air, which, in addition, eliminated the risk of localised strain. The smaller output power of the DFB fibre laser under 1480 nm pumping is sufficient for sensor applications.

5 Single longitudinal mode polarimetric DFB fibre laser sensor

The need for simultaneous strain and temperature measurements with good accuracy for a variety of applications has been identified in Chapter 2, where it was concluded that DFB fibre laser sensors would be the most promising devices to meet this need. In the present Chapter the first single longitudinal mode DFB fibre laser sensor for such simultaneous strain and temperature measurements will be demonstrated.

5.1 Simultaneous strain and temperature sensor

The sensor was a $L = l_{\mathrm{DFB}} = 50\,\mathrm{mm}$ long DFB fibre laser written into the $Er^{3+}:Yb^{3+}$ fibre described in Section 3.2. The grating coupling coefficient was $\kappa \approx 230\,\mathrm{m}^{-1}$, and the phase shift was positioned at the centre of the FBG. The laser operated in a single longitudinal mode at $\lambda \sim 1550\,\mathrm{nm}$ which split into two orthogonal polarisation modes due to the birefringence of the laser. The beat frequency between the two polarisation modes was only $\sim 1\,\mathrm{GHz}$, corresponding to a wavelength separation of $\approx 8\,\mathrm{pm}$, which could be measured with a commercial RF spectrum analyser[1].

This new sensor was based on an earlier pressure and temperature sensor demonstrated by Kringlebotn *et al.* [11]. Besides the different response to lateral pressure

[1] Tektronix 2782

and longitudinal strain the previous sensor did not determine its two measurands simultaneously.

5.1.1 Summary of theoretical background

The wavelengths of the two orthogonal polarisation modes of a DFB fibre laser are given by (2.6)

$$\lambda_{x,y} = 2n_{x,y}\Lambda, \tag{5.1}$$

where $\lambda_{x,y}$ denotes the wavelengths of the two orthogonally polarised laser modes, $n_{x,y}$ are the refractive indices of the fibre, and Λ is the grating pitch. The strain and temperature dependence of $\lambda_{x,y}$ is given by

$$\Delta\lambda_{x,y}/\lambda_{x,y} = (1+p_e)\epsilon\Big|_{T=\text{const}} + (\alpha+\xi)\Delta T\Big|_{\epsilon=\text{const}} \tag{5.2}$$

(see Section 2.2.3). The discrimination between mechanical strain and free thermal expansion is denoted by $|_{T=\text{const}}$ and $|_{\epsilon=\text{const}}$.

The polarisation beat frequency ν between the two polarisation modes is

$$\begin{aligned} \nu &= \frac{c}{\lambda_x} - \frac{c}{\lambda_y} && (5.3)\\ &= \frac{c}{2n_x\Lambda} - \frac{c}{2n_y\Lambda} && (5.4)\\ &= c(n_y - n_x)/(2n_x n_y \Lambda), && (5.5) \end{aligned}$$

which for a low birefringent fibre with $n_x \approx n_y \approx n$ becomes

$$\nu = cB/(2n^2\Lambda), \tag{5.6}$$

were $B = n_y - n_x$ is the birefringence of the fibre. A first order Taylor expansion of (5.6) around $\epsilon = 0\,\mu\epsilon$, $T = 0°\text{C}$ gives

$$\frac{\Delta\nu}{\nu} = \left[\frac{1}{B}\frac{dB}{d\epsilon} - (1+2p_e)\right]\epsilon\Big|_{T=\text{const}} + \left[\frac{1}{B}\frac{dB}{dT} - (\alpha+2\xi)\right]\Delta T\Big|_{\epsilon=\text{const}}. \tag{5.7}$$

By writing the responses $\Delta\lambda_{x,y}$ and $\Delta\nu$ of the DFB fibre laser to strain and temperature (equations (5.2) and (5.7)) in matrix form one obtains

$$\begin{aligned} \begin{pmatrix}\Delta\lambda_{x,y}\\ \Delta\nu\end{pmatrix} &= \begin{pmatrix}k_{11} & k_{12}\\ k_{21} & k_{22}\end{pmatrix}\begin{pmatrix}\epsilon\\ \Delta T\end{pmatrix} && (5.8)\\ &= \boldsymbol{K}\begin{pmatrix}\epsilon\\ \Delta T\end{pmatrix}. \end{aligned}$$

For a well conditioned matrix $\boldsymbol{K}$, i.e. $\det \boldsymbol{K} \neq 0$, (5.8) can be inverted. Strain and temperature can then be determined simultaneously by measuring either $\Delta\lambda_x$ or $\Delta\lambda_y$ and $\Delta\nu$.

5.1.2 Minimum gauge length

It has been shown theoretically in Section 3.6.1 that the intensity of a DFB fibre laser is concentrated around the position of the phase shift of the grating. As a result the lasing wavelength is mainly determined by the grating wavelength around the phase shift. This has been verified experimentally in [52] showing that the wavelength response of a DFB fibre laser to local heating decreased as a heat source was moved along the laser away from position of the phase shift. The same behaviour can be expected for localised strain. Consequently, in order to obtain accurate strain and temperature measurements the fibre section around the phase shift has to be in mechanical and thermal contact with its environment. The required length of this sensing section corresponds to the minimum gauge length for strain measurements and the spatial resolution of temperature measurements.

With the model developed in Chapter 3 the lasing wavelength and the output power of a DFB fibre laser has been calculated for step grating wavelength profiles of different magnitude $\Delta\lambda$ and sensing section length l_{sens} centred at the position of the phaseshift. Thus this grating wavelength profile was described as

$$\begin{aligned} &\lambda_0 + \Delta\lambda \quad \text{for } \Delta l \leq z \leq l_{\text{DFB}} - \Delta l \\ &\lambda_0 \qquad\quad \text{for } 0 \leq z < \Delta l \text{ and} \\ &\qquad\quad\ \ l_{\text{DFB}} - \Delta l < z \leq l_{\text{DFB}}. \end{aligned} \tag{5.9}$$

Here $l_{\text{sens}} = l_{\text{DFB}} - 2\Delta l$ is the length of the sensing section. The results are shown in Figure 5.1 for $l_{\text{DFB}} = 50\,\text{mm}$ and $\Delta\lambda$ corresponding to local strain or temperature increases of $100\mu\epsilon/14.5°\text{C}$, $500\mu\epsilon/72.5°\text{C}$ and $1000\mu\epsilon/145.1°\text{C}$. Here the experimental strain and temperature responses of the DFB fibre laser sensor listed in Section 5.1.4 have been used. The length of the sensing section was varied between $l_{\text{sens}} = l_{\text{DFB}}$, i.e. uniform grating, and $l_{\text{sens}} = 0.52 l_{\text{DFB}}$. Only a minimal deviation of the lasing wavelength from the uniform DFB fibre laser, caused by numerical errors, were

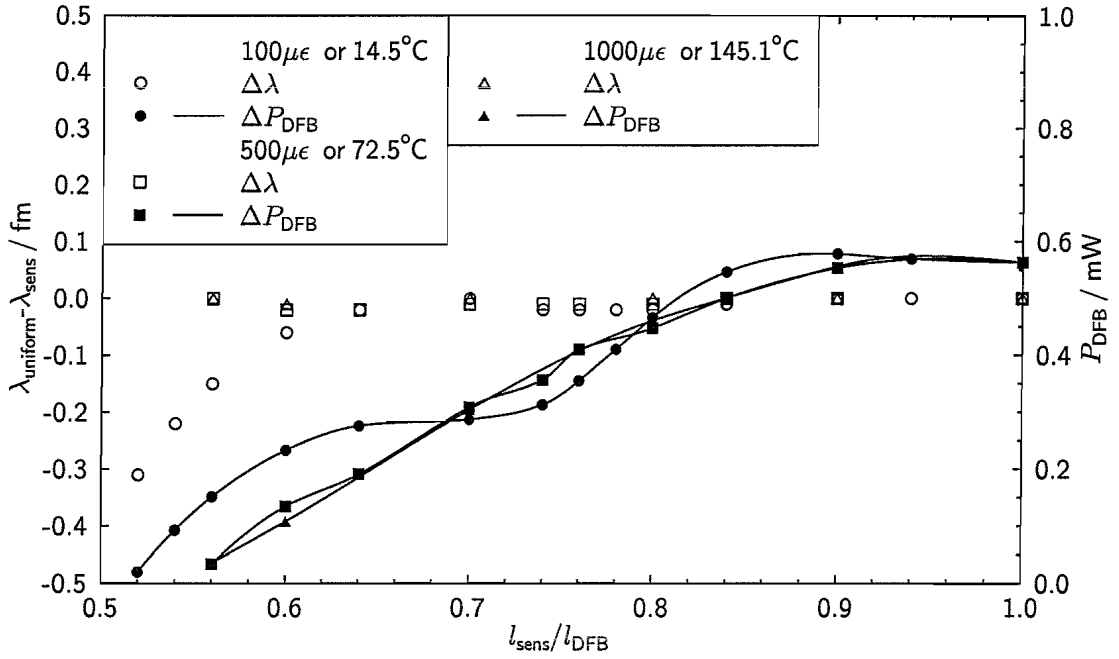

Figure 5.1. Simulated wavelength change and output power of a DFB fibre laser subject to localised strain or temperature changes along a region centred at the position of the phase shift.

observed for $l_{\text{sens}}/l_{\text{DFB}} > 0.6$. However, the output power dropped with decreasing $l_{\text{sens}}/l_{\text{DFB}}$. Because the simulated DFB fibre laser operated at the grating wavelength of the sensing section $\lambda + \Delta\lambda$ it experienced feedback from the grating only over the length l_{sens}. Consequently, the output power dropped as the effective grating strength κl_{sens} decreased. The 'S'-shaped output power variation for $\epsilon = 100\,\mu$m arose from the fact that the spectrum from the centre grating section strongly overlapped with the spectrum from the grating ends. The total feedback of the grating then varied in a more complex form with $l_{\text{sens}}/l_{\text{DFB}}$ and the DFB fibre laser operated even for $l_{\text{sens}}/l_{\text{DFB}} < 0.6$. In this case lasing wavelength decreases slightly as the laser is 'pulled' towards the lower wavelength of the grating outside the sensitive region. It was confirmed by the model that a short uniform DFB fibre laser with a length equal to $l_{\text{sens}}/l_{\text{DFB}} < 0.6$ would operate at the same wavelength as a DFB fibre laser with $l_{\text{sens}}/l_{\text{DFB}} = 1$.

In summary this simulation showed that the sensing region of a DFB fibre laser sensor should be larger than $0.7\,l_{\text{DFB}}$ to prevent the output power from dropping by more than a factor of 2 (–3 dB). In this case the lasing wavelength, which is the

measure for the experienced strain or temperature, is not affected by the length of the sensitive region. For a 50 mm long DFB fibre laser sensor the minimum gauge length therefore is 35 mm. Shorter gauge lengths are possible with shorter DFB fibre lasers with larger κ, e.g. $l_{\mathrm{DFB}} = 25\,\mathrm{mm}$ and $\kappa = 300\,\mathrm{m}^{-1}$.

5.1.3 Experimental sensor arrangement

The experimental sensor arrangement is shown in Figure 5.2. Polyamide coated single mode standard telecommunication fibre was spliced to both sides of the DFB fibre laser, approximately 5 mm away from the grating ends. The laser itself remained uncoated. The gauge length of the strain sensor was defined by bonding the

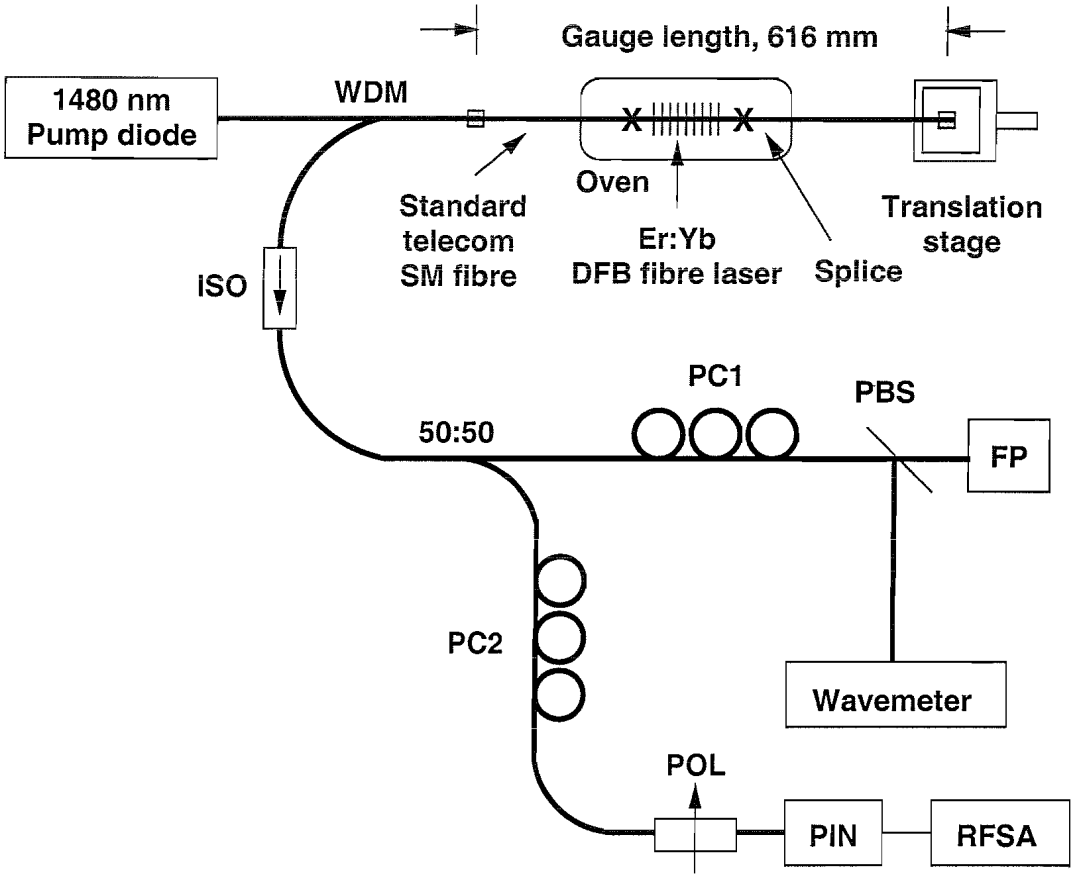

Figure 5.2. Experimental arrangement for investigating the strain and temperature dependence of the polarimetric DFB fibre laser sensor. WDM=wavelength division multiplexer, ISO=isolator, 50:50=coupler, PC1 and PC2=polarisation controllers, PBS=polarising beam splitter, POL=polariser, FP=Fabry-Perot spectrometer, PIN=photodiode, RFSA=RF spectrum analyser.

coated telecommunication fibre to a fixed metal post and a manual translation stage[2] with cyanoacrylate. Each bonded region was 10–15 mm long. The gauge length was $l_g = 616\,\text{mm}$. If one assumes a positioning accuracy of the translation stage of $1\,\mu\text{m}$, i.e. a tenth of the tick mark separation, the strain could be set to within $1.6\,\mu\epsilon$. An oven, consisting of a $150\,\text{mm} \times 15\,\text{mm} \times 15\,\text{mm}$ aluminium block and a Peltier element, was used to heat the DFB fibre laser. A duct ($3\,\text{mm} \times 3\,\text{mm}$) along the longitudinal axis of the aluminium block accommodated the DFB fibre laser. Care was taken so that the laser did not touch the aluminium block preventing unwanted strain caused by friction. Furthermore, twist in the fibre was avoided in order not to introduce additional birefringence. The temperature of the aluminium block was regulated with a commercial temperature controller[3]. The thermistor of the temperature controller's feedback loop was placed on the outer surface of the aluminium block $\approx 10\,\text{mm}$ away from the edge of the Peltier element. The actual temperature of the aluminium block was measured with a K-Type thermocouple which was placed next to the thermistor. The readout unit for the thermocouple[4] had a resolution of $\pm 0.1°\text{C}$, and the temperature controller kept the temperature of the oven to within this resolution. The oven was isolated by 5–15 mm thick polystyrene. The dimensions of the Peltier element were $40\,\text{mm} \times 40\,\text{mm}$ and clearly did not match the dimensions of the aluminium block. However, due to the sufficiently high thermal conductivity of aluminium of $247\,\text{Wm}^{-1}\text{K}^{-1}$ [88] and the efficient polystyrene insulation the temperature difference between the centre and the fibre entrance of the oven was within the 0.1°C resolution of the thermometer. In addition the temperature will be uniform over the length of the Peltier element which corresponds to $0.8\,l_{\text{DFB}}$. From the results shown in Figure 5.1 it can be concluded that the output power and lasing wavelength of the DFB fibre laser sensor would not be affected by eventual temperature variations along the oven away from the Peltier element.

[2]Specifications: 25 mm travel, ball bearings, spindle driven by micrometer screw with tick marks every $10\,\mu\text{m}$.

[3]ILX LDT5412.

[4]Fluke 51

The free thermal expansion of the fibre was constrained by the two fixing points of the fibre. Therefore temperature changes of the fibre section in the oven induced thermal stress along the whole length of fibre. The strain related to this thermal stress becomes

$$\epsilon_T = l_{\text{oven}}\,\alpha\,\Delta T/l_g, \tag{5.10}$$

where l_{oven} is the length of the fibre section in the oven.

The DFB fibre laser was pumped by a 1480 nm diode laser[5] and the sum of the optical powers contained in the two polarisation modes after the WDM and isolator was 430 μW for 82 mW of launched pump power. Pumping at 1480 nm was chosen in order to keep self heating of the laser due to non-radiative decay to a minimum (see Sections 3.6.2 and Chapter 4). The output of the DFB fibre laser was split into two arms by a 50:50 coupler. One arm was used to measure the wavelength $\lambda_{x,y}$ of one polarisation with a wavemeter[6]. The wavemeter had a resolution of ± 0.1 pm which is one to two orders of magnitude better than commercial spectrum analysers (wavelength measurement resolution typically $1-10$ pm). The polarisation controller PC1 was used to align the polarisation axes of the laser output parallel to the axes of a fibre pigtailed polarising beam splitter (PBS) so that only the x-polarisation (labelling of the polarisation axes is arbitrary) was incident on the wavemeter. The alignment of the polarisation axes was monitored at the second output of the PBS with a scanning Fabry-Perot spectrum analyser[7] with a free spectral range of 6 GHz and a resolution of 1.2 MHz, which was sufficient to separate the two polarisation modes. The polarisation controller PC1 was adjusted until the signal from the x-polarisation vanished on the Fabry-Perot trace. Measuring $\Delta\lambda_{x,y}$ of only one polarisation offers a greater accuracy than measuring the change of the mean wavelength of both polarisations. The latter method could suffer from relative intensity fluctuations between the two polarisation modes. In the other arm of the coupler the two polarisation modes were mixed in a polariser, and the light was

[5]Manufactured by Anritsu.

[6]Burleigh WA-1500

[7]Newport SR-170

detected with a photodiode[8]. The frequency of the beat signal was detected with an RF spectrum analyser[9]. A polarisation controller (PC2) was used to align the polarisation axes at 45° with respect to the polariser, thereby optimising the signal amplitude on the RF spectrum analyser.

5.1.4 Sensor response

The wavelength λ_x of the unstrained DFB fibre laser at room temperature was 1549.5 nm whilst the polarisation beat frequency was $\nu = 1$ GHz with a linewidth of ≈ 10 kHz. Inserting ν, $\lambda_x \approx 2n\Lambda$, and $n = 1.46$ into (5.6) leads to a birefringence of $B \approx 7.5 \times 10^{-6}$. This small birefringence is a combination of the intrinsic fibre birefringence and the birefringence induced by the inscription of the DFB grating. In this case the UV light was polarised parallel to the fibre axis before passing through the phase mask — as opposed to perpendicularly polarised for manufacturing single polarisation DFB fibre lasers [82]. The polarisation beat frequency of the DFB fibre laser used in this experiment is about 2.3 times bigger than in the one used in [11]. Two immediate explanations are conceivable: the use of different fibres for the lasers in the two experiments while the grating writing process was essentially the same and the dependence of the net polarisation on the angle between the intrinsic fibre polarisation and the UV-induced polarisation.

The sensor was calibrated by measuring λ_x and ν at four different temperatures with nine strain levels each. The accuracies of the measurements were $\sigma(\lambda_x) \approx \pm 0.5$ pm and $\sigma(\nu) \approx \pm 10$ kHz, limited by small wavelength and beat frequency fluctuations of the laser. The results are shown in Figures 5.3 and 5.4. Two

[8] New Focus 1611, bandwidth 1 GHz.

[9] Tektronix 2782

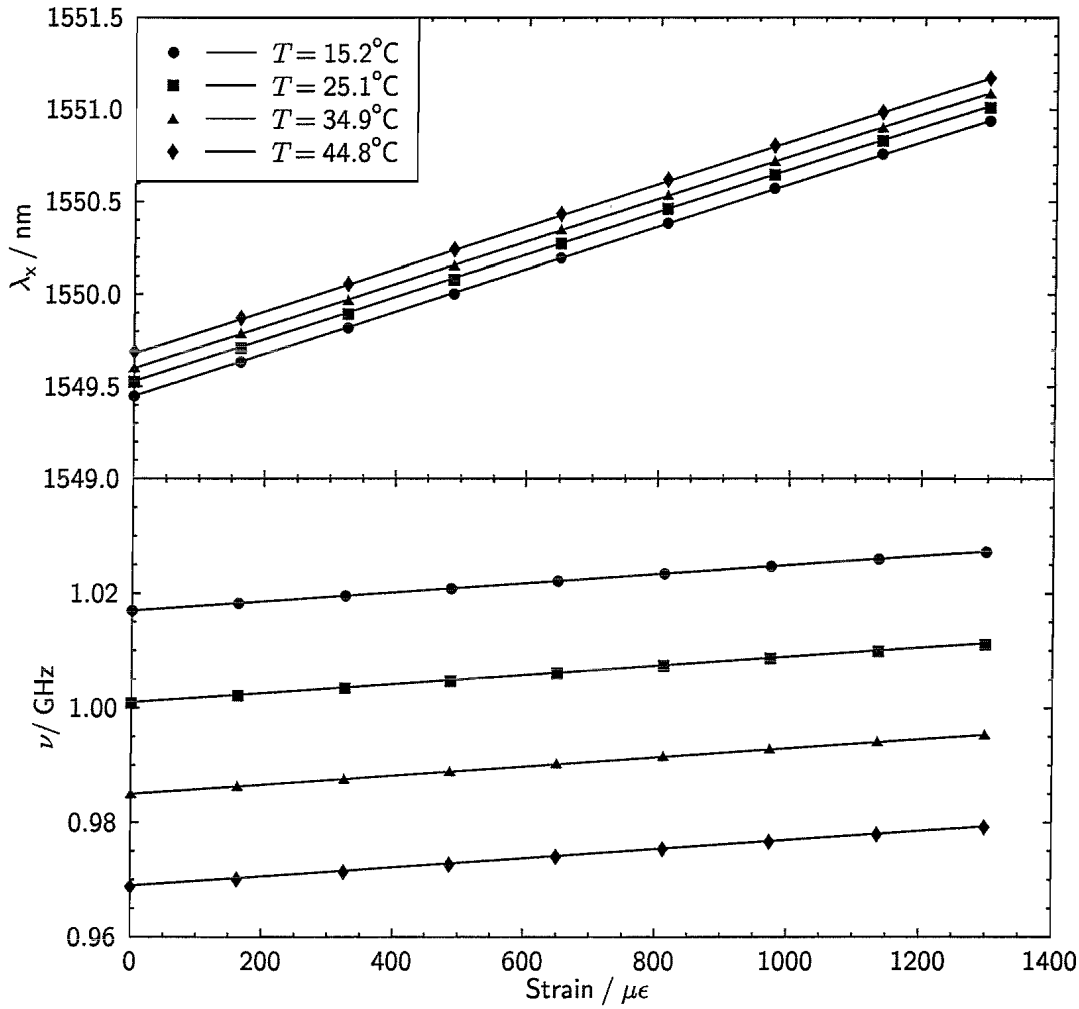

Figure 5.3. Wavelength of x-polarisation λ_x and polarisation beat frequency ν as a function of strain ϵ measured at four different temperatures. No cross-sensitivity between strain and temperature is observed, i.e. the responses $\Delta\lambda_x/\Delta\epsilon$ and $\Delta\nu/\Delta\epsilon$ are independent of temperature. It can be concluded from the positive slope $\Delta\nu/\Delta\epsilon$ that the fibre birefringence increases with strain. Additional asymmetric stress is probably introduced in the strained fibre.

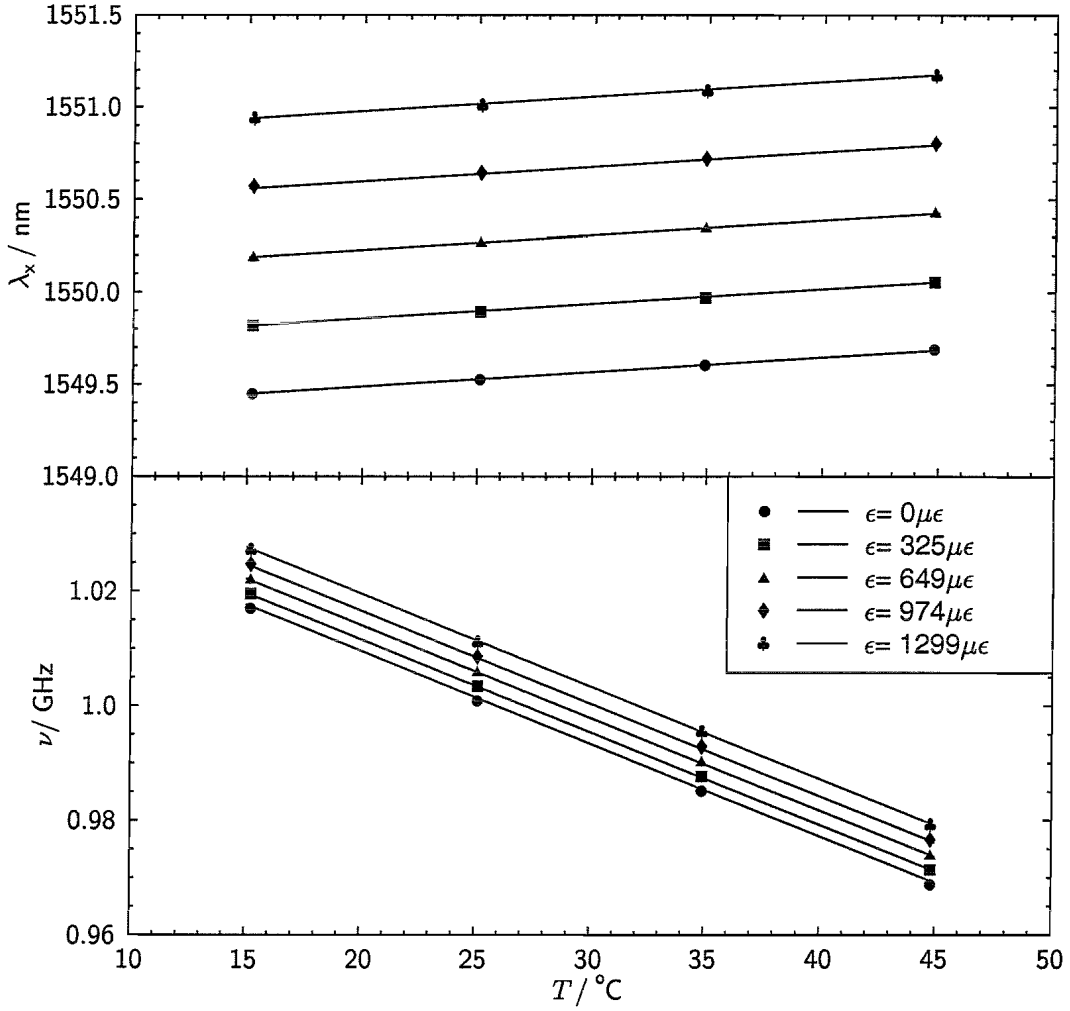

Figure 5.4. Wavelength of x-polarisation λ_x and polarisation beat frequency ν as a function of temperature T. Data of only five strain levels is shown for clarity of the graph. The decrease of ν with increasing temperature is expected from theory as the glass softens and internal stresses decrease. The slope $\Delta\nu/\Delta T$ depends on the actual thermal properties of the fibre used.

planes, $\lambda_x(\epsilon, T)$ and $\nu(\epsilon, T)$, were fitted to the data yielding the following regression coefficients and their standard deviations:

$$\begin{aligned} k_{11} &= (1.147 \pm 0.002)\,\mathrm{pm}/\mu\epsilon, \\ k_{12} &= (7.946 \pm 0.065)\,\mathrm{pm}/^{\circ}\mathrm{C}, \\ k_{21} &= (7.946 \pm 0.043)\,\mathrm{kHz}/\mu\epsilon, \\ k_{22} &= (-1.623 \pm 0.002)\,\mathrm{MHz}/^{\circ}\mathrm{C}. \end{aligned}$$

Note that the numerical equality of k_{12} and k_{21} is a pure coincidence.

The strain dependence $\Delta\lambda_x/\lambda_x = k_{11} \times \epsilon/\lambda_x = 0.74\epsilon$ is in good agreement with theoretical predictions from Eq. (2.10-a) of $\Delta\lambda_x/\lambda_x = 0.78\epsilon$. The temperature coefficient $k_{12}/\lambda_x = 5.1 \times 10^{-6}\,\mathrm{K}^{-1}$ is smaller than $9 \times 10^{-6}\,\mathrm{K}^{-1}$, the value commonly quoted for silica fibre in the literature. This discrepancy probably arises from the rare earth doping of the fibre as the value is similar to $4.9 \times 10^{-6}\,\mathrm{K}^{-1}$ calculated from the results published in [11]. From the beat frequency measurement ν it can be concluded that the birefringence increased with strain. This finding is in contradiction with the simple theory presented in [90]. Additional asymmetric stress is probably induced in the strained fibre due to different mechanical properties of the $Er^{3+}:Yb^{3+}$ core, the B/Ge-doped ring and the cladding. The decrease of ν with increasing temperature is expected from theory. The slope $\Delta\nu/\Delta T$ depends on the actual thermal properties of the fibre used.

At this point it is informative to compare the conditioning of the matrix $\boldsymbol{K}$ in (5.8) and the corresponding matrices of passive FBG sensors for simultaneous strain and temperature measurements. Two such sensors have been mentioned in Section 2.2.4, one employing two superimposed gratings [30] and another using a FBG written into birefringent fibre [39]. As the measurand encoding of this polarimetric DFB fibre laser sensor differs from that of the two passive FBG sensors, i.e. a combination of one wavelength and one RF frequency in the former and two wavelengths in the latter, it is necessary to use the relative sensor responses for this comparison:

$$\begin{aligned} \begin{pmatrix} \Delta\Phi_1/\Phi_1 \\ \Delta\Phi_2/\Phi_2 \end{pmatrix} &= \begin{pmatrix} m_{11} & m_{12} \\ m_{21} & m_{22} \end{pmatrix} \begin{pmatrix} \epsilon \\ \Delta T \end{pmatrix} \\ &= \boldsymbol{M} \begin{pmatrix} \epsilon \\ \Delta T \end{pmatrix}. \end{aligned} \tag{5.11}$$

In the case of the polarimetric DFB fibre laser sensor the Φ_i represent λ_x and ν, while for the passive FBG sensors they stand for the two measured wavelengths [30, 39].

It is well known that the larger $|\det \boldsymbol{M}|$ the better the conditioning of $\boldsymbol{M}$. This improves the discrimination between strain and temperature and increases the potential measurement accuracy of the sensor. The matrices $\boldsymbol{M}$, the determinants $\det \boldsymbol{M}$ and the obtained measurement accuracies of the three different sensors are listed in Table 5.1.[10]

Table 5.1 shows that for this DFB fibre laser sensor $|\det \boldsymbol{M}|$ is a factor of $\sim 1500 - 3200$ larger than for the two passive FBG sensors. In other words, the matrix of the DFB fibre laser sensor is significantly better conditioned than that of the passive FBG sensors. This DFB fibre laser sensor should therefore offer a considerably higher measurement accuracy than the two passive FBG sensors.

[10]The measurement accuracy of this DFB fibre laser sensor will be calculated in the next Section.

Table 5.1. Conditioning of $\boldsymbol{M}$ in (5.11) for two passive FBG sensors for simultaneous strain and temperature measurements and this DFB fibre laser sensor. For the DFB fibre laser sensor $|\det \boldsymbol{M}|$ is a factor of $\sim 1500 - 3200$ larger than for the two passive FBG sensors, i.e. the matrix of the first is significantly better conditioned than that of the latter two. The actual measurement accuracies $\sigma(\epsilon)$ and $\sigma(T)$ depend not only on $|\det \boldsymbol{M}|$ but also on the measurement accuracies $\sigma(\Delta\Phi_i/\Phi_i)$ and the calibration errors $\sigma(m_{ij})$. The stated measurement accuracies of the three sensors take these last two error sources into account.

FBG sensor type	$\boldsymbol{M}$	$\det \boldsymbol{M}$ $/\epsilon^{-1}\,^\circ\mathrm{C}^{-1}$	$\sigma(\epsilon)$ $/\mu\epsilon$	$\sigma(T)$ $/^\circ\mathrm{C}$
Superimposed	$\begin{pmatrix} 0.74\,\epsilon^{-1} & 6.71\cdot 10^{-6}\,^\circ\mathrm{C}^{-1} \\ 0.69\,\epsilon^{-1} & 7.41\cdot 10^{-6}\,^\circ\mathrm{C}^{-1} \end{pmatrix}$	$0.85\cdot 10^{-6}$	10	5
Birefringent	$\begin{pmatrix} 0.866\,\epsilon^{-1} & 6.58\cdot 10^{-6}\,^\circ\mathrm{C}^{-1} \\ 0.873\,\epsilon^{-1} & 6.19\cdot 10^{-6}\,^\circ\mathrm{C}^{-1} \end{pmatrix}$	$-0.39\cdot 10^{-6}$	20	2
DFB fibre laser	$\begin{pmatrix} 0.74\,\epsilon^{-1} & 5.13\cdot 10^{-6}\,^\circ\mathrm{C}^{-1} \\ 7.95\,\epsilon^{-1} & -1.62\cdot 10^{-3}\,^\circ\mathrm{C}^{-1} \end{pmatrix}$	$-1.24\cdot 10^{-3}$	3	0.04

However, the measurement accuracy is not only a function of $|\det \boldsymbol{M}|$ but also depends on the measurement accuracies $\sigma(\Delta\Phi_i/\Phi_i)$ and calibration errors $\sigma(m_{ij})$. The actual measurement accuracy of this DFB fibre laser sensor will be investigated in the following Section.

5.1.5 Sensor accuracy and resolution

A careful analysis of the residuals was carried out to check the validity of the linear model (5.8) and to discover possible causes for the observed measurement errors. The residuals are shown in Figures 5.5 and 5.6. The residuals show no systematic deviation from the linear model and no signs of cross-sensitive strain and temperature responses. It can, however, be seen in the top graph of Figure 5.5 that the deviations of the wavelength measurements from the fitted straight line are correlated with the applied strain. The most probable cause is the uneven motion of the manual translation stage which is common for this type of equipment. This assumption is supported by the 'periodic' dependence of the residuals on the applied strain. A similar behaviour can be seen in the bottom graph of the same Figure, although the frequency residuals are dominated by temperature measurement errors. The top graph also gives an idea about the positioning repeatability of the translation stage by examining the spread of the residuals for a fixed strain value. The positioning repeatability was similar to the error from the uneven motion. The bottom graph of Figure 5.6 again shows the dominance of temperature measurement errors on the frequency residual, E.g. a small temperature fluctuation of $\approx 0.1\,°\mathrm{C}$ around $T = 15.2\,°\mathrm{C}$ remained undetected by the thermometer but is clearly visible in Figure 5.5. In the top graph of the same Figure positioning errors of the translation stage are, once more, the primary source of the wavelength residuals. The standard deviation of the wavelength residuals was $\sigma(\lambda_{\mathrm{res}}) = 4.1\,\mathrm{pm}$ which corresponds to $\sigma(\lambda_{\mathrm{res}})/k_{11} = 3.6\,\mu\epsilon$, or a positioning error of the manual translation stage of $3.6\,\mu\epsilon \cdot l_g = 2.2\,\mu\mathrm{m}$. Similarly the standard deviation of the frequency measurements was $\sigma(\nu_{\mathrm{res}}) = 103\,\mathrm{kHz}$ which corresponds to $0.06\,°\mathrm{C}$. The accuracy of the regression coefficients k_{11} and k_{12} which describe the wavelength dependency of the sensor

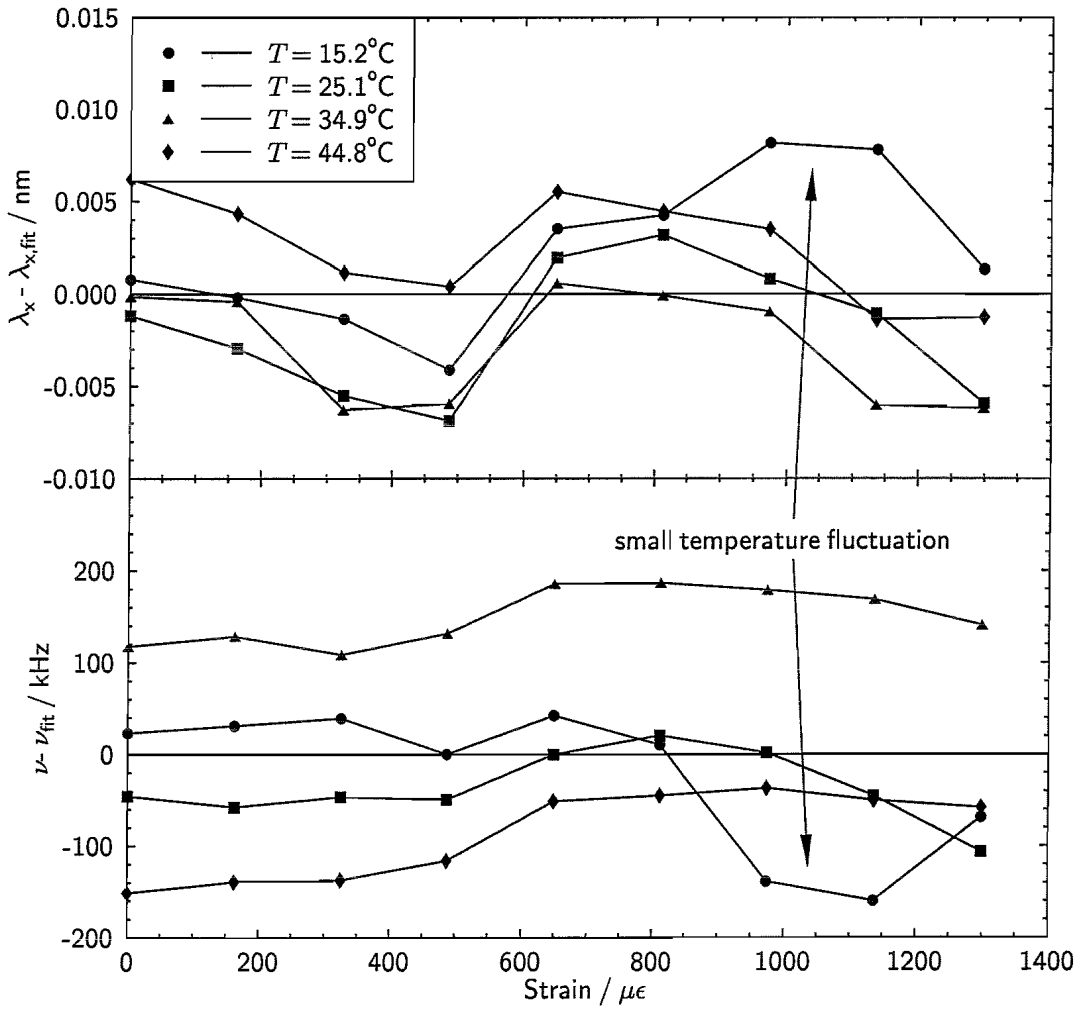

Figure 5.5. Residuals of wavelength of x-polarisation and polarisation beat frequency as a function of strain. The 'periodic' strain dependence of the residuals is probably caused by the uneven motion of the translation stage. A small temperature fluctuation of $\approx 0.1\,^{\circ}\mathrm{C}$ around $T = 15.2\,^{\circ}\mathrm{C}$ remained undetected by the thermometer but is clearly recorded by the DFB fibre laser sensor and is consequently transformed in a correlated excursion of the residuals.

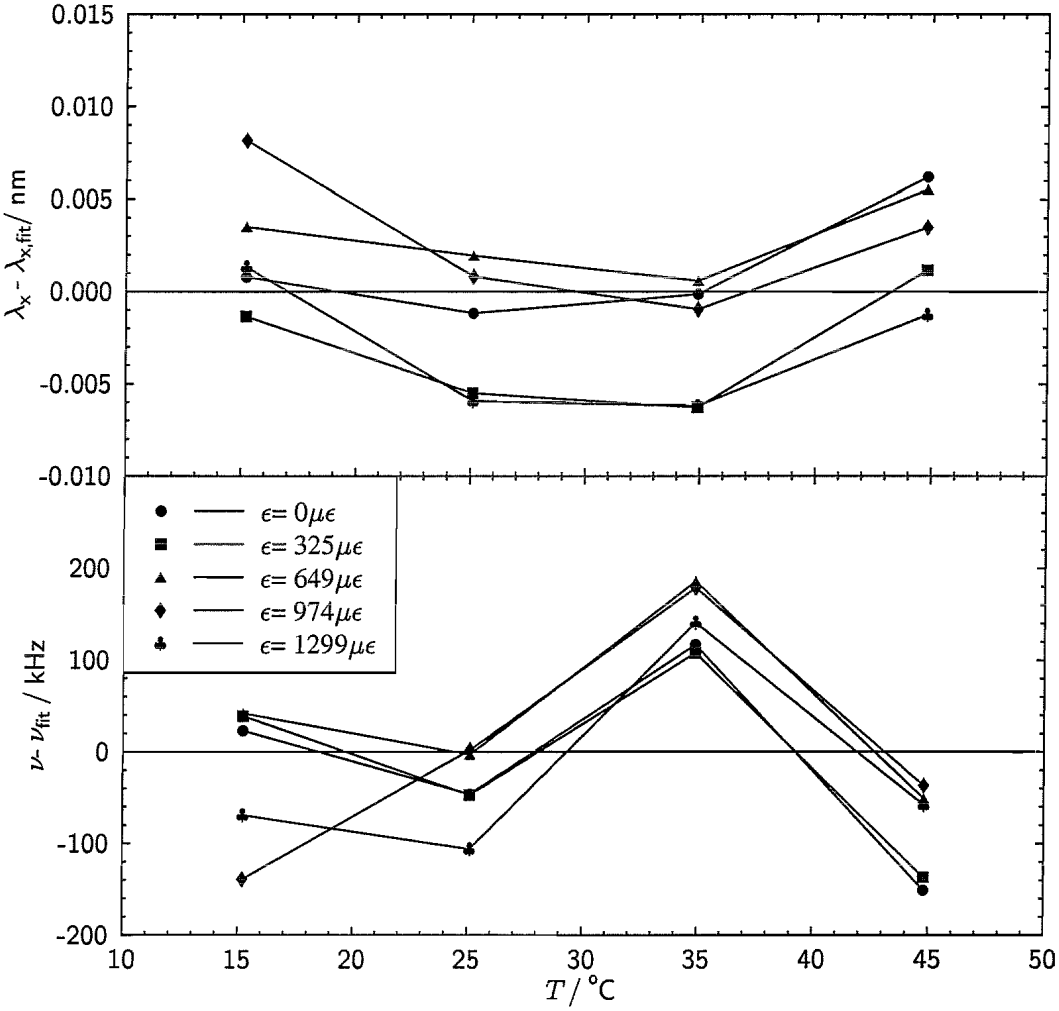

Figure 5.6. Residuals of wavelength of x-polarisation and polarisation beat frequency measurement as a function of temperature. The residuals of the beat frequency measurements depend predominantly on the errors of the temperature measurements.

were therefore limited by the uneven motion and the positioning repeatability of the translation stage. The accuracy of the regression coefficients k_{21} and k_{22} which describe the frequency response was limited by the accuracy of the temperature control loop and the resolution of the thermometer.

By adding the calibration errors, i.e. the errors of $\boldsymbol{K}^{-1}$, and the accuracies of the wavelength and polarisation beat frequency measurements, $\sigma(\lambda_x)$ and $\sigma(\nu)$, in quadrature, the accuracy of this strain and temperature sensor was calculated to be $\pm 3\,\mu\epsilon$ and ± 0.04°C. The repeatability of the strain measurements was determined separately (not shown in the Figures) to be $\pm 2.5\,\mu\epsilon$ which is in agreement with the data shown in the Figures, i.e. wavelength residuals for a given strain setting scatter by about a factor of 1.4 less than the standard deviation $\sigma(\lambda_{\text{res}})$.

While the accuracy of this sensor was limited by the positioning accuracy of the translation stage and the thermometer resolution, the resolution of the sensors was given by the accuracy of the wavelength and beat frequency measurements. Although the resolution of the wavemeter was 0.1 pm small wavelength fluctuations of the DFB fibre laser reduced the achieved measurement accuracy to $\sigma(\lambda_x) = 0.5$ pm. A combination of beat frequency fluctuations and the linewidth of the beat signal resulted in an accuracy of the beat frequency measurement of $\sigma(\nu) = 10$ kHz. The achieved sensor resolution can be calculated from $\sigma(\lambda_x)$ and $\sigma(\nu)$ by first inverting (5.8) and then conducting a conventional error analysis. The accuracy of the wavelength and beat frequency measurements corresponded to a sensor resolution of $\pm 0.4\,\mu\epsilon$ and $\pm 6 \times 10^{-3}$°C. The wavelength and beat frequency fluctuations were probably caused by vibrations of the setup, air flow through the oven, small temperature variations and/or pump power fluctuations. A reduction of these external noise sources together with the use of more accurate interrogation systems would increase the sensor resolution. However, the optical linewidth of the DFB fibre laser, which also determines the linewidth of the polarisation beat signal, would impose a natural limit on the sensor resolution.

Although the telecommunication fibre was coated no slipping or creep of the fibre was observed. However, at higher strain levels or over longer periods of time slipping and creep are potential problems which can be solved by choosing appropriate glues

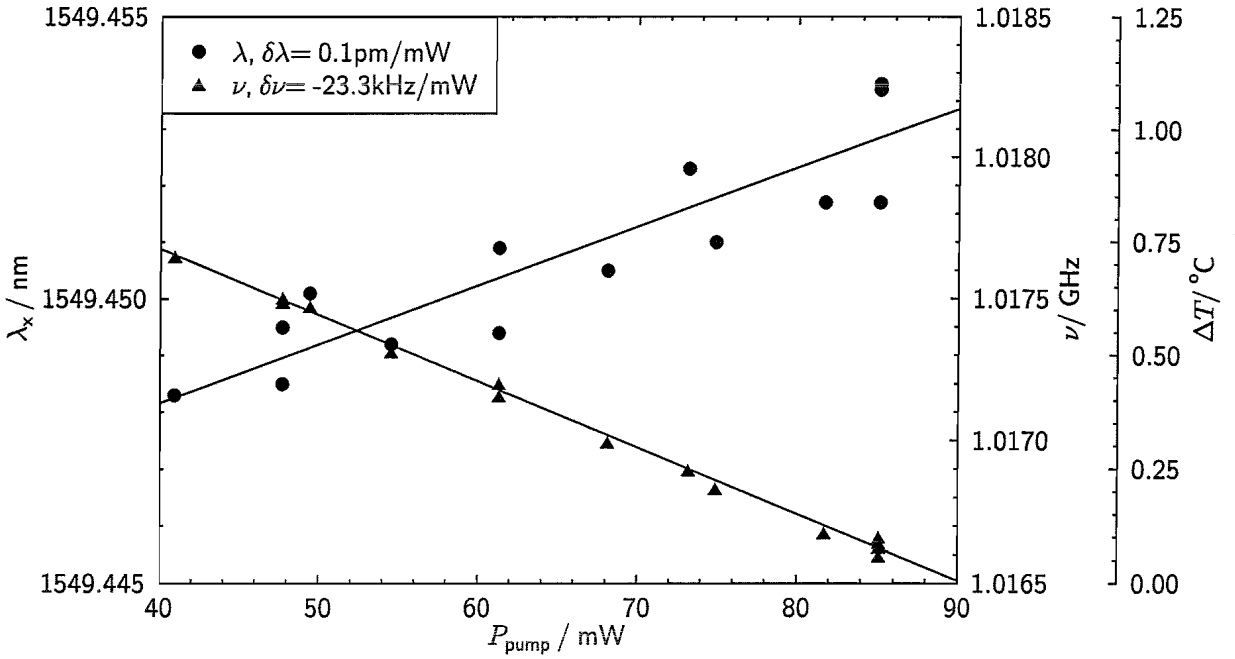

Figure 5.7. Change of wavelength and beat frequency with pump power at 1480 nm due to self heating of the DFB fibre laser sensor. To maintain the 0.04 °C measurement accuracy the pump power must not vary by more than 2.8 mW.

and using either uncoated fibre or harder coatings. The thermal stress induced by the rise of the fibre temperature from room temperature (25°C) to 45°C led to a strain of $\approx 2.4\,\mu\epsilon$ (5.10) which lay within the accuracy of the sensor. A possible calibration error of the thermometer is not included in the above stated accuracy of the sensor.

Figure 5.7 shows the response of the sensor to pump power variations. Laser wavelength and polarisation beat frequency varied linearly with pump power due to self-heating of the DFB fibre laser. This effect had been further investigated in Section 4.4.1. The temperature increase with pump power is 0.014 °C/mW. Therefore, in order to maintain the sensor accuracy of ±0.04°C the pump power must not vary by more than 2.8 mW. This poses no problem in a laboratory environment. However, if the sensor is to be employed as a remote sensor with a long length of fibre delivering the pump then variable optical losses might lead to pump power fluctuations of this magnitude.

5.2 DFB fibre laser sensors embedded in concrete

The strain and temperature accuracies of the DFB fibre laser sensor presented in the previous Section are adequate for a variety of applications, including civil engineering. Therefore, a laboratory trial was carried out in which three polarimetric single longitudinal mode DFB fibre laser strain and temperature sensors were embedded in a concrete test specimen. A new miniature package has been developed to protect the sensors and allow them to be employed in these typically small concrete laboratory test structures. The objective of this preliminary experiment was to study the performance of these sensors in a concrete structure and to establish where practical problems lie, e.g. handling by technicians unfamiliar with fibre optics and the level of dust, water and aggressive chemicals.

5.2.1 Sensor calibration

The three DFB fibre laser sensors were calibrated following the procedure described in Section 5.1.4. Because the 1480 nm pump diode had since degraded (lower output power, broader optical spectrum) the output power of the DFB fibre lasers was reduced by a factor of 16 compared to the results presented in Section 5.1. As a result the measurement accuracy was reduced by a factor of ≈ 10 compared to the previously presented results. However, the accuracy was still sufficient to justify the laboratory trial. The wavemeter could not be used because of the low output power of the DFB lasers and had to be replaced by an optical spectrum analyser[11]. The lower wavelength resolution made the polarising beam splitter (see Figure 5.2) redundant. Furthermore, it was observed that coupling of optical power between the two orthogonal polarisations along the non-polarisation maintaining lead fibre was large enough to produce a sufficient polarisation beat signal on the detector without the need for the polarisation controller and polariser.

The calibration constants of the three sensors are listed in Table 5.2. It should be noted that the strain and temperature responses of the polarisation beat frequency

[11] Manufactured by Ando, resolution 0.1 nm.

of sensor 2 are smaller than for the other two sensors. A possible explanation is the relative alignment between the birefringence axes of the fibre and the UV-induced grating, resulting in a different total birefringence.

5.2.2 Sensor protection

Fibre optic sensors need to be protected in order to survive the embedding process in concrete. This does not only include the risk from the large forces generated during concrete placement, but also from the chemical environment as good structural concrete will have a pH $\approx$ 14. Therefore, the sensor protection must be adequate to withstand such forces and to prevent the ingress of high pH moisture from the concrete mix during the wet stage. In addition, the protection must not impede the transfer of strains from the concrete to the fibre through shear lag. A further requirement is that appropriately protected sensors should be easy to install. As this experiment was serving as a first test for embedding the DFB fibre laser sensors in concrete the design of the sensor protection was kept as straightforward as possibly. By avoiding over-engineering the sensors could be produced more easily and faster. The simpler design would also facilitate the identification of unexpected problems.

On the basis of these specifications the DFB fibre laser sensors were protected by tubes made from either epoxy resin (sensor 1), aluminium (sensor 2) or steel (sensor 3). The tubes were about 60 mm long and 3–5 mm in diameter and therefore compact enough to be embedded in a concrete test beam with the dimensions of

Table 5.2. Calibration constants of the three DFB fibre laser strain and temperature sensors embedded in concrete. These calibrations were carried out prior to being protected by tubes made from either epoxy resin, aluminium or steel.

sensor	$k_{11}/(\mathrm{pm}/\mu\epsilon)$	$k_{12}/(\mathrm{pm/K})$	$k_{21}/(\mathrm{kHz}/\mu\epsilon)$	$k_{22}/(\mathrm{MHz/K})$
1, epoxy	1.18	8.40	6.54	-1.54
2, aluminium	1.20	9.80	5.35	-0.85
3, steel	1.17	8.50	6.54	-1.54

500 mm × 100 mm × 100 mm. The tubes were only about 10 mm longer than the DFB fibre laser sensors and care had to be taken to prevent the glue from touching the lasers themselves in order to avoid any perturbations of them. Therefore, the DFB fibre lasers were only bonded to the ends of the tubes over a length of ≈ 2 mm by epoxy glue[12]. In all three cases, the fibre outside the tube was protected by a thin (0.25 mm inner and 0.75 mm outer diameter) loose-tube PTFE sheath. Heat shrink with an inner glue lining was fastened around the ends of the tube and the PTFE sleeve in order to prevent the ingress of moisture and provide strain relief. The use of tubes has the additional advantage of having the same cylindrical symmetry as the fibre, reducing the build up of local stress.

The three different materials used to protect the three DFB fibre lasers employed in this trial were chosen because they were easily available with the required dimensions. Furthermore, the effects of different mechanical and thermal properties on the sensor performance, e.g. strain transfer, could be investigated. The relevant material properties are listed in Table 5.3. The table shows that steel has approximately the same thermal expansion coefficient as concrete ($12 \times 10^{-6}\,\mathrm{K}^{-1}$), so only very small thermal induced stresses would be expected to occur at the concrete-steel interface.

[12]Devcon 2 Ton Epoxy

Table 5.3. Mechanical and thermal properties of the materials used to protect the embedded DFB fibre laser sensors and concrete [88, 91]. E Young's modulus, G shear modulus, and α thermal expansion coefficient.

	E	G	α
	$10^9\,\mathrm{N/m^2}$	$10^9\,\mathrm{N/m^2}$	$10^{-6}/\mathrm{K}$
epoxy resin	≈ 2	≈ 1	≈ 50
aluminium	70	40	23
mild steel	200	79	≈ 12
concrete	21–40	≈ 14	≈ 12
optical fibre	75		0.5

The thermal expansion coefficient of aluminium is ≈ 1.6 larger than that of steel and concrete. However, its modulus of elasticity is only $E = 72 \times 10^9\,\mathrm{N/m^2}$ which is closer to that of concrete ($E = 40 \times 10^9\,\mathrm{N/m^2}$). Therefore, an aluminium protection in a concrete structure should cause a smaller mismatch in terms of its mechanical properties compared to steel.

Because the modulus of elasticity of the epoxy[12] is only $\approx 2 \times 10^9\,\mathrm{N/m^2}$ [88] one might expect that the strain transfer from concrete to the fibre sensor is poor as the epoxy deforms plastically. Consequently a simple shear lag analysis has been carried out, using the following two equations [92]:

$$\epsilon_s(z) = \epsilon_{s,\mathrm{inf}}(1 - \exp(-\beta z)) \tag{5.12}$$

and

$$\beta = \sqrt{\frac{2G}{r^2 E \ln(R/r)}}, \tag{5.13}$$

where $\epsilon_s(z)$ is the local strain experienced by a specimen embedded in a structure made of a material with shear modulus G which is strained to $\epsilon_{s,\mathrm{inf}}$. The modulus of elasticity of this specimen is E, its radius is r and $R/r \approx 5$ [92]. The strain transfer from concrete to the embedded epoxy protection is calculated by inserting the shear modulus of concrete, the modulus of elasticity of epoxy and the radius of the epoxy tube into (5.13). Similarly, the strain transfer from the epoxy protection to the optical fibre is calculated by inserting the shear modulus of epoxy, the modulus of elasticity of the fibre and the radius of the fibre into (5.13). The combined shear lag parameter β can then be used in (5.12) to calculate the required length of the sensor in order to ensure good strain transfer. The shear modulus G_c of concrete was estimated by the following relation [13]:

$$E_c/2 > G_c > E_c/3, \tag{5.14}$$

where E_c is the modulus of elasticity of concrete (see Table 5.3). Therefore the approximation $20 \times 10^9\,\mathrm{N/m^2} > G_c > 7 \times 10^9\,\mathrm{N/m^2}$ holds, with a mean value of $G_c \approx 14 \times 10^9\,\mathrm{N/m^2}$. The epoxy protection tube had an outer diameter of 5 mm,

[12]Devcon 2 Ton Epoxy, i.e. the same epoxy was used for the protective tube and the glue.

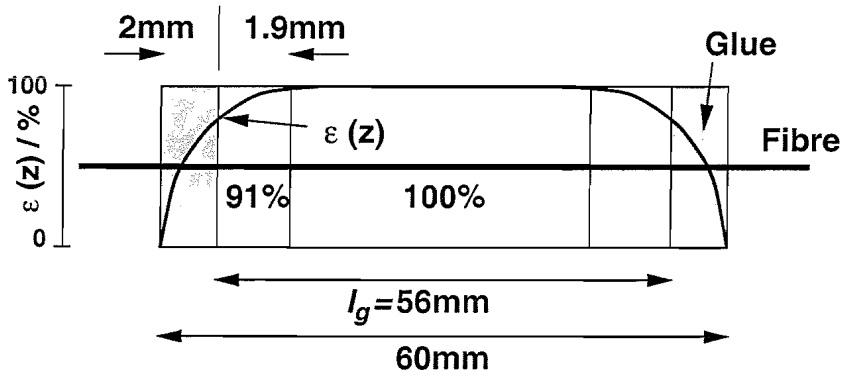

Figure 5.8. Schematic of the strain distribution along the epoxy protective tube. The fibre is glued into the tube over a length of 2 mm at the ends of the tube. At a position 2 mm away from the ends the local strain inside the tube has reached 91 % of its actual value, at 3.9 mm this value has increased to almost 100 %. Since the fibre optic strain sensor measures the mean strain level over its entire gauge length, defined by the glue points, the measurement error is only 1 %.

an inner diameter of 1 mm, and was 60 mm long. For simplicity the epoxy tube is regarded as a solid rod. Inserting the above values into (5.13) yields $\beta = 1180/\text{m}$ for the strain transfer from concrete to epoxy. Inserting β into (5.12) shows that the strain in the epoxy tube has reached 63 % of the strain in the concrete after a length of 0.8 mm, and 99 % after a length of 3.9 mm. Hence, to provide perfect strain transfer the points defining the gauge length should lie $\sim$ 3.9 mm inwards from the ends of the tube. As the fibre is bonded to the epoxy over a length of only 2 mm (see Figure 5.8), the strain in the epoxy tube at the end of the gauge length has only reached 91 % of the strain in the concrete. Because the gauge length is 60 mm $-$ 2 $\times$ 2 mm $=$ 56 mm this results in a strain measurement error of 1 %, assuming that over a length of 60 mm $-$ 2 $\times$ 3.9 mm $=$ 52.2 mm at the centre the sensor experiences the full strain and over a length of 3.9 mm $-$ 2 mm $=$ 1.9 mm at either end only 91 %. This result suggests that adequate strain transfer can be achieved with such an epoxy tube.

The epoxy tube was fabricated by means of a mould. Other shapes of epoxy packages could be easily fabricated to meet different needs. Small indentations were made into the steel tube to potentially increase the bonding with the concrete and make the strain transfer from the concrete through to the sensor more effective.

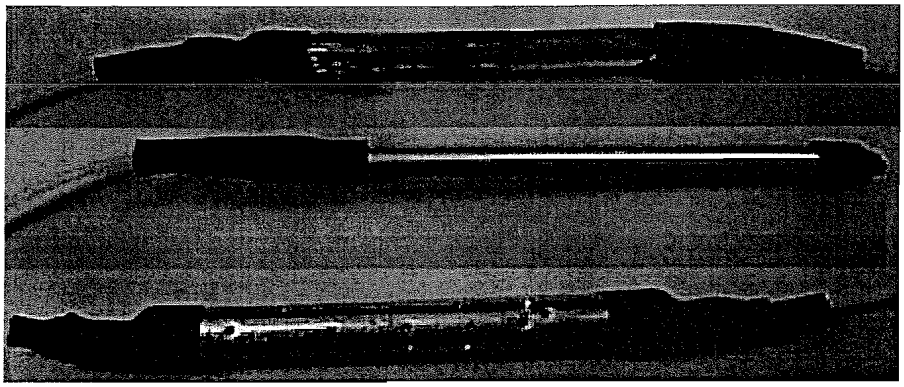

Figure 5.9. Photograph of the packaged DFB fibre laser sensors. From top to bottom: Epoxy tube protection, aluminium tube protection, and steel tube protection.

The sensors, shown in Figure 5.9, were easy to handle and no special care was taken during installation of the sensors and casting the concrete beam.

5.2.3 Concrete test specimen

A standard 500 mm × 100 mm × 100 mm concrete beam was cast from a C35 N/mm^2 mix design. The maximum aggregate size was limited to 10 mm due to concerns by the civil engineers[13], who were unfamiliar with fibre optic strain sensors, that a larger aggregate size could damage the fibre during compaction of the concrete. The smaller aggregate size also allowed a gauge length of $\approx$ 55 mm to be used since this was in excess of the recommended five times the largest aggregate size [93]. The beam was singly reinforced with two No. 6 mm diameter mild steel bars located in the tension zone (Figure 5.10).

Three DFB fibre laser sensors were installed within the mould. They were held in position by thin steel wire attached to the steel reinforcement as shown in Figure 5.10. The sensors 2 and 3 were located in the tension zone of the beam, in the same plane as the reinforcement bars, whereas sensor 1 was located in the compression zone of the beam. In addition, 5mm foil backed strain gauges were attached directly to the steel reinforcement allowing reinforcement strains to be measured directly during the beam test. In addition a thermistor was located at the centre of the con-

[13] A group led by D. J. Richards, Department of Civil and Environmental Engineering, University of Southampton.

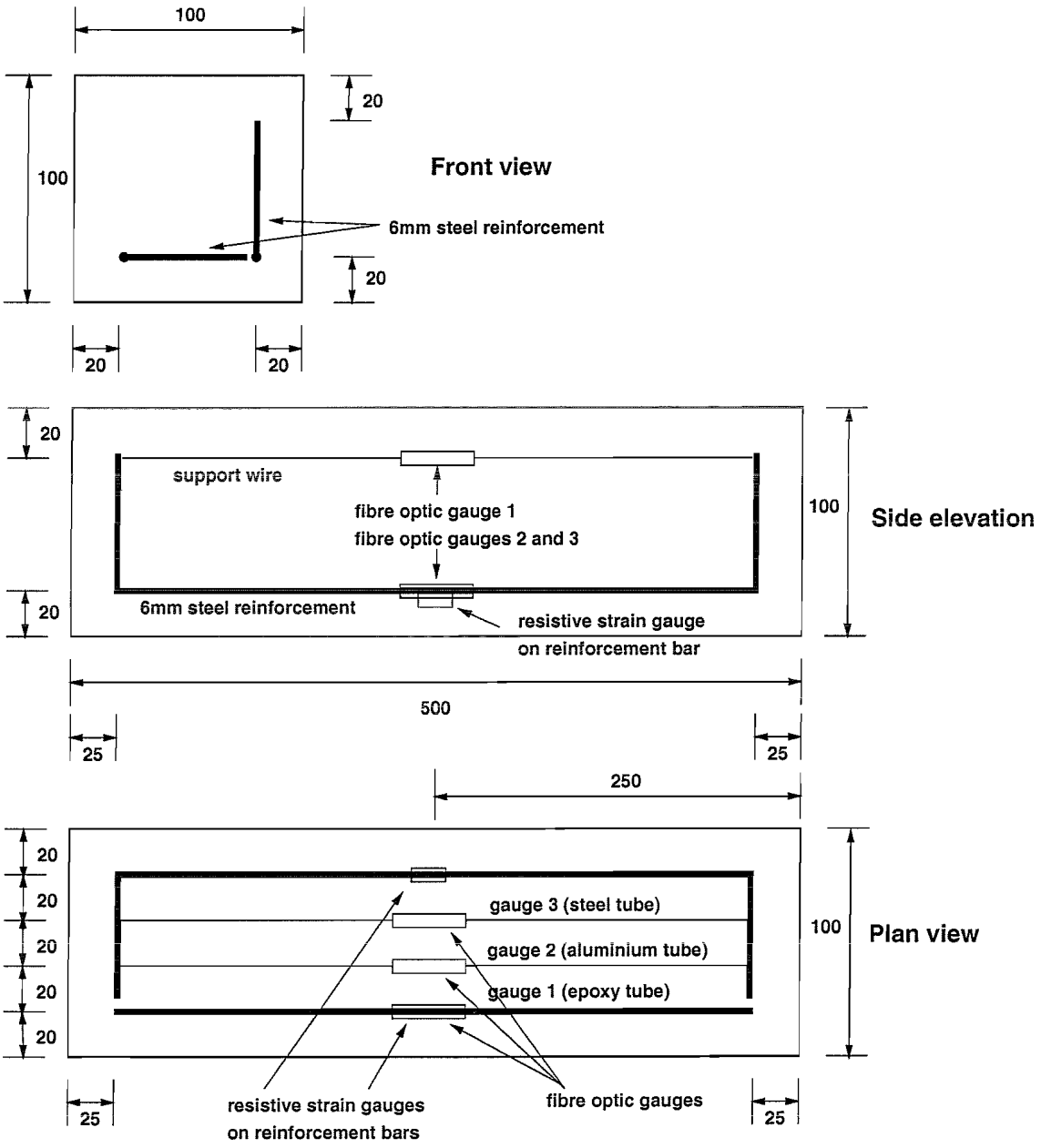

Figure 5.10. Layout of the concrete beam. Three DFB fibre laser strain and temperature sensors were installed, two in the tension zone on the bottom, and one in the compression zone in the top of the beam. Two resistive strain gauges were bonded to the reinforcement bars. The reinforcement bars were bent to provide convenient fixing points for the wires supporting the fibre laser sensors.

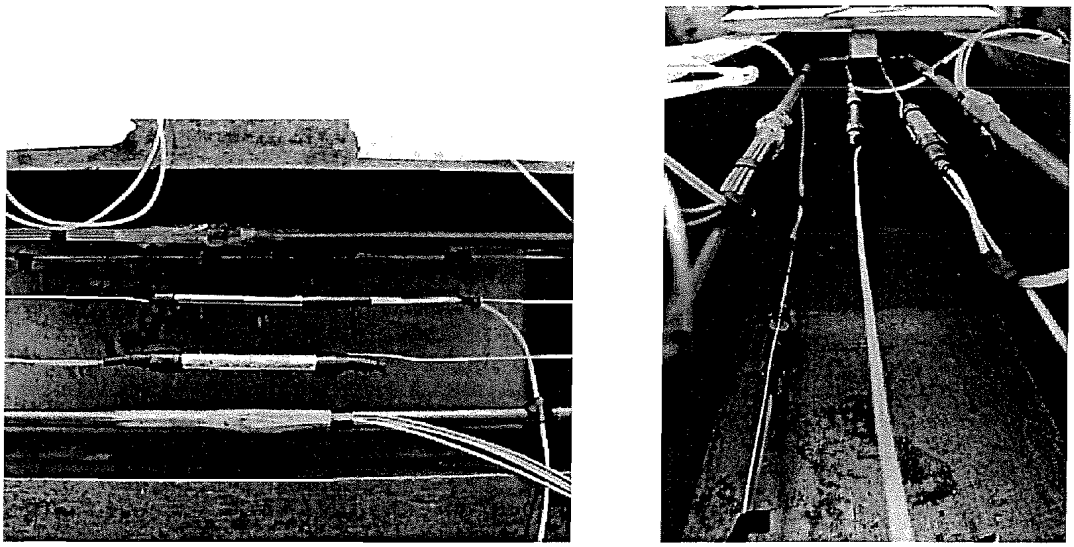

Figure 5.11. Two photographs of the three fibre optic sensors and two resistive strain gauges installed inside the mould prior to casting the beam. The two resistive strain gauges were bonded onto the steel reinforcement with epoxy resin. The three fibre optic strain sensors were suspended from thin metal wire running along the length of the mould. These wires were attached to the steel reinforcement at both ends of the beam and provide enough support for the sensor to be held in place during the placement of the concrete.

crete beam to measure its internal temperature. Figure 5.11 shows two photographs of the sensors put in place inside the mould.

5.2.4 Experimental results

Immediately after the beam had been cast, the embedded DFB fibre laser strain and temperature sensors were tested to ensure that they were still functioning. The sensor protected by the aluminium tubing (sensor 2) failed early into the test. Since no sign of amplified spontaneous emission (ASE) was detected from the Er^{3+}-doped fibre section it had to be assumed that the lead fibre to the sensor broke during the time between packaging of the laser and casting of the beam. The mechanically weakest points of the sensor are the ends of the tubes where the fibre is most likely to snap. The protective PTFE and heatshrink tubing might not have been robust enough to prevent this happening. The other two fibre laser sensors were still working, and wavelength and polarisation beat frequency readings were taken while the beam remained in the mould.

Free thermal expansion

The beam mould was struck two days after casting and the beam was then placed into a water bath. The free thermal expansion of the beam was monitored by increasing the water temperature in steps of $5-10°C$ and noting the response of the embedded fibre laser sensors. This experiment made it possible to re-calibrate the thermal response of the sensors, which becomes necessary as the thermal expansion of the concrete beam introduces apparent strain in the sensors, given by

$$\epsilon = \alpha_c \Delta T, \tag{5.15}$$

where α_c is the thermal expansion coefficient of concrete. The wavelength and polarisation beat frequency responses of the DFB fibre laser sensor to free thermal expansion of the concrete beam become

$$\Delta\lambda = k_{11}\alpha_c \Delta T + k_{12}\Delta T \tag{5.16-a}$$

$$\Delta\nu = k_{21}\alpha_c \Delta T + k_{22}\Delta T. \tag{5.16-b}$$

Here the small thermal expansion coefficient of the fibre can be neglected compared to α_c. Figure 5.12 shows the responses of the sensors while the beam was heated. The wavelength and beat frequency of the sensor protected by the epoxy tube (sensor 1) varied linearly with temperature. From linear fits to the measured data the responses of this sensor were found to be $\mathrm{d}\lambda/\mathrm{d}T = 41\,\mathrm{pm}/\,°\mathrm{C}$ and $\mathrm{d}\nu/\mathrm{d}T = -1.14\,\mathrm{MHz}/\,°\mathrm{C}$. The sensor was more sensitive than expected from (5.16-a,b) and the data of Table 5.2. A possible explanation is that the epoxy tube, which had a relatively high thermal expansion coefficient, expanded inside the heat shrink as a void has probably formed where the outer diameter was reduced from $\approx 5\,\mathrm{mm}$ at the epoxy tube to $\approx 1\,\mathrm{mm}$ at the PTFE tubing. The strain sensor packaged in the steel tube (sensor 3) followed the thermal expansion up to approximately $30\,°\mathrm{C}$. The slope of $\mathrm{d}\lambda/\mathrm{d}T = 27\,\mathrm{pm}/\,°\mathrm{C}$ is in good agreement with the value predicted from the thermal expansion of steel and concrete of $23\,\mathrm{pm}/\,°\mathrm{C}$. Above $30\,°\mathrm{C}$ the temperature dependence suddenly dropped to $\mathrm{d}\lambda/\mathrm{d}T \approx 8.6\,\mathrm{pm}/\,°\mathrm{C}$, the value previously measured for the unpackaged fibre. Debonding of the fibre from the steel tube had probably occurred. Due to the poor performance of the pump laser, and subsequently of the

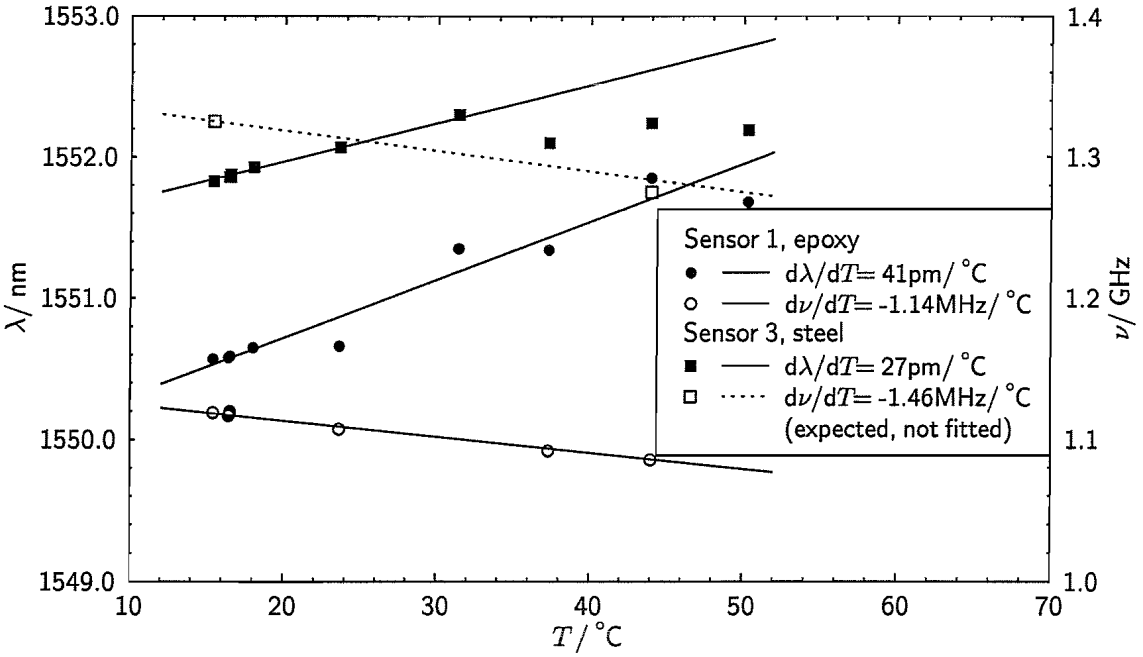

Figure 5.12. Free thermal expansion of the concrete beam. The solid lines represent best fits through the data points. No fit was carried out through the two beat frequency data points of sensor 3 (open squares). Instead the dotted line is the expected response of the sensor protected by the steel tube, assuming a thermal expansion coefficient of concrete of $12 \times 10^{-6}\mathrm{K}^{-1}$, and taking the calibration constants from Table 5.2.

DFB fibre laser, at the time of these thermal tests, only two beat frequency measurements could be taken with this DFB laser sensor. Rather than fitting a straight line through the two data points (open squares in Figure 5.12) the beat frequency response of sensor 3 was calculated from its calibration constants and the thermal expansion coefficient of concrete listed in Tables 5.2 and 5.3. As this procedure gives only the slope but not the absolute value of the beat frequency a constant offset was added such that the calculated beat frequency response passes throught the first beat frequency data point. This calculated response is shown as a dotted line in Figure 5.12. As a result of debonding, the data point at 42 °C lies below this line.

Three point bending

A standard three point bending test was undertaken on the concrete beam in an Instrom 100 kN test machine. The beam was placed on two roller supports 400mm apart as shown in Figure 5.13. A single point load was applied to the beam at

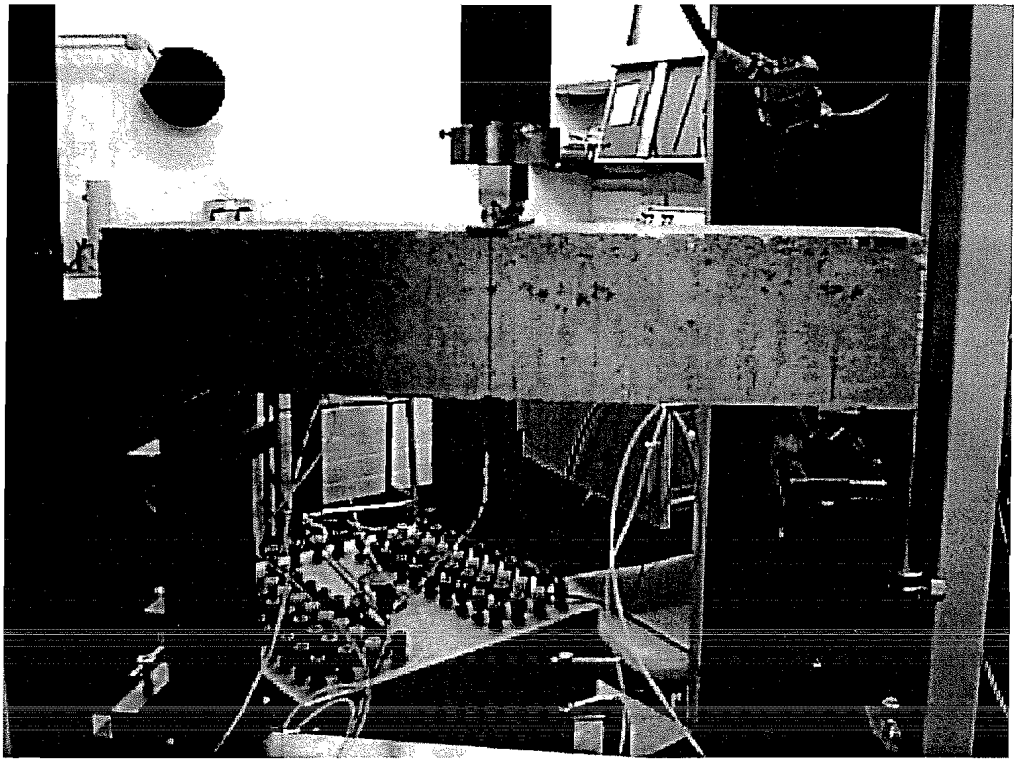

Figure 5.13. Three point bending of the concrete test specimen. The roller supports were 400 mm apart and a load of up to 8 kN was applied to the beam at its midspan.

its midspan. From the beam section moment of resistance, length of support and position of the applied load D. J. Richards calculated that the maximum load that could be applied to the beam would be 8 kN. However, following concerns about the level of reinforcement present and the assumptions used in the analysis of the section, it was decided to load the beam up to a maximum of 5 kN. The beam was initially loaded up to 5 kN in increments of 0.5 kN and then unloaded in decrements of 1.67 kN. Then the cycle was repeated with steps of 1 kN and 1.67 kN respectively. At each load level the strain of the resistive gauges located on the reinforcement was noted together with the readings from the remaining functional DFB fibre laser strain sensor (sensor 1). The temperature within the beam was also recorded at each load increment/decrement and allowed direct comparison between the temperature output from the DFB fibre laser sensor. In the final loading test, the load was increased to a maximum value of 8 kN, at which point the beam failed.

The strain recorded by the remaining functional DFB fibre laser sensor (sensor 1) is shown in Figure 5.14. During the initial loading of the beam the strain measured

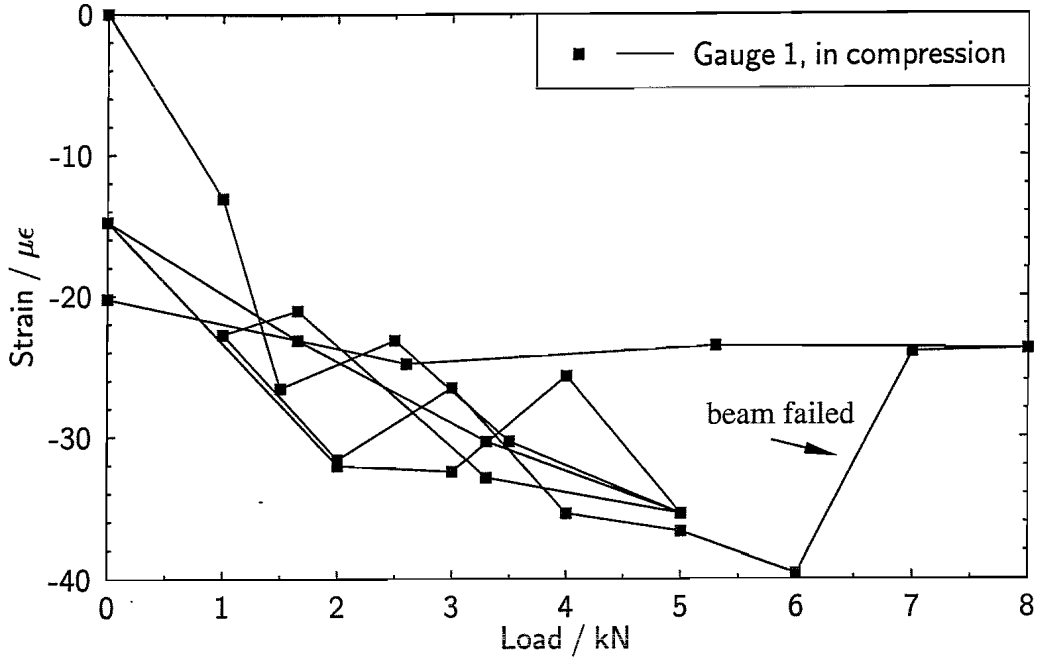

Figure 5.14. Strain measured in the compression zone with sensor 1. The beam was loaded in two cycles with load increments of 0.5 kN and 1.0 kN up to 5 kN. After each cycle it was unloaded in decrements of 1.67 kN. After the initial loading hair cracks formed in the beam and a residual compression (negative strain) of 15 $\mu\epsilon$ remained on the beam when it was completely unloaded. In the final cycle the beam was loaded up to 8 kN. The failure of the beam can clearly be seen at the load increment from 6 to 7 kN as the compression suddenly decreased. The strain inside the compression zone remained nearly constant when the beam was finally unloaded.

by sensor 1 decreased with load. After unloading the beam, the top beam was still under compression. As expected from the mechanical properties of reinforced concrete hair cracks developed in the tension zone at the bottom of the beam during the initial loading cycle. As a result the upper part of the beam remained under slight compression. The strain suddenly increased above a load of 6 kN and remained almost constant as the load was decreased. This signature indicates the failure of the beam and small cracks could be seen propagating through the concrete.

Because this sensor is placed in the compression zone of the beam and the resistive strain gauges are mounted on the steel reinforcement in the tension zone, no direct comparison between the strain readings was possible without the exact knowledge of the mechanical properties of the beam.

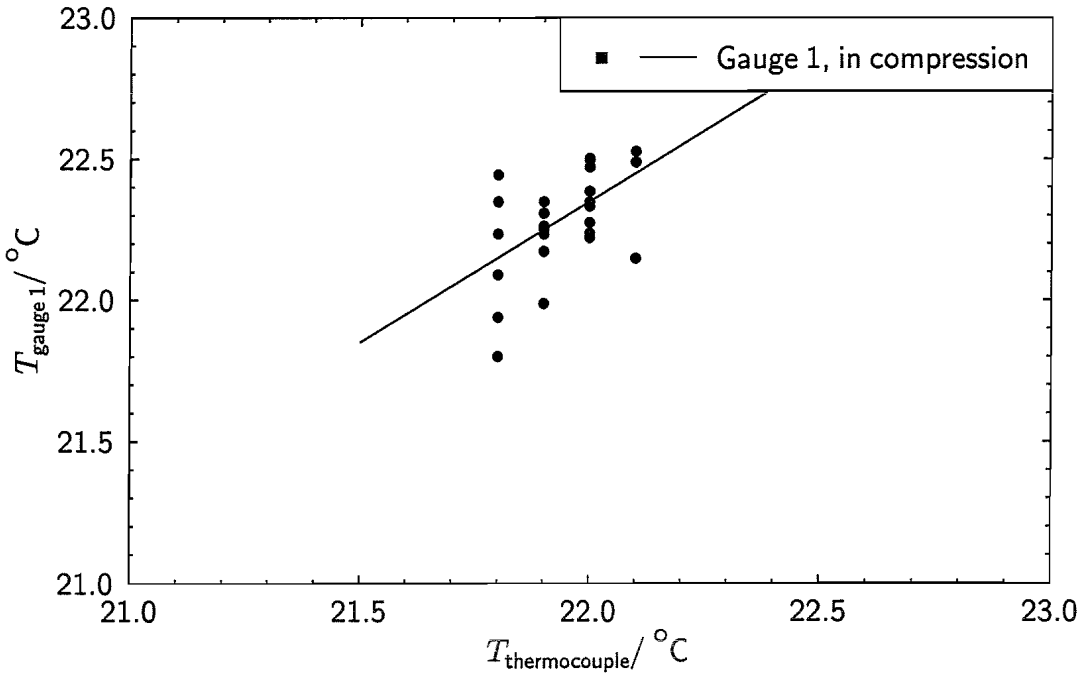

Figure 5.15. Temperature measured simultaneously with sensor 1. The calculated temperature from the laser sensor scatters between $\pm 0.1 - \pm 0.3$°C which is caused by the unstable operation of the laser and the resulting spread of the beat frequency measurement. The line fitted to the data has a slope of ≈ 1, indicating that the temperature drift has been recorded correctly by the laser sensor. The temperatures offset between the thermocouple and the DFB fibre laser sensor of ≈ 0.3°C could either be caused by a temperature gradient inside the concrete beam while the laboratory was heating up, or a temperature offset of the thermocouple.

According to the thermocouple measurements the temperature inside the concrete beam increased by 0.3°C over the test cycle. Figure 5.15 shows a comparison between the calculated temperature output from the DFB fibre laser sensor and the thermocouple. The calculated temperature from the laser sensor scatters between $\pm 0.1 - \pm 0.3$°C which is caused by the unstable operation of the laser and the resulting spread of the beat frequency measurement. The fitted line drawn through the data has a slope of ≈ 1, indicating that the temperature drift has been recorded correctly by the laser sensor. The fitted line exhibits a temperature difference between the temperatures measured by thermocouple and the laser sensor of ≈ 0.3°C which could either be caused by a temperature gradient inside the concrete beam while the laboratory was heating up, or a temperature offset between the thermocouple and the DFB fibre laser.

5.3 Annealing of DFB fibre lasers for high temperature sensor applications

5.3.1 Motivation

It is well known that the UV-induced refractive index modulation $\overline{\delta n}_{\text{eff}}$ of Bragg gratings decreases with time [94, 95]. From (3.18) and (3.24) it is evident that this ageing process leads to a, usually unwanted, decrease of κ and λ_B, respectively. Wavelength drift of the DFB fibre laser sensors — and indeed all wavelength based passive FBG sensors — should be prevented in order to maintain the sensor calibration over time. Similarly, DFB fibre laser sources used in telecommunication applications must remain within their assigned wavelength channel spacing. Furthermore, κ should remain constant over the lifetime of passive FBGs and DFB fibre lasers in order to maintain their peak reflectivity and output power, respectively, as a reduction of these parameters degrades the signal-to-noise ration (SNR) of optical sensors and telecommunication networks.

Annealing of FBGs and DFB fibre lasers at an elevated temperature T_{anneal} for several hours greatly accelerates this ageing process [94]. As long as the ambient temperature T_{op} after the annealing process remains sufficiently far below T_{anneal} any further decay of $\overline{\delta n}_{\text{eff}}$ will be insignificant over the grating lifetime [94, 95]. In this way wavelength and reflectivity drifts can be effectively eliminated. The required T_{anneal} depends on the expected maximum T_{op} and the lifetime of the grating. The lifetime of a telecommunication device is about 25 years and the maximum T_{op} is typically specified as 85 °C. For an embedded sensor a lifetime of several decades might be required with temperatures reaching several hundred °C. Therefore, a higher T_{anneal} is likely to be required for FBGs applied in sensor applications.

The following experiments quantify the reduction of λ_B and κ during the annealing process of two DFB fibre lasers and a passive reference FBG up to $T_{\text{anneal}} = 475\,°\text{C}$. From these measurements the required T_{anneal} and the initial κ_0 immediately after the grating writing process can be determined as a function of lifetime and maximum T_{op}. In addition laser operation at high temperatures will be demon-

strated and the response of a polarimetric DFB fibre laser temperature sensor will be measured up to 200 °C.

Another source of wavelength drift of FBGs arises from the common practice of loading Ge-doped fibres with deuterium prior to grating fabrication to increase their photosensitivity [96, 97]. After the formation of the FBG the deuterium is allowed to diffuse out of the fibre which leads to a reduction of the effective refractive index n_{eff} of the fibre and consequently λ_B [98]. The diffusivity increases with temperature allowing to accelerate the deuterium outdiffusion by keeping the passive FBG or DFB fibre laser at an elevated temperature for some time. The effect of deuterium outdiffusion on λ_B and κ will also be investigated experimentally.

5.3.2 Theory of deuterium outdiffusion

The deuterium diffusion out of the fibre is governed by the diffusion equation [99]

$$\frac{\partial C}{\partial t} = D(T)\nabla^2 C, \tag{5.17}$$

where C is the deuterium concentration and D is the temperature dependent diffusivity. If the deuterium concentration is assumed to be constant over the fibre cross-section the solution of the diffusion equation is of the form $C = C_0 \exp(-Dt/b)$, where C_0 is the initial deuterium concentration and b is the outer diameter of the fibre. From [98] n_{eff} and λ are expected to follow the same exponential decay as C.

5.3.3 Empirical model of grating decay

A simple but effective empirical model describing the formation of FBGs and their thermally induced decay is presented in [94]. These two processes and the associated change of $\overline{\delta n}_{\text{eff}}$ are attributed to trapping and releasing of electrons at defect sites within the glass matrix. During the FBG formation free electrons are generated by the UV radiation. These diffuse to the minima of the UV interference pattern where they are subsequently trapped by defects in the glass structure. This redistribution of electrons in the glass matrix is believed to give rise to the periodic index change [19] — although other processes may also be responsible [19].

According to this model the trapped electrons occupy a continuous distribution of energy levels ($E < 0$) below the conduction band ($E_c = 0$). The thermal decay of FBGs is the result of the depletion of these traps via thermal excitation of the trapped electrons. The higher T_{anneal} the faster the initial detrapping rate and the deeper — on the energy scale — the depletion of the traps, i.e. when the annealing process is terminated the traps are depleted down to an energy $E_d < 0$. As long as after the annealing process T_{op} of the FBG remains lower than the critical temperature required to thermally activate electrons trapped below E_d further depletion of the traps is negligible and $\overline{\delta n}_{\text{eff}}$ remains practically constant over the lifetime of the FBG. In accordance with this model the decay of $\overline{\delta n}_{\text{eff}}$ follows a power law function with a small exponent [94]:

$$\overline{\delta n}_{\text{eff}} = \frac{\overline{\delta n}_{\text{eff},0}}{1 + A(t/t_1)^{\alpha}}, \tag{5.18}$$

where $t_1 = 1\,\text{min}$ is introduced to keep A and α dimensionless, and $\overline{\delta n}_{\text{eff},0}$ is the initially induced refractive index change. According to (3.18) $\kappa \propto \overline{\delta n}_{\text{eff}}$ and the last equation can be written in terms of κ

$$\kappa = \frac{\kappa_0}{1 + A(t/t_1)^{\alpha}}. \tag{5.19}$$

Equations (3.25) or (3.23) can be used to calculate κ from the measured grating bandwidth or its maximum reflectivity. The parameter

$$A(T) = A_0 \exp(aT) \tag{5.20}$$

is a measure for the initial decay rate and

$$\alpha(T) = T/T_0 < 1 \tag{5.21}$$

determines the final value of $\overline{\delta n}_{\text{eff}}$ or κ which is reached asymptotically. The temperature dependence of A and α reflects the thermodynamic nature of the depletion of the electron traps. $A(T)$ and $\alpha(T)$ can be obtained by fitting (5.19) to the measured decay of κ at individual temperatures. The fibre specific constants A_0, a and T_0 which describe the thermally induced decay of a FBG as a function of T_{anneal} are best obtained by fitting (5.20) and (5.21) to $A(T)$ and $\alpha(T)$.

5.3.4 Experimental arrangement

A $L_{\mathrm{DFB}} = 50\,\mathrm{mm}$ long single polarisation DFB fibre laser with asymmetric phase shift position at $0.44L_{\mathrm{DFB}}$[14] and a passive $L_{\mathrm{FBG}} = 10\,\mathrm{mm}$ long reference Bragg grating were written into the same deuterium loaded $Er^{3+}:Yb^{3+}$ fibre used in the previous experiments. Both devices were written with an Ar^{+}-laser using the moving fibre-scanning beam technique [55].

The telecommunication fibre was spliced close to the DFB fibre laser to minimise losses in the $Er^{3+}:Yb^{3+}$ lead fibre and subsequently achieve a high output power. As resplicing would have been impossible without damaging the DFB fibre laser the risk of deuterium exploding in the electric arc of the splicer had to be eliminated. Therefore, the DFB fibre laser was kept at $\sim 100\,^{\circ}\mathrm{C}$ for twelve hours to allow the deuterium to outdiffuse before splicing. However, because optical losses were not important it was possible to measure the decay of the reference FBG at $100\,^{\circ}\mathrm{C}$ as the fibre ends a few centimetres away from the FBG could be heated locally prior to fusion splicing without damaging the FBG.

The experimental arrangement for measuring the decay of the DFB fibre laser and the reference FBG is shown in Figure 5.16. The reference FBG and the DFB fibre laser were placed inside a fan assisted oven which was operated up to 475°C with a temperature stability of $\sim 1\,^{\circ}\mathrm{C}$. In order to obtain clear reflectivity spectra both devices had to be prevented from moving in the air stream of the oven which would have introduced variable strain and consequently changes of λ_B. The reference FBG was, therefore, placed on the base plate of the oven and held in place with magnets. The DFB fibre laser was laid on an aluminium block and covered with a second, light, aluminium block to prevent any movements but also to ensure good thermal contact between the DFB fibre laser and these aluminium heat sinks under lasing conditions (see Section 4.4.2). Care was taken that neither the DFB fibre laser nor the reference FBG were subject to thermal expansion of the aluminium heat sinks or the oven base plate.

[14] The position of the phase shift is of only minor importance to DFB fibre laser sensors (see p. 50).

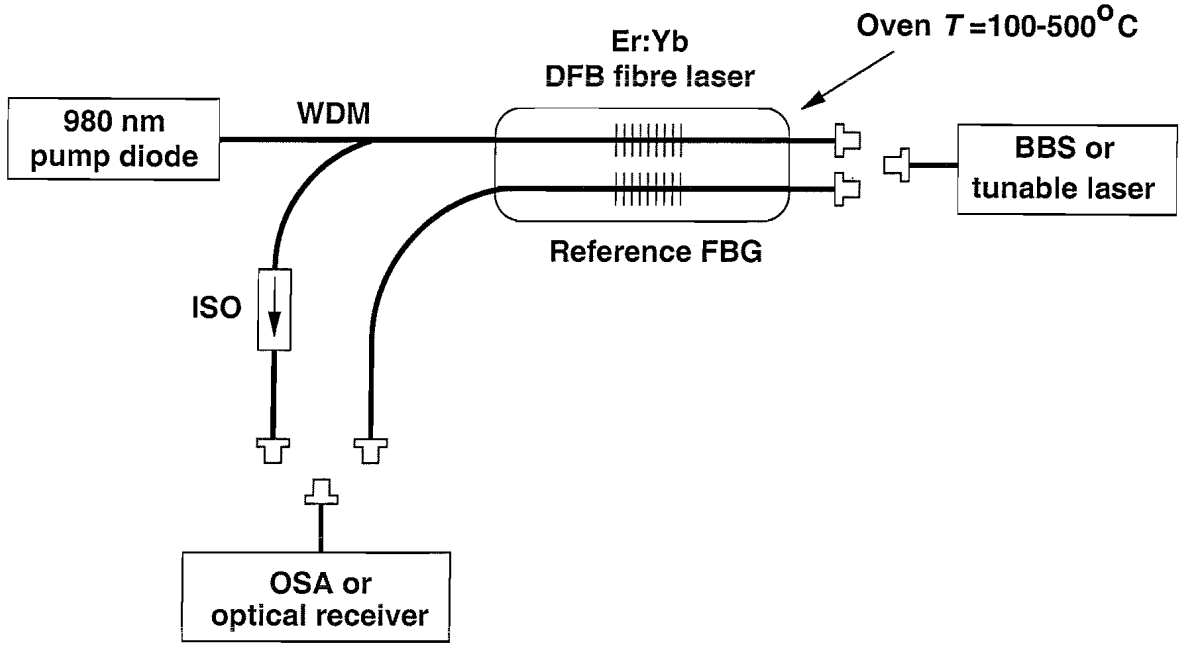

Figure 5.16. Experimental arrangement to monitor annealing of a DFB fibre laser and a reference FBG: WDM = wavelength division multiplexer, ISO = isolator, OSA = optical spectrum analyser, BBS = broad band source. The broad band source and optical spectrum analyser were used to obtain fast scans of the transmission spectra of the reference FBG and the DFB fibre laser. Higher resolution transmission spectra were obtained by scanning a tunable laser over the same wavelength range. Intensity modulation of the tunable laser in combination with the optical receiver increased sensitivity but also increased the scan time to eight minutes. The output power and wavelength of the DFB fibre laser could be monitored on the OSA.

A broad band amplified spontaneous emission (ASE) source was connected to either the reference FBG or the DFB fibre laser. During the annealing process their transmission spectra were recorded on an optical spectrum analyser[15] with a measurement resolution of 10 pm. At the beginning of each temperature setting the spectra were recorded every 3–5 min. As the annealing process slowed down the measurement intervals were increased up to 120 min. Each spectrum took about 15 s to record. For comparison some transmission spectra with a resolution of 2 pm were taken of both devices by scanning a tunable laser across the same wavelength range. However, the higher resolution could only be obtained at the expense of scan time,

[15] Advantest Q8384

which increased to 8 minutes. Therefore, tunable laser scans where only possible after the initial fast decay of the reference FBG and the DFB fibre laser.

Prior to annealing the minimum transmission through the reference FBG was $T_{\min} = 5.4\%(\hat{=}10\log(0.054) = 12.7\,\text{dB}$ transmission loss) at $\lambda_B = 1546.2\,\text{nm}$. From (3.23) one finds $\kappa = 214\,\text{m}^{-1}$ and a grating strength $\kappa L_{\text{FBG}} = 2.1$. The large κL_{DFB} of the DFB grating resulted in $T_{\min} \approx 0$ or $R_{\max} \approx 1$, both of which were difficult to measure accurately enough. However, the bandwidth of the DFB grating could be determined with sufficient accuracy to calculate κ. The bandwidth of the DFB grating prior to annealing was $\delta\lambda = 133\,\text{pm}$. Inserting this value into equations (3.25) and (3.18) yields $\kappa = 254\,\text{m}^{-1}$. The grating strength of the DFB grating then becomes $\kappa L_{\text{DFB}} = 12.7$ which is significantly stronger than the reference FBG. Therefore, for the weak reference FBG κ was calculated from the minimum transmission, while for the strong DFB grating $\delta\lambda$ was used throughout the entire experiment.

In order to verify that the DFB fibre laser could operate at elevated oven temperatures it was pumped with a 975 nm grating stabilised pump diode[16]. The maximum launched pump power was 79 mW. The backward output power and the operating wavelength of the laser were measured on the optical spectrum analyser.

Once the DFB fibre laser and the reference FBG were in place inside the oven any further fibre alignment was avoided to prevent strain induced wavelength changes and, more importantly, alterations of the carefully adjusted heat sinks of the DFB fibre laser. Movement of the latter could easily cause output power changes. The deuterium outdiffusion and annealing process were then carried out in one continuous experiment.

5.3.5 Wavelength shift as a result of deuterium outdiffusion

The reference FBG was kept at $-35\,^{\circ}\text{C}$ for several days before this outdiffusion experiment was carried out. The low temperature ensured that outdiffusion of deuterium was minimised over this period. The oven temperature was then first set

[16]SDLO-2564-150.

to 100 °C. From data presented in [95] it was assumed that κ would only decrease by a minimal amount at this temperature, but the reduction of λ_B as a result of deuterium outdiffusion would be significant [98]. Figure 5.17 shows λ_B and κ of the reference grating as a function of time. The centre wavelength λ_B decayed exponentially with a time constant of 250 min to a final value which was $\approx$ 0.4 nm lower than its initial value. After twelve hours at 100 °C the wavelength was still 22 pm larger than the final value, while after 24 hours this difference had reduced to 1.3 pm. The first value corresponds to a frequency difference of 2.8 GHz from the final value which is acceptable in a telecommunication network with 50 GHz channel spacing. Using the strain and temperature responses of the DFB fibre laser sensor from Section 5.1.4 22 pm correspond to a strain of 19 $\mu\epsilon$, or a temperature difference of 2.8 °C which would introduce a significant systematic measurement error in

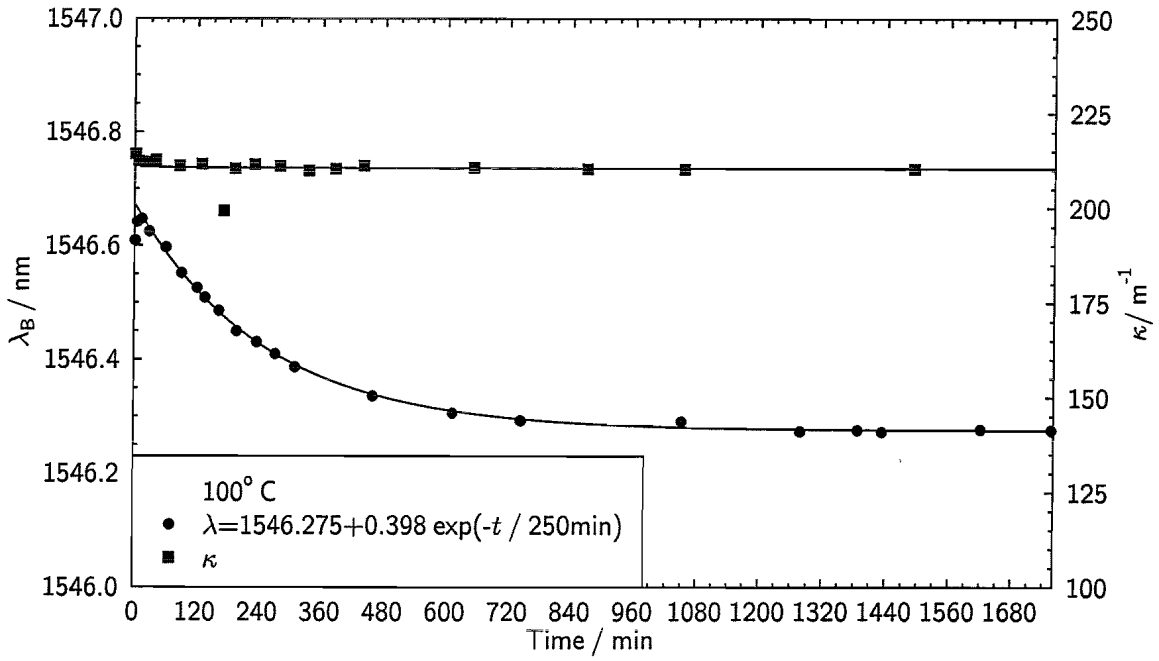

Figure 5.17. Deuterium outdiffusion from the reference FBG at 100 °C. The centre wavelength λ_B decayed exponentially with time while the deuterium was diffusing out of the fibre. After twelve hours the wavelength was within 22 pm ($\hat{=}$2.8 GHz) of its final value. While this wavelength difference is acceptable for telecommunication applications, it would introduce a significant systematic error into a strain or temperature sensor. Consequently, for sensor applications the outdiffusion time has to be extended to 24 hours. The grating coupling coefficient κ decreased by only 2% which reduced the grating reflectivity insignificantly by 0.4%.

sensor applications. Therefore, the outdiffusion time for this particular fibre, initial deuterium concentration and temperature should be 24 hours in order to meet the more stringent sensor specifications.

During the deuterium outdiffusion at 100 °C κ decreased by only 2%. This small decrease corresponds to an insignificant reduction of the grating reflectivity of 0.4%.

The lasing wavelength shift and the reduction of κ of the DFB fibre laser during deuterium outdiffusion was not monitored because the necessary lead fibres could only be spliced to it after all deuterium had diffused out of the fibre.

5.3.6 Annealing up to 475 °C

A selection of characteristic transmission spectra of the reference FBG and the DFB fibre laser during the annealing process is shown in Figures 5.18 and 5.19. The temperature induced wavelength shift was subtracted from the spectra in order to overlay them in the Figures. The transmission spectra of the reference FBG were

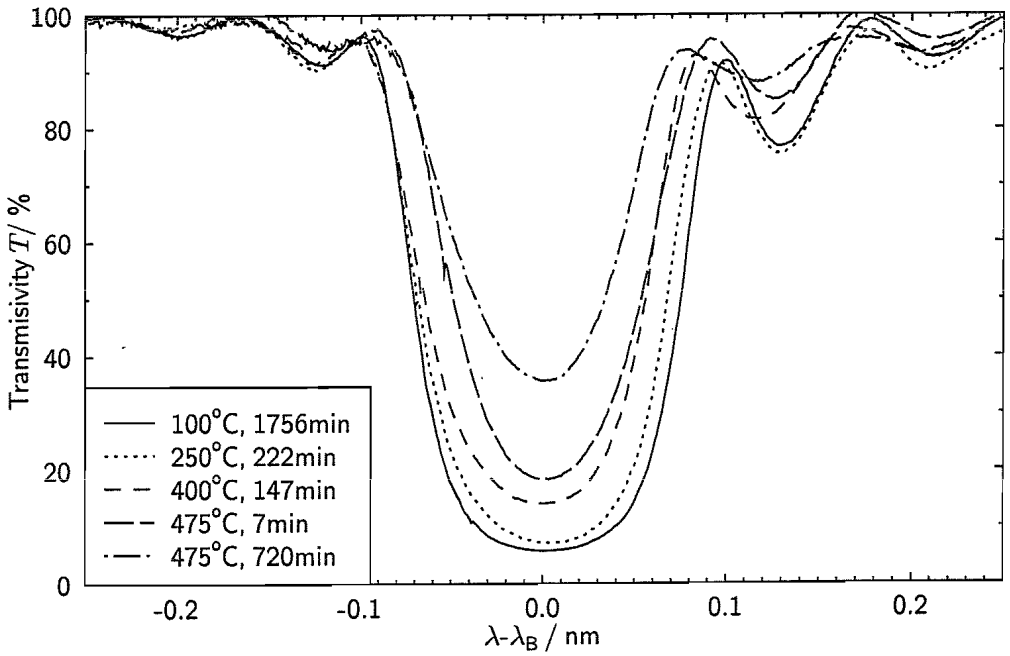

Figure 5.18. Superposition of characteristic reference FBG transmission spectra at various stages during the annealing process. The shown spectra were recorded at the end of each temperature setting. Temperature induced wavelength shifts are subtracted from the grating spectra. The transmissivity increased as the UV-induced refractive index modulation of the grating becomes smaller.

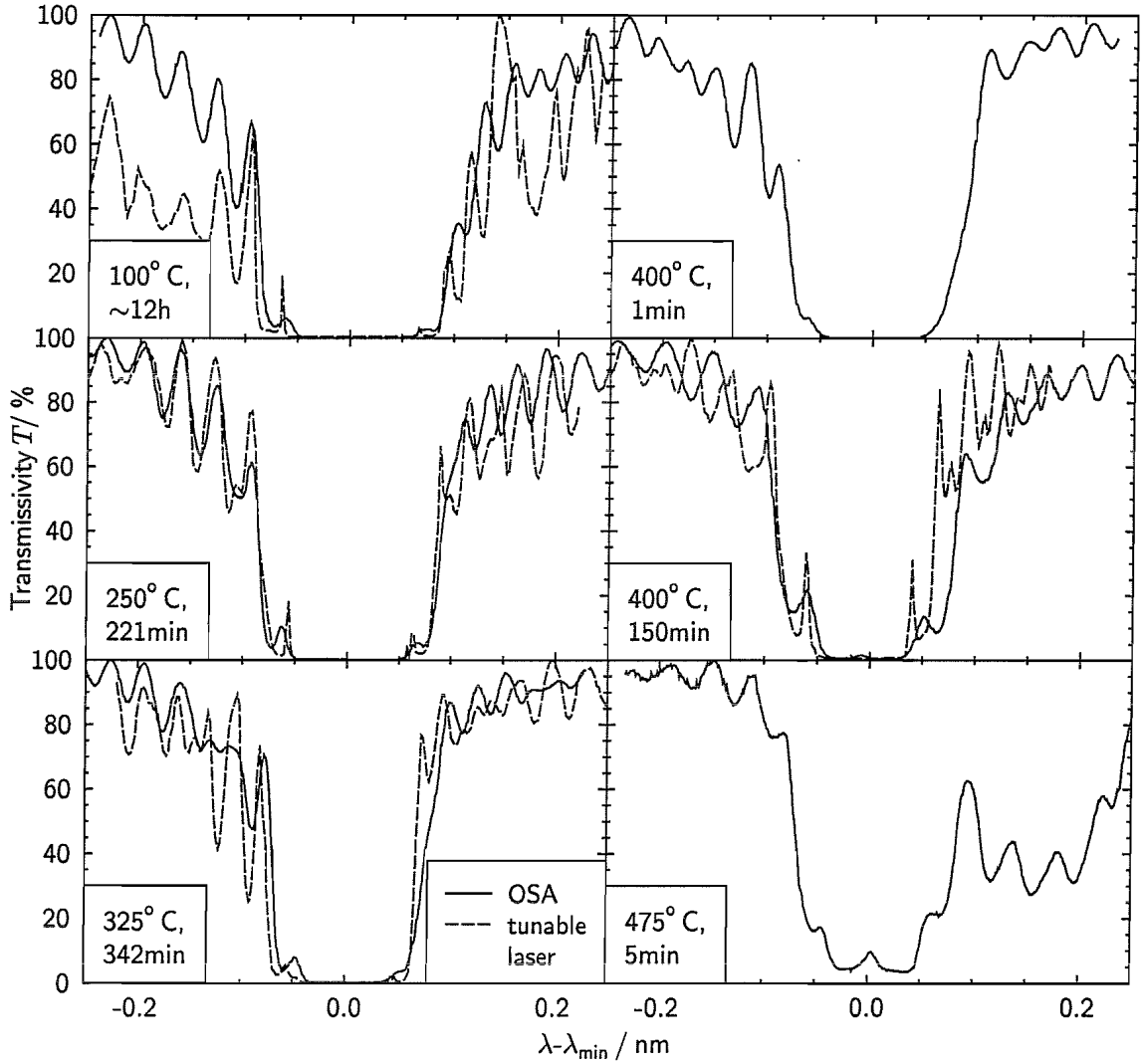

Figure 5.19. Characteristic transmission spectra of the DFB fibre laser at different times and temperatures during the annealing process. Spectra obtained by the two different methods described in Section 5.3.4 are in good agreement. The grating bandwidth decreases as the grating decays. After 150 min at 400 °C the transmission dip at the centre of the stopband becomes just visible. The spectral features at the long wavelength side at 475 °C are a result of grating chirp caused by the movement of the aluminium cover block.

in close agreement with simulated spectra. The minima and maxima were clearly visible and the minimum transmissivity could be easily measured. As the annealing progresses the decay of the reference FBG could clearly be observed in form of the increase of $T_{\min}$ (3.23) and decrease of FBG bandwidth (3.25).

The spectral features of the DFB grating were less clearly visible which made the bandwidth measurement less accurate. Because of the great strength κL_{DFB} of the DFB grating, its minimum transmissivity remained close to 0 %. The extremely narrow transmission peak at the centre of the stop band could not be resolved by the spectrum analyser. After 150 min annealing at 400 °C the transmission peak became just visible as κL_{DFB} decreased sufficiently and the peak widened. At 475 °C the grating coupling coefficient decayed significantly which led to an increase of the minimum transmissivity and a further widening of the transmission peak at the centre. The actual width of the peak, however, was narrower than it appeared in the spectrum. The latter was limited by the spectral resolution of the optical spectrum analyser. The spectral features at the long wavelength side at 475 °C were a result of grating chirp probably caused by the movement of the aluminium cover block due to vibrations of the oven.

Figure 5.20 shows the decay of the maximum reflectivity $R_{\max} = 1 - T_{\min}$ and the calculated κ of the reference FBG with time and temperature during the annealing process. A fit of equation (5.19) to the calculated κ is shown as solid lines in the Figure. While for this grating the empirical model is in excellent agreement with the experimental results there is some disagreement in the literature whether or not this model can actually be applied to gratings written into hydrogen loaded fibre [100]. The fit parameters of the power law function (5.19) are shown in Figure 5.21 together with fits according to equations (5.20) and (5.21), respectively. Equation (5.20) fits the calculated A very well, whereas α deviates significantly from the fitted line. The calculated values of A and α as well as the quality of the fits are in agreement with the results presented in [94].

Figure 5.22 shows the narrowing of the grating bandwidth $\delta\lambda$ of the DFB fibre laser and the decrease of the calculated κ during the annealing process. The grating

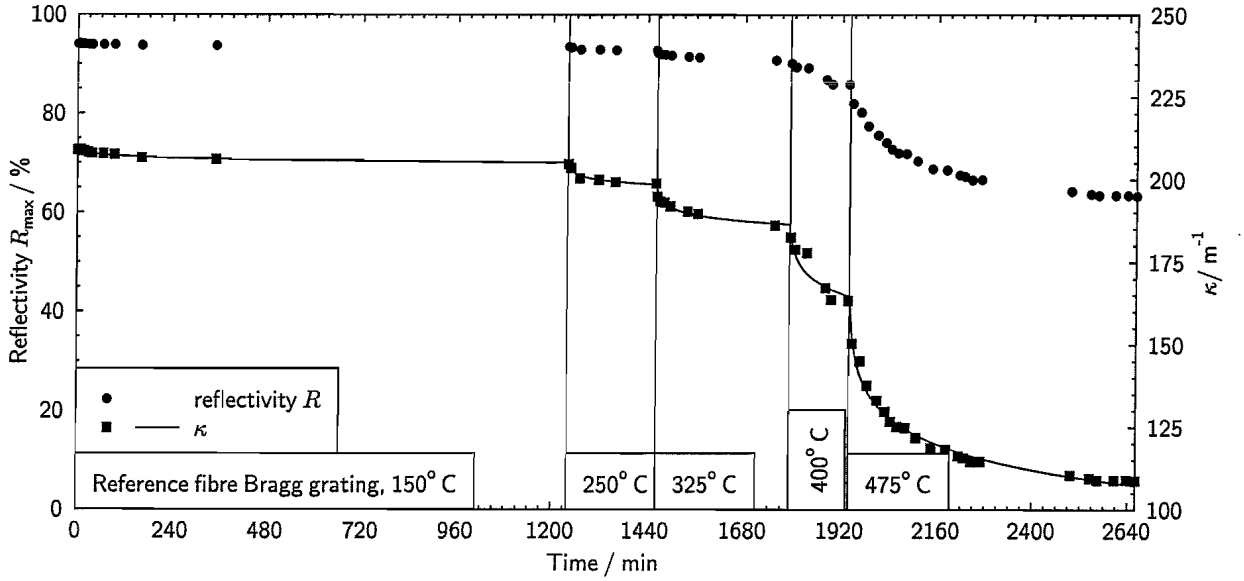

Figure 5.20. Maximum reflectivity $R_{\max}$ of the reference FBG as a function of time and temperature during the annealing process. The coupling coefficient κ was calculated using equation (3.23). The lines represent a fit according to equation (5.19), the empirical power law model.

bandwidth was measured between the first peaks of the transmission spectrum, which are equivalent to the first zeros in the corresponding reflection spectrum.

It was expected that the decay parameters A_0, a and T_0 would be the same for the DFB fibre laser and the reference FBG because both devices were written into the same fibre under the same conditions. The dotted curves in Figure 5.22 show the expected decay of the DFB fibre laser grating using the decay parameters of the reference FBG. It can be seen that these parameters underestimate the decay of κ in this case. Separate power law curves, shown as solid lines, were fitted to the experimental data. Because of the lower accuracy of the bandwidth measurement some measured data points clearly lie outside the expected decay curves and are omitted from the fitting process. The fit parameters A and α are shown in Figure 5.23. They scatter significantly as a result of the bandwidth measurement errors. The solid straight lines represent a least square fit but should not be regarded as the true functional relationships. The fit obtained from the reference FBG are also shown for comparison. The reason for the unexpected difference between the decay parameters of the reference FBG and the DFB grating is unknown to date and

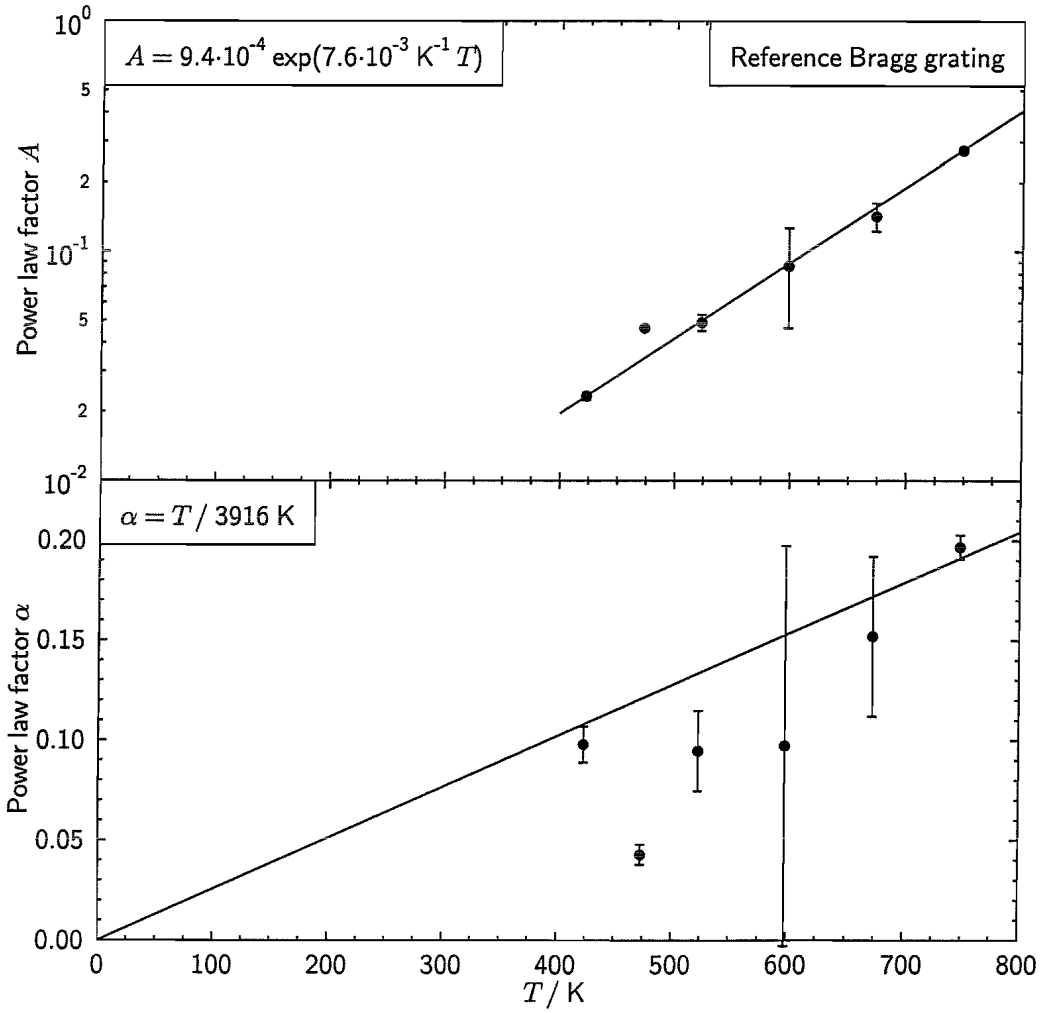

Figure 5.21. Power law factors A and α as function of temperature and fit according to (5.20) and (5.21), respectively. Note, it follows from (5.21) that $\alpha(T = 0\,\mathrm{K}) = 0$.

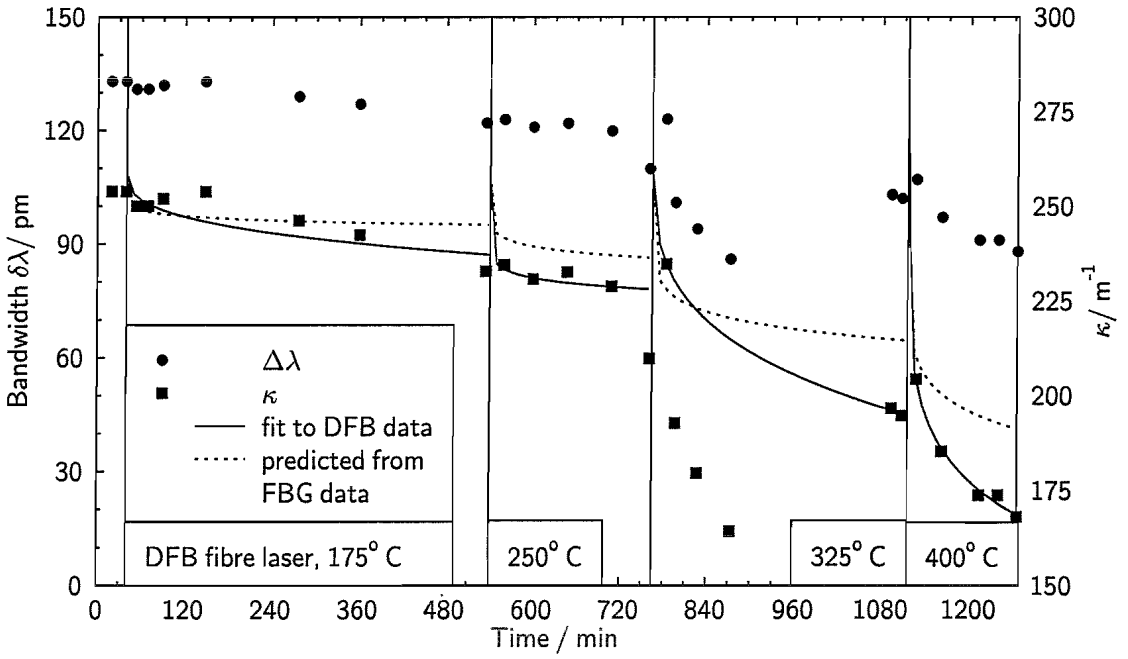

Figure 5.22. Bandwidth of the DFB laser grating as a function of time and temperature during the annealing process.The coupling coefficient κ was calculated using equations (3.18) and (3.25). Also shown is the predicted decay of κ using the annealing parameters of the reference FBG.

further experiments with a larger number of DFB fibre lasers and reference FBGs should be carried out to improve the statistical significance of the data.

Because the rise of the oven temperature from one setting to the next takes approximately 15 min the initial rapid decay of κ does not take place at a constant temperature. The data shown in the Figures 5.20 and 5.22 is taken after the oven temperature reached its target value so the early part of the rapid decay was not measured. This procedure was chosen to allow the DFB fibre laser to remain undisturbed inside the oven avoiding parasitic influences on its output power from the way it was mounted. The reference FBG was also kept inside the oven permanently to experience the same thermal history as the DFB fibre laser. The large error bars at $T = 598\,\mathrm{K} = 325°\mathrm{C}$ in Figure 5.21 arose from the lack of accurate data during the initial fast decay at rising temperature. At low temperatures the initial decay is relatively slow and therefore only slightly affected by the time lack of the oven. At high temperatures, $\geq 400°\mathrm{C}$, the difference between the initial and final κ is large so that the lack of data during the very first minutes of the rapid decay again

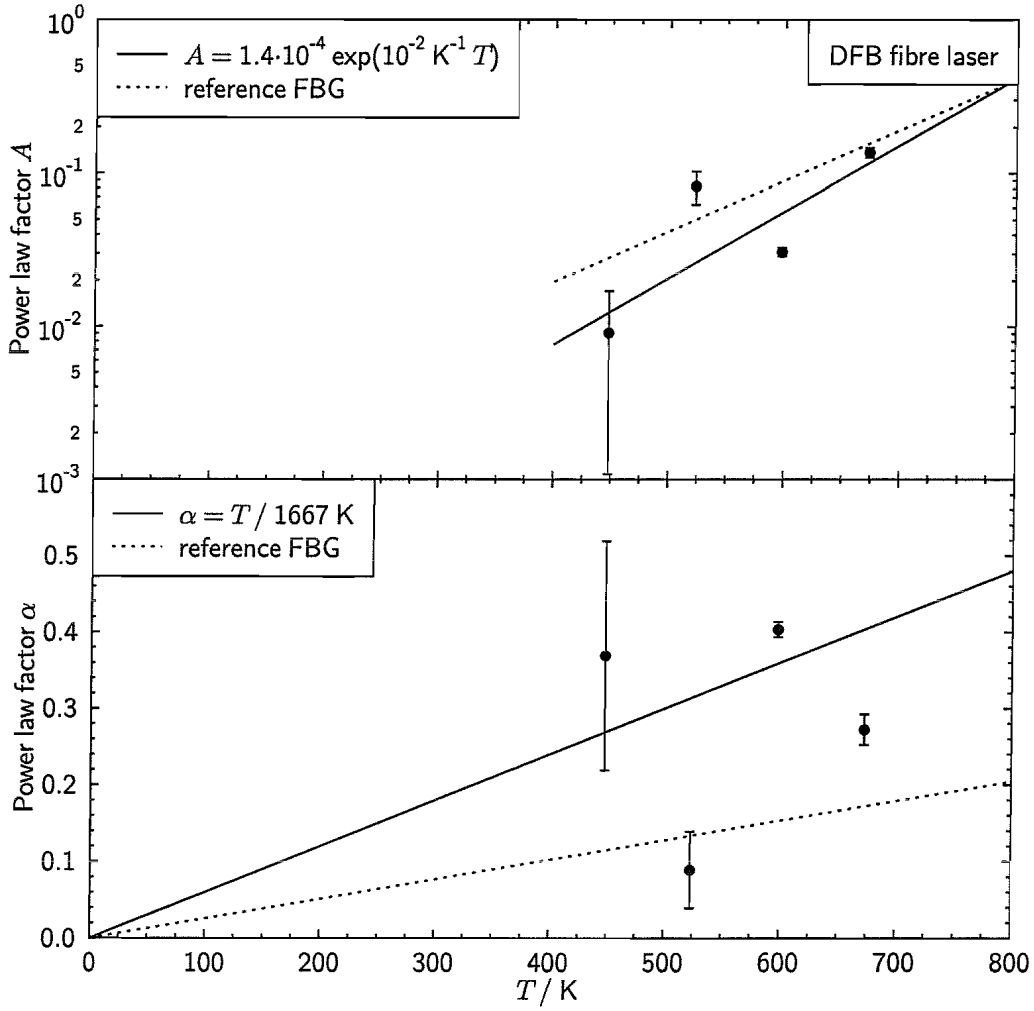

Figure 5.23. Power law factors A and α as function of temperature for the DFB fibre laser. Because of the larger measurement errors the lines which were fitted according to (5.20) and (5.21) should be treated with caution.

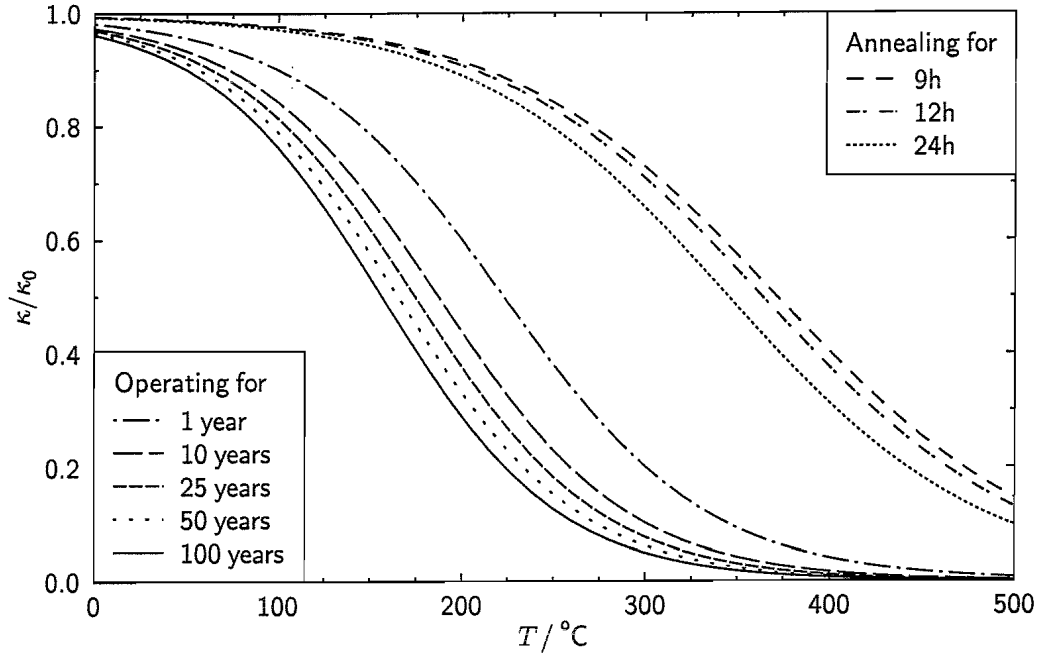

Figure 5.24. Relative grating decay κ/κ_0 as a function of temperature for different points in time. Example: after 25 years at $T = 85\,^{\circ}\mathrm{C}$ κ would have reduced to 87 % of its initial value κ_0. The same decay can be achieved by annealing the grating at $T_{\mathrm{anneal}} = 214\,^{\circ}\mathrm{C}$ for 24 hours. The annealing time can be reduced to 12 hours if T_{anneal} is increased to $230\,^{\circ}\mathrm{C}$.

plays only a minor role. The error bars are, therefore, largest in the intermediate temperature regime.

From the data presented in Figures 5.21 or 5.23, which fully describes the grating decay with time as a function of temperature, one can calculate the initially required κ_0 in order to obtain the optimum or specified κ at the end of the annealing process. As discussed in Section 5.3.1 T_{anneal} depends on the grating application. Furthermore, the required annealing time is a function of T_{anneal} which allows these two parameters to be adjusted to speed up the annealing process or to use lower temperatures at the expense of a longer annealing time. Figure 5.24 shows the relative decay κ/κ_0 as a function of ambient temperature after different points of time. The left set of curves in the Figure depicts the relative decay while the grating is operational, i.e. over many years. The right set of curves shows by how much a grating can be annealed during a few hours at a given temperature. All curves are calculated using the data presented in Figure 5.23, i.e. for the DFB fibre laser which is of interest here. If the FBG or DFB fibre laser will be used in a telecommunication

application with T_{op} not exceeding 85 °C over 25 years then the κ will decay to 87 % of κ_0. The same decay can be induced by annealing the grating at $T_{anneal} = 214$ °C for 24 hours. The annealing time can be reduced to 12 hours if T_{anneal} is increased to 230 °C. The Figure shows that the grating decay becomes significant over long timescales if T_{op} is increased above $\sim 150 - 200$ °C. Therefore, κ_0 has to be about three to four times larger than the optimum value for $T_{op} \sim 200$ °C and up to ten times larger for $T_{op} \sim 300$ °C. In the latter case the grating has to be annealed at $T_{anneal} \sim 450$ °C for 24 hours.

5.3.7 DFB fibre laser operating up to 400 °C

It is well known that in order to achieve low threshold and high output power from a DFB fibre laser the product κL has to be carefully chosen [57]. As κ decreased during the annealing process it was expected that the threshold and the output power of the DFB fibre laser would vary. DFB fibre lasers employed in telecommunication applications are not expected to experience operating temperature in excess of 85 °C.

From the experimental data presented in the last Section κ would decrease by 13 % over 25 years which is expected to alter the threshold and output power of the DFB fibre laser. The variations of the threshold and output power where measured during the annealing process up to $T = 475$ °C described in the previous Section. The output power of the DFB fibre laser as a function of pump power at several points in time during the annealing process is shown in Figure 5.25. The initial $\kappa_0 = 250\,\mathrm{m}^{-1}$ was higher than the optimum value. Therefore, the slope efficiency first increased as the DFB fibre laser was annealed up to 325 °C. The lasing threshold remained constant. When the annealing temperature was raised to 400 °C a small drop of the slope efficiency was observed during the first two minutes. Then within the next ~ 40 min the slope efficiency dropped dramatically and the maximum laser output power decreased to less than 0.1 mW, two orders of magnitude less than the maximum power reached at 325 °C. The drop of output power can be attributed to the further decrease of κ below its optimum value. The theoretical dependence of the output power on κ will be described in the next paragraph.

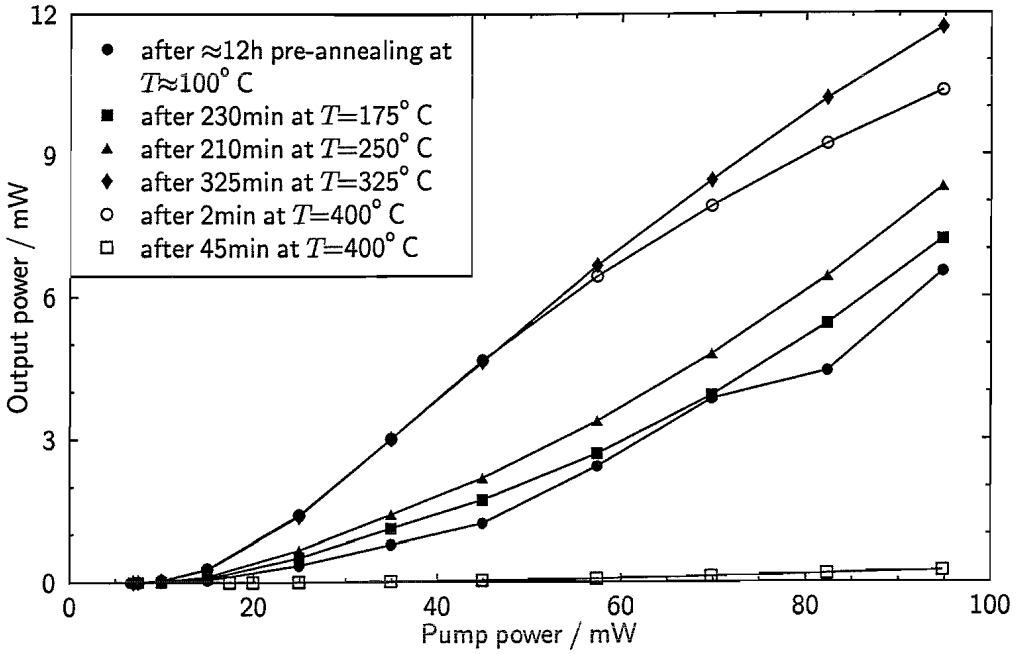

Figure 5.25. Output power of the DFB fibre laser as a function of launched pump power at 975 nm at different times during the annealing process. The DFB fibre laser was $L = 50\,\text{mm}$ long and its phase shift was positioned at $0.44L$. The initial κ was $\approx 250\,\text{m}^{-1}$ which was higher than the optimum value. As a result of the decreasing κ the slope efficiency first increased up to $T = 325\,°\text{C}$ and dropped significantly at $T = 400\,°\text{C}$ (see also Figure 5.26). The laser threshold remained almost constant.

Although the output power predicted by the model described in Chapter 3 is higher than the measured output power of a DFB fibre laser when pumped near 980 nm its dependence on κ can be examined qualitatively. In Figure 5.26 the predicted output power at 80 mW of pump power at 975 nm is shown as a function of κ. The calculated output power was normalised to its maximum value at $\kappa = 212\,\text{m}^{-1}$, which for this 50 mm long DFB fibre laser corresponds to $\kappa L = 10.6$. The experimental result shows a similar behaviour, with the output power at its maximum for $\kappa = 197\,\text{m}^{-1}$ which is in good agreement with the calculated value. However, the measured output power dropped far more rapidly than expected as κ decreased. One possible reason is that the laser has moved slightly inside the oven between the two aluminium heat sinks as a result of vibrations of the oven. This small movement could have caused chirp along the DFB fibre laser grating and consequently reducing the feedback inside the laser. Excessive chirp at 475 °C can be observed in Figure 5.19. However, visual inspection did not reveal any

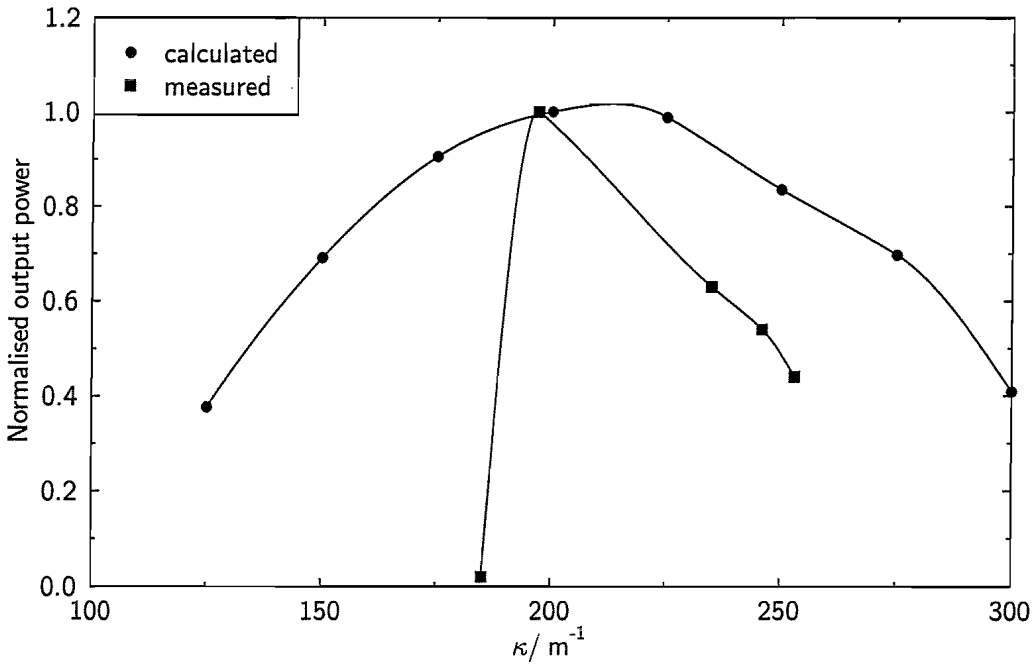

Figure 5.26. Calculated and measured output power at $P_{\text{pump}} = 80\,\text{mW}$ as a function of κ for a $L = 50\,\text{mm}$ long DFB fibre laser with the π phase shift positioned at $0.44L$. The output power has been normalised to its maximum value. The unexpected decrease of the measured output power might have been caused by a small movement of the carefully aligned DFB fibre laser between the aluminium heat sinks. This could have induced grating chirp, as observed at 475 °C in Figure 5.19, and consequently reduced the feedback.

obvious movement of the DFB fibre laser and careful realignment was impossible at $T = 400\,°\text{C}$.

5.3.8 High temperature polarimetric DFB fibre laser sensor

A dual polarisation DFB fibre laser with an initial $\kappa \approx 230\,\text{m}^{-1}$, $L = 50\,\text{mm}$ and asymmetric phase shift position was annealed at $T = 350\,°\text{C}$ for just over nine hours. From Figure 5.24 one finds that this allows the DFB fibre laser sensor to operate at 200 °C, 170 °C or 140 °C over 1, 10 or 100 years, respectively. As expected from Figure 5.25, after the annealing process the DFB fibre laser was operating with a reduced output power of 1.3 mW for 85 mW launched pump power at 975 nm. This is not the desired pump wavelength for a DFB fibre laser sensor but no 1480 nm pump diode was available at that time. The laser was placed inside the fan assisted oven and held down onto the base plate of the oven by a heavy metal weight several

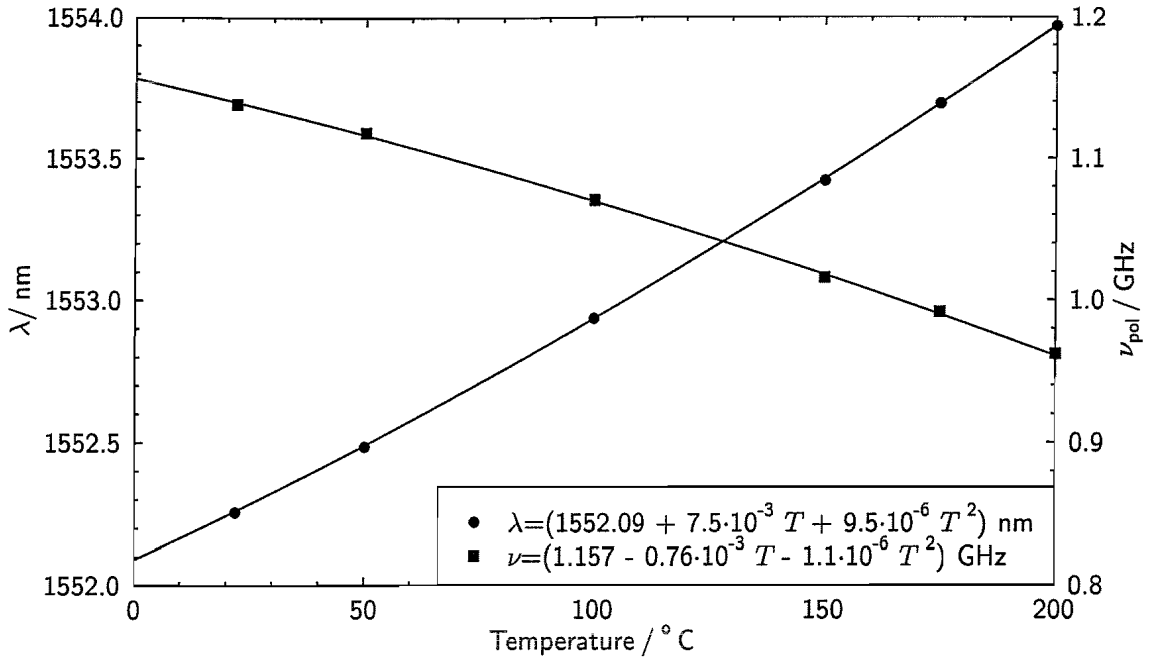

Figure 5.27. Wavelength and polarisation beat frequency as a function of temperature for a DFB fibre laser previously annealed at 350 °C. Wavelength and beat frequency response show a small quadratic term due to the non-linear expansion coefficient of silica. The linear terms, however, are in agreement with the sensor presented in Sections 5.1 and 5.2. Self heating as a result of pumping at 975 nm prevented the sensor to operate above 200 °C.

centimetres away from the laser itself. The other side was held down by a lightweight metal rod which allowed the laser to expand freely as the temperature was increased. The lasing wavelength was measured on a wavemeter[17] with an accuracy of 1 pm. The polarisation beat frequency signal was mixed down from $\sim$ 1 GHz to $\sim$ 0.3 GHz so it could be measured on a 400 MHz RF spectrum analyser[18]. Figure 5.27 shows the wavelength and polarisation beat frequency as a function of oven temperature. The solid lines represent quadratic fits to the measured data.

The linear terms of the thermal response are in good agreement with the calibration of the sensor described in Sections 5.1 and 5.2. A small quadratic dependence was observed which is in agreement with previous reports [20]. This quadratic response becomes noticeable when the sensor is used over large temperature ranges. It remained undetected within the small temperature range over which the sensors

[17]Burleigh WA-1500

[18]Marconi 2380

were calibrated in Sections 5.1.4 and 5.2.1. The reason for the non-linear response lies in the fact that the expansion coefficient of silica varies with temperature. From an analysis of the residuals the sensor accuracy was found to be ±2.1 °C. This accuracy was limited by errors of the beat frequency measurements which were caused by self heating of the sensor and forced convection in the air flow in the oven. Using only the wavelength measurement, which was more accurate due to the longer internal averaging time of the wavemeter, yielded an accuracy of ±0.4 °C. Self heating caused instable laser operation above $T = 200\,°C$. Changing to a 1480 nm pump, which minimises self heating, should make it possible to operate this polarimetric DFB fibre laser temperature sensor at higher temperatures if its annealing temperature is increased accordingly. The reduced self heating should also limit beat frequency fluctuations and therefore increase the measurement accuracy.

5.4 Conclusion

In conclusion, the first birefringent DFB fibre laser sensor capable of measuring strain and temperature simultaneously has been demonstrated. The achieved accuracy was ±3 $\mu\epsilon$ and ±0.04°C, respectively, limited by the equipment used to calibrate the sensor. A higher sensor accuracy should therefore be obtainable by improving the accuracy of the calibration. It should be noted that the achieved strain measurement accuracy is sufficient for most applications. The temperature measurement accuracy is about a factor of 2–10 better than what is usually required. No cross-sensitive strain and temperature responses were observed, the sensor responded linearly independent to both measurands which makes this sensor extremely useful for structural health monitoring applications where strain and temperature have to measured simultaneously.

It was verified that this sensor can operate at temperatures up to 400 °C. However, in order to obtain maximum output power the initial coupling coefficient κ_0 has to be high enough such that it decreases to the optimum value while the DFB fibre laser is annealed. From the experimental and theoretical data the optimum value for a 50 mm long DFB fibre laser written into the particular $Er^{3+}:Yb^{3+}$ fibre

is $\kappa \approx 200\,\mathrm{m}^{-1}$. While κ will only decrease by 13 % over 25 years at 85 °C, which are typical telecommunication specifications, at temperatures of several hundred °C κ might reduce to 1/10 or less of its original value, depending on the temperature and lifetime of the FBG. Therefore κ_0 and T_{anneal} have to be chosen sufficiently high.

An appropriately annealed DFB fibre laser sensor was calibrated between 20 – 200 °C. Higher temperatures should be possible if self-heating of the laser can be reduced by using a 1480 nm pump diode instead of the available 980 nm diode. This sensor calibration revealed a small quadratic temperature response because of the temperature dependent thermal expansion coefficient of silica.

For the first time DFB fibre laser strain and temperature sensors have been embedded in concrete. Three sensors were protected by miniature tubes of $\sim$ 60 mm length and 3 – 5 mm diameter made from aluminium, steel and epoxy resin, respectively. This protection was one of the smallest used so far for fibre optic sensors embedded in concrete. It allowed the DFB fibre laser sensors to be embedded in the confined space of a small test specimen typical for civil engineering laboratory experiments. As expected the temperature response of the sensors had to be recalibrated after the embedment in order to take the free thermal expansion of the concrete into account. Damage caused to one sensor and debonding of another require improvements to the protection system to increase general robustness and reliability before these sensors can be used in real civil engineering applications. A possible improvement is the use of 3 mm jacketed fibre instead of fibre protected by simple PTFE tubing. Beside increasing the ruggedness of the lead fibre this would also minimise the diameter mismatch between the protective tube around the DFB fibre laser and the lead fibre, strengthening the mechanical joint at this point. The exact reason for the debonding of one DFB fibre laser sensor from its protective tube remains unknown. It might be prevented by choosing a more appropriate glue to stop the fibre from slipping inside the package. However, sensor 1 (epoxy resin protection) was successful in providing simultaneous strain and temperature readings during the entire concrete testing phase. Finally, it should also be noted that one of the two resistive strain gauges failed during the test, returning a signal too noisy to provide useful strain readings.

This DFB fibre laser sensor is expected to be very versatile allowing it to be employed in a variety of civil engineering, marine and aerospace structures from small laboratory test specimens to real size structures. It should also be possible to embed these sensors in carbon fibre composites used in the above engineering topics. In this case local perturbations of the DFB grating by the host matrix have to be minimised in order to prevent grating chirp and feedback reductions.

In order to reduce cost of the interrogation system the wavemeter and RF spectrum analyser can be substituted by purpose designed devices, such as frequency counters and optical filters or interferometers. This would also allow to take full advantage of the available measurement resolution of the DFB fibre laser sensors.

As external perturbations of the lead fibre will change the polarisation state at the input of the PBS active polarisation control or the use of polarisation maintaining fibre should be considered if measurements with the above stated accuracy need to be achieved. More importantly pump power fluctuations, caused e.g. by bends in the lead fibre, have to be kept below 2.8 mW (for a 1480 nm pump) in order to avoid loss of accuracy due to self heating of the sensor.

6 Dual longitudinal mode polarimetric DFB fibre laser sensor operating entirely in the RF domain

The main disadvantage of the single longitudinal mode DFB fibre laser sensor presented in Chapter 5 was the need for two separate interrogation systems for wavelength and beat frequency measurements. In order to reduce system complexity and cost a DFB fibre laser sensor which operates entirely in either the wavelength or the RF domain would be highly desirable. Operating in the RF rather than in the optical wavelength domain would have the advantage that the laser output can be immediately processed electronically without the need for cumbersome wavelength-to-electrical signal conversion, such as optical filters or interferometers. A low birefringent DFB fibre laser operating in two longitudinal modes which split into two polarisation modes respectively could provide the necessary RF beat frequencies between longitudinal and polarisation modes to allow simultaneous strain and temperature measurements. While the low natural birefringence of the single longitudinal mode DFB fibre laser sensor ensured that its polarisation beat frequency lay within the RF domain the longitudinal mode spacing of a dual longitudinal mode DFB fibre laser has to be chosen close enough such that their optical frequency difference lies within the RF domain.

The use of this type of laser is not limited to sensor applications. It could potentially be employed in telecommunication applications [102] too, where it could serve as a dual- or even multi-wavelengths source or as a RF frequency generator [103, 104].

In this Chapter the first dual longitudinal mode DFB fibre laser sensor operating entirely in the RF domain will be presented in greater detail.

6.1 Moiré DFB fibre lasers

A Moiré DFB fibre laser is essentially a superposition of two individual DFB fibre lasers. Writing the second DFB grating on top of an existing one would increase the effective refractive index n_{eff} and reduce the fringe visibility v of the index modulation (see 3.17) [105]. Consequently λ_B of the first DFB fibre laser grating would increase and its κ would decrease, altering the laser threshold and slope efficiency. It is therefore advantageous to write the Moiré structure in one step. The scanning phase-mask moving-fibre technique [55] allows the fabrication of such high quality gratings with accurately controlled characteristics [101]. The Moiré structure of this dual longitudinal mode DFB fibre laser was generated by writing a series of sinusoidally apodised grating sections of length p and introducing a π phase shift between them.[1] In this way the slowly varying envelope, corresponding to the difference frequency of the two superimposed gratings, is generated. The periodicity p of the envelope or superstructure is given by [102]

$$p = \lambda^2/(2n_{\text{eff}}\Delta\lambda), \tag{6.1}$$

where $\Delta\lambda$ is the desired wavelength separation between the two modes, n_{eff} is the refractive index and λ is the mean wavelength. In order to obtain the necessary net π phase shift in this superstructure DFB grating, the phase shift was omitted between the pair of adjacent grating sections either side of the position of the DFB π phase shift [102].

[1]The laser was fabricated by M. Ibsen, ORC, University of Southampton.

Figure 6.1 shows the calculated reflection spectra of dual wavelength Moiré DFB laser for different design mode spacings $\Delta\lambda$. Because for these calculations the DFB fibre laser always consisted of an integer number of superstructure periods its length varied by ± 3.5 mm around a mean of 61.2 mm. Two separate DFB reflection peaks, each with the characteristic narrow reflection dip, were visible. As the wavelength separation between the two reflection peaks was reduced, the

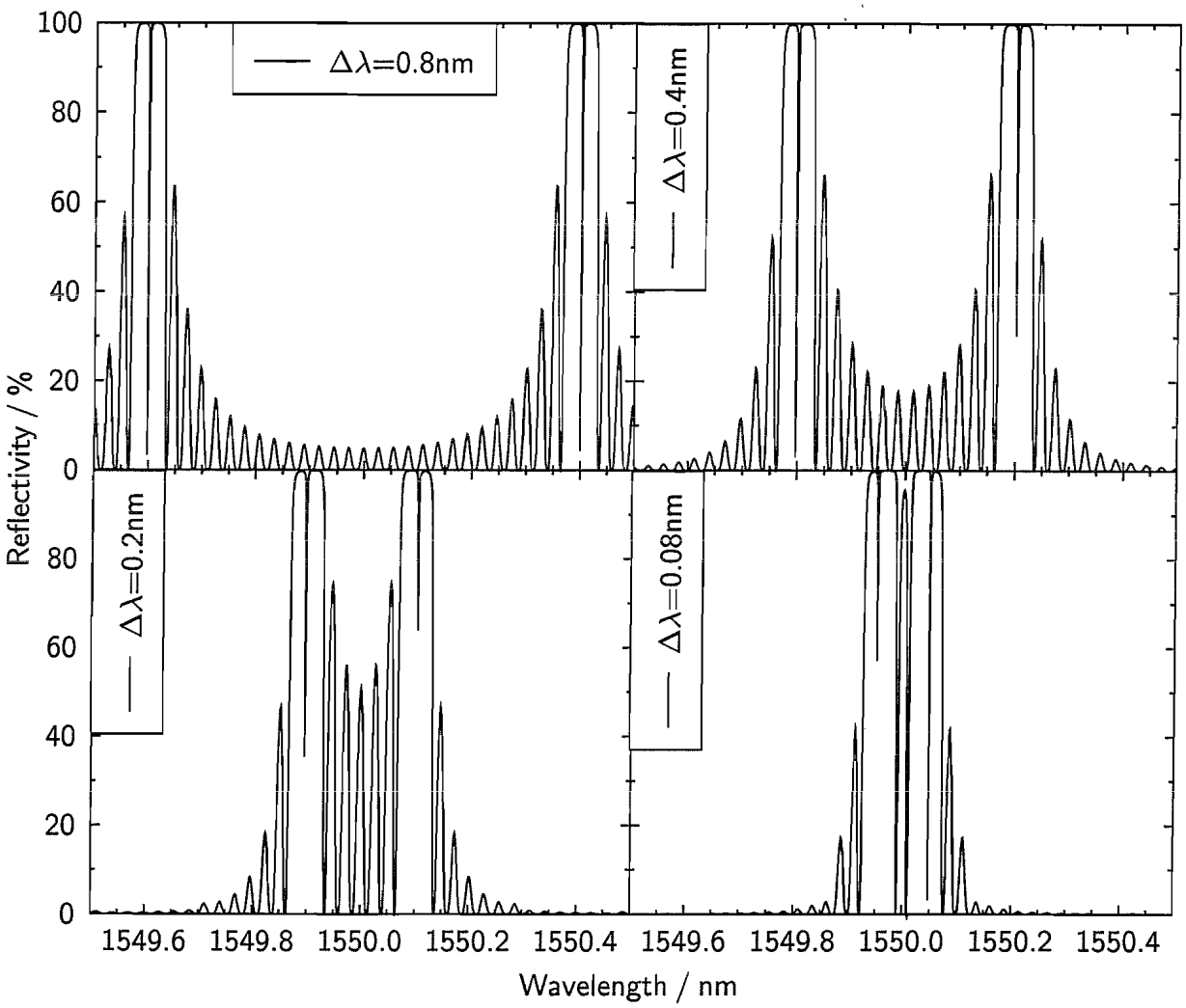

Figure 6.1. Calculated reflection spectra of Moiré DFB laser gratings for different design wavelength separations (0.8 nm, 0.4 nm, and 0.2 nm wavelength separation corresponding approximately to the telecommunication channel separation on the 100 GHz, 50 GHz, and 25 GHz ITU grids). Two separate DFB reflection peaks, each with the characteristic narrow reflection dip, are visible. As the wavelength separation between the two reflection peaks is reduced, the reflection dips are pushed away from the centre of the peaks towards the outside. The actual wavelength separation of the laser modes would therefore be larger than the designed separation.

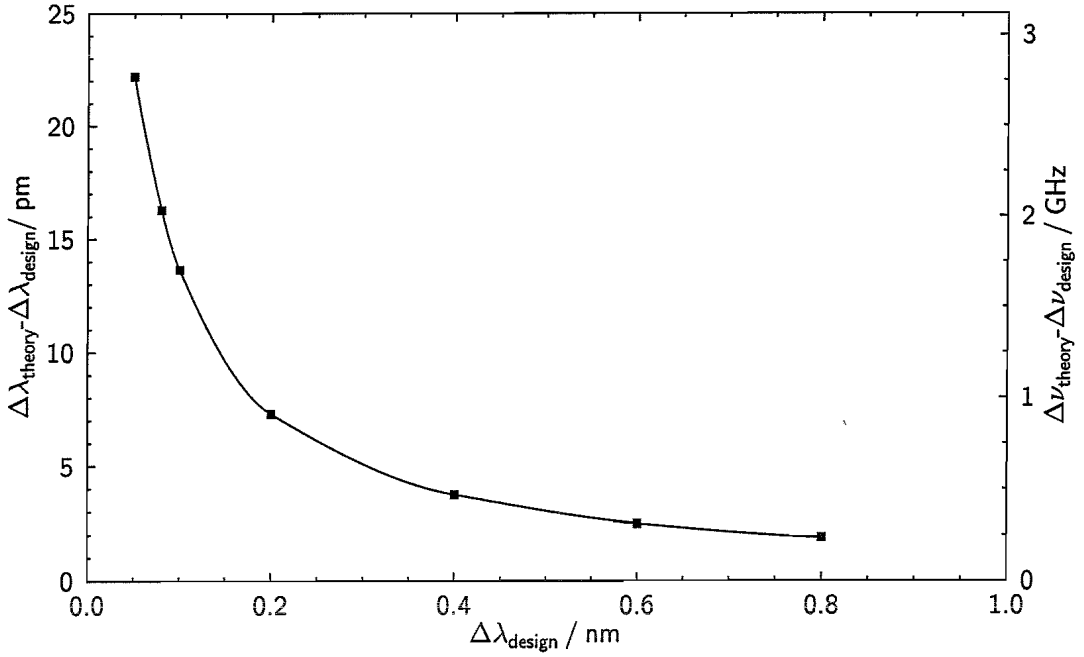

Figure 6.2. Difference between design and actual wavelength separation of a dual wavelength Moiré DFB fibre laser. At small separations required for sensor applications, i.e. $\leq$ 0.1 nm$\widehat{=}$10 GHz, a considerable deviation from the separation calculated by (6.1) is observed.

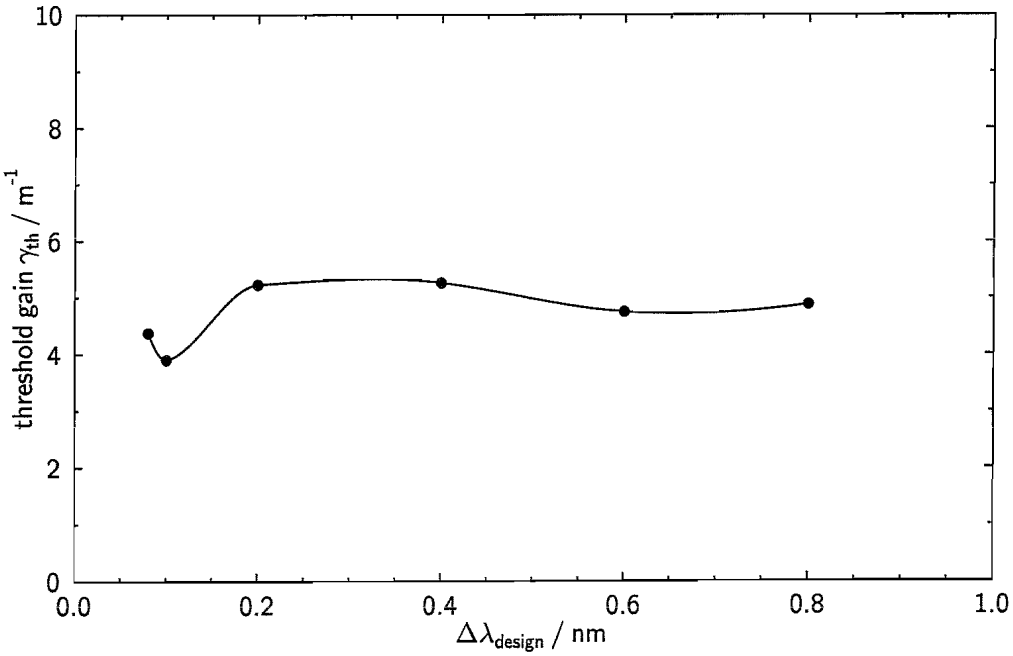

Figure 6.3. Calculated threshold gain of the individual longitudinal laser modes as a function of mode separation. The threshold gain variations are a result of the varying length of the simulated lasers which always consisted of an integer number of superstructure periods.

reflection dips were pushed away from the centre of the peaks towards the outside. The actual wavelength separation of the laser modes would therefore be larger than the designed separation. This difference is shown in Figure 6.2.

Figure 6.3 shows the simulated threshold gain of the two individual laser modes. The threshold gain fluctuations shown in Figure 6.3 are a result of the length variation. In theory the threshold gains of the two longitudinal modes are equal. In reality, however, small imperfections would favour one laser mode. The closer the mode spacing the greater are the expected effects of spatial holeburning. From the point of laser stability larger wavelength separations have to be favoured. While this would be possible for telecommunication applications, the DFB fibre laser sensor described here relies on the close wavelength separation in order to detect the beat signal between the two modes without the need for further frequency mixing.

The mode structure of the dual longitudinal mode polarimetric DFB laser sensor is shown in Figure 6.4. At room temperature the wavelength separation between the two longitudinal laser modes, determined by the period of the grating superstructure, was about 0.12 nm. This corresponds to a frequency separation of 14.9 GHz at a centre wavelength of 1551 nm. The designed mode separation was 10 GHz or 0.08 nm. About 17 pm of the difference between designed and achieved wavelength

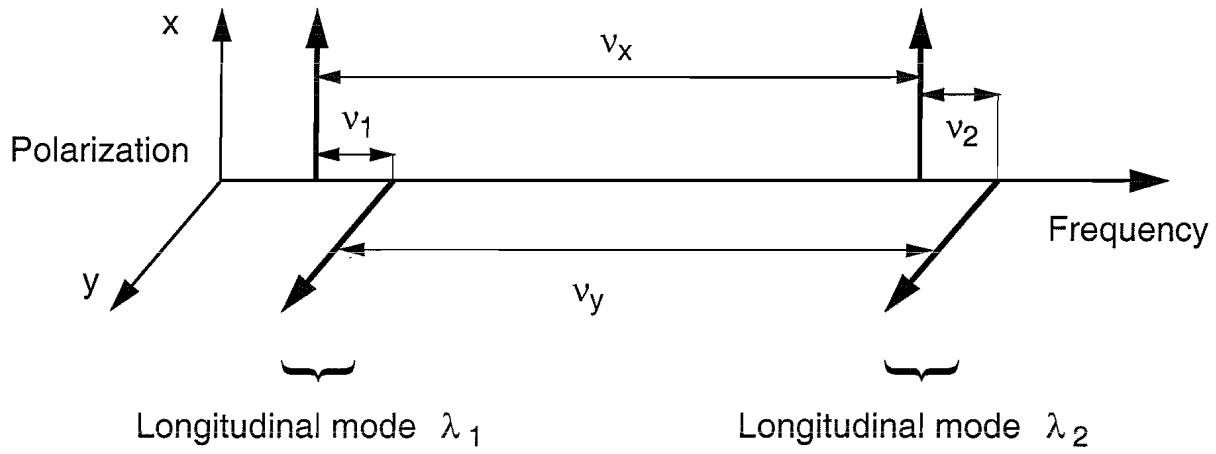

Figure 6.4. Mode structure and resulting RF beat frequencies of the birefringent Moiré DFB fibre laser used as a strain and temperature sensor. The longitudinal beat frequencies are determined by the period of the Moiré structure. The polarisation beat frequencies depend on the birefringence of the DFB fibre laser.

separation can be attributed to the additional 'outward push' of the dips of the reflection spectra. The remaining difference might have been caused by tolerances in the fabrication process. Because of a small birefringence of the DFB fibre laser each longitudinal mode was split into two orthogonal polarisation modes with a frequency difference of about 650 MHz at room temperature. The linewidths of the RF beat signals between two laser modes are a convolution of the particular optical linewidths. Assuming that all four laser modes have approximately the same optical linewidth then the electrical beat signal linewidth and the optical linewidth are approximately equal.

6.2 Theoretical sensor response

The strain ϵ and temperature T dependences of the wavelengths $\lambda_{m,e}$ of the two longitudinal laser modes and their two polarisations are given by the well known equation [16]

$$\Delta\lambda_{m,e}/\lambda_{m,e} = (1 + p_{m,e})\epsilon + (\alpha + \xi_{m,e})\Delta T, \quad m = 1, 2 \text{ and } e = x, y, \tag{6.2}$$

where $p_{m,e} = (1/n_{m,e})\,\mathrm{d}n_{m,e}/\mathrm{d}\epsilon$ and $\xi_{m,e} = (1/n_{m,e})\,\mathrm{d}n_{m,e}/\mathrm{d}T$ are the strain-optic and thermo-optic coefficients, respectively, α is the thermal expansion coefficient of the fibre and $n_{m,e}$ is the effective refractive index experienced by the particular laser mode. The indices m and e denote the longitudinal mode and the plane of polarisation, respectively. The relevant parameters can be obtained from the DFB fibre laser sensor presented in Chapter 5, for which the same fibre had been used. Hence $p = -0.26$, $\alpha = 0.5 \times 10^{-6}\,\mathrm{K}^{-1}$, and $\xi = 4.6 \times 10^{-6}\,\mathrm{K}^{-1}$. The wavelength responses to strain and temperature of the two longitudinal modes differ by a small amount due to the wavelength dependences of p and ξ, respectively. For large wavelength separations of several hundred nanometres this effect can be measured with an optical spectrum analyser [30]. From the difference between the sensor responses at 850 nm and 1300 nm presented in [30] one can estimate that for this dual longitudinal mode DFB fibre laser sensor the responses would differ by $10^{-4}\,\mathrm{pm}/\mu\epsilon$ and $6 \times 10^{-4}\,\mathrm{pm}/^{\circ}\mathrm{C}$ between the two longitudinal modes. Therefore, the wavelength

resolution offered by commercial spectrum analysers would be insufficient to detect strain or temperature induced changes of the wavelength separation between the two longitudinal modes. However, the small wavelength separation between the longitudinal modes makes it possible to measure their RF beat frequency precisely with an RF spectrum analyser.

The longitudinal mode beat frequency between the two modes polarised in the same direction is

$$\nu_e = c\frac{\lambda_{2,e} - \lambda_{1,e}}{\lambda_{1,e}\,\lambda_{2,e}}, \quad e = x, y, \tag{6.3}$$

where c is the speed of light. Expanding (6.3) into a linear equation in ϵ and ΔT yields

$$\begin{aligned}\frac{\Delta\nu_e(\epsilon, \Delta T)}{\nu_e} &= \left[\frac{1}{L_e}\frac{\mathrm{d}L_e}{\mathrm{d}\epsilon} - (2 + p_{1,e} + p_{2,e})\right]\epsilon\Big|_{T=\text{const}} + \\ &\quad \left[\frac{1}{L_e}\frac{\mathrm{d}L_e}{\mathrm{d}T} - (2\alpha + \xi_{1,e} + \xi_{2,e})\right]\Delta T\Big|_{\epsilon=\text{const}},\end{aligned} \tag{6.4}$$

where $L_e = \lambda_{2,e} - \lambda_{1,e}$.

It has been shown in Section 5.1.4 that the birefringence of DFB fibre lasers is a linear function of strain and temperature. Therefore, the polarisation beat frequency between the two polarisations of each longitudinal mode can be expressed as

$$\begin{aligned}\frac{\Delta\nu_m(\epsilon, \Delta T)}{\nu_m} &= \left[\frac{1}{B_m}\frac{\mathrm{d}B_m}{\mathrm{d}\epsilon} - (1 + 2p_m)\right]\epsilon\Big|_{T=\text{const}} + \\ &\quad \left[\frac{1}{B_m}\frac{\mathrm{d}B_m}{\mathrm{d}T} - (\alpha + 2\xi_m)\right]\Delta T\Big|_{\epsilon=\text{const}},\end{aligned} \tag{6.5}$$

where it is assumed that the strain-optic and thermo-optic coefficients are polarisation independent, i.e. $p_{m,x} = p_{m,y} = p_m$ and $\xi_{m,x} = \xi_{m,y} = \xi_m$.

The exact strain and temperature responses of the four beat frequencies between the laser modes are the result of an interplay between the variations of the grating periods $\Lambda_{1,2}$, the refractive indices $n_{1,2}$ at the two wavelengths, and the birefringence $B_{1,2}$. As can be seen in Figure 6.4 the beat frequencies must always obey

$$\nu_x + \nu_2 = \nu_y + \nu_1. \tag{6.6}$$

Strain and temperature can be determined by measuring two out of the four beat frequencies simultaneously and inverting the following set of linear equations

$$\begin{pmatrix} \Delta\nu_\alpha \\ \Delta\nu_\beta \end{pmatrix} = \boldsymbol{K}_{\text{sensor}} \begin{pmatrix} \epsilon \\ \Delta T \end{pmatrix}, \tag{6.7}$$

where $\boldsymbol{K}_{\text{sensor}}$ is a 2×2 matrix. The choice of the beat frequency pair (ν_α, ν_β) determines the accuracy of the sensor which is proportional to $\det \boldsymbol{K}$, i.e. the difference between the two beat frequency responses to strain and temperature, respectively. Conventional error analysis will be employed in Section 6.5 to choose the pair of beat frequency measurements that provides the highest strain and temperature accuracy.

6.3 Experimental arrangement

The experimental arrangement is shown in Figure 6.5. A 60 mm long Moiré DFB fibre laser operating around $\lambda = 1551$ nm was written into the uncoated photosensitive Er^{3+}:Yb^{3+}-doped fibre described in Section 3.2. The grating coupling coefficient was $\kappa \approx 175\,\text{m}^{-1}$ for each of the two longitudinal modes and the effective *pi* phase

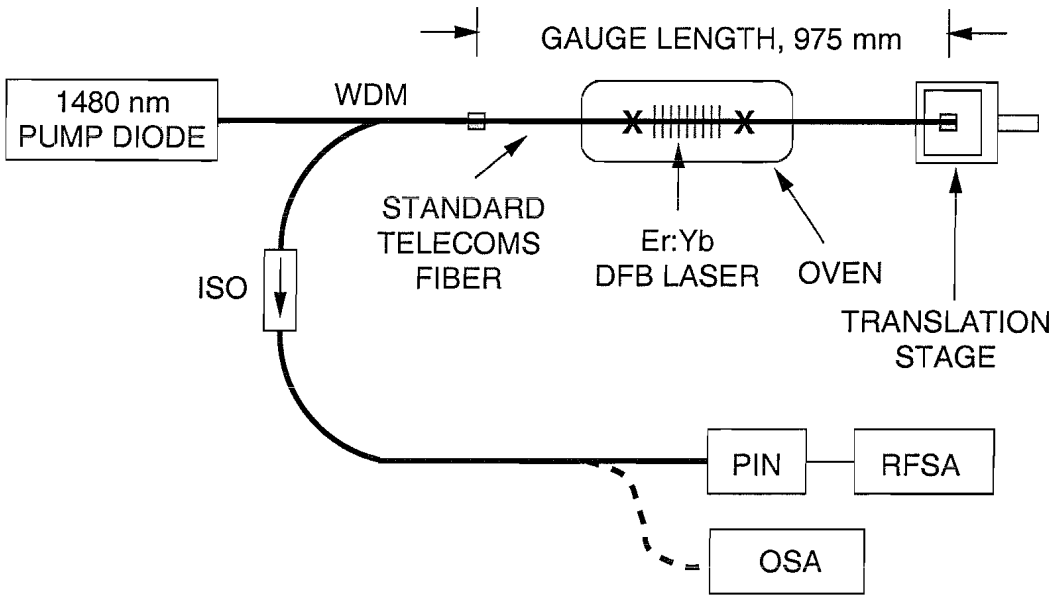

Figure 6.5. Experimental arrangement to investigate the strain and temperature dependence of the dual longitudinal mode polarimetric DFB fibre laser sensor. Note the simpler interrogation system compared with the single longitudinal mode sensor (Figure 5.2). WDM=wavelength division multiplexer, ISO=isolator, PIN=photodiode, RFSA=RF spectrum analyser.

shift was positioned at the centre. Standard telecommunication fibre was spliced to both sides of the laser, approximately 5 mm away from the grating ends. The DFB fibre laser was pumped with a 1480 nm pump[2] which ensured that pump induced thermal effects inside the laser could be kept to a minimum (see Chapter 4). The output of the DFB fibre laser was detected with two photodetectors, with bandwidths of 1 GHz[3] and 7 GHz[4]. The latter was still capable of detecting the longitudinal beat signals at 14.9 GHz, where its response had rolled off by −20 dB. The lower bandwidth detector was used to detect the polarisation beat frequencies because of its higher sensitivity and lower noise. The fibre between the laser and the detectors was standard single mode telecommunication fibre. Bend induced birefringence in this non-polarisation maintaining fibre led to coupling of power between the orthogonal linearly polarised laser modes as they propagated along the fibre. This coupling between polarisation modes was sufficient to detect a beat signal on the detectors without the need for carefully adjusting the polarisation state by means of additional polarisation controllers and polarisers. Only one interrogation system was required to detect the strain and temperature dependent RF beat frequencies between the longitudinal and polarisation modes. As a result this setup is much simpler compared with the experimental arrangement of the single longitudinal mode DFB fibre laser sensor shown in Figure 5.2. Strain and temperature of the DFB fibre laser were controlled by the same arrangement described in Section 5.1.3. The gauge length in this experiment was increased to $l_g = 975$ mm. Strain and temperature were applied to the DFB fibre laser with an accuracy of about $\pm 3\,\mu\epsilon$ and $\pm 0.1\,^{\circ}\mathrm{C}$, limited by the positioning accuracy of the manual translation stage and the temperature resolution of the thermometer (see Section 5.1.5).

[2]Philips, CQF 858 1480nm pump diode

[3]New Focus 1611

[4]Tektronix SA42

6.4 Optical spectrum and output power

Figure 6.6 shows the optical spectrum of the dual longitudinal mode DFB fibre laser at different strain levels. The resolution of the spectrum analyser[5] was 1 pm, which did not allow to resolve the two polarisations of each longitudinal mode. Therefore, each peak in the spectrum was the sum of both polarisations. For unstrained DFB fibre laser its output power at each of the two longitudinal modes, summed over both polarisations, was 40 μW with 79 mW of launched pump power at 1480 nm. With increasing strain the output powers of the two modes started to differ with the power at λ_1 increasing and at λ_2 decreasing. The total laser output power increased with strain.

Figure 6.7 shows the output power of the two longitudinal modes of the slightly strained DFB fibre laser versus pump power at 1480 nm. The output power of the

[5]Photonetics, Walics HR 15

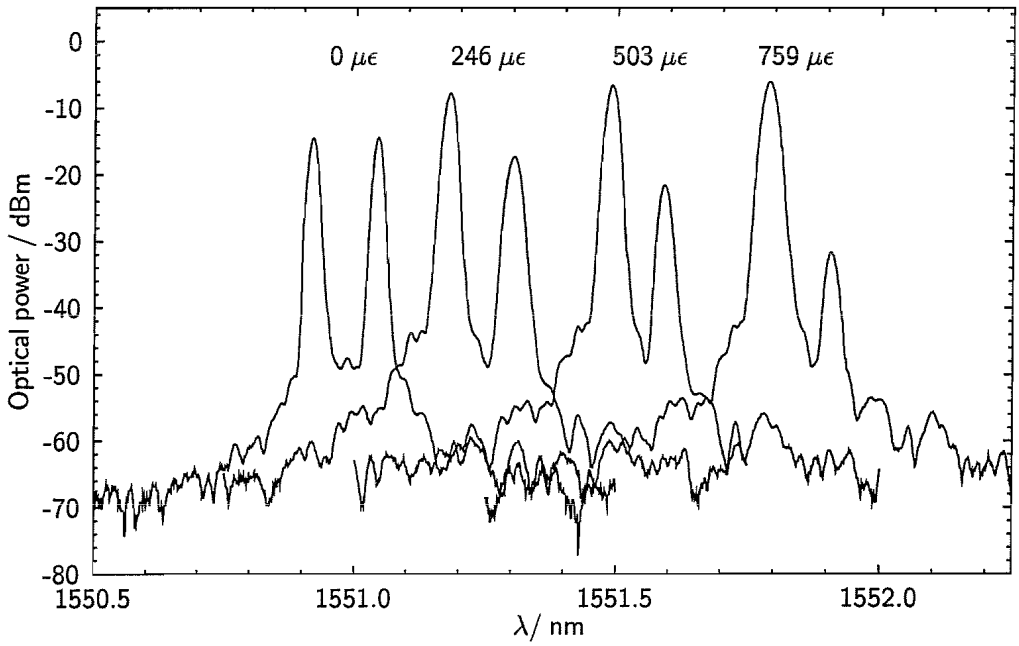

Figure 6.6. Optical spectrum of the dual longitudinal mode DFB fibre laser taken with 1 pm resolution at different strain levels. The centre wavelength of the double peak structure increased with strain. The mode spacing was 0.12 nm, corresponding to a frequency difference of 14.9 GHz. The small change of the mode spacing with strain was not detectable with the optical spectrum analyser. The power of the two longitudinal modes varied with strain because of possible small perturbations of the grating.

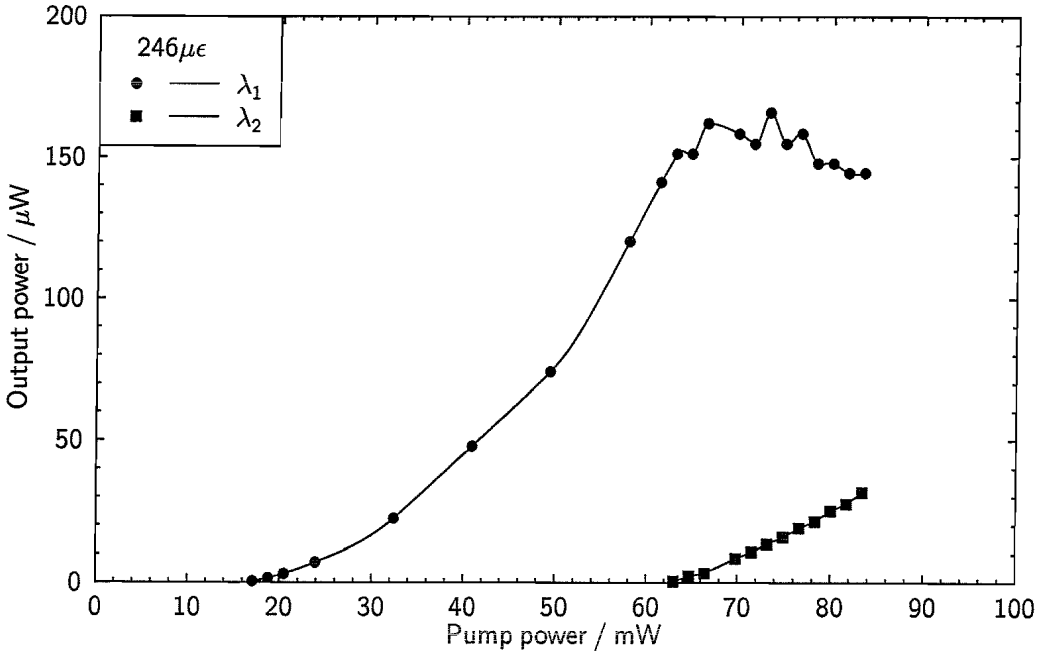

Figure 6.7. Output power of the two longitudinal modes as a function of pump power at 1480 nm while the DFB fibre laser was strained by 246 $\mu\epsilon$. The shorter wavelength mode (λ_1) has a much lower lasing threshold than the longer wavelength mode (λ_2), possibly because of different coupling coefficients κ. Gain competition, spatial holeburning, and self heating of the fibre laser are possible reasons for the decrease of output power of the shorter wavelength mode when the second mode started lasing.

two modes was measured on the optical spectrum analyser. In agreement with the spectra in Figure 6.6 the output power was devided unequally between the two modes, with a maximum output power of 165 μW and to 32 μW at the mode with the shorter (λ_1) and longer (λ_2) wavelength, respectively.. The lasing thresholds were $\approx$ 20 mW and $\approx$ 65 mW at λ_1 and λ_2, respectively. The slope efficiency of the mode at λ_1 suddenly decreased when the second mode started lasing. As the output power of the second mode increased the output power of the first mode gradually decreased, and power fluctuations of about 10% were observed. Gain competition, spatial holeburning, small imperfections of the π phase shifts between the apodised grating sections and a small difference between coupling coefficients κ of the two longitudinal modes are likely explanations for this behaviour.

In a non-ideal DFB fibre laser strain and temperature might affect the intensity distribution of the laser modes and consequently the output power. Better grating designs are expected to overcome the differential "fading" of the two modes.

Furthermore, self heating of the laser might also have played a role. The grating might have become chirped as a result of a non-uniform heat distribution along the laser (see Chapter 4) which reduced the feedback. This last point was very pronounced when the laser was pumped at 980 nm. Then large heat induced cavity detuning caused one of the two longitudinal laser modes to stop operating.

6.5 Observed sensor response

As expected from Section 6.2 Figure 6.6 shows that the wavelengths of the two longitudinal modes increased with strain. However, the wavelength separation between the two modes remained practically constant. The same behaviour is expected when the DFB fibre laser is subject to temperature variations. Therefore, simultaneous strain and temperature measurements are not possible in the wavelength domain and the DFB fibre laser sensor has to be based on the beat frequencies between the four laser modes.

The sensor was calibrated by measuring all four beat frequencies $\nu_{1,2,x,y}$ at five different temperatures with six strain levels each. The drop of laser output power in the mode at λ_2 restricted the strain and temperature range over which this sensor could be calibrated. The linewidths of the electrical beat signals between the individual laser modes were about 10 kHz. Following the discussion in Section 6.2 the optical linewidths of the individual modes of this dual longitudinal mode DFB fibre laser were about 10 kHz, i.e. similar to that of the single mode DFB fibre laser discussed in Chapter 5. The accuracies of the measurements were $\sigma(\nu_{x,y}) \approx \pm 30$ kHz and $\sigma(\nu_{1,2}) \approx \pm 10$ kHz, given by the resolution bandwidth of the RF spectrum analyser and a small jitter of the longitudinal beat frequencies. Figures 6.8 and 6.9 show the measurements of one polarisation beat frequency and one longitudinal beat frequency as a function of strain and temperature. The other polarisation and longitudinal beat frequency exhibited a similar behaviour.

As observed previously in Chapter 5 the polarisation beat frequency increased with strain and decreased with temperature. Small deviations from the circular symmetry of the fibre and the DFB laser grating increase when the fibre contracts

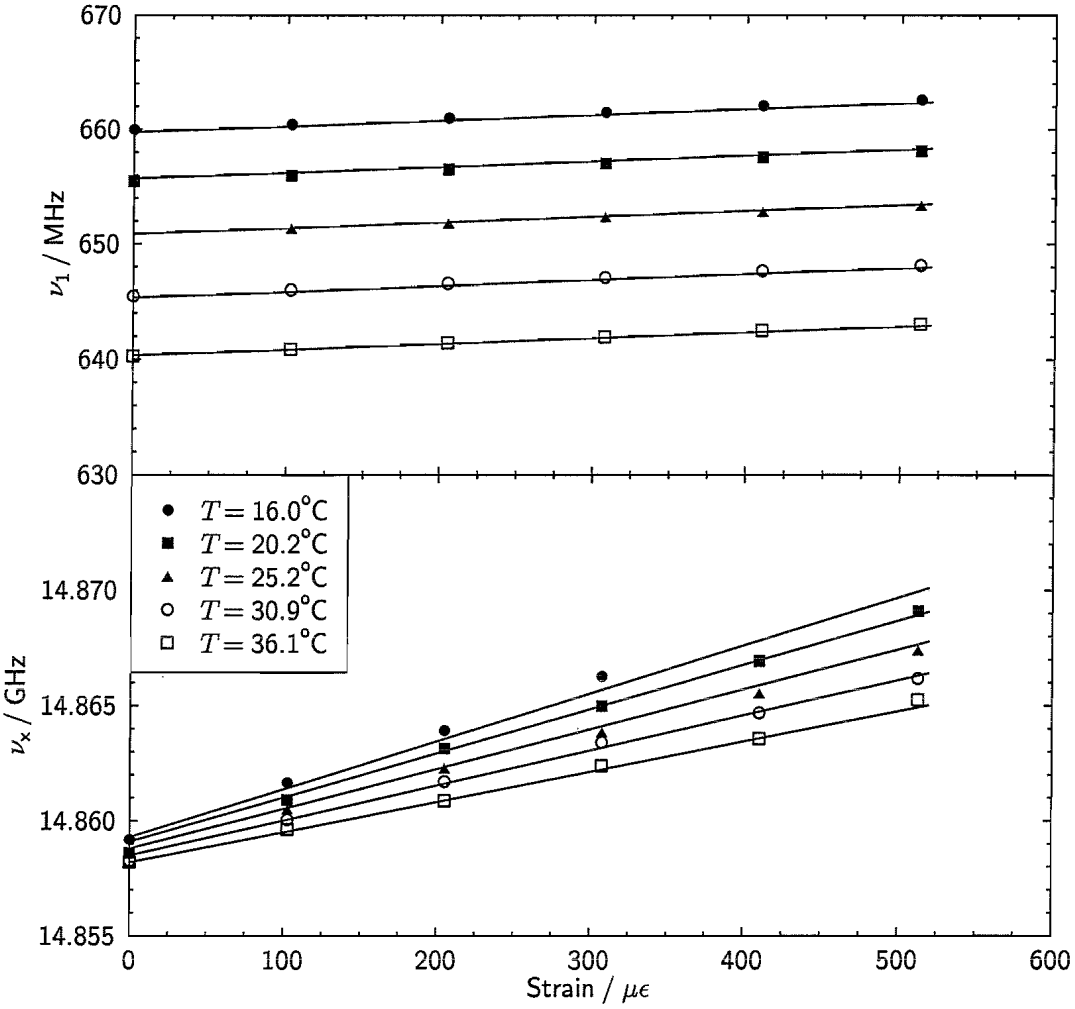

Figure 6.8. Polarisation ν_1 and longitudinal ν_x beat frequencies of the dual longitudinal mode DFB fibre laser as a function of strain at different temperatures. Lines represent best fits, including the strain-temperature cross-sensitivity of the longitudinal beat frequency response. This cross-sensitivity might be explained by including a small temperature dependence of the strain-optic coefficient into (6.4). The polarisation beat frequency response was in good agreement with the results from the single longitudinal mode DFB laser sensor (Section 5.1.4).

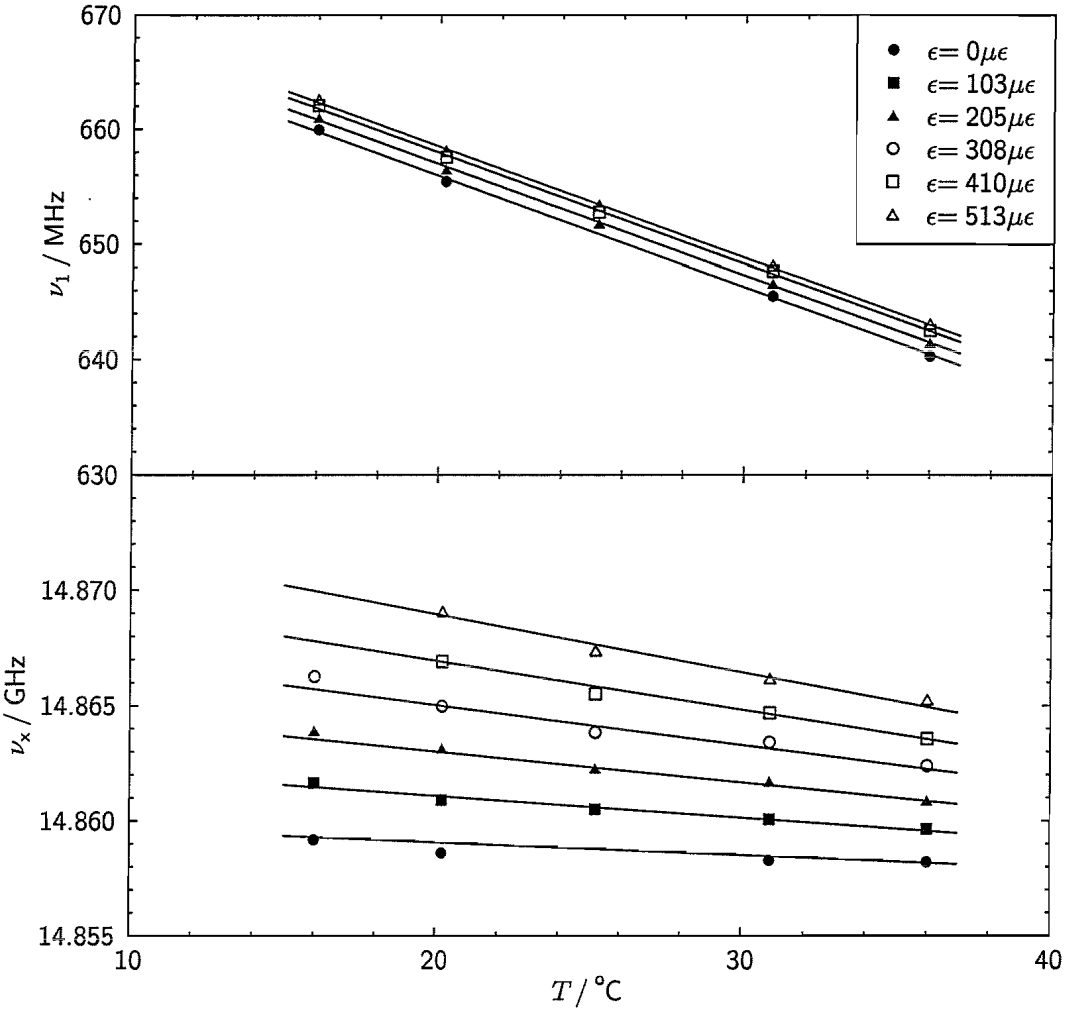

Figure 6.9. Polarisation ν_1 and longitudinal ν_x beat frequencies as a function of temperature at different strain levels. Data of only four strain levels is shown for clarity of the top graph. Lines represent best fits, including strain-temperature cross-sensitivity of the longitudinal beat frequency response. Again, the polarisation beat frequency response was in good agreement with the results from the single longitudinal mode DFB laser sensor (Section 5.1.4).

radially under longitudinal strain. When the fibre temperature increases asymmetric stress which had been building up in the fibre during fabrication is released and the birefringence decreases. If the relative wavelength responses to strain and temperature $\Delta\lambda(\epsilon, \Delta T)/\lambda$ were identical for both longitudinal modes, i.e. $p_1 = p_2$ and $\xi_1 = \xi_2$, then it follows from (6.4) that the longitudinal beat frequency would increase with strain and temperature. The experimental results show that the longitudinal beat frequency indeed increased with strain but decreased with temperature. It will be shown in Section 6.7 that small differences of the parameters $p_{1,e}$, $p_{2,e}$ and $\xi_{1,e}$, $\xi_{2,e}$ between the two longitudinal modes at $\lambda_{1,2}$ can explain this result. Unlike the polarisation beat frequency, the response of the longitudinal beat frequency showed a cross-sensitivity to strain and temperature, i.e. the strain response $\mathrm{d}\nu_e/\mathrm{d}\epsilon$ depended on the fibre temperature and vice versa. This is clearly visible in the bottom graphs of Figures 6.8 and 6.9. A possible explanation for this behaviour will be given in Section 6.7.

Using Equation (6.5), planes $\nu_{1,2}(\epsilon, T)$ were fitted to the polarisation beat frequencies, which in matrix form can be written as:

$$\begin{pmatrix} \Delta\nu_1 \\ \Delta\nu_2 \end{pmatrix} = \begin{pmatrix} k_{11} & k_{12} \\ k_{21} & k_{22} \end{pmatrix} \begin{pmatrix} \epsilon \\ \Delta T \end{pmatrix} = \boldsymbol{K}_e \begin{pmatrix} \epsilon \\ \Delta T \end{pmatrix}. \tag{6.8}$$

The fit parameters $k_{i,j}$, i.e. the beat frequency responses, and $\nu_m(\epsilon = 0\,\mu\epsilon, T = 0\,^\circ\mathrm{C})$ are shown in Table 6.1-a and -b, respectively. The relative strain and temperature dependences of the polarisation beat frequency $(\Delta\nu_m/\nu_m)$ are in agreement with the DFB fibre laser sensors presented in Chapter 5. Similarly curved planes $\nu_{x,y}(\epsilon, \Delta T)$ were fitted to the longitudinal beat frequencies, with a term proportional to $\epsilon\Delta T$ being added to (6.4) in order to take the strain-temperature cross-sensitivity of the longitudinal beat frequency responses into account. The modified equation (6.4) can be expressed in matrix form as

Table 6.1. Beat frequency responses k_{ij} and beat frequencies at $\epsilon = 0\,\mu\epsilon, T = 0\,°\mathrm{C}$ found by fitting Equations (6.8) and (6.9) to the experimental data.

k_{ij}	j		
	1	2	3
i	/kHz/$\mu\epsilon$	/kHz/°C	/Hz/($\mu\epsilon$°C)
1	5.05 ± 0.19	-966 ± 5	
2	5.18 ± 0.15	-944 ± 5	
3	26.85 ± 0.12	-56 ± 12	-381 ± 43
4	24.82 ± 0.09	-54 ± 8	-294 ± 32

a

$\nu(\epsilon = 0\,\mu\epsilon, T = 0\,°\mathrm{C})$
$\nu_1 = (675.21 \pm 0.14)$ MHz
$\nu_2 = (658.63 \pm 0.13)$ MHz
$\nu_x = (14.8602 \pm 0.0003)$ GHz
$\nu_y = (14.8442 \pm 0.0002)$ GHz

b

$$\begin{pmatrix} \Delta\nu_x \\ \Delta\nu_y \end{pmatrix} = \begin{pmatrix} k_{31} & k_{32} & k_{33} \\ k_{41} & k_{42} & k_{43} \end{pmatrix} \begin{pmatrix} \epsilon \\ \Delta T \\ \epsilon\Delta T \end{pmatrix} = \boldsymbol{K}_m \begin{pmatrix} \epsilon \\ \Delta T \\ \epsilon\Delta T \end{pmatrix}. \tag{6.9}$$

Again, the fit parameters $k_{i,j}$ and $\nu_e(\epsilon = 0\,\mu\epsilon, T = 0\,°\mathrm{C})$ are shown in Table 6.1-a and -b, respectively.

Because the fibre birefringence changes very little over the longitudinal mode spacing of 0.12 nm, the relative strain and temperature responses $(\Delta\nu_m/\nu_m)$, $m = 1, 2$, differ by a very small amount only. Thus employing the two polarisation beat frequencies $\nu_{1,2}$ results in large strain and temperature errors because $\det \boldsymbol{K}_e \approx 0$. The errors $\sigma(\epsilon)$ and $\sigma(T)$ can be calculated by adding the calibration errors $\sigma(k_{ij})$ and frequency measurement errors $\sigma(\nu_{1,2})$ in quadrature. Over a strain range of $0 - 1000\,\mu\epsilon$ $\sigma(\epsilon)$ increases from $\pm 28\,\mu\epsilon$ to $\pm 1630\,\mu\epsilon$. Similarly, $\sigma(T)$ increases from $\pm 0.2\,°\mathrm{C}$ to $\pm 8.8\,°\mathrm{C}$ over a temperature range of $0 - 50\,°\mathrm{C}$. Clearly measuring the two polarisation beat frequencies does not allow to determine strain and temperature with the necessary accuracy. Inserting $\nu_1 \approx \nu_2$ into (6.6) yields $\nu_x \approx \nu_y$ which explains why the responses of the two longitudinal beat frequencies to strain and temperature, respectively, are almost identical. Consequently, measuring the two longitudinal beat frequencies $\nu_{x,y}$ also results in large errors with $\sigma(\epsilon)$ ranging from $\pm 24\mu\epsilon$ to $\pm 1100\,\mu\epsilon$ and $\sigma(T)$ from $\pm 3\,°\mathrm{C}$ to $\pm 450\,°\mathrm{C}$ over the same strain and temperature span as above. It is, therefore, neither practical to replace the wavelength

measurement of the polarimetric single longitudinal mode DFB fibre laser sensor in Chapter 5 by the second polarisation beat frequency nor to rely entirely on the different strain and temperature responses at the two longitudinal modes. However, the fit parameters in Table 6.1(a) and Figures 6.8 and 6.9 show that the polarisation and longitudinal beat frequency responses were sufficiently different. Therefore a pair of one polarisation beat frequency and one longitudinal beat frequency provided the necessary parameters to measure strain and temperature simultaneously. For the pair (ν_1, ν_x) the set of linear equations can be written as

$$\begin{pmatrix} \Delta\nu_1 \\ \Delta\nu_x \end{pmatrix} = \begin{pmatrix} k_{11} & k_{12} & 0 \\ k_{31} & k_{32} & k_{33} \end{pmatrix} \begin{pmatrix} \epsilon \\ \Delta T \\ \epsilon\Delta T \end{pmatrix} = \boldsymbol{K}_{1,x} \begin{pmatrix} \epsilon \\ \Delta T \\ \epsilon\Delta T \end{pmatrix}, \tag{6.10}$$

and similarly for the three other pairs of polarisation and longitudinal beat frequency. Figure 6.10 shows a contour plot of $\Delta\nu_1$ and $\Delta\nu_x$ in the strain-temperature plane. Because of the strain-temperature cross-sensitive response the $\Delta\nu_x$-contour lines are curved. The strain response of $\Delta\nu_x$ decreases with increasing temperature while its temperature response increases with increasing strain (see also Figures 6.8 and 6.9). Solving (6.10) for ϵ and ΔT results in two pairs of solutions. In the strain and temperature range over which this sensor has been calibrated one pair corresponded to the actual strain and temperature while the other yielded a strain of the order of several thousand $\mu\epsilon$, i.e. well above the breaking point of the fibre, and a temperature close to 70 °C so the correct solution could be easily identified.

6.6 Sensor accuracy

The measurement accuracy of this sensor, which employed the beat frequency pair (ν_1, ν_x), was calculated by adding the errors of the corresponding frequency responses $\sigma(k_{ij})$ and the frequency measurement errors $\sigma(\nu_1)$, $\sigma(\nu_x)$ in quadrature. The result is superimposed on the contour plot in Figure 6.10 in form of error bars. It can be seen that the measurement error increased as the crossing angle between two frequency contour lines decreases. Because of the strain-temperature cross-sensitive

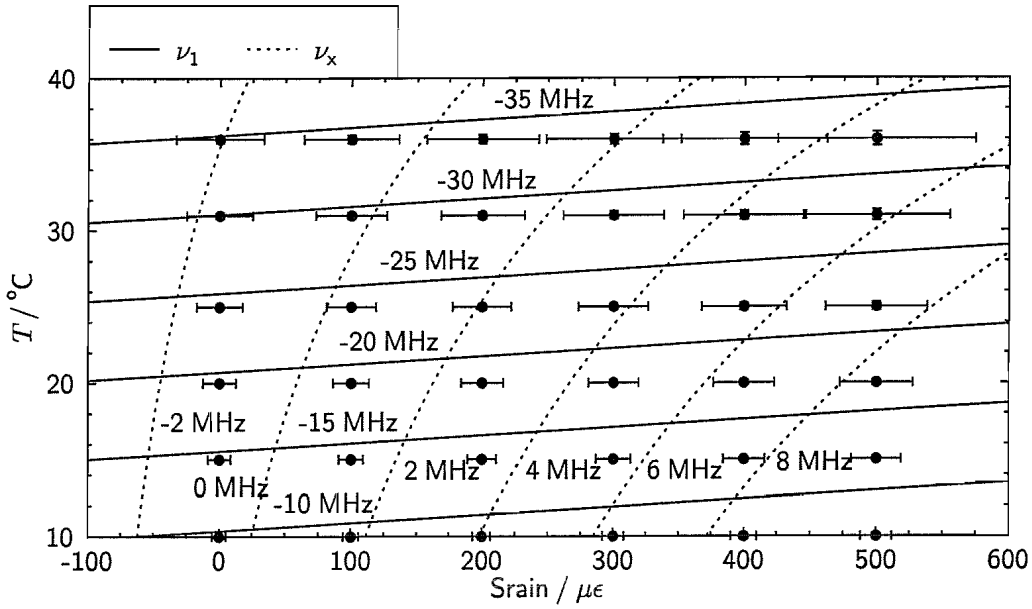

Figure 6.10. Contour plot of polarisation beat frequency change $\Delta\nu_1$ and longitudinal beat frequency change $\Delta\nu_x$ in the strain-temperature plane. Error bars show the accuracy of the sensor calculated from the uncertainties of the fit parameters, i.e. calibration errors, and the frequency measurements at the applied strains and temperatures. The temperature accuracy is $\pm 0.1 - \pm 0.3\,^{\circ}\mathrm{C}$ and its error bars are not visible at low temperatures.

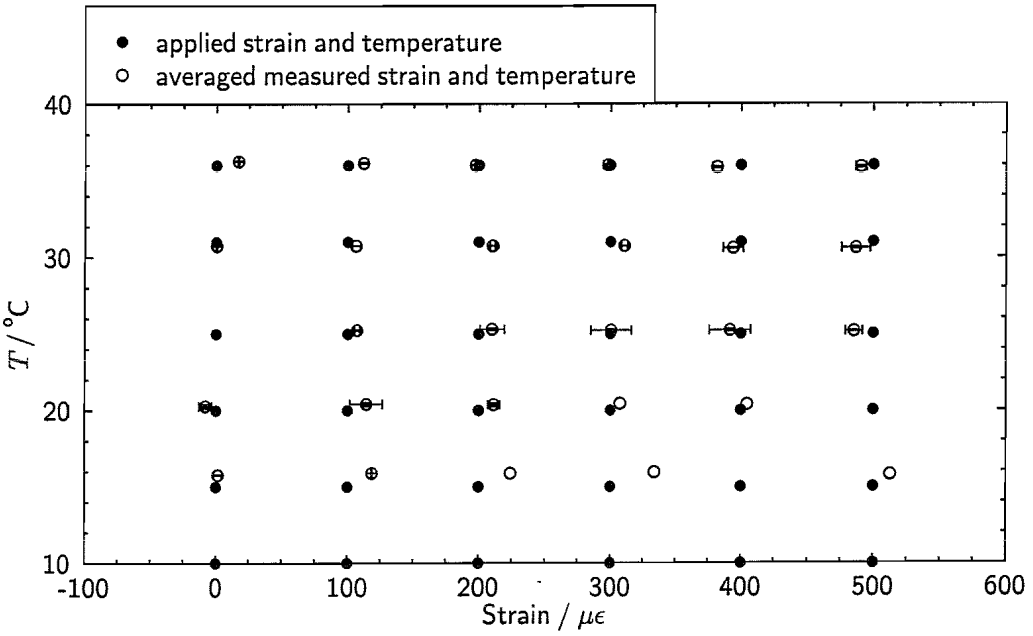

Figure 6.11. Averaged strain and temperature calculated by using all four pairs of longitudinal and polarisation beat frequencies. The error bars represent the error of the averaged value.

response the calculated strain error became unacceptably large for many applications at elevated strain and temperature values (up to 38% at $\epsilon = 500\,\mu\epsilon$, $T = 50\,^{\circ}\mathrm{C}$). The calculated temperature error was between $\pm 0.1\,^{\circ}\mathrm{C}$ and $\pm 0.3\,^{\circ}\mathrm{C}$ at low and high temperatures, respectively. Its error bars are therefore not visible in the graph at low temperatures.

These strain and temperature errors originated mainly from $\sigma(k_{ij})$. These systematic calibration errors could be reduced by using a more accurate translation stage and thermometer. If the observed strain and temperature dependent intensity ratio between the two longitudinal modes was caused by variable mode competition and self heating, it is plausible that this effect could have altered the longitudinal mode spacing slightly. Systematic beat frequency errors would be the consequence. These errors could potentially be reduced by minimising imperfections of the grating structure and spatially separating the intensity profiles of two longitudinal modes.

The frequency measurement errors $\sigma(\nu_1)$ and $\sigma(\nu_x)$ are statistical errors. Although (6.6) always holds, the individual frequency measurements are statistically independent. Therefore, four combinations of polarisation and longitudinal beat frequency pairs can be used to calculate four statistically independent (ϵ, T) pairs from which the mean values $\overline{\epsilon}$ and $\overline{T}$ can be calculated. Figure 6.11 shows the average of the four (ϵ, T) pairs together with the actually applied strain and temperature. The statistical errors $\sigma(\overline{\epsilon})$ and $\sigma(\overline{T})$ of $(\overline{\epsilon}, \overline{T})$ were much smaller than the systematic calibration errors shown in Figure 6.10. While $\overline{\epsilon}$ lied well within these systematic calibration errors $\overline{T}$ and the applied temperature differ by more than the systematic calibration error. This difference seemed to be systematic and could have been caused by an inaccurate reading of the applied temperature. Finally, the standard deviation of the differences between applied and measured ϵ and T gives an estimate of the actually achieved accuracy of this sensor, which is $\pm 15\,\mu\epsilon$ and $\pm 0.2\,^{\circ}\mathrm{C}$, respectively.

6.7 Cross-sensitive response

Finally the origin of the significant strain-temperature cross-sensitivity of the longitudinal beat frequency response will be investigated. To recapitulate, the measured strain and temperature responses of the longitudinal beat frequency depend on the small difference between the relative wavelength changes $\Delta\lambda_m(\epsilon, \Delta T)/\lambda_m$ of the two longitudinal modes $m = 1, 2$. These differences can only be predicted theoretically if the wavelength dependent strain-optic and thermo-optic properties of the different materials which make up the optical fibre are known precisely. However, the numerical values of these differences can easily be calculated from the experimental data. The strain and temperature dependent terms of Equation (6.4) may be treated separately. Then inserting the experimental strain and temperature responses $\Delta\nu_e(\epsilon)/\nu_e(\epsilon = 0, T) = f(T)$ and $\Delta\nu_e(T)/\nu_e(T = 0, \epsilon) = f(\epsilon)$ $(e = x, y)$, which can be calculated from the fitted planes, into the separated terms of (6.4) leads to

$$p_2 - p_1 = \left(\frac{1}{\epsilon}\frac{\Delta\nu_e}{\nu_e} + 3\right)\frac{L_e}{\lambda - L_e} = f(T) \tag{6.11}$$

and

$$\xi_2 - \xi_1 = \left(\frac{1}{T}\frac{\Delta\nu_e}{\nu_e} + 3\alpha\right)\frac{L_e}{\lambda - L_e} = f(\epsilon), \tag{6.12}$$

where $\lambda_2/L_e - 1 \approx \lambda_1/L_e + 1$ and $\lambda_1 \approx \lambda_2 \approx \lambda$ have been used. As indicated $p_2 - p_1$ and $\xi_2 - \xi_1$ are functions of temperature and strain, respectively, representing the strain-temperature cross-sensitivity. Figures 6.12 and 6.13 show the relative differences $(p_2 - p_1)/p_0$ and $(\xi_2 - \xi_1)/\xi_0$ as a function of temperature and strain, where $p_0 = -0.26$ and $\xi_0 = 4.6 \times 10^{-6}/\mathrm{K}^{-1}$ are the mean strain and temperature responses of the wavelengths of the two longitudinal modes. The small relative difference in the order of $10^{-4} - 10^{-3}$ shown in Figures 6.12 and 6.13 would explain the observed strain and temperature responses of the longitudinal beat frequency. The calculated relative differences $(p_2 - p_1)/p_0$ and $(\xi_2 - \xi_1)/\xi_0$ decrease by $-1.1 \times 10^{-9}/°\mathrm{C}$ and $-4.2 \times 10^{-7}/\mu\epsilon$, respectively. This small decrease would explain the observed strain-temperature cross-sensitivity of the longitudinal beat frequency response. Furthermore, if one assumes that $p_2 - p_1$ and $\xi_2 - \xi_1$ are constant then the strain-temperature cross-sensitivity, expected from the exact equation (6.3), would

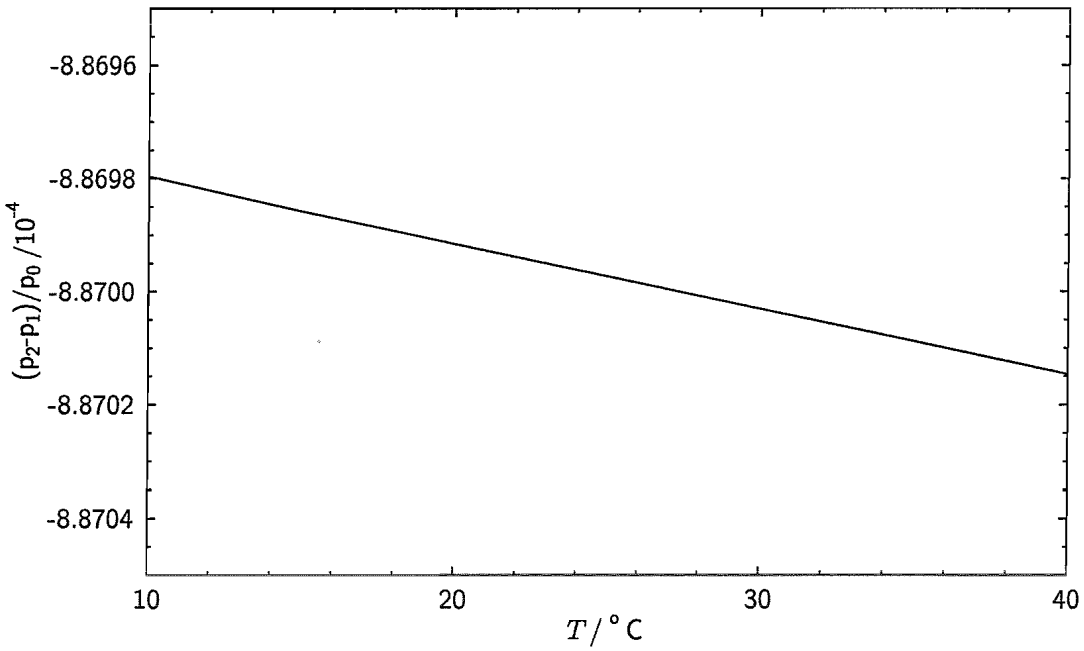

Figure 6.12. Relative difference between the strain responses at the two longitudinal modes as a function of temperature, calculated from the planes fitted to the experimental data in Figures 6.8 and 6.9.

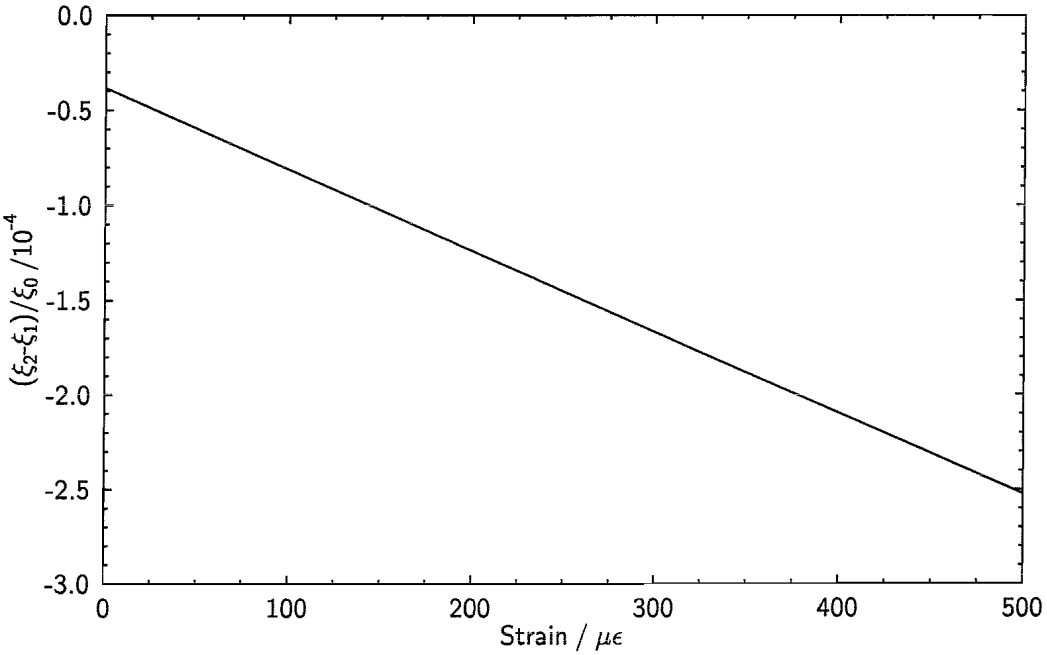

Figure 6.13. Relative difference between the temperature responses at the two longitudinal modes as a function of strain, calculated from the planes fitted to the experimental data in Figures 6.8 and 6.9.

only be $0.3\,\mathrm{Hz}/(\mu\epsilon°\mathrm{C})$, three orders of magnitude smaller than the experimentally observed value. Hence, this initially expected cross-sensitivity would have been negligible, justifying the original linear expansion of (6.3) into (6.4). These small differences and their variation with strain and temperature would remain undetected if commercial spectrum analysers with a wavelength resolution of 0.1–1 pm are used. However, the frequency resolution $\sigma(\nu_x) = 30\,\mathrm{kHz}$ of this sensor corresponds to a wavelength resolution $\sigma(\lambda_{1,x}) = \lambda_{1,x}^2\,\sigma(\nu_x)/c = 0.24\,\mathrm{fm}$ at $\lambda_{1,x} = 1550\,\mathrm{nm}$ revealing this, here significant, strain-temperature cross-sensitivity.

The underlying physical reason for this cross-sensitivity becomes evident from the definitions of [43]

$$p = -0.5\,n^2(p_{12} - \mu(p_{11} + p_{12}) \tag{6.13}$$

and [45]

$$\xi = \frac{1}{n}\left(\frac{\partial n}{\partial T} + \frac{\partial n}{\partial \rho}\frac{\partial \rho}{\partial T}\right), \tag{6.14}$$

where p_{11} and p_{12} are the photo-elastic coefficients, μ is the Poisson ratio and ρ is the density of the fibre. While p and ξ are regarded as constant in wavelength based strain and temperature sensors, the cross-sensitivity arises from the temperature dependent refractive index $n(T)$ in (6.13) and the strain dependent density $\rho(\epsilon)$ in (6.14). Furthermore, it is reasonable to assume that μ, p_{11} and p_{12} are temperature dependent while $\partial n/\partial T$ is strain dependent which might be responsible for parts of the observed strain-temperature cross-sensitive responses.

No cross-sensitivity could be detected in the polarisation beat frequency responses. Replacing n in (6.13) by $n(T) = n_0(1 + \xi)$ and inserting this modified p_m into the strain dependent term of (6.5) shows that the expected cross-sensitivity of the polarisation beat frequency response lies within the experimental error of the fit parameters.

6.8 Conclusion

In conclusion, the first polarimetric sensor for simultaneous strain and temperature measurements based on a birefringent dual longitudinal mode Moiré DFB fibre laser has been demonstrated. Strain and temperature could be determined by measuring one longitudinal and one polarisation beat frequency. The use of two RF frequencies, as opposed to one RF frequency and one wavelength measurement in Chapter 5 offers the possibility of employing a variety of low cost and precise frequency detection schemes. By averaging the strain and temperature measurements obtained from four frequency pairs an accuracy of $\pm 15\,\mu\epsilon$ and $\pm 0.2°C$ could be achieved. Systematic calibration errors were probably related to the quality of the DFB fibre laser, in particular small imperfections of the π phase shifts. The sensor responded linearly to strain and temperature but a cross-sensitivity of the longitudinal beat frequency response was observed which limited the accuracy of the sensor at higher strain levels. It has been shown that the observed strain-temperature cross-sensitive response can be explained by taking small temperature and strain dependences of the strain-optic and thermo-optic coefficients into account.

The fit parameters k_{ij} of the sensor calibration contain only the fibre specific parameters $p_{m,e}$, $\xi_{m,e}$, α, and $n_{m,e}$. Consequently the k_{ij} are expected to be valid for all DFB fibre laser sensors made in a particular type of fibre. However, to account for possible variations of fibre properties and grating writing conditions each sensor should be calibrated individually — a procedure that could potentially be automated in serial production.

The sensor accuracy might be increased in future by reducing imperfections of the DFB fibre grating and separating the two longitudinal modes spatially along the fibre laser. The latter could potentially minimise gain competition and spatial holeburning which should reduce intensity variations with strain. Furthermore, the polarisation beat frequency responses of a birefringent $Er^{3+}:Yb^{3+}$ DFB fibre laser operating at widely separated wavelengths, e.g. 1060 nm and 1550 nm, might differ significantly to realise a more practical sensor without suffering from cross-sensitive frequency responses.

7 Detrimental effects caused by external feedback

Remote pumping and interrogation of DFB fibre laser sensors through a long lead fibre might be desirable or even required in many applications. In this case the laser will experience Rayleigh backscattering from the lead fibre. When several DFB fibre laser sensors at different wavelengths are multiplexed along the same fibre [106] each laser may also experience reflections from the grating sidelobes of other lasers. It is well known that external feedback can cause excess frequency and intensity noise and self pulsing in semiconductor DFB lasers [107]. Therefore such backreflections and backscattering should also be avoided in the case of DFB fibre lasers. Intensity noise and self pulsing have detrimental effects on the performance of telecommunication networks, e.g. increased error rate, while frequency noise reduces the sensor accuracy.

Inserting an isolator near the sensing laser could reduce unwanted feedback from Raleigh backscattering and grating side lobes by typically 40–55 dB[1]. However, the use of optical isolators near the sensing point may be undesirable in confined spaces. Inserting isolators between serially multiplexed DFB fibre laser sensors to reduce backreflections from grating sidelobes may also lead to an unacceptable attenuation of the 1480 nm pump light. A more favourable solution could be the reduction of grating sidelobes, by apodising the DFB fibre laser grating [108].

The optical coherence length and the Q-factor and centre frequency of relaxation oscillations are important parameters for the stability of DFB lasers [107]. However,

[1]Single and dual stage isolators manufactured by FOCI.

these parameters differ greatly between semiconductor and fibre DFB lasers. Therefore a series of experiments has been carried out, partly together with co-worker E. Rønnekleiv[2], to characterise the influence of external feedback on the output power stability of DFB fibre lasers in telecommunication and sensor applications and on the measurement resolution of DFB fibre laser sensors. External feedback in the form of Rayleigh scattering, discrete reflections and grating sidelobes has been taken into account.

7.1 Theory of external feedback

External feedback into DFB lasers is characterised by its power reflection coefficient $r_{\text{ext}} = P_{\text{refl}}/P_{\text{laser}}$ and its phase $\Phi_{\text{ext}} = 2\pi\nu\tau_{\text{ext}}$ [107], where P_{laser} is the laser output power, P_{refl} is the power backreflected into the laser cavity, ν is the optical frequency and τ_{ext} is the external roundtrip delay. External feedback might reduce the internal threshold gain of the laser causing laser intensity and frequency fluctuations or mode hopping [107, 68]. The effects of external backscattering increase with decreasing laser mirror reflectivity and with increasing distance to the external reflector [107].

For weak feedback the optical frequency ν of the solitary laser will at most be slightly changed [107]. However, the linewidth of the laser can be broadened significantly. As the feedback increases phase noise and mode hopping might occur. If the feedback is increased beyond a critical value $r_{\text{ext}} = r_{\text{ext,c}}$ the laser becomes unstable upon which noise burst and pulsing can be observed.

Because the dynamics of the laser are largely determined by the relaxation oscillations the critical feedback level $r_{\text{ext,c}}$ depends largely on the damping rate of these oscillations. The stronger the damping, i.e. the smaller the Q-factor of the relaxation oscillations Q_r, the larger is the critical feedback level for the onset of noise bursts [107]. Mathematical models have shown that saturable absorbers play an important role in the relaxation oscillation dynamics of rare earth doped fibre lasers [109]. The concentration and the lifetime of these saturable absorbers affect the damping rate

[2]Then on leave from Optoplan AS, Box 1963, 7002 Trondheim, Norway and Norwegian Univ. of Science and Technology, Dept. of Phys. El., 7034 Trondheim, Norway

of relaxation oscillations and determine whether a fibre laser operates in a stable or unstable regime. In the former initial relaxation oscillations decay while in the latter the laser pulses continuously. It has been shown that by increasing the pump power above a critical level the fibre laser can pass from unstable to the stable operation [109]. In the DFB fibre laser studied in this thesis Er^{3+}-ion pairs act as saturable absorbers through homogenous upconversion.

7.2 Experimental arrangements — discrete back-reflections and Rayleigh scattering

The effects of external feedback from discrete reflectors and Rayleigh scattering were investigated at the same DFB fibre laser used in Section 5.1, i.e. $L = 50\,\text{mm}$ π phase shift at the centre, $\kappa = 231\,\text{m}^{-1}$, $\lambda = 1549\,\text{nm}$ and pumped at 1480 nm. For the solitary DFB fibre laser the output power of the laser was measured with an optical spectrum analyser[3] (see Figure 3.2 on p. 22) and an InGaAs photodiode[4]. The photodiode was connected to a RF spectrum analyser[5] to spectrally resolve the output power fluctuations of the DFB fibre laser. Figure 7.1 shows a typical relative intensity noise (RIN) spectrum [64] of a DFB fibre laser. In this case the DFB fibre laser was pumped at 980 nm and gave an output power of 1.1 mW. In this case relaxation oscillations appeared around 300 kHz. The noise peak near 600 MHz is the polarisation beat frequency signal used by the DFB fibre laser sensors described in Chapters 5 and 6.

The Q-factor of the relaxation oscillation is given by

$$Q_r = \nu_r / \Delta\nu_r, \tag{7.1}$$

where ν_r and $\Delta\nu_r$ denote the centre frequency and linewidth of the relaxation oscillations, respectively. Both parameters where obtained from the RIN spectrum of the laser output.

[3]Manufactured by Ando, spectral resolution 0.1 nm.

[4]HP, PDT0411 followed by an OPA 655 transimpedance amplifier.

[5]Tektronix 2782

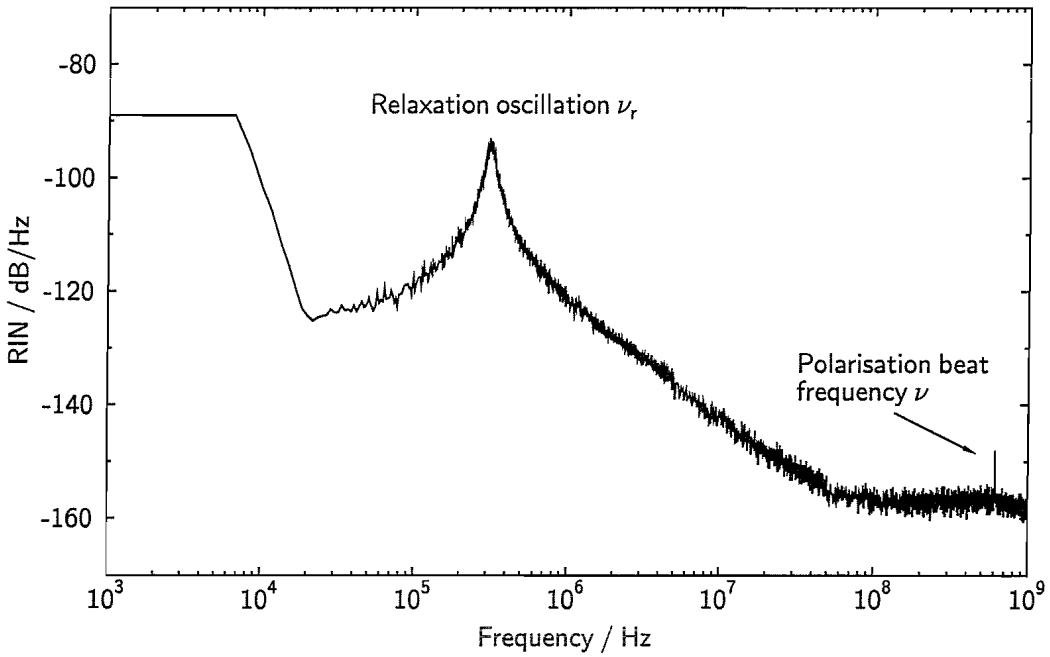

Figure 7.1. Relative intensity noise (RIN) of a DFB fibre laser. A broad relaxation oscillation peak is visible around 300 kHz. The wider this peak the higher the damping of the relaxation oscillations, i.e. the smaller the relaxation oscillation Q-factor and the higher the stability of the laser. The polarisation beat signal, which is used by the DFB fibre laser sensors in Chapters 5 and 6 is visible near 600 MHz. The low frequency cut-off of the detector was 20 kHz.

External feedback from discrete backreflections and Rayleigh scattering from a long length of fibre was provided to the DFB fibre laser by means of the experimental arrangement shown in Figure 7.2. The DFB fibre laser was pumped from the left, and the left output power was guided through a wavelength division multiplexer (WDM), a polarisation controller (PC2), an isolator (ISO), and a polarisation beam splitter (PBS) to two InGaAs detectors D1 and D2[6]. PC2 was adjusted such that each detector received light from only one laser polarisation mode. Backreflections into the right hand end of the laser with variable attenuation, phase shift, polarisation, and delay were generated by use of a variable attenuator (VA), a piezoelectric fibre stretcher (PZT), a polarisation controller (PC1), and a selection of delay coils of various length L_{ext} with 3.5 % (−14.5 dB) end reflection. By terminating the delay

[6]Same as in footnote 4

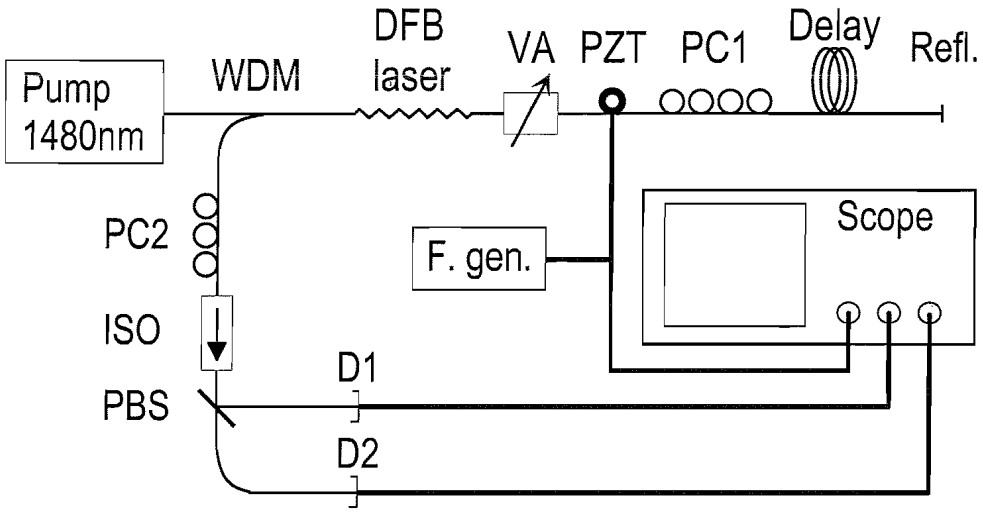

Figure 7.2. Experimental arrangement to study the effects of external backreflections on relaxation oscillations as a function of backreflection intensity, phase, and polarisation. WDM=wavelength division multiplexer, VA=variable attenuator, PZT=piezoelectric fibre stretcher, ISO=isolator, PC1 and PC2=polarisation controllers, PBS=polarising beam splitter, POL=polariser, D1 and D2=photodiodes, F.gen.=function generator.

coils with bend losses the effects of Rayleigh backscattering into the laser could be investigated.

7.3 Solitary DFB fibre laser

Figure 7.3 shows the relaxation oscillation Q-factor Q_r of the solitary DFB fibre laser as a function of launched pump power superimposed onto the laser output power already shown in Figure 3.8. Figure 7.3 shows that, parallel to an increase of the slope efficiency, Q_r decreased steeply above a pump power of 40 mW, i.e. relaxation oscillations were increasingly damped. As a result the DFB fibre laser was expected to become more stable and less susceptible to external feedback. An increase in lasing stability was indeed observed: below 40 mW pump power the laser was continously pulsing, while above pulsing stopped.

Paired Er^{3+}-ions in the DFB fibre laser, whose effect on the slope efficiency was discussed in Section 3.3.1, are subject to homogeneous upconversion (see p. 28). This process reduces the population inversion and therefore leads to a smaller gain. Figure 3.10 shows that at low optical power the population inversion of paired

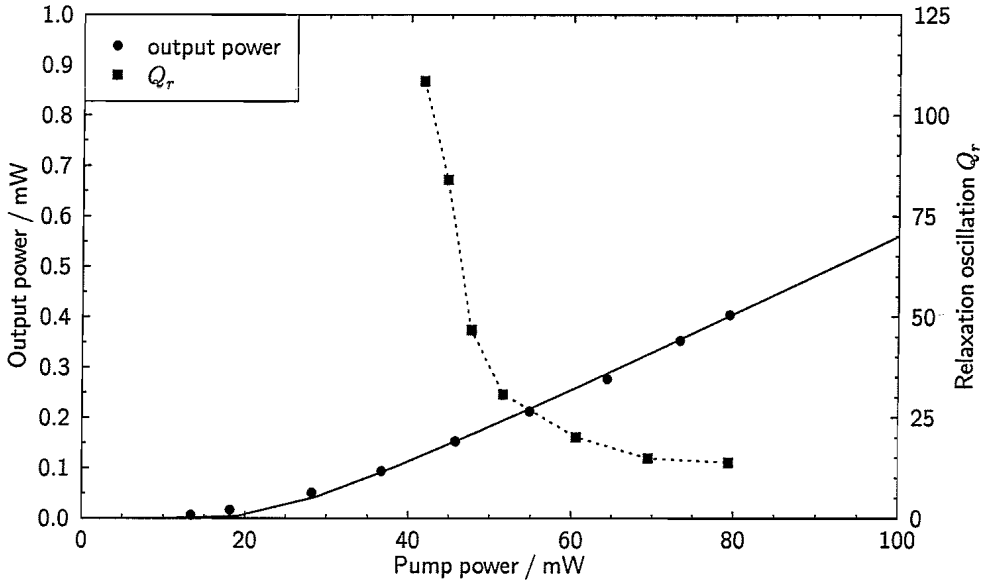

Figure 7.3. Measured laser output power and relaxation oscillation Q-factor Q_r versus launched pump power at 1480 nm. As the saturable absorbers in form of Er^{3+}-ion pairs were bleached with increasing pump power the relaxation oscillations were increasingly damped and consequently Q_r decreased dramatically above 40 mW of launched pump power.

ions is even negative ($N_{1,\text{pair}} > N_{2,\text{pair}}$) and as a result generates loss at the lasing wavelength. However, the finite lifetime of the upconversion process $C_{up}N_2$ (see Eq. 3.8) allows to obtain a positive population inversion when the optical power is increased. This is shown in Figure 3.11, where it can also be observed that the paired ions contribute gain rather than loss at the lasing wavelength.[7] In summary, the absorption of paired Er^{3+}-ions decreases with increasing optical power. They therefore act as saturable absorbers [56].

External feedback at the lasing wavelength will cause small deviations from the steady state population densities, changing the losses inside the DFB fibre laser cavity. From (3.2-a), (3.2-b), (3.3), the saturable loss $\alpha_{\text{sat}} = \sigma_{12}N_{1,\text{pair}} - \sigma_{21}N_{2,\text{pair}}$ and setting, for simplicity, $W_{12} = W_{21} = W$ and $\sigma_{12} = \sigma_{21} = \sigma$ it follows that

$$\frac{\mathrm{d}\alpha_{\text{sat}}}{\mathrm{d}W} = \frac{2\sigma}{R + 2W + A_2'}\Delta N, \tag{7.2}$$

where $\Delta N = N_2 - N_1 \leq 0$ is the population inversion of the paired ions and

[7] Although the actual population inversion does not appear to be positive it contributes gain since $\sigma_{21} > \sigma_{12}$. For $\sigma_{21} = \sigma_{12}$ the population inversion would indeed be positive.

$A_2' = 1/\tau_2'$. Consequently, for small internal optical power, i.e. small W, R and $\Delta N << 0$, small fluctuations $\mathrm{d}W$ of the internal power at the lasing wavelength due to external feedback cause large loss variations $\mathrm{d}\alpha_{\mathrm{sat}}$. These in turn lead to output power fluctuations, i.e. spiking or relaxation oscillations. With increasing pump power W and R increase while $|\Delta N|$ decreases, i.e. the absorption at the lasing wavelength caused by Er^{3+} ion pairs is bleached. Therefore $\mathrm{d}\alpha_{\mathrm{sat}}/\mathrm{d}W$ decreases, relaxation oscillations are largely damped and the DFB fibre laser becomes less susceptible to external feedback.

A more quantitative discussion would include the difference between σ_{12} and σ_{21} as well as the non-uniform distribution of the population densities of paired ions shown in Figures 3.10 and 3.11.

7.4 Critical feedback level

7.4.1 Discrete backreflection

Figure 7.4 shows intensity noise bursts of the DFB fibre laser subject to the external backreflection from the cleaved end of a $L_{\mathrm{ext}} = 22.3\,\mathrm{m}$ long fibre. The launched pump power was 79 mW and the DFB fibre laser gave an output power of 400 μW. The phase of the external backreflection was modulated by applying a triangular waveform to the PZT. The external amplitude reflection coefficient was adjusted to its critical value $r_{\mathrm{ext,c}} = -28.3 \pm 1\,\mathrm{dB}$ where relaxation oscillation noise bursts started to occur for worst case settings of PC1 and PZT drive voltage. At these worst case settings the noise amplitude was at its maximum. It can clearly be seen that noise bursts of the optical power occurred when the external roundtrip phase Φ_{ext} was a multiple of 2π. The feedback periodically reached its critical value and the laser became unstable.

When PC1 was in its worst case position, the fast power fluctuations of the two laser polarisation modes were practically equal in amplitude and in phase. This indicated equal backreflection phase delay Φ_{ext} for the two polarisation modes. For other settings of PC1, the relaxation oscillation frequencies of the two polarisation

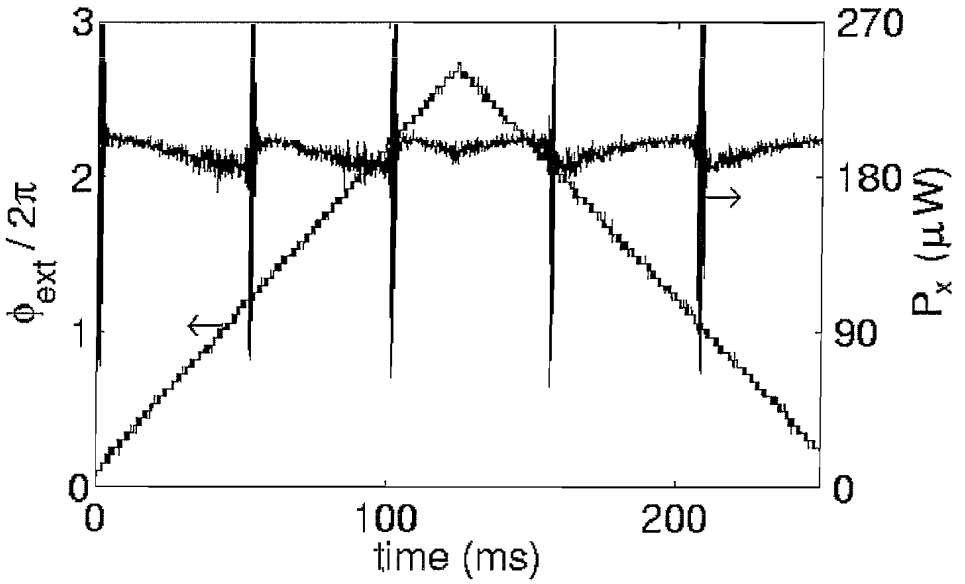

Figure 7.4. Oscilloscope trace of the laser output power P_x of the x-polarised mode (see Figure 7.2) and of the triangular phase modulation signal Φ_{ext} applied to the PZT. $L_{ext} = 22.3\,\text{m}$ and $r_{ext} = r_{ext,c}$. Noise burst of the optical power were observed when Φ_{ext} was a multiple of 2π.

modes would still be equal, but the sign of these power fluctuations could be made opposite for the two modes. The critical external reflection coefficient $r_{ext,c}$ could then be increased by at least 10 dB as one polarisation mode was backreflected into the orthogonal mode. Because the two polarisation modes had slightly different optical frequencies ν the backreflected light was out of phase with the light in the laser cavity and a higher backreflected amplitude was required to cause laser instabilities.

It has been pointed out in Section 7.1 that the critical backreflection coefficient $r_{ext,c}$ does not only depend in the phase delay Φ_{ext} but also on the external cavity length L_{ext}. Therefore in the following experiment $r_{ext,c}$ has been measured as a function of L_{ext} at different pump powers and with PC1 adjusted to its worst case setting. Simulation results reported for semiconductor lasers [110] predict that $r_{ext,c}$ versus L_{ext} decreases by more than 20 dB per decade for $L_{ext} < L_r = c/2n_{eff}\nu_r$ and flattens out for longer external cavity lengths. Here L_r corresponds to a feedback delay of one relaxation oscillation period. The experimental results for the DFB fibre laser shown in Figure 7.5 were in qualitative agreement with these simulations. For $L_{ext} = 22.3\,\text{m}$ and $L_{ext} = 318\,\text{m}$ the measurements satisfy $r_{ext,c} \propto Q_r^{-1}$ which

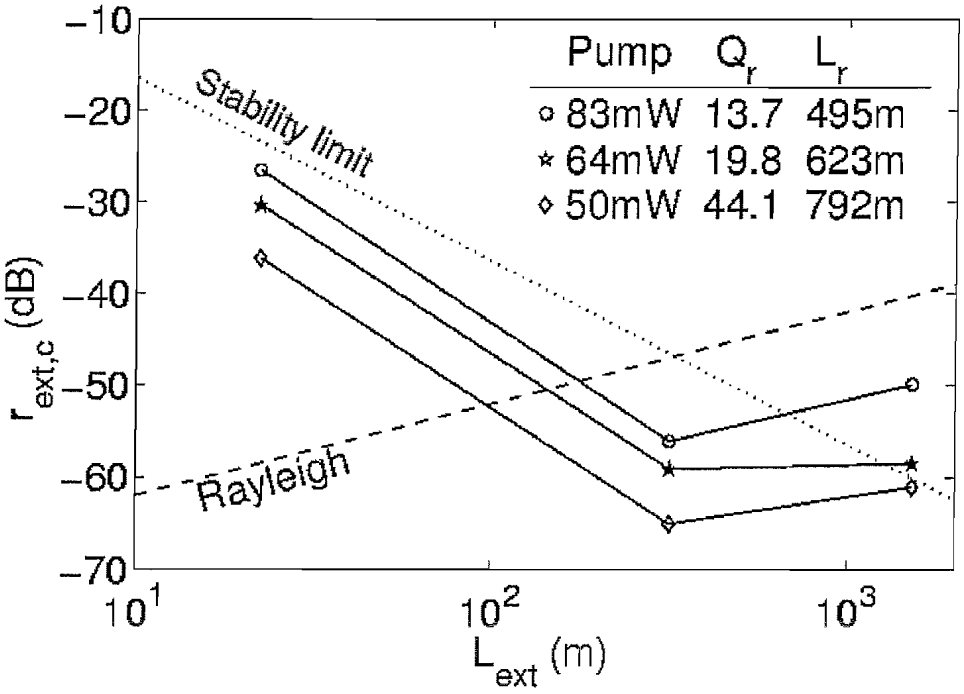

Figure 7.5. Measured critical external reflection coefficient $r_{\mathrm{ext,c}}$ for several external-cavity lengths L_{ext} and pump powers. According to the theory developed for semiconductor DFB lasers the laser should be stable below the "stability limit" line. However, this DFB fibre laser showed sustained relaxation oscillations in this regime (see main text). Also shown is the expected Rayleigh backscattering level of -72 dB/m from a fibre of length L_{ext}. It was confirmed experimentally that for 83 mW pump power the DFB fibre laser operation was stable when subject to Rayleigh backscattering from $L_{\mathrm{ext}} < 135\,\mathrm{m}$.

is expected because the more the relaxation oscillations of the solitary laser are damped (decreasing Q_r) the higher the backreflection level has to be to drive such oscillations. For $L_{\mathrm{ext}} = 1518\,\mathrm{m}$ deviations from $r_{\mathrm{ext,c}} \propto Q_r^{-1}$ were observed. A possible explanation is that Q_r of the solitary lasers was modified slightly by the presence of external Rayleigh backscattering from the long length of fibre.

The estimated limit below which the DFB fibre laser should always be stable [107, 77] is shown as a dotted line in Figure 7.5. However, sustained relaxation oscillations of the DFB fibre laser were observed in this regime. This could have been partly due to uncertainties of the parameters used to estimated the stability limit. Another explanation could be that DFB fibre lasers with a comparatively high Q_r become unstable because Q_r will be modified to some extent by the external reflections.

7.4.2 Rayleigh scattering

For 83 mW of pump power at 1480 nm, the DFB fibre laser (output power 400 μW) was found to be stable when subjected to Rayleigh scattering from $\leq$ 135 m of fibre, corresponding to a reflectivity of −51 dB. At 135 m noise burst could be observed in response to acoustic noise, such as clapping hands in the laboratory. For a fibre length above 200 m (reflectivity −49 dB) the laser was continuously pulsing. The dashed line in Figure 7.5 shows the typical Rayleigh backreflection level of −72 dB/m. The cross-over point with the straight line connecting the points of the discrete reflection measurements is at 175 m, (reflectivity −50 dB) which is in good agreement with the Rayleigh backscattering measurements.

7.5 Experimental arrangements — backreflections from grating sidelobes

Backreflections from grating sidelobes and their impact on laser stability and measurement resolution were studied with the experimental arrangement shown in Figure 7.6. One dual polarisation DFB fibre laser (DFB1) was set up in a similar way as the sensor described in Section 5.1.3. Its output was split by a 50:50 coupler and could be detected in one arm after an isolator. The other arm was connected to the output of a second DFB fibre laser (DFB2). Its output could be monitored at the forth arm of the 50:50 coupler. A variable attenuator was inserted between the two DFB fibre laser, reducing backreflections from grating sidelobes and the laser output power from one laser incident on the other. The two DFB fibre lasers were pumped by two separate pump diodes, thereby avoiding laser intensity noise in the second DFB fibre laser as a result of variable pump absorption in the first. The latter would be caused by laser intensity noise in the first DFB fibre laser. Because only one 1480 nm pump diode was available DFB2 was pumped at 980 nm. Taking the 50:50 coupler and isolator into account the output powers of the DFB fibre lasers were $P_{\mathrm{DFB1}} = 230\,\mu$W and $P_{\mathrm{DFB1}} = 200\,\mu$W for launched pump powers of 82 mW at 1480 nm and 50 mW at 980 nm, respectively. Both lasers were placed together in

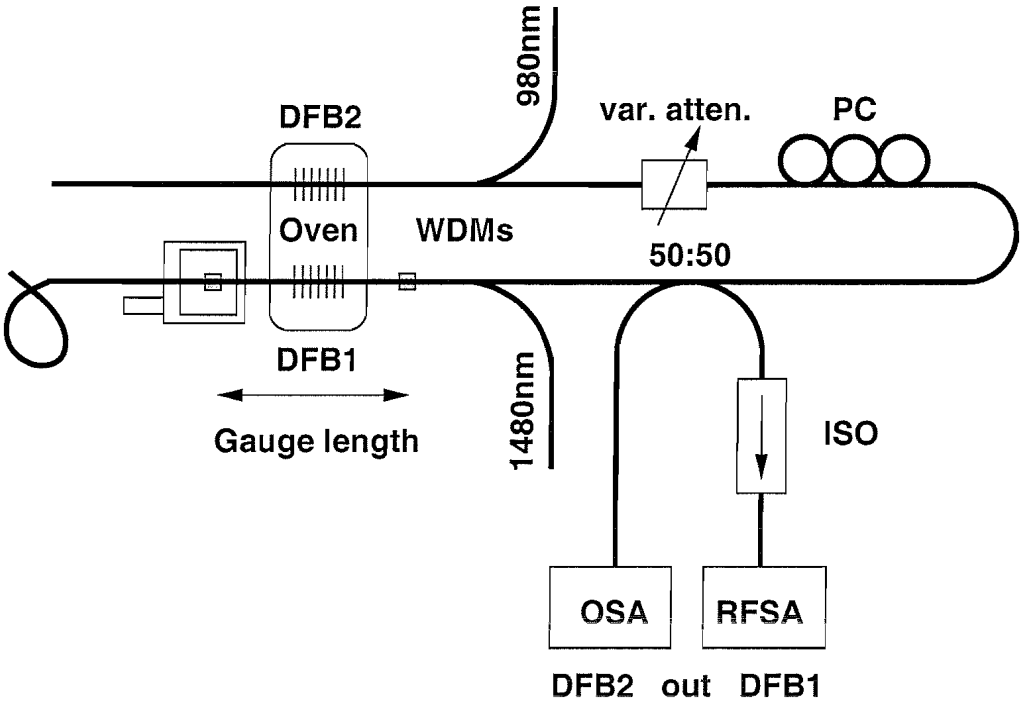

Figure 7.6. Experimental arrangement to investigate laser stability and measurement resolution as a function of backreflections from a second DFB fibre laser. The wavelength difference between the two DFB fibre lasers could be strain tuned from -1 to $+2.5$ nm. A variable attenuator (var. atten.) was used to adjust the level of coherent backreflections from grating sidelobes of DFB2 into DFB1. PC=polarisation controller, WDM=wavelength division multiplexer, ISO=isolator, OSA=optical spectrum analyser, RFSA=RF spectrum analyser.

an oven to prevent relative wavelength drifts due to variable environmental temperature differences. The wavelength separation $\lambda_{\mathrm{DFB2}} - \lambda_{\mathrm{DFB1}}$ between the two lasers could be tuned from -1 to $+2.5$ nm. The wavelength tuning was carried out in two steps: coarse strain tuning of DFB2 over ≈ 2.5 nm and fine tuning with a manual translation stage of DFB1 over 1 nm. The amplitude of the backreflections from DFB2 into DFB1 could be adjusted by a variable attenuator between the two DFB fibre lasers.

7.6 Reduction of sensor accuracy

The experiments described in Section 7.4 clearly show that amplitude and phase of backreflections have a critical influence on the stability of DFB fibre lasers. The

grating sidelobes in a serially multiplexed DFB fibre laser sensor network represent reflectors with wavelength dependent reflectivity and phase delay. In addition narrow linewidth optical signals emitted from other DFB fibre laser sensors are incident on a particular DFB fibre laser.

The reflectivity and time delay spectrum of DFB2 is shown in Figure 7.7. The decreasing reflectivity with increasing distance from the reflection peak is expected from modelled grating spectra. The increasing time delay fluctuations were probably induced by phase noise in the grating and in the detection electronics. Modelled time delay spectra of uniform noiseless gratings predict a sharp decrease of time delay variations with increasing distance from the centre wavelength.

The top axis of the Figure shows the wavelength difference between the two DFB fibre lasers. A guardband of ≈ 1 nm would typically be left between the wavelengths of multiplexed passive and active Bragg grating sensors to avoid ambiguous sensor readouts.

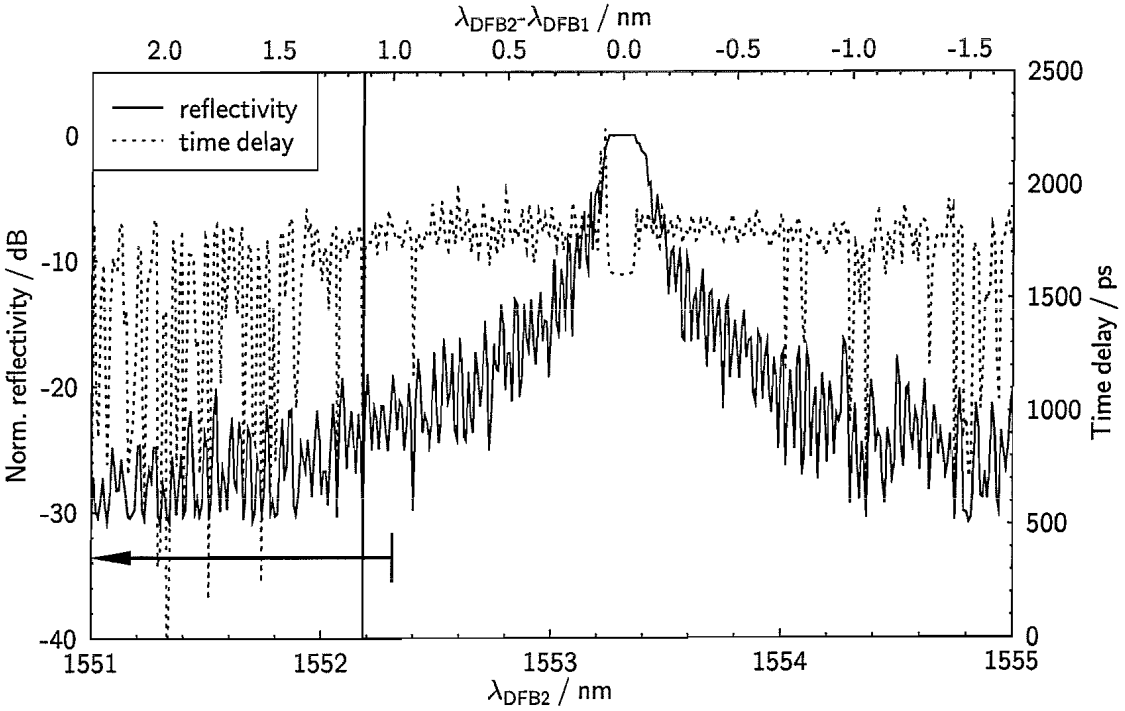

Figure 7.7. Reflectivity and time delay spectrum of DFB2. The wavelength difference between the two multiplexed DFB fibre lasers (see Figure 7.6) is shown on the top x-axis. The effects of backreflections from DFB2 into DFB1 have been characterised at the wavelength differences indicated by the thick vertical line and the horizontal arrow.

The channel spacing in current telecommunication networks is 100 GHz≙0.8 nm and is likely to decrease to 50 GHz≙0.4 nm or even 25 GHz≙0.2 nm in the near future. For the latter two cases backreflections from grating sidelobes would increase significantly unless the DFB gratings are apodised.

Although the wavelength difference between the two DFB fibre laser sensors should be kept above $\approx$ 1 nm, first the worst case scenario was investigated with maximum backreflection from the grating stopband of DFB2. The wavelength of DFB1 was strain tuned from 0.42 nm below to 0.42 nm above the operating wavelength of DFB2 by applying a strain of $0 - 707\,\mu\epsilon$. The wavelength and polarisation beat frequency of DFB1 as a function of applied strain are shown in Figure 7.8 for $P_{\mathrm{DFB2}} = 0$ W and $P_{\mathrm{DFB2}} = 200\,\mu$W, of which 50 % where incident on DFB1. Straight lines were fitted to the data. Small deviations from the expected linear responses were caused by the uneven motion of the manual translation stage. Wavelength

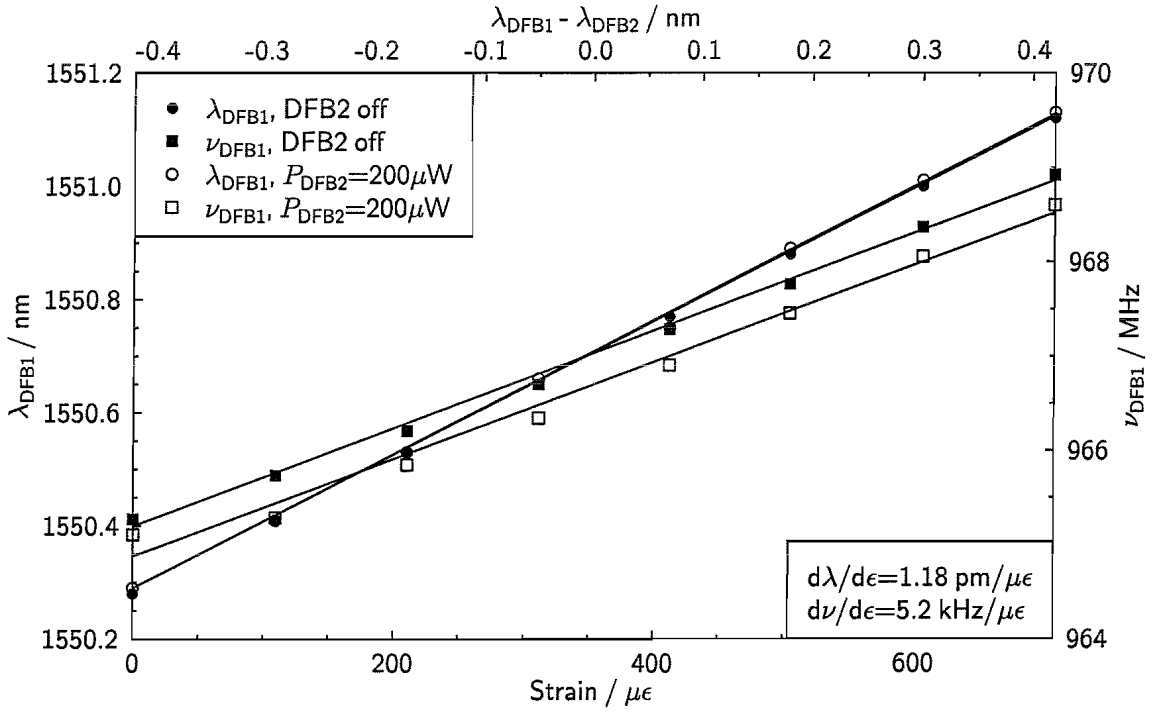

Figure 7.8. Wavelength and beat frequency of DFB1 as a function of applied strain for DFB2 being switched off and operating with 200 μW output power, respectively. The wavelength and frequency response do not depend on the operation of DFB2. Small deviations from the fitted straight lines are due to the uneven motion of the manual translation stage used to strain DFB1. A temperature increase of $\approx +0.3\,^{\circ}$C is the likely reason for the beat frequency downshift of $\approx$ 500 kHz between the two sets of measurements.

and beat frequency response were independent of the mode of operation of DFB2. The beat frequency was shifted down between the two measurements by $\approx 500\,\text{kHz}$, which is probably due to a small temperature change of $\approx +0.3\,^{\circ}\text{C}$ between the two measurements. The beat frequency response is in agreement with the responses of the sensors in Section 5.2.1.

While the sensor response was not altered by the presence of the second DFB fibre laser it is of great interest to investigate how the sensor accuracy depends on backreflections, in particular on those from grating sidelobes of DFB2. Optical frequency, or wavelength, noise and polarisation beat frequency noise determine the measurement resolution of the sensor. The accuracies of the wavelength and polarisation beat frequency measurements $\sigma(\lambda_x)$ and $\sigma(\nu)$ (see Section 5.1.5) are directly proportional to this noise.

Optical frequency noise as a function of backreflection intensity has been measured by Rønnekleiv and Løvseth [65]. The maximum frequency variation was $\pm 170\,\text{kHz}$ caused by Rayleigh backscattering from 13 km of fibre ($\hat{=} -31\,\text{dB}$ backscattered power). This optical frequency noise corresponds to wavelength fluctuations of $\Delta\lambda = c/\nu^2\,\Delta\nu \approx \pm 1\,\text{fm}$ which is two orders of magnitude smaller than the wavelength resolution of the wavemeter used to measure the wavelength of the DFB fibre laser sensor in Section 5.1. Optical frequency noise of DFB fibre lasers is therefore negligible for most practical strain and temperature sensors.

In the following experiment the fluctuations of the polarisation beat frequency of DFB1, i.e. the second parameter of the polarimetric strain and temperature sensor described in Section 5.1, has been measured as a function of the backreflection level of grating sidelobes.

While the instantaneous linewidth of the polarisation beat frequency signal remained at around 10 kHz, its centre frequency fluctuated considerably as a result of backreflections. Figure 7.9 shows the FWHM of the fluctuations of the beat frequency signal $\text{FWHM}(\nu)$ as a function of wavelength separation for three cases of backreflection: DFB2 lasing with 60 μW output power, DFB2 off, and DFB2 off with 20 dB additional attenuation induced by the variable attenuator between the two lasers. The frequency fluctuations were measured by averaging the instantaneous

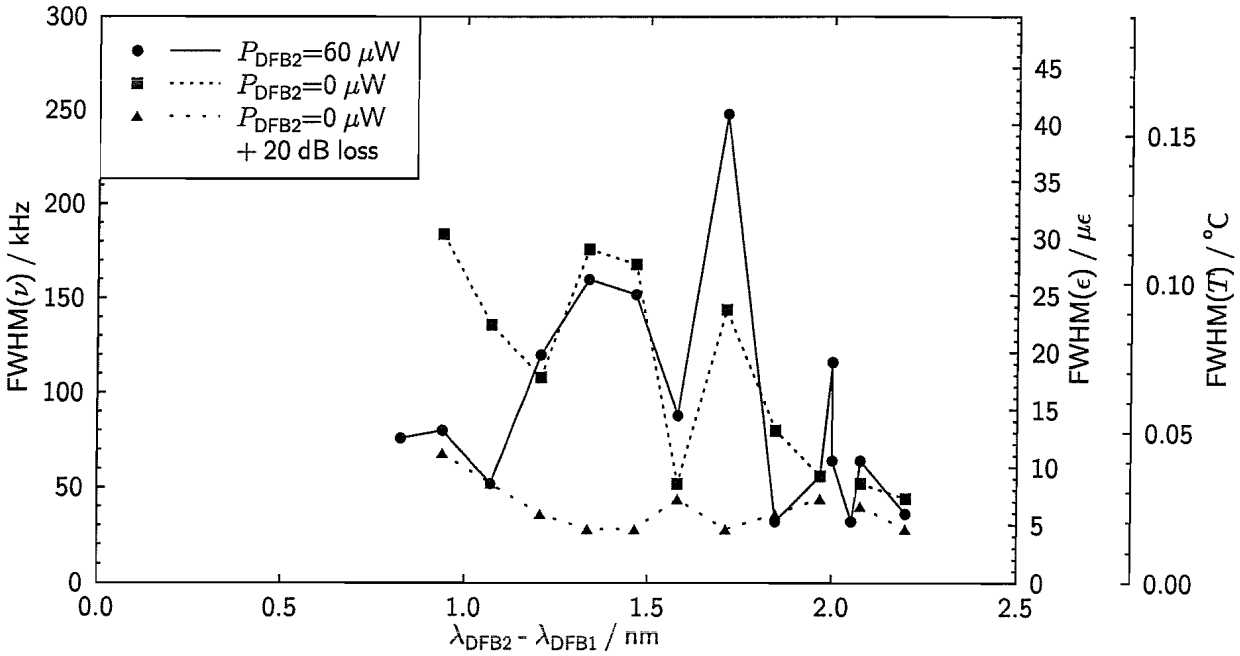

Figure 7.9. FWHM of the polarisation beat frequency fluctuations FWHM(ν) of DFB1 as a function of wavelength separation between the two DFB lasers. The effects of backreflections from DFB2 into DFB1 are shown for three different cases: DFB2 operating with 60 μW output power, DFB2 off, and DFB2 off with 20 dB additional attenuation between the two lasers. DFB1 was operating with an output power of 250 μW in all three cases. The frequency fluctuations are measured with a resolution bandwidth of 30 kHz. The right axes show the corresponding FWHM of strain and temperature measurements, i.e. the measurement accuracy. FWHM(ν) was dependent on the backreflection level from the sidelobes of DFB2. Additional attenuation of backreflection levels significantly reduced FWHM(ν).

beat frequency signals on the RF spectrum analyser whose a resolution bandwidth had been set to 30 kHz. As expected, FWHM(ν) generally decreased with increasing wavelength separation because of the decreasing reflectivity of the sidelobes of DFB2. However, large fluctuations of FWHM(ν) were observed as the wavelength difference was increased. An explanation is the wavelength dependent backreflection level into DFB1, caused by the sidelobes of DFB2. The fluctuations of FWHM(ν) were of the same order of magnitude whether DFB2 was operating or turned off. Hence, there was no evidence that the optical output of DFB2 affected DFB1 at wavelength separations > 1 nm, although the ratio $0.5\,P_{DFB2}/P_{DFB1} = r_{ext} = -9.2$ dB[8] was high

[8]The factor 0.5 accounts for the 50:50 coupler, so only half of P_{DFB2} is incident on DFB1.

compared to reflection levels in the previous experiments. The FWHM(ν) could be reduced to the measurement resolution of 30 kHz by introducing an additional loss of 20 dB between the two DFB fibre lasers.

These results can be interpreted by keeping in mind the difference between coherent backreflection from grating sidelobes and the out-of-resonance optical signal from DFB2. Similar to backreflections from discrete reflectors and Rayleigh backscattering coherent backreflection from grating sidelobes cause laser instabilities. These can be reduced by decreasing the backreflection coefficient, i.e. by introducing additional loss between the two DFB fibre lasers. Compared to coherent backreflections from grating sidelobes the output of DFB2, which is not in resonance with the optical field inside DFB1 because of their wavelength mismatch, has an insignificant effect on beat frequency fluctuations and measurement accuracy of the sensor.

Figure 7.9 shows that if the temperature resolution of $\pm 6 \times 10^{-3}$°C reported in Section 5.1.5 should not be exceeded the maximum permissable backreflection level is equal to the DFB2 grating reflectivity at $\lambda_{\mathrm{DFB2}} - \lambda_{\mathrm{DFB1}} = 1.4\,\mathrm{nm}$ minus a further 20 dB attenuation. From Figure 7.7 one finds a reflectivity of $\approx -22\,\mathrm{dB}$ at this wavelength separation. Therefore the total backreflection into the DFB fibre laser sensor should not exceed $r_{\mathrm{ext}} \approx -42\,\mathrm{dB}$. The typical wavelength separation between multiplexed FBG sensors is 1 nm. If the DFB fibre laser sensors are employed in a serially multiplexed network they have to be apodised in order to suppress sideband reflections below $\approx -42\,\mathrm{dB}$. An alternative approach is to multiplex the DFB fibre lasers in a parallel sensor network.

7.7 Potential role of the grating time delay

It has been shown theoretically [107] and experimentally (Figure 7.4) that the laser stability depends on the magnitude and phase of the backreflections. The grating sidelobes are not only described by their wavelength dependent reflectivity but also by the wavelength dependent time delay they impose onto the reflected light. One can therefore expect that small wavelength variations of the light emitted by DFB1 lead to backreflections with varying intensity P_{refl} and roundtrip phase Φ_{ext}. On

the other hand, for small wavelength variations $\Delta\lambda$ a cleaved fibre end represents a reflector with constant reflectivity and roundtrip delay if phase changes $\Delta\Phi_{\text{ext}} = 2\pi L_{\text{ext}}/\lambda^2\,\Delta\lambda$ due to the varying wavelength can be neglected.

In a preliminary experiment frequency and Q-factor of the relaxation oscillations and variations of the polarisation beat frequency FWHM(ν) were measured as a function of backreflection levels from one grating sidelobe and a cleaved fibre end. In both cases the external cavity length was $L_{\text{ext}} \approx 4\,\text{m}$. For reflections from grating sidelobes the wavelength difference between the two DFB fibre lasers in Figure 7.6 was kept at 1.13 nm and DFB2 was switched off. The resolution bandwidth of the RFSA was 10 kHz. The DFB fibre laser was pumped with 82 mW at 1480 nm and emitted $P = 230\,\mu\text{W}$.

Figure 7.10 shows FWHM(ν), ν_r and Q_r as a function of the optical power reflection coefficient r_{ext} for reflections from the chosen grating sidelobe. The top graph shows that FWHM(ν) remained between 15–35 kHz for $r_{\text{ext}} < -42\,\text{dB}$ For larger backreflections levels FWHM(ν) increased steeply. This behaviour is in agreement with the results shown in Figure 7.9 where a value of $r_{\text{ext}} \approx -42\,\text{dB}$ was found above which FWHM(ν) would increase above $\approx 30\,kHz$. It can also be seen in Figure 7.9 that at a wavelength separation of 1.13 nm FWHM(ν) increased significantly when the backreflection level was increased by 20 dB.

The relaxation oscillation frequency ν_r remained constant below a backreflection coefficient $r_{\text{ext}} = -50\,\text{dB}$ and increased above. Around the same r_{ext} Q_r decreased in a step-like function. The decreasing Q_r-factor is a clear sign of increasing laser stability (see also Figure 7.3). A possible explanation is that the DFB fibre laser moved from one stability regime into another [107, 109].

Figures 7.11 shows the same laser parameters when the backreflections originated from the fibre end cleave. Qualitatively the DFB fibre laser behaved similarly to the previous case. However, the laser appeared to be less stable as for $r_{\text{ext}} < -37\,\text{dB}$ Q_r was higher. It is intuitively reasonable that as a result of small lasing wavelength fluctuations the roundtrip phase delay $\Phi_{\text{ext}}(\lambda)$ caused by the wavelength dependent time delay of the grating sidelobe could have stabilised the DFB fibre laser. This behaviour is similar to a harmonic oscillator which is driven by a periodic external

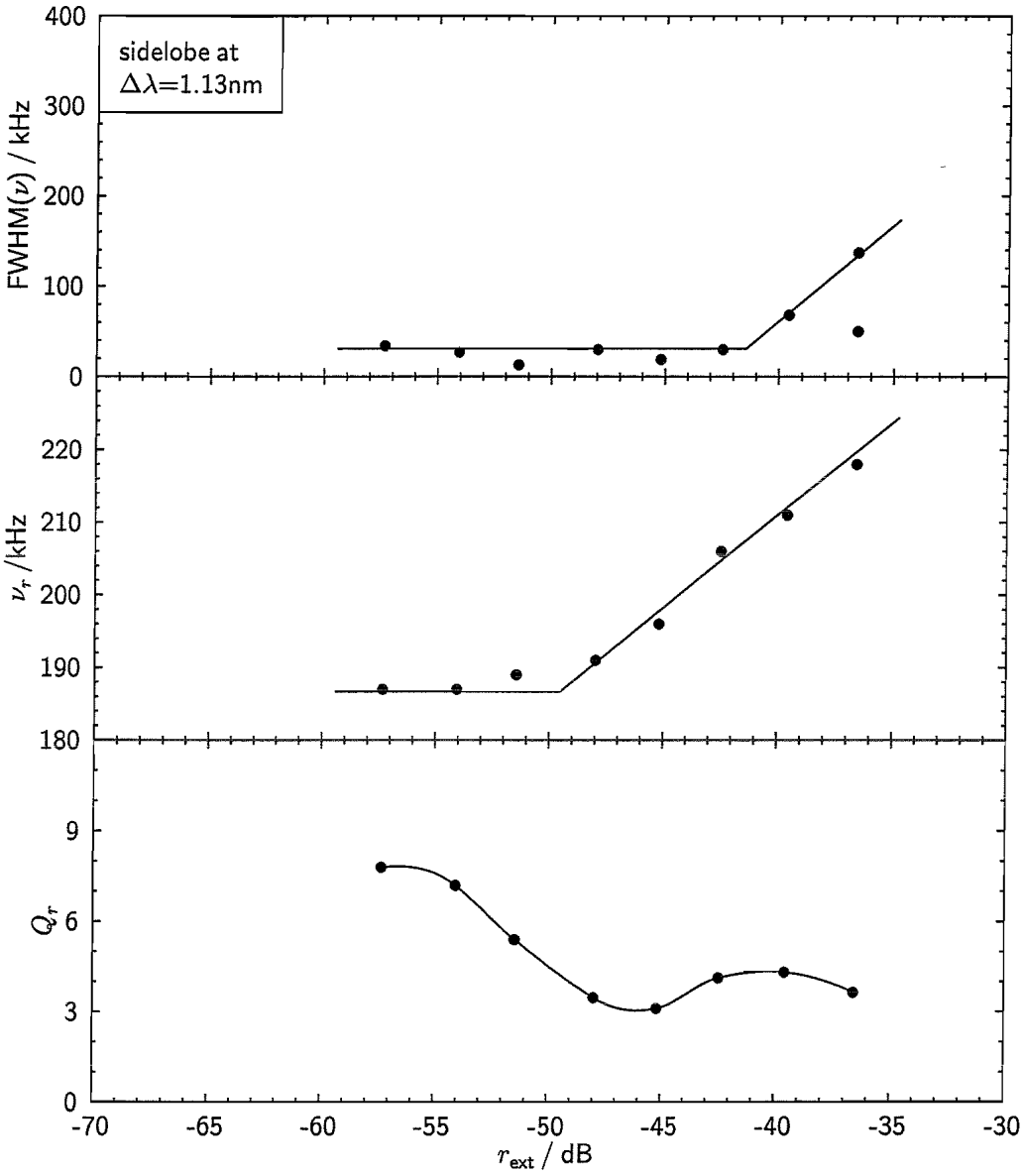

Figure 7.10. FWHM of the polarisation beat frequency fluctuations, relaxation oscillation frequency ν_r and Q-factor Q_r as a function of the reflection coefficient r_{ext} for reflections from a grating sidelobe. The wavelength difference between the two DFB fibre lasers was 1.13 nm. DFB2 remained unpumped during these measurements. Solid lines are superimposed on the data to guide the eye. The increase of FWHM(ν) is in agreement with the results presented in Figure 7.9. The DFB fibre laser appears more stable, i.e. smaller Q_r, under backreflections from grating sidelobes than from a fibre end cleave (see Figure 7.11). The resolution bandwidth of the RFSA was 10 kHz.

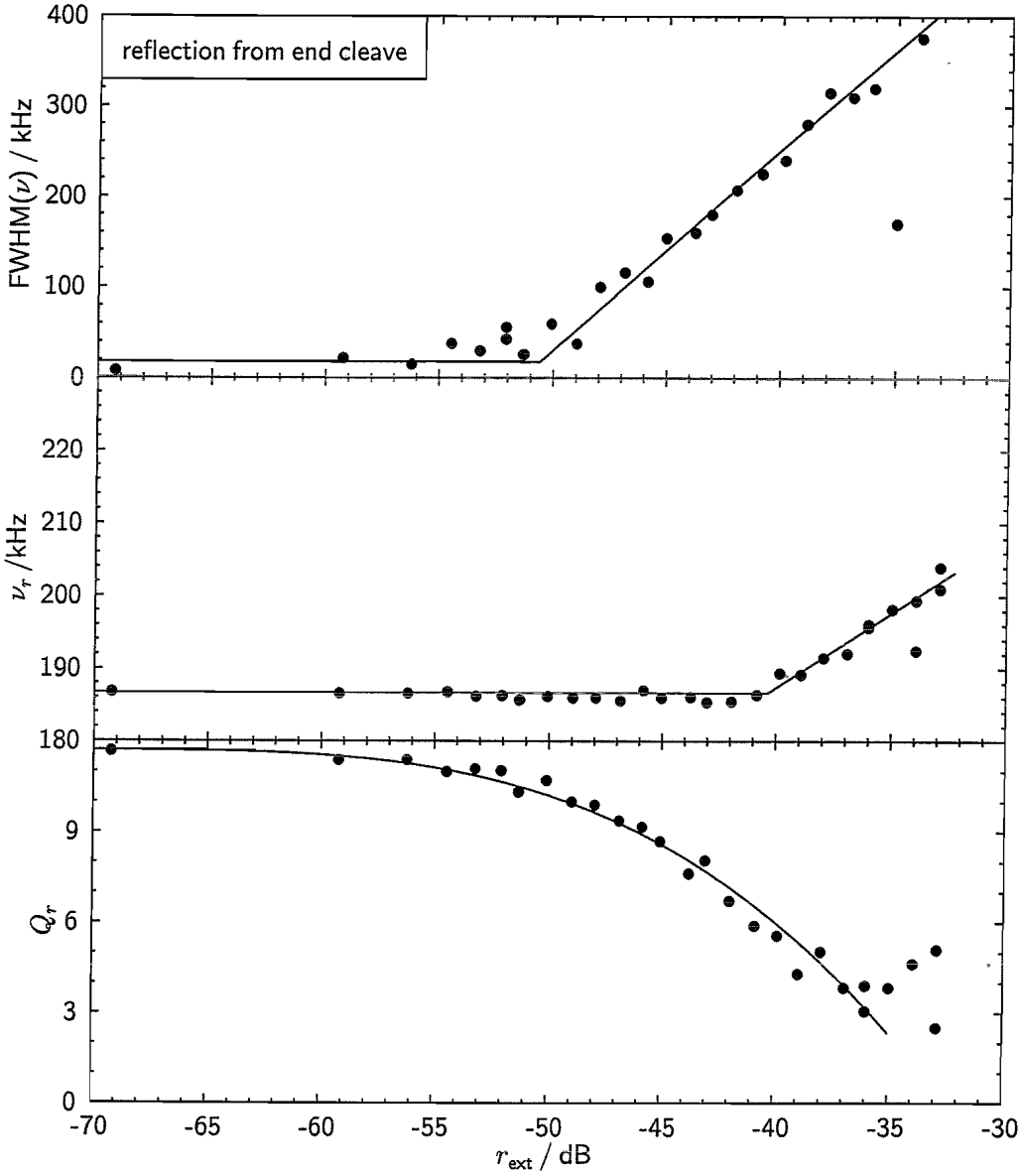

Figure 7.11. FWHM of the polarisation beat frequency fluctuations, relaxation oscillation frequency ν_r and Q-factor Q_r as a function of the reflection coefficient r_{ext} for reflections from a fibre end cleave. Solid lines are superimposed on the data to guide the eye. In this case FWHM(ν) is larger than for backreflections from grating sidelobes.

force whose phase is time dependent. It can be seen in the top graph in Figure 7.11 that the DFB fibre laser tolerated only $r_{\text{ext}} = -51\,\text{dB}$ backreflection from the fibre cleave before FWHM(ν) increased steeply upon which the potential sensor resolution would have decreased.

Further theoretical and experimental investigations are needed to understand in detail the observed dependence of FWHM(ν), ν_r and Q_r on r_{ext} and Φ_{ext}. The steady state DFB fibre laser model presented in Chapter 3 includes the Er^{3+}-ion pairs whose population dynamics play an important role in the laser stability. This model could potentially be developed into a dynamic model. In order to investigate time delay variations due to lasing wavelength fluctuations gratings with constant reflectivity but different chirp could be used as reflectors.

7.8 Conclusion

As expected from the behaviour of their semiconductor counterparts DFB fibre lasers were susceptible to external feedback from discrete reflectors and Rayleigh scattering which lead to increased intensity noise.

The tolerable external optical power incident on a DFB fibre laser depended on the external cavity length, the phase of the incident optical wave and the relaxation oscillation Q-factor Q_r of the DFB fibre laser. Er^{3+}-ion pairs which undergo homogeneous upconversion acted as saturable absorbers. At low pump and lasing power their absorption coefficient was high and very sensitive to power fluctuations at the lasing wavelength, caused e.g. by external feedback. This resulted in the experimentally observed noise bursts and sustained relaxation oscillations of the DFB fibre laser. With increasing pump and lasing power the loss caused by Er^{3+}-ion pairs became smaller and less sensitive to those power fluctuations. The DFB fibre laser therefore became more stable, which was reflected in a decreasing Q-factor of the relaxation oscillations.

Under typical operating conditions of a DFB fibre laser sensor, i.e. 83 mW pump power at 1480 nm and 400 μW output power, Rayleigh backscattering from up to about 135 m of fibre were tolerable without the onset of intensity noise. This would

limit the length of lead fibre acceptable for a remote sensor application. Longer fibre lengths might be possible if Q_r could be decreased, e.g. by reducing the number of saturable absorbers, i.e. Er^{3+} ion pairs.

For the first time backreflections from grating sidelobes of another DFB fibre lasers have been investigated. Wavelength dependent phase delay of the backreflected light seemed to increase the stability of DFB fibre lasers compared to discrete backreflections from a fibre end cleave.

Beside the output power fluctuations the effect of external feedback on the measurement resolution of the polarisation beat frequency was investigated. It was found that in order to maintain the sensor resolution achieved for a single DFB fibre laser sensor in Section 5.1 only −42 dB backreflection were permissible. This low backreflection level will usually be exceeded by standard multiplexed DFB fibre laser sensors. Apodisation of the DFB fibre laser grating might be a solution to this problem.

8 Conclusion

Although a large variety of fibre optic strain and temperature sensors has been developed over the last two decades they only play a small role compared to well established conventional sensors. Greater acceptance and widespread use of fibre optic strain and temperature sensors can only be achieved if their well known technological advantages are paired with lower cost and higher practicability.

The aim of this project was to address these two important issues and develop new accurate, practical and cost effective fibre optic sensors for simultaneous strain and temperature measurements which can be used in a variety of applications such as aerospace, marine and civil engineering. Based on the advanced and relatively widely accepted technology of passive fibre Bragg grating sensors two novel polarimetric DFB fibre laser, i.e. active fibre Bragg grating, sensors were developed.

The first type of polarimetric DFB fibre laser sensor operated in a single longitudinal mode which split into two polarisation modes as a result of a small birefringence of the fibre and the DFB grating. Wavelength of one polarisation mode and the RF beat frequency between the two polarisation modes were used to determine strain and temperature simultaneously. The maximum demonstrated operating temperature of this DFB fibre laser sensor was 200 °C but experimental and theoretical evidence suggests that operation up to 400 °C is possible. The measurement accuracy of the sensor was $\pm 3\,\mu\epsilon$ and $\pm 0.04\,^{\circ}\mathrm{C}$ while its resolution was $\pm 0.4\,\mu\epsilon$ and $\pm 6 \times 10^{-3}\,^{\circ}\mathrm{C}$. These specifications are suitable for many applications, especially in the field of civil engineering. The accuracy and resolution could potentially be increased further by using more accurate calibration equipment, reducing external noise sources such as pump power fluctuations and replacing the employed com-

mercial multi-purpose laboratory test equipment by a purpose built interrogation system. However, the cost and practicality of the various interrogation systems have to be kept in mind.

Three single longitudinal mode polarimetric DFB fibre laser sensors were bonded into prototypes of miniature protective tubes and subsequently embedded in a small concrete laboratory test specimen. These tubes allowed the fibre optic sensors to be installed by personal who was unfamiliar with such sensors. Thermal cycling and a three point bending test were carried out as a proof of principle. It was demonstrated that a protective tube made from epoxy resin provides sufficient strain transfer from the concrete to the DFB fibre laser sensor. Potentially the epoxy resin could be moulded into other shapes, depending on the application. Building on the experience gained from this simple demonstration further applications of this simultaneous strain and temperature sensor should emerge.

Detailed experiments have revealed a reduction of the strain and temperature measurement accuracy up to a factor of two and five, respectively, as a result of external feedback into DFB fibre laser sensors and pump induced self-heating. These two effects are likely to occur if these sensors are multiplexed or installed remotely. It is expected that the detrimental effects of external optical feedback could be reduced by optimising the DFB grating design and reducing the number of paired Er^{3+}-ions, which act as saturable absorbers. It was shown that sufficient thermal contact between the DFB fibre laser and its environment reduces the self-heating of DFB fibre lasers.

The complexity of the interrogation system of the single longitudinal mode DFB fibre laser sensor could be reduced to a minimum with the development of the second type of polarimetric DFB fibre laser sensor. This birefringent DFB fibre laser operated in two longitudinal modes which split into two polarisation modes respectively. The longitudinal mode spacing was chosen small enough to lie within the RF domain. Therefore, the strain and temperature dependent beat frequencies between longitudinal and polarisation modes could be measured with a single frequency meter without the need for cumbersome wavelength-to-electrical signal conversion. In a first laboratory demonstration a single commercial RF spectrum

analyser was used but purpose build frequency meters would lead to an even simpler, more compact and cheaper interrogation system. The sensor accuracy was $\pm 15\,\mu\epsilon$ and $\pm 0.2\,^{\circ}\mathrm{C}$ limited by an unexpected strain-temperature cross-sensitive response of the longitudinal beat frequency which was probably caused by previously undetected small temperature and strain dependences of the strain-optic and thermo-optic coefficients, respectively. Increasing the longitudinal mode spacing by operating the $Er^{3+}:Yb^{3+}$ DFB fibre laser simultaneously in the 1060 nm and 1550 nm band and employing only the two polarisation beat frequencies might be a way to eliminate the unwanted cross-sensitive response while still operating entirely in the RF domain. Mode competition, spatial hole burning and self-heating together with small fabrication errors limited the strain and temperature measurement range. Minimising fabrication errors and/or spatially separating the internal intensity distributions of the two longitudinal modes along the DFB fibre laser are potential ways to increase its measurement range. In the medium term such an improved version of the dual longitudinal mode polarimetric DFB fibre laser sensor could be employed in a real aerospace or civil engineering application.

Self-heating of DFB fibre lasers, caused by non-radiative transitions, was identified as a major problem area. Heat-induced non-uniform grating chirp was responsible for a significant reduction of the output power and an increase of the lasing wavelength. Under extreme self-heating the DFB fibre lasers ceased to operate. Sufficient heat transfer from the laser to its environment could prevent or at least reduce these unwanted effects. It was pointed out that heat management would play an important role in the design of DFB fibre laser packages for telecommunication applications.

In order to further the understanding of these unwanted effects a DFB fibre laser model was developed which for the first time included self-heating caused by non-radiative transitions. The conventionally used two-level Er^{3+} laser model was extended to take two Yb^{3+}- and four Er^{3+}-energy levels and the relevant radiative and non-radiative transitions into account. In addition, homogeneous upconversion of a fraction of paired Er^{3+}-ions was included. The traditional Runge-Kutta algorithm for solving the laser rate equations was replaced by a new, about three orders

of magnitude faster, iterative approach based on analytical solutions of the rate equations. The model calculated laser output power, lasing wavelength, internal pump and lasing intensities, population density distributions, core and surface temperature distributions and grating chirp. The increased speed of the new algorithm allowed to almost instantly observe the influence of several physical parameters on the predicted behaviour of a DFB fibre laser. The unknown values of those parameters could be determined by comparing the predicted laser behaviour with experimental data. This comparison also revealed that, in a next step, additional optical processes, e.g. ASE, have to be incorporated into the model to fully describe the DFB fibre laser. Additional spectroscopic investigations of various $Er^{3+}:Yb^{3+}$ fibres would be needed to provide enough experimental data for a meaningful extension of the model.

In conclusion DFB fibre lasers are excellent candidates for successful strain and temperature sensors and for optical sources in telecommunication applications. Despite their apparently simple design and mode of operation some important problems and fundamental questions are still waiting for solutions and answers.

References

[1] J. Gowar, *Optical Communication Systems*, 2nd edition (Prentice-Hall, New York, 1993)

[2] K. T. V. Grattan, and T. Sun, "Fiber optic sensor technology: an overview", *Sensors and Actuators A* **82**, pp. 40–61 (2000)

[3] E. J. Friebele, "Fiber Bragg Grating Strain Sensors: Present and future applications in smart structures", *Optics and Photonics News*, August 1998, pp. 33–37

[4] E. Udd, "Fibre optic smart structures for aerospace and natural applications", *Proc. SPIE* **2574**, pp. 2–5 (1995)

[5] D. R. Hjelme, L. Bjerkan, S. Neegard, J. S. Rambech, and J. V. Aarsnes, "Application of Bragg grating sensors in the characterization of scaled marine vehicle models", *Appl. Opt.* **36**, pp. 328–336 (1997)

[6] P. Foote and I. Read, "Sea trials of a fibre Bragg grating based 'smart' mast", in *IEE Colloquium on Optical Fibre Gratings*, IEE, London, pp. 12/1–6 (1999)

[7] R. K. Krishnamoorthy, A. Belarbi, K. Chandrashekhara, and S. E. Watkins, "Hybrid composite rebars for smart concrete structures", *Proc. SPIE* **3043**, pp. 65–71 (1997)

[8] P. M. Nellen, P. Anderegg, R. Brönnimann, and U. Sennhauser, "Application of fiber optical and resistance strain gauges for long-term surveillance of civil engineering structures", *Proc. SPIE* **3043**, pp. 77–86 (1997)

[9] L. Thévenaz, M. Facchini, A. Fellay, P. Robert, D. Inaudi, and B. Dardel, "Monitoring of large structure using Brillouin fibre sensing", in *13th Int. Conf. Opt. Fiber Sens., Proc. SPIE* **3746**, pp. 345–348 (1999)

[10] G. Wehrle, H. J. Kalinowski, P. I, Torres, and L. C. Guedes Valente, "Fibre optic Bragg grating strain sensor used to monitor the respiratory system", in *14th Int. Conf. Opt. Fiber Sens., Proc. SPIE* **4185**, pp. 310–313 (2000)

[11] J. T. Kringlebotn, W. H. Loh, and R. I. Laming, "Polarimetric Er^{3+}-doped fiber distributed-feedback laser sensor for differential pressure and force measurements", *Opt. Lett.* **21**, pp. 1869–1871 (1996)

[12] L. D. Landau and E. M. Lifshitz, *Theory of Elasticity*, 1st edition, (Pergamon Press, 1959)

[13] C. Gerthsen, H. O. Kneser, and H. Vogel, *Physik*, 16th edition, (Springer Verlag, Berlin, 1989)

[14] C. D. Butter and G. B. Hocker, "Fibre optic strain gauge", *Appl. Opt.* **17**, pp. 2867–2869 (1978)

[15] E. Udd, "An overview of fiber-optic sensors", *Rev. Sci. Instrum.* **66**, pp. 4015–4030 (1995)

[16] A. D. Kersey, M. A. Davis, H. J. Patrick, M. LeBlanc, K. P. Koo, C. G. Askins, M. A. Putnam, E. J. Friebele, "Fiber grating sensors", *J. Lightwave Technol.* **15**, pp. 1442–1463 (1997)

[17] Y.-J. Rao, "In-fibre Bragg grating sensors", *Meas. Sci. Technol.* **8**, pp. 355–375 (1997)

[18] I. Bennion, J. A. R. Williams, L. Zhang, K. Sugden, and N. J. Doran, "UV-written in-fibre Bragg gratings", *Opt. Quantum Electron.* **28**, pp. 93–135 (1996)

[19] A. Othonos, "Fiber Bragg gratings", *Rev. Sci. Instrum.* **68**, pp. 4309–4341 (1997)

[20] K. O. Hill and G. Meltz, "Fiber Bragg grating technology fundamentals and overview", *J. Lightwave Technol.* **15**, pp. 1263–1276 (1997)

[21] C. Belleville and G. Duplain, "White-light interferometric multimode fiber-optic strain sensor", *Opt. Lett.* **18**, pp. 78–88 (1993)

[22] J. J. Lesko, G. P. Carman, B. R. Fogg, W. V. Miller III, A. M. Vengsarkar, K. L. Reifsnider, and R. O. Claus, "Embedded Fabry-Perot fiber optic strain sensors in macromodel composites", *Opt. Eng.* **31**, pp. 13–22 (1992)

[23] V. Bhatia, M. B. Sen, K. A. Murphy, and R. O. Claus, "White light interferometry for highly sensitive strain and temperature measurements", in *11th Int. Conf. Opt. Fiber Sens.*, (Japan Soc. Appl. Phys., Tokyo, 1996), pp. 308–311

[24] J. Sirkis, T. A. Berkoff, R. T. Jones, H. Singh, A. D. Kersey, E. J. Friebele, and M. A. Putman, "In-line fibre etalon (ILFE) fibre-optic strain sensors", *J. Lightwave Technol.* **13**, pp. 1256–1263 (1995)

[25] D. Inaudi, A. Elamari, L. Pflug, N. Gisin, J. Brequet, and S. Vurpillot, "Low-coherence deformation sensors for the monitoring of civil-engineering structures", *Sensors and Actuators A* **44**, pp. 125–130 (1994)

[26] H. Geiger and J. P. Dakin, "Low-cost high-resolution time-domain reflectometry for monitoring the range of reflective points", *J. Lightwave Technol.* **13**, pp. 1282–1288 (1995)

[27] R. I. MacDonald, "Frequency domain optical reflectometer", *Appl. Opt.* **20**, pp. 1840–1844 (1981)

[28] A. D. Kersey, T. A. Berkoff, W. W. Morey, "Multiplexed fiber Bragg grating strain-sensor system with fiber Fabry-Perot wavelength filter", *Opt. Lett.* **18**, pp. 1370–1372 (1993)

[29] M. G. Xu, H. Geiger, J.-L. Archambault, L. Reekie, and J. P. Dakin, "Novel interrogating system for fibre Bragg grating sensors using an acousto-optic tunable filter", *Electron. Lett.* **29**, pp. 1510–1511 (1993)

[30] M. G. Xu, J.-L. Archambault, L. Reekie, and J.P. Dakin, "Discrimination between strain and temperature effects using dual-wavelength fibre grating sensors", *Electr. Lett.* **30**, pp. 1085–1087 (1994)

[31] S. M. Melle, A. T. Alavi, S. Karr, T. Conroy, K. Liu, and R. M. Measures, "A Bragg grating-tuned fiber laser strain sensor system", *IEEE Photon. Technol. Lett.* **5**, pp. 263–266 (1993)

[32] G. A. Ball, G. Meltz, and W. W. Morey, "Polarimetric heterodyning Bragg-grating fiber-laser sensor", *Opt. Lett.* **18**, pp. 1976–1978 (1993)

[33] A. T. Alavie, S. E. Karr, A. Othonos, and R. M. Measures, "A multiplexed Bragg grating fiber laser sensor system," *IEEE Phot. Technol. Lett.* **5**, pp. 1112–1114 (1993)

[34] J. Hübner, P. Varming, and M. Kristensen, "Five wavelength DFB fibre laser source for WDM systems," *Electr. Lett.*, **33**, pp. 139–140 (1997)

[35] H. H. Kee and T. P. Newson, "1.5 μm Brillouin-based fibre optic distributed temperature sensor with high spatial resolution of 20 cm", in *14th Int. Conf. Opt. Fiber Sens., Proc. SPIE* **4185**, pp. 800–803 (2000)

[36] K. Hotate and T. Hasegawa, "A correlation-based continuous-wave technique for measuring Brillouin gain spectrum distribution along an optical fiber with centimeter-order spatial resolution", in *14th Int. Conf. Opt. Fiber Sens., Proc. SPIE* **4185**, pp. 651–661 (2000)

[37] T. Horiguchi, T. Kurashima, and M. Tateda, "Tensile strain dependence of Brillouin frequency shift in silica optical fibres", *IEEE Phot. Technol. Lett.* **1**, pp. 107–108 (1989)

[38] X. Bao, D. J. Webb, and D. A. Jackson, "32-km distributed temperature sensor based on Brillouin loss in an optical fiber", *Opt. Lett.* **18**, pp. 1561–1563 (1993)

[39] M. Sudo, M. Nakai, K. Himeno, S. Suzaki, A. Wada, and R. Yamauchi, "Simultaneous measurement of temperature and strain using PANDA fiber grating", in *12th Int. Conf. Opt. Fiber Sens.*, Vol. 16, OSA Tech. Digest Series (Optical Society of America, Washington DC, 1997), pp. 170–173

[40] H. Singh and J. Sirkis, "Simultaneously measuring temperature and strain using optical fiber microcavities", *J. Lightwave Technol.* **15**, pp. 647–653 (1997)

[41] T. Erdogan, "Fiber grating spectra", *J. Lightwave Technol.* **15**, pp. 1277–1294 (1997)

[42] Y. Namihira, "Opto-elastic constant in single mode optical fibre", *J. Lightwave Technol.* **LT-3**, pp. 1078–1083 (1985)

[43] G. Meltz, W. W. Morrey, W. H. Glenn, and J. D. Farina, "In-fiber Bragg grating sensors", in *5th Int. Conf. Opt. Fiber Sens.*, Vol. 2, OSA Tech. Digest Series (Optical Society of America, Washington DC, 1988), pp. 163–166

[44] G. B. Hocker, "Fiber-optic sensing of pressure and temperature", *Appl. Opt.* **18**, pp. 1445–1448 (1979)

[45] R. M. Waxler and G. W. Cleek, "The effect of temperature and pressure on the refractive index of some oxide glasses", *J. Res. Nat. Bur. Stand.* **77A**, pp. 755–763 (1973)

[46] M. G. Xu, L. Dong, L. Reekie, J. A. Tucknott, and J. L. Cruz, "Temperature-independent strain sensor using a chirped Bragg grating in a tapered optical fibre", *Electr. Lett.* **31**, pp. 823–825 (1995)

[47] S. H. Yun, D. J. Richardson, and B. Y. Kim, "Interrogation of fibre grating sensor arrays using a wavelength-swept laser", *Opt. Lett.* **23**, pp. 843–845 (1998)

[48] G. A. Ball, W. W. Morey, and P. K. Cheo, "Single- and multipoint fiber-laser sensors", *IEEE Photon. Technol. Lett.* **5**, pp. 267–270 (1993)

[49] J. T. Kringlebotn, J.-L. Archambault, L. Reekie, and D. N. Payne, "Er^{3+}:Yb^{3+}-codoped fiber distributed-feedback laser", *Opt. Lett.* **19**, pp. 2101–2103 (1994)

[50] A. Asseh, H. Storoy, J. T. Kringlebotn, W. Margulis, B. Sahlgren, S. Sandgren, R. Stubbe, and G. Edwall, "10 cm Yb^{3+} DFB fibre laser with permanent phase shifted grating", *Electron. Lett.* **31**, pp. 969–970 (1998)

[51] J. L. Zyskind, V. Mizrahi, D. J. DiGiovanni, and J. W. Sulhoff, "Short single frequency erbium-doped fibre laser", *Electron. Lett.* **28**, pp. 1385–1387

[52] E. Rønnekleiv, M. Ibsen, M. N. Zervas, and R. I. Laming, "Characterization of fiber distributed-feedback lasers with an index perturbation method", *Appl. Opt.* **38**, pp. 4558–4565 (1999)

[53] H. Kogelnik and C. V. Shank, "Coupled-wave theory of distributed feedback lasers", *J. Appl. Phys.* **43**, pp. 2327–2335 (1972)

[54] W. H. Loh and R. I. Laming, "1.55 μm phase-shifted distributed feedback fibre laser", *Electron. Lett.* **31**, pp. 1440-1442 (1995)

[55] W. H. Loh, M. J. Cole, M. N.Zervas, S. Barcelos, and R. I. Laming, "Complex grating structures with uniform phase masks based on the moving fiber-scanning beam technique", *Opt. Lett.* **20**, pp. 2051–2053 (1995)

[56] O. Svelto, *Principles of Lasers*, 4rd edition (Plenum Press, New York and London, 1998)

[57] V. C. Lauridsen, J. H. Povlsen, and P. Varming, "Design of DFB fibre lasers", *Electron. Lett.* **34**, pp. 2028–2030 (1998)

[58] V. C. Lauridsen, J. H. Povlsen, and P. Varming, "Optimising erbium-doped DFB fibre laser length with respect to maximum output power", *Electron. Lett.* **35**, pp. 300–302 (1999)

[59] Y. Qian, P. Varming, J. H. Povlsen, and V. C. Lauridsen, "Dynamic noise responses of DFB fibre lasers in presence of pump power fluctuations", *Electron. Lett.* **35**, pp. 299–300 (1999)

[60] L. Dong, W. H. Loh, J. E. Caplen, and J. D. Minelly, "Efficient single-frequency fiber lasers with novel photosensitive Er/Yb optical fibers", *Opt. Lett.* **22**, pp. 694–696 (1997)

[61] W. H. Loh, B. N. Samson, and J. P. de Sandro, "Intensity profile in a distributed feedback fiber laser characterized by a green fluorescence scanning technique", *Appl. Phys. Lett.* **69**, pp. 3773–3775 (1996)

[62] F. Di Pasquale, "Modelling of highly-efficient grating-feedback and Fabry-Perot Er^{3+}-Yb^{3+} co-doped fiber lasers", *IEEE J. Quant. Electron.* **32**, pp. 326–332 (1996)

[63] M. Karásek and J. Kaňka, "Numerical analysis of Yb^{3+}-sensitised, Er^{3+}-doped, fibre-ring laser", *IEE Proc.-Optolecetron.* **145**, pp. 133–137 (1998)

[64] A. Yariv, *Optical Electronics*, 4^{th} edition (Saunders College Publishing, 1991)

[65] E. Rønnekleiv and S. W. Løseth, "Stability of distributed feedback fiber lasers with optical feedback" in *13th Int. Conf. Opt. Fiber Sens., Proc. SPIE* **3746**, pp. 466–469 (1999)

[66] E. Desurvire, *Erbium-doped Fiber Amplifiers: Principles and Applications*, 1^{st} edition, (John Wiley & Sons, 1994)

[67] C. Barnard, P. Myslinski, J. Chrostowski, and M. Kavehrad, "Analytical model for rare-earth-doped fiber amplifiers and lasers", *IEEE J. Quant. Electron.* **30**, pp. 1817–1830 (1994)

[68] A. E. Siegman, *Lasers*, (Oxford University Press, 1986)

[69] D. L. Dexter, "A theory of sensitized luminescence in solids", *J. Chem. Phys.* **21**, pp. 836–850 (1953)

[70] M. P. Hehlen, N. J. Cockroft, T. R. Gosnell, and A. J. Bruce, "Spectroscopic properties of Er^{3+}- and Yb^{3+}-doped soda-lime silicate and aluminosilicate glasses", *Phys. Rev. B (Condensed matter)* **56**, pp. 9302–9318 (1997)

[71] J. Nilsson, P. Blixt, B. Jaskorzynska, and J. Babonas, "Evaluation of parasitic upconversion mechanisms in Er^{3+}-doped silica-glass fibers by analysis of fluorescence at 980 nm", *J. Lightwave Technol.* **13**, pp. 341–349 (1995)

[72] E. Maurice, G. Monnom, B. Dussadier, and D. B. Ostrowsky, "Clustering-induced nonsaturable absorption phenomenon in heavily erbium-doped silica fibers", *Opt. Lett.* **20**, pp. 2487–2489 (1995)

[73] B. J. Ainslie, "A review of the fabrication and properties of erbium-doped fibers for optical amplifiers", *J. Lightwave Technol.* **9**, pp. 220-227 (1991)

[74] S. E. Koorin, *Computational Physics*, 1st edition, (Addison-Wesley, Wokingham, 1986)

[75] E. Maurice, G. Monnom, B. Dussadier, A. Saïssy, and D. B. Ostrowsky, "Thermalization effects between upper levels of green fluorescence in Er-doped silica fibers", *Opt. Lett.* **19**, pp. 990–992 (1994)

[76] P. A. Krug, M. G. Sceats, G. R. Atkins, S. C. Guy, and S. B. Poole, "Intermediate excited-state absorption in erbium-doped fiber strongly pumped at 980 nm", *Opt. Lett.* **16**, pp. 1976-1978 (1991)

[77] E. Rønnekleiv, O. Hadeler, and G. G. Vienne, "Stability of Er/Yb-doped fiber DFB lasers with external reflections", *Opt. Lett.* **24**, pp. 617-619 (1999)

[78] W. L. Barnes, R. I. Laming, E. J. Tarbox, and P. R. Morkel, "Absorption and emission cross sections of Er^{3+} doped silica fibers" *IEEE J. Quant. Electron.* **27**, pp. 1004–1010 (1991)

[79] C. Lester, A. Bjarkalev, T. Rasmussen, and P. G. Dinesen, "Modelling of Yb^{3+}-sensitised Er^{3+}-doped silica waveguide amplifiers", J. Lightwave Technol. **13**, pp. 740-743 (1995)

[80] J. Y. Allain, M. Monerie, and H. Poignant, "Ytterbium-doped fluoride fibre laser operating at 1.02 μm", *Electron. Lett.* **28**, pp. 988-989 (1992)

[81] G. P. Agrawal, A. H. Bobeck, "Modelling of distributed feedback semiconductor lasers with axially-varying parameters", *IEEE J. Quant. Electron.* **24**, pp. 2407–2414 (1988)

[82] M. Ibsen, E. Rønnekleiv, G. J Cowle, M. O. Berendt, O. Hadeler, M. N. Zervas, and R. I. Laming, "Robust high power (> 20 mW) all-fibre DFB lasers with unidirectional and truly single polarisation outputs", in *Conf. on Lasers and Electro-Optics 1999*, (Optical Society of America, Washington DC, 1999), pp. 245–246

[83] J. T. Kringlebotn, J.-L. Archambault, L. Reekie, R. I. Laming, and D. N. Payne, "Nd:YLF pumped grating-feedback $Er^{3+}:Yb^{3+}$ co-doped silica fiber laser operating at 1.49 μm", *Opt. Fib. Technol.* **2**, pp. 69–74 (1996)

[84] Y. Z. Xu, H. Y. Tam, S. Y. Liu, and M. S. Demokan "Pump-induced thermal effects in Er-Yb fiber grating DBR lasers", *IEEE Photon. Technol. Lett.* **10**, pp. 1253–1255 (1998)

[85] W. S. Man, Y. Z. Xu, H. Y. Tam, and M. S. Demokan, "Frequency instability in Er/Yb fiber grating lasers due to heating by nonradiative transitions", *IEEE Phot. Technol. Lett.* **11**, pp. 1390–1392 (1999)

[86] F. Kreith and W. Z. Black, *Basic Heat Transfer*, 1st edition, (Harper & Row, Publishers, New York, 1980)

[87] M. K. Davis, M. J. F. Digonnet, and R. H. Pantell, "Thermal effects in doped fibers", *J. Lightwave Technol.* **16**, pp. 1013–1023 (1998)

[88] W. D. Calister, jr. *Materials Science and Engineering*, 3rd edition, (John Wiley & Sons, New York, 1994)

[89] D. R. Lide, editor *Handbook of Chemistry and Physics*, 75th edition, (CRC Press, 1995)

[90] S.-Y. Huang, J. N. Blake, and B. Y. Kim, "Perturbation effects on mode propagation in highly elliptical core two-mode fibers", *J. Lightwave Technol.* **8**, pp. 23–33 (1990)

[91] J. Faber and F. Mead, *Reinforced Concrete*, Reprint, (E. & F. N. Spon Ltd., London, 1967)

[92] C. Galiotis and A. Paipetis, "Definition and measurement of shear-lag parameter, β, as an index of stress transfer efficiency in polymer composites", *J. Mat. Sci.* **33**, pp. 1137–1143 (1998)

[93] "Strain gage selection criteria, procedures, recommendations", *Tech Note* **TN-505-4** (Measurements Group, Inc., Raleigh, NC, USA, 1989)

[94] T. Erdogan, V. Mizrahi, P. J. Lemaire, and D. Monroe, "Decay of ultraviolet-induced fiber Bragg gratings", *J. Appl. Phys.* **76**, pp. 73–80 (1994)

[95] S. R. Baker, H. N. Rourke, V. Baker, and D. Goodchild, "Thermal decay of fiber Bragg gratings written in boron and germanium codoped silica fiber", *J. Lightwave Technol.* **15**, pp. 1470–1477 (1997)

[96] P. J. Lemaire, R. M. Atkins, V. Mizrahi, and W. A. Reed, "High pressure H_2 loading as a technique for achieving ultrahigh UV photosensitivity and thermal sensitivity in GeO_2 doped optical fibres", *Electron. Lett.* **29**, pp. 1191–1193 (1993)

[97] V. Mizrahi, P. J. Lemaire, T. Erdogan, W. A. Reed, D. J. DiGiovanni, and R. M. Atkins, "Ultraviolet laser fabrication of ultrastrong optical fiber gratings and of germania-doped channel waveguides", *Appl. Phys. Lett.* **63**, pp. 1727–1729 (1993)

[98] B. Malo, J. Albert, K. O. Hill, F. Bibileau, and D. C. Johnson, "Effective index drift from molecular hydrogen diffusion in hydrogen-loaded optical fibres and its effect in Bragg grating fabrication", *Electron. Lett.* **30**, pp. 442-444 (1994)

[99] L. D. Landau and E. M. Lifshitz, *Fluid Mechanics*, 1st edition, Reprint, (Pergamon Press 1982)

[100] H. Patrick, S. L. Gilbert, A. Lidgard, and M. D. Gallagher, "Annealing of Bragg gratings in hydrogen-loaded optical fiber", *J. Appl. Phys.* **78**, pp. 2940–2945 (1995)

[101] M. Ibsen, M. K. Durkin, M. J. Cole, and R. I. Laming, "Sinc-sampled fibre Bragg gratings for identical multiple wavelength operation", *IEEE Photon. Technol. Lett.* **10**, pp. 842–844 (1998)

[102] M. Ibsen, E. Rønnekleiv, O. Hadeler, G. J. Cowle, M. N. Zervas, and R. I. Laming, "Stable multiple wavelength generation in all-fibre DFB lasers", in *Bragg Gratings, Photosensitivity, and Poling in Glass Waveguides* Vol. 33 OSA Trends in Optics and Photonics Series (Optical Society of America, Washington DC, 2000), pp. 17–19

[103] W. H. Loh, J. P. de Sandro, G. J. Cowle, B. N. Samson, and A. D. Ellis, "40 GHz optical-millimetre wave generation with a dual polarisation distributed feedback fibre laser", *Electron. Lett.* **33**, pp. 594–595 (1997)

[104] W. Zhang, Y. C. Lai, J. A. R. Williams, L. Zangh, and I. Bennion, "A fibre grating DFB fibre laser for generation of optical microwave signal", *Opt. and Laser Technol.* **32**, pp. 369-371 (2000)

[105] A. Othonos, X. Lee, and R. M. Measures, "Superimposed multiple Bragg gratings", *Electron. Lett.* **30**, pp. 1972–1974 (1994)

[106] K. P. Koo and A. D. Kersey, "Noise and cross talk of a 4-element serial fiber laser sensor array", in *Optical Fibre Communication Conference* Vol. 2, OSA Tech. Digest Series (Optical Society of America, Washington DC, 1996), pp. 266–267

[107] K. Petermann, "External optical feedback phenomena in semiconductor lasers", *IEEE J. Selected Topics Quantum Electron.* **1**, pp. 480–489 (1995)

[108] D. Y. Stepanov, J. Canning, L. Pladian, R. Wyatt, G. Maxwell, R. Smith, and R. Kashyap, "Apodized distributed-feedback fiber laser", *Opt. Fiber Technol.* **5**, pp. 209-214 (1999)

[109] D. Marcuse, "Pulsing behaviour of a three-level laser with saturable absorber", *IEEE J. Quant. Electron.* **29**, pp. 2390–2396 (1993)

[110] N. Schunk and K. Petermann, "Stability analysis for laser diodes with short external cavities", *IEEE Photon. Technol. Lett.* **1**, pp. 49–51 (1989)

List of publications

1. O. Hadeler, M. Ibsen, and M. N. Zervas, "Distributed feedback fiber laser sensor for simultaneous strain and temperature measurements operating in the RF domain", *Appl. Opt.* **40**, pp. 3169–3175 (2001)

2. O. Hadeler and M. N. Zervas, "Application of a DFB fibre laser temperature sensor for characterizing pump induced temperature distribution along another DFB fibre laser", in *14th Int. Conf. Opt. Fiber Sens., Proc. SPIE* **4185**, pp. 142–145 (2000)

3. O. Hadeler, M. Ibsen, and M. N. Zervas, "Distributed feedback fibre laser sensor for simultaneous strain and temperature measurements in the RF domain", in *14th Int. Conf. Opt. Fiber Sens., Proc. SPIE* **4185**, pp. 588–591 (2000)

4. O. Hadeler, E. Rønnekleiv, M. Ibsen, and R. I. Laming, "Polarimetric distributed feedback fiber laser sensor for simultaneous strain and temperature measurements", *Appl. Opt.* **38**, pp. 1953–1958 (1999)

5. O. Hadeler, E. Rønnekleiv, M. Berendt, and M. Zervas, "Temperature distribution along DFB fibre lasers", *IEE Colloquium on Optical Fibre Gratings*, pp. 15/1–15/6 (1999)

6. O. Hadeler, D. J. Richards, and J. P. Dakin, "DFB fiber laser sensor for simultaneous strain and temperature measurements in concrete structures", in *6th Annual Int. Sympos. on Smart Materials and Structures, Proc. SPIE* **3670**, pp. 332–341 (1999)

7. M. Ibsen, E. Rønnekleiv, O. Hadeler, G. J. Cowle, R. I. Laming, and M. N. Zervas, "Advanced grating laser designs for microwave generation", *Rank Prize Fund Mini Symposium: Microwave Photonics* (Grasmere, 2000)

8. M. Ibsen, E. Rønnekleiv, O. Hadeler, G. J. Cowle, M. N. Zervas, and R. I. Laming, "Stable multiple wavelength generation in all-fibre DFB lasers",

in *Bragg Gratings, Photosensitivity, and Poling in Glass Waveguides*, Vol. 33, OSA Trends in Optics and Photonics Series (Optical Society of America, Washington DC, 2000), pp. 17–19

9. E. Rønnekleiv, O. Hadeler, and G. Vienne, "Stability of an Er-Yb-doped fiber distributed-feedback laser with external reflections", *Opt. Lett.* **24**, pp. 617–619 (1999)

10. M. Ibsen, E. Rønnekleiv, G. J Cowle, M. O. Berendt, O. Hadeler, M. N. Zervas, and R. I. Laming, "Robust high power (> 20 mW) all-fibre DFB lasers with unidirectional and truly single polarisation outputs", in *Conf. on Lasers and Electro-Optics 1999*, (Optical Society of America, Washington DC, 1999), pp. 245–246

11. J. P. Dakin, V. Foufelle, S. J. Russell, O. Hadeler, W. Ecke, E. Geinitz, R. Willsch, "Sensor network for structural strain and high hydraulic pressure using optical fiber grating pairs interrogated in the coherence domain", in *13th Int. Conf. Opt. Fiber Sens., Proc. SPIE* **3746**, pp. 157–160 (1999)

Acknowledgements

First of all I thank my supervisor Prof Michalis Zervas for his continuous interest in my research. A large part of this thesis is the result of the stimulating discussions about fundamental and theoretical aspects of DFB fibre lasers.

A special thank you goes to Mr Morten Ibsen who spent seemingly endless hours in the laboratory fabricating all the DFB fibre lasers without which this work would not have been possible.

Many thanks also to Dr Erlend Rønnekleiv and Dr Li-Bin Fu for the fruitful collaboration and some late hours in the laboratory.

I would like to say thank you to all past and present staff and students at the Optoelectronics Research Centre who have intentionally or unintentionally supported my work through technical, scientific and private conversations.

Dr Mike Lovegrove, Dr David Richards, Dr Duncan Lillistone, Mr Ken Yeates and Mr David Taylor from the Department of Civil and Environmental Engineering should not be forgotten for their help and expertise on all the issues related with embedding the DFB fibre laser sensors in concrete.

This thesis was partly supported through a CASE award by the BICC Group. Many thanks to Dr Bruce Butler, Dr Merrion Edwards, Richard Linton, Ian Knight and Nigel Taylor for the valuable discussions and their support.

Thanks also goes to Southampton Photonics Inc. for their interest in my research on DFB fibre lasers and their financial support.

And there has been a life away from fragile fibres, infrared photons, endless simulations and dirty concrete. Many thanks to the musicians I have seen performing in Turner Sims Concert Hall, the members of the various orchestras at the University

of Southampton and Southampton Concert Wind Band. As life in the form we know it would be non-existing without water I would like to thank the members of the University Staff Sailing Club for all the hours we have spent on the water and the mud. I also express my thanks to all my former housemates with whom I have spent many hours eating, drinking, hiking, cycling, and discussing work over dinner.
Thanks also go to my friends back in Germany, who still cannot understand how I can drink warm beer and go home at 11 pm. Maybe their interest in treating optical fibres and DFB fibre lasers with ultrasound will continue.
I would like to express my special thanks to Silvia for her patience and understanding while I was spending so much time with my two friends erbium and ytterbium.
Finally I wish to say thank you to my parents for their support during all my university life.